

2004

## Measurement of the branching fraction for neutral kaon(long) decaying to muon-electron-positron

andrew J. Norman  
*College of William & Mary - Arts & Sciences*

Follow this and additional works at: <https://scholarworks.wm.edu/etd>



Part of the [Physics Commons](#)

---

### Recommended Citation

Norman, andrew J., "Measurement of the branching fraction for neutral kaon(long) decaying to muon-electron-positron" (2004). *Dissertations, Theses, and Masters Projects*. Paper 1539623447.  
<https://dx.doi.org/doi:10.21220/s2-fzvr-xe97>

This Dissertation is brought to you for free and open access by the Theses, Dissertations, & Master Projects at W&M ScholarWorks. It has been accepted for inclusion in Dissertations, Theses, and Masters Projects by an authorized administrator of W&M ScholarWorks. For more information, please contact [scholarworks@wm.edu](mailto:scholarworks@wm.edu).

MEASUREMENT OF THE BRANCHING FRACTION FOR

$$K_L^0 \rightarrow \mu^+ \mu^- e^+ e^-$$

---

A Dissertation

Presented to

The Faculty of the Department of Physics

The College of William and Mary in Virginia

In Partial Fulfillment

Of the Requirements for the Degree of

Doctor of Philosophy

---

by

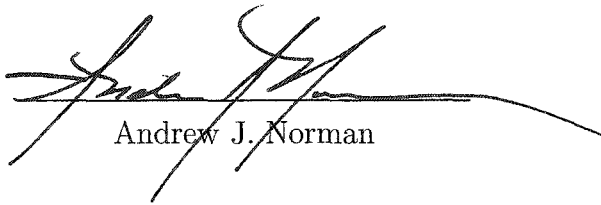
Andrew J. Norman

2004

## APPROVAL SHEET

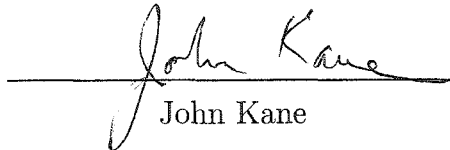
This dissertation is submitted in partial fulfillment of  
the requirements for the degree of

Doctor of Philosophy

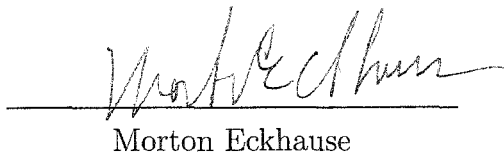


Andrew J. Norman

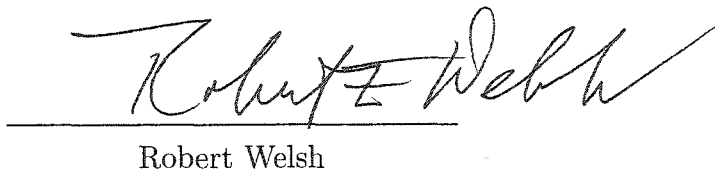
Approved, January 2004



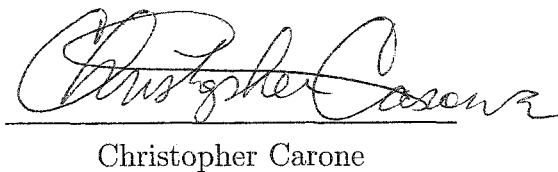
John Kane



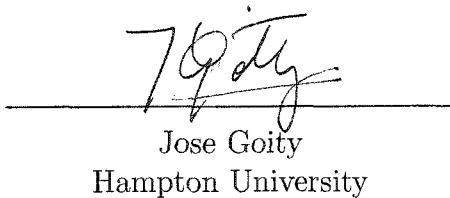
Morton Eckhause



Robert Welsh



Christopher Carone



Jose Goity  
Hampton University

To James and Mary Norman

“L’essentiel est invisible pour les yeux.” – Antoine de Saint-Exupéry



## CONTENTS

ACKNOWLEDGEMENTS . . . . .	x
LIST OF TABLES . . . . .	xii
LIST OF FIGURES . . . . .	xviii
ABSTRACT . . . . .	xix
CHAPTER	
1 Introduction . . . . .	2
2 Theory and Phenomenology . . . . .	5
2.1 The Standard Model . . . . .	5
2.1.1 Weak Flavor Changing Currents . . . . .	10
2.1.2 GIM Mechanism . . . . .	12
2.1.3 CKM Mixing . . . . .	13
2.1.4 Unitarity Bound . . . . .	17
2.2 The K Meson . . . . .	20
2.3 Weak Eigenstates and Basic Symmetries . . . . .	23
2.4 CP Violation . . . . .	27
2.4.1 Indirect and Direct CP Violation . . . . .	29
2.4.2 Measurement of $\varepsilon'/\varepsilon$ . . . . .	32
3 The Phenomenology of $K_{\gamma^*\gamma^*}$ and the Decay $K_L^0 \rightarrow \mu^+\mu^-e^+e^-$ . . . . .	36
3.1 Dispersive Amplitude and $K_L^0 \rightarrow \gamma^*\gamma^*$ . . . . .	36
3.2 Vector Meson Dominance Model (VDM) . . . . .	39

3.3	QCD model of $K_{\gamma^*\gamma^*}$ . . . . .	42
3.4	$\chi PT$ model of $K_{\gamma^*\gamma^*}$ . . . . .	47
3.5	CP violation and $\mathcal{F}(K_{\gamma^*\gamma^*})$ . . . . .	50
<b>4</b>	<b><math>K_L^0 \rightarrow \mu^+\mu^-e^+e^-</math> at E871</b> . . . . .	<b>53</b>
4.1	Motivation for $K_L^0 \rightarrow \mu^+\mu^-e^+e^-$ at E871 . . . . .	53
4.2	Prior Measurements of $K_L^0 \rightarrow \mu^+\mu^-e^+e^-$ . . . . .	56
4.3	Event Signature for $K_L^0 \rightarrow \mu^+\mu^-e^+e^-$ at E871 . . . . .	57
4.3.1	Decay Vertex . . . . .	60
4.3.2	Tracking Stubs . . . . .	60
4.4	Physics Backgrounds . . . . .	62
4.4.1	$K_L^0 \rightarrow \mu^+\mu^-\gamma$ . . . . .	62
4.4.2	$K_L^0 \rightarrow \pi^+\pi^-\gamma$ . . . . .	68
4.4.3	$K_L^0 \rightarrow \pi^+\pi^-\pi^0$ . . . . .	73
4.4.4	$K_L^0 \rightarrow \pi^+\pi^-e^+e^-$ . . . . .	74
4.4.5	$K_{e3}$ and $K_{\mu 3}$ Pileup . . . . .	75
<b>5</b>	<b>Experiment E871 Detector</b> . . . . .	<b>79</b>
5.1	E871 Detector System . . . . .	79
5.2	Kaon Production Target . . . . .	84
5.3	Neutral Beam Collimation . . . . .	85
5.4	Decay Tank . . . . .	86
5.5	Spectrometer . . . . .	89
5.6	Straw Drift Chambers . . . . .	91
5.7	Spectrometer Magnets . . . . .	95
5.8	Neutral Beam Stop . . . . .	96
5.9	Helium Balloons . . . . .	101
5.10	Drift Chambers . . . . .	102

5.11	Trigger Scintillation Counters . . . . .	103
5.12	Threshold Čerenkov Counter . . . . .	109
5.13	Lead Glass Array (PBG) . . . . .	116
5.14	The Muon Hodoscope . . . . .	119
5.15	Muon Range Stack . . . . .	123
5.16	Muon Range Finder . . . . .	127
<b>6</b>	<b>Hardware Trigger and Data Acquisition . . . . .</b>	<b>133</b>
6.1	Overview . . . . .	133
6.2	Level 0 Trigger . . . . .	134
6.3	Level 1 Trigger . . . . .	137
6.4	Level 3 Trigger . . . . .	139
<b>7</b>	<b>Monte Carlo Modeling . . . . .</b>	<b>144</b>
7.1	Monte Carlo Simulations . . . . .	144
7.1.1	Geant Simulation . . . . .	145
7.1.2	E871 Detector Simulation . . . . .	146
7.2	Blind Analysis . . . . .	147
7.3	Monte Carlo Goals . . . . .	149
7.3.1	Event Characteristics . . . . .	149
7.3.2	Detector Acceptances . . . . .	151
7.3.3	Physics Background . . . . .	152
7.4	Kaon Modeling . . . . .	155
7.4.1	Kaon Momentum . . . . .	156
7.4.2	Kaon Decay . . . . .	158
7.4.3	Multiple Coulomb Scattering . . . . .	160
7.5	Monte Carlo Form Factors . . . . .	163
7.5.1	Four Body Decay Kinematics . . . . .	163

7.5.2	Vector Meson Dominance Model Form Factor . . . . .	165
7.5.3	QCD Form Factor . . . . .	166
7.5.4	$\chi PT$ Form factor . . . . .	169
<b>8</b>	<b>Vertex and Stub Analysis . . . . .</b>	<b>172</b>
8.1	Event Reconstruction . . . . .	172
8.1.1	Invariant Mass . . . . .	174
8.1.2	Vertex Definition . . . . .	180
8.1.3	Transverse Momentum and Collinearity . . . . .	182
8.2	Distance of Closest Approach (DOCA) . . . . .	186
8.2.1	Track to Track . . . . .	187
8.2.2	Vertex Position . . . . .	188
8.2.3	Track to Point . . . . .	189
8.2.4	Punctured Plane . . . . .	190
8.2.5	Secant Correction . . . . .	192
8.2.6	Standard Minimization . . . . .	194
8.3	Partial Tracking Stubs . . . . .	196
8.3.1	Stub Recognition . . . . .	197
8.3.2	Decay Plane Correlation . . . . .	200
8.3.3	Stub Pair Correlation . . . . .	207
8.4	Primary vertex reconstruction with partial tracks . . . . .	212
8.4.1	Three and Four body Invariant mass . . . . .	215
8.4.2	Three and Four Body Event Transverse Momentum . . . . .	217
8.5	Tracking and Vertex Corrections . . . . .	219
8.5.1	Magnetic fringe field deflection . . . . .	220
<b>9</b>	<b>Production Analysis and Cuts . . . . .</b>	<b>226</b>
9.1	$\mu\mu$ Vertex Cuts . . . . .	226

9.1.1	Primary Vertex Fiducial Volume Cut . . . . .	227
9.1.2	Muon Track Momentum Cut . . . . .	228
9.1.3	Muon Track $\chi^2$ Cut . . . . .	230
9.1.4	$\mu\mu$ Vertex DOCA and $\chi^2$ Cut . . . . .	232
9.1.5	$K_{\mu\mu}$ Invariant Mass Cut . . . . .	233
9.1.6	$K_{\mu\mu}$ Transverse Momentum Cut . . . . .	233
9.2	Muon Particle Id Cuts . . . . .	236
9.3	Partial Tracking Id Cuts . . . . .	238
9.3.1	Segment Ambiguity Cut . . . . .	238
9.3.2	Single Stub Vertex DOCA . . . . .	239
9.3.3	Stub To Stub DOCA . . . . .	240
9.3.4	Primary/Secondary Vertex Separation . . . . .	241
9.3.5	Secondary Vertex Fiducial Volume Cut . . . . .	243
9.4	Stub Correlation Cuts . . . . .	243
9.4.1	Single Stub To Primary Decay Plane Cut . . . . .	244
9.4.2	Stub To Stub Opening Angle Cut . . . . .	244
9.4.3	Secondary To Primary Decay Plane Cut . . . . .	246
9.5	Event Reconstruction Cuts . . . . .	246
9.5.1	Invariant Mass Reconstruction Cuts . . . . .	247
9.5.2	Transverse momentum Cuts . . . . .	250
9.6	Summary of Production Analysis Cuts . . . . .	251
<b>10</b>	<b>Normalization . . . . .</b>	<b>253</b>
10.1	$K_L^0 \rightarrow \mu^+\mu^-$ Data Sample . . . . .	254
10.2	$K_L^0 \rightarrow \mu^+\mu^-e^+e^-$ Data Sample . . . . .	255
10.3	Acceptances . . . . .	259
10.4	Model Dependent Normalization . . . . .	259

<b>11 Results and Conclusions</b> . . . . .	<b>261</b>
11.1 Results . . . . .	261
11.2 Errors . . . . .	262
11.2.1 Statistical Error ( $\sigma_{stat}$ ) . . . . .	263
11.2.2 Systematic Error ( $\sigma_{sys}$ ) . . . . .	264
11.3 Conclusions . . . . .	265
11.4 Collaborative Effort and Contributions . . . . .	266
<b>APPENDIX A</b>	
<b>E871 Collaboration</b> . . . . .	<b>268</b>
<b>APPENDIX B</b>	
<b>Four body phase space transforms</b> . . . . .	<b>270</b>
<b>BIBLIOGRAPHY</b> . . . . .	<b>273</b>
<b>VITA</b> . . . . .	<b>276</b>

## ACKNOWLEDGEMENTS

The research included in this dissertation could not have been performed if not for the assistance, patience, and support of many individuals. I would like to extend my gratitude first and foremost to my thesis advisor John Kane for mentoring me over the course of my undergraduate and graduate studies. His insight led to the original proposal to examine the possibility of re-examining the sensitivities of the E871 data set, and ultimately led to the undertaking of the search for  $K_L^0 \rightarrow \mu^+ \mu^- e^+ e^-$  at E871. He has helped me through extremely difficult times over the course of the analysis and the writing of the dissertation and for that I sincerely thank him for his confidence in me.

I would additionally like to thank Morton Eckhause for his support in both the research and especially the revision process that has led to this document. His knowledge and understanding of the written word has allowed me to fully express the concepts behind this research.

I would also like to extend my appreciation to Robert Welsh who has served as a voice of quiet wisdom in matters ranging from the most basic aspects of the experiment, to the paths that my career has eventually taken.

This research would not have been possible without the assistance of the E871 experimental collaboration who constructed the experimental apparatus and built the foundations for the data analysis. In particular I would like to thank David Ambrose for his work on muon identification and extraction of the  $K_L^0 \rightarrow \mu^+ \mu^-$  data stream.

Finally I would like to extend my deepest gratitude to my parents James and Mary Norman without whose love, support and understanding I could never have completed this doctoral degree.

This research was supported in part by the National Science Foundation, Grant PHY 98-03848 and Grant PHY 00-99687.

## LIST OF TABLES

2.1	Lepton Properties . . . . .	6
2.2	Quark Properties . . . . .	8
2.3	Unitary limits on dilepton decays of $K_L^0$ . . . . .	19
2.4	Kaon properties . . . . .	25
3.1	Parameter sets for the chiral expansion of $\mathcal{F}(t, t')$ . . . . .	49
3.2	Branching fraction calculations for $K_L^0 \rightarrow \mu^+ \mu^- e^+ e^-$ . . . . .	50
4.1	Pair production material properties . . . . .	64
4.2	Pair production interaction lengths . . . . .	65
4.3	Pair production probabilities . . . . .	65
4.4	Expected $K_L^0 \rightarrow \mu^+ \mu^- \gamma$ background events . . . . .	67
4.5	Geometrically accepted $K_L^0 \rightarrow \mu^+ \mu^- \gamma$ background events . . . . .	68
5.1	Transverse momentum for $K_L$ decay modes [12] . . . . .	98
5.2	Čerenkov threshold momenta . . . . .	112
5.3	Muon hodoscope detector placement . . . . .	120
5.4	Muon hodoscope scintillator dimensions . . . . .	122
5.5	Muon range finder material properties . . . . .	127
5.6	Muon range stack material placement . . . . .	128



5.7	Muon range finder stopping momenta . . . . .	130
6.1	Level 1 event triggers . . . . .	139
7.1	Multiple scattering materials and apertures . . . . .	162
9.1	Vertex Position Cuts . . . . .	228
9.2	Vertex Position Cuts . . . . .	230
9.3	Muon Track $\chi^2$ Cuts . . . . .	231
9.4	Primary Event Vertex $\chi^2$ Cuts . . . . .	232
9.5	$K_L^0 \rightarrow \mu^+\mu^-$ Invariant Mass Window . . . . .	235
9.6	$\mu\mu$ Transverse Momentum Cuts . . . . .	235
9.7	Stub Identification Cuts . . . . .	242
9.8	Secondary Vertex Position Cuts . . . . .	243
9.9	Summary of Cuts for $K_L^0 \rightarrow \mu^+\mu^-$ . . . . .	252
10.1	$K_L^0 \rightarrow \mu^+\mu^-$ Signal and Background . . . . .	255
10.2	Acceptance Ratios for Differing Form Factor models . . . . .	260
10.3	$K_L^0 \rightarrow \mu^+\mu^-e^+e^-$ Branching Fraction Differing Form Factor models . . . . .	260

## LIST OF FIGURES

2.1 Primitive electro-weak lepton interactions . . . . .	7
2.2 Primitive strong, E&M, and weak quark interactions . . . . .	9
2.3 First order weak flavor changing kaon decay processes . . . . .	11
2.4 Second order weak $\Delta S = 1$ contributions to $\Gamma(K_L^0 \rightarrow \mu^+ \mu^-)$ . . . . .	14
2.5 Geometric representation of the unitary triangle . . . . .	16
2.6 Leading order absorptive contribution to $K_L^0 \rightarrow \ell \bar{\ell}$ . . . . .	19
2.7 $K^0$ to $\bar{K}^0$ mixing via an intermediate pion loop . . . . .	22
2.8 $K^0$ to $\bar{K}^0$ mixing via a second order $\Delta S = 2$ weak interaction . . . . .	22
2.9 Leading order box diagrams contributing $K^0$ to $\bar{K}^0$ mixing . . . . .	23
2.10 Neutral kaon production via strong interaction . . . . .	26
2.11 Intermediate quark contributions to $K^0$ to $\bar{K}^0$ mixing . . . . .	33
3.1 Short distance weak diagrams contributing to $K_L^0 \rightarrow \mu^+ \mu^-$ . . . . .	37
3.2 Long distance dispersive diagram for $K_L^0 \rightarrow \mu^+ \mu^-$ . . . . .	39
3.3 Long distance dispersive pole diagram for $K_L^0 \rightarrow \gamma^* \gamma^*$ . . . . .	40
3.4 Long distance dispersive diagram for $K_L^0 \rightarrow \gamma^* \gamma^*$ with vector meson couplings . . . . .	41
3.5 Loop order QCD diagrams contributing to $K_L^0 \rightarrow \gamma^* \gamma^*$ . . . . .	43
3.6 Lowest order effective quark diagrams contributing to $K_L^0 \rightarrow \gamma^* \gamma^*$ . . . . .	45
4.1 Long distance dispersive diagram for $K_L^0 \rightarrow \mu^+ \mu^- e^+ e^-$ . . . . .	55

4.2	Monte Carlo invariant mass reconstructions for $K_L^0 \rightarrow \mu^+\mu^-e^+e^-$ . . .	59
4.3	Low momentum $e^+e^-$ -partial tracking stubs . . . . .	61
4.4	$K_L^0 \rightarrow \mu^+\mu^-\gamma$ differential and integrated decay rates . . . . .	66
4.5	Inner Bremsstrahlung and Direct Emission contributions to $K_L^0 \rightarrow \pi^+\pi^-\gamma$ . . . . .	69
4.6	Maximum invariant mass reconstructions for $K_L^0 \rightarrow \pi^+\pi^-\gamma$ . . . . .	72
4.7	$K_{\mu 3}$ and $K_{e 3}$ Dalitz plots . . . . .	77
5.1	Brookhaven National Labs AGS . . . . .	80
5.2	E871 Experimental apparatus . . . . .	81
5.3	E871 Experimental apparatus . . . . .	82
5.4	E871 Spectrometer and particle identification . . . . .	83
5.5	AGS B5 neutral beamline for experiment E871 . . . . .	87
5.6	E871 primary decay region geometry . . . . .	88
5.7	Residual gas spectrum . . . . .	89
5.8	E871 spectrometer overview . . . . .	90
5.9	E871 forward spectrometer detailed schematic . . . . .	91
5.10	Straw drift chamber layer geometry . . . . .	93
5.11	Straw drift chamber X/Y layer arrangement . . . . .	93
5.12	Analyzing magnets 96D40/D02 and 100D40/D03 . . . . .	97
5.13	Cross sectional view of E871 compact beam stop . . . . .	100
5.14	Drift chamber rate comparison . . . . .	100
5.15	E871 primary decay tank window including He filled Mylar bag . . .	102
5.16	X-measuring hexagonal drift cells cross section . . . . .	104
5.17	Simple single edge readout scintillator and phototube readout system	105

5.18	Trigger Scintillation Counters in modules TSC1 and TSC2 . . . . .	107
5.19	Trigger Scintillation Counter slat plane designs for TSC1 and TSC2 . . . . .	108
5.20	Čerenkov light cone construction . . . . .	111
5.21	E871 Čerenkov counter exterior geometry . . . . .	112
5.22	Burle 8854 phototube with mu shielding . . . . .	113
5.23	Overlap of Čerenkov mirrors with X measuring TSC slats . . . . .	115
5.24	E871 Čerenkov counter interior geometry . . . . .	115
5.25	E871 lead glass array . . . . .	117
5.26	Muon Hodoscope detector plane layout . . . . .	120
5.27	Muon Hodoscope detector plane design . . . . .	121
5.28	Laboratory frame muon momenta for $K_L^0 \rightarrow \mu^+ \mu^- e^+ e^-$ . . . . .	123
5.29	E871 muon range stack . . . . .	129
5.30	Muon Range Finder extrusion panel . . . . .	131
6.1	E871 DAQ system overview . . . . .	135
6.2	Schematic overview of a level 1 event trigger . . . . .	140
7.1	Signal region blackout for blind analysis . . . . .	148
7.2	Decay planes as defined by the event vertex and particle momenta $p_{\ell_i}$ . . . . .	151
7.3	Uniform Dalitz plot for $K_L^0 \rightarrow \mu^+ \mu^- \gamma$ in the kaon rest frame . . . . .	153
7.4	Laboratory frame muon momenta for $K_L^0 \rightarrow \mu^+ \mu^- \gamma$ . . . . .	154
7.5	Invariant mass reconstructions for $K_L^0 \rightarrow \mu^+ \mu^- \gamma$ using $\mu^+ \mu^-$ tracking pairs . . . . .	154
7.6	E871 $K_L^0$ production cross section . . . . .	158
7.7	E871 $K_L^0$ momentum spectrum . . . . .	159

7.8	E871 $K_L^0$ primary decay point simulation . . . . .	160
7.9	Electron and positron momentum spectra for $K_L^0 \rightarrow \mu^+ \mu^- e^+ e^-$ . . . . .	162
7.10	Double internal conversion of a pseudoscalar meson into lepton pairs . . . . .	165
7.11	Model of the QCD form factor for $K_L^0 \rightarrow \mu^+ \mu^- e^+ e^-$ . . . . .	168
7.12	Model of the Chiral form factor for $K_L^0 \rightarrow \mu^+ \mu^- e^+ e^-$ . . . . .	171
8.1	Multi-body invariant mass reconstructions . . . . .	178
8.2	E871 accepted multi-body invariant mass reconstructions . . . . .	179
8.3	XY Vertex Distribution . . . . .	181
8.4	Vertex definition . . . . .	182
8.5	Collinearity definition . . . . .	184
8.6	Electron and Muon transverse momenta . . . . .	185
8.7	$e^-$ to $e^+$ momentum asymmetry . . . . .	185
8.8	Secant correction to DOCA value . . . . .	192
8.9	SDC PATREC Hit Cluster . . . . .	199
8.10	SDC1/SDC2 Cluster Matching . . . . .	200
8.11	Stub Candidate to Primary Vertex DOCA . . . . .	201
8.12	Primary decay plane angles . . . . .	202
8.13	Singlet stub correlations . . . . .	205
8.14	Fits to singlet stub correlations . . . . .	206
8.15	Monte Carlo opening angle of stub pairs . . . . .	208
8.16	Opening angle of stub pairs . . . . .	209
8.17	Primary and secondary decay plane geometries . . . . .	210
8.18	Secondary decay plane angle (X) . . . . .	210
8.19	Secondary decay plane angle (Y) . . . . .	211

8.20	Secondary decay plane angle ( $Z$ ) . . . . .	211
8.21	Primary to secondary decay plane correlation . . . . .	212
8.22	Muon pair transverse momentum . . . . .	213
8.23	Collinearity angles for electron stubs . . . . .	214
8.24	Reconstructed partial track momentum . . . . .	215
8.25	$K_{\mu\mu ee}$ four body invariant mass reconstructions . . . . .	216
8.26	$K_{\mu\mu ee}$ three body invariant mass reconstructions . . . . .	217
8.27	Transverse momentum reconstructs . . . . .	219
8.28	Low energy electron deflection in magnetic fringe field . . . . .	222
8.29	Field strength and angular dependence of deflection in magnetic fringe field . . . . .	223
8.30	Low energy electron deflection geometry . . . . .	224
8.31	In-bend/out-bend deflection of low energy $e^-/e^+$ pairs . . . . .	225
9.1	Vertex Distributions and Fiducial Volume Cuts . . . . .	229
9.2	Invariant Mass Window and Transverse Momentum Cuts . . . . .	234
9.3	$K_L^0 \rightarrow \mu^+\mu^-$ Signal Box . . . . .	236
9.4	Lead glass array electron/pion separation contour . . . . .	237
9.5	Total Event Stubs Cuts . . . . .	239
9.6	Stub to Vertex DOCA Cut . . . . .	240
9.7	Stub to Stub DOCA Cut . . . . .	241
9.8	Primary to Secondary Vertex Separation Cut . . . . .	242
9.9	Stub to decay plane angle cut . . . . .	244
9.10	Stub to Stub opening angle cut . . . . .	245
9.11	Primary to Secondary Decay Plane Angle Cut . . . . .	247

9.12	Two body Invariant Mass Cut . . . . .	248
9.13	Three body Invariant Mass Cut . . . . .	249
9.14	Two body Invariant Mass Cut . . . . .	250
9.15	$K_L^0 \rightarrow \mu^+\mu^-e^+e^-$ Invariant Mass Under Rough Cuts . . . . .	251
10.1	$K_L^0 \rightarrow \mu^+\mu^-$ Signal Peak (FT) . . . . .	256
10.2	$K_L^0 \rightarrow \mu^+\mu^-$ Signal Peak (QT) . . . . .	257
10.3	$K_L^0 \rightarrow \mu^+\mu^-e^+e^-$ Signal Peak . . . . .	258

## ABSTRACT

This dissertation describes the measurement of the decay of the long lived neutral kaon into two muons and two electrons. The measurement was performed using the data taken during experiment E871 which was performed on the B5 beamline at the Alternating Gradient Synchrotron (AGS) of the Brookhaven National Laboratory (BNL). The branching ratio  $B(K_L^0 \rightarrow \mu^+ \mu^- e^+ e^-)$  is sensitive to the absorptive portion of the long distance amplitude for decays of the form  $K_L^0 \rightarrow \ell^+ \ell^-$  and can be used to properly extract the short distance weak interaction amplitudes from the dileptonic events.

Measurement of  $K_L^0 \rightarrow \mu^+ \mu^- e^+ e^-$  additionally allows for the exploration of the form factor for the  $K_L^0 \rightarrow \gamma^* \gamma^*$  vertex. Measurement of the  $K_L^0 \rightarrow \mu^+ \mu^- e^+ e^-$  branching fraction from the E871 data set provides a sensitive probe to distinguish between form factors arising from a chiral theory near the kaon mass, a low energy quark/QCD theory, a vector meson dominance model, models with CP violation and models which exhibit a uniform phasespace.

The analysis of the data from the E871  $\mu\mu$  data stream observed 119  $K_L^0 \rightarrow \mu^+ \mu^- e^+ e^-$  events on a measured background of 52 events. The  $K_L^0 \rightarrow \mu^+ \mu^- e^+ e^-$  event sample was normalized using a simultaneously measured sample of 5685  $K_L^0 \rightarrow \mu^+ \mu^-$  events. The resulting branching fraction for  $K_L^0 \rightarrow \mu^+ \mu^- e^+ e^-$  was calculated to be  $2.78 \pm 0.41 \pm 0.09 \times 10^{-9}$  under the assumption of a  $\chi$ PT form factor. The results are consistent with the previous world average for  $B(K_L^0 \rightarrow \mu^+ \mu^- e^+ e^-)$  of  $2.6 \pm 0.4 \times 10^{-9}$  and increase the total number of  $K_L^0 \rightarrow \mu^+ \mu^- e^+ e^-$  events observed world wide from 133 to 252.



MEASUREMENT OF THE BRANCHING FRACTION FOR  $K_L^0 \rightarrow \mu^+ \mu^- e^+ e^-$

# CHAPTER 1

## Introduction

This thesis details the experimental search for the decay of a long lived neutral kaon into a four lepton final state consisting of two muons and two electrons. Searches for rare decays access high energy regimes found through the interaction of virtual particle states and allow measurement of the fundamental processes by which matter interacts. The kaon sector in particular is rich in the manner by which it accesses the strong, weak and electromagnetic interactions. The melding of these three interactions at low laboratory energies provides a rich system in which to test our understanding of their couplings and assess the validity of recent models that have been postulated to describe this moderate energy regime.

The four lepton final state examined here is motivated by multiple factors. The decay branch  $B(K_L^0 \rightarrow \mu^+\mu^-e^+e^-)$  is closely tied to the dileptonic decays  $B(K_L^0 \rightarrow \mu^+\mu^-)$  and  $B(K_L^0 \rightarrow e^+e^-)$ . In each case proper extraction of the decay amplitudes relating to the highly suppressed second order diagrams involving a weak flavor changing neutral current, requires knowledge of the intermediate virtual decay state  $K_L^0 \rightarrow \gamma^*\gamma^*$ . This amplitude can be recovered directly from knowledge of the branching ratio for  $K_L^0 \rightarrow \mu^+\mu^-e^+e^-$  and the unitary bound on the decay. In the

case of  $B(K_L^0 \rightarrow \mu^+\mu^-)$  this is of particular interest in order to measure the mixing angles of the CKM matrix relating the top and charm quarks.

The second motivation for measuring the decay  $K_L^0 \rightarrow \mu^+\mu^-e^+e^-$  is to determine the influence of various form factors on the resulting decay spectrum of the interaction. These form factors are accessible in the decay owing to the distinct nature of the final state particles. In particular, interference caused by cross terms arising from particle interchange in the other four lepton final state decays  $K_L^0 \rightarrow \mu^+\mu^- \mu^+\mu^-$  and  $K_L^0 \rightarrow e^+e^-e^+e^-$  are absent in the distinct final state of  $K_L^0 \rightarrow \mu^+\mu^-e^+e^-$ . This allows for the decay to distinguish the competing theories of a vector meson dominated model(VDM), a model with CP violating currents, and models using effective low energy coupling for the quarks within the framework of chiral perturbation theory. The enhancements in the kinematic spectrum for each of these is distinct and of value in marking the validity of each model.

Prior to the examination of this data set a single event for this decay had been observed and reported with a branching fraction of  $2.9_{-2.4}^{+6.7} \times 10^{-9}$  by the KTeV experiment E799 [1]. Through study of the four body decay and its kinematic signatures under the various form factors in question, it was determined that improvement in this measurement was possible using the  $K_L^0 \rightarrow \mu^+\mu^-$  data set from experiment E871 performed at the Alternating Gradient Synchrotron (AGS) of the Brookhaven National Lab (BNL).

Experiment E871 was designed and constructed as a search for rare dileptonic decay modes of the long lived neutral kaon. The experiment was a collaboration among researchers from the *University of Texas (Austin)*, *Stanford University*, *University of California (Irvine)*, the *College of William and Mary*, and the *University of Richmond*. Over 30 researchers participated in the collaboration. They are listed in Appendix A, together with the set of E871 publications. The primary goals of E871 were the measurement of the decay branching fractions for  $K_L^0 \rightarrow \mu^+\mu^-$  [2],

$K_L^0 \rightarrow e^+e^-$  [3], and a search for the decay  $K_L^0 \rightarrow \mu^\pm e^\mp$  [4]. In addition to these primary investigations, other processes were examined which could be extracted from the primary data streams.

The data used in the examination of the decay  $K_L^0 \rightarrow \mu^+\mu^-e^+e^-$  were extracted from the  $K_L^0 \rightarrow \mu^+\mu^-$  data stream of E871. The data were analyzed using the E871 analysis code and Monte Carlo modeling system, as well as with Geant simulations. Normalization of the final branching fraction results was performed with respect to the decay rate for  $K_L^0 \rightarrow \mu^+\mu^-$  [2].

Due to the nature of the experiment and the complexity of the extraction of the decay amplitude substantial analysis both of the theoretical and experimental methods is discussed herein. Chapter 2 discusses the rich theory and phenomenology that applies to the neutral kaon system. Chapter 3 relates the general phenomenology to the model dependent aspects and characteristics of measuring  $B(K_L^0 \rightarrow \mu^+\mu^-e^+e^-)$ .

Chapter 4 discusses the experimental aspects of measuring the decay rate. The event signatures and background decay contributions that were considered in E871 are specifically included as well as analysis of the allowed phase space to which the experiment was sensitive. The experimental equipment and data systems are discussed in chapters 5 and 6.

Key aspects of the data analysis unique to the search for  $K_L^0 \rightarrow \mu^+\mu^-e^+e^-$  are covered in chapter 8 dealing with the methods used to determine the event vertex and the identification of partial tracking stubs in the forward spectrometer. The full production analysis is presented in chapter 9 and the normalization of the data to  $K_L^0 \rightarrow \mu^+\mu^-$  is covered in chapter 10.

The final results and conclusions are covered in chapter 11 along with recent findings and prospects for the future.

# CHAPTER 2

## Theory and Phenomenology

### 2.1 The Standard Model

The standard model of modern particle physics developed in the 1970's attempts to describe on the most basic level, the particle structure of matter and its interactions via the fundamental forces. Within the standard model all matter consists of a finite irreducible set of spin-1/2 particles denoted as fermions that interact via the exchange of integral spin bosons. The bosons in the theory act as the force carriers for the electro-weak and strong nuclear forces. The fermions are subdivided into the classifications of leptons and quarks based on their electric charge and their ability to interact with the strong nuclear force.

Leptons are observed to exist with integral or zero electric charge as defined in units of the charge of the electron. There are three flavors of leptons forming a progressive mass hierarchy in a doublet arranged structure whereby each charged

Lepton	Mass	Charge	$L_e$	$L_\mu$	$L_\tau$
$e^-$	0.51 MeV	$-1e$	1	0	0
$\mu^-$	105.65 MeV	$-1e$	0	1	0
$\tau^-$	1777.03 MeV	$-1e$	0	0	1
$\nu_e$	$< 3$ eV	0	1	0	0
$\nu_\mu$	$< 0.19$ MeV	0	0	1	0
$\nu_\tau$	$< 18.2$ MeV	0	0	0	1

TABLE 2.1: Lepton Properties

lepton is associated with a light, neutrally charged particle denoted as a neutrino,

$$\begin{pmatrix} e \\ \nu_e \end{pmatrix} \quad \begin{pmatrix} \mu \\ \nu_\mu \end{pmatrix} \quad \begin{pmatrix} \tau \\ \nu_\tau \end{pmatrix} \quad (2.1)$$

The three leptons, the electron, muon, and tau each with negative charge are taken as the base particles states while their charge conjugates the  $e^+$ ,  $\mu^+$ , and  $\tau^+$  are denoted as their anti-particles states. The neutrinos are taken to be essentially massless, grouped into three generations corresponding to their associated leptons. Within the standard model there exists no mechanism which in a direct fashion provides for horizontal mixing between the lepton families; as a result members of each family are assigned a quantum number  $L_\ell$  corresponding to the lepton flavor of the particle.

The distinguishing feature of the leptons is that they do not experience a direct interaction with the strong nuclear force. All lepton interactions occur through primitive electro-weak interaction couplings, shown in Fig. 2.1, and as such are a sensitive probe into the structure of the weak currents.

In contrast to leptons, quarks are distinguished by their interactions with the strong nuclear force and their fractional electric charge. Strong force binding and confinement lead quarks to form the fundamental substructure for all hadronic mat-

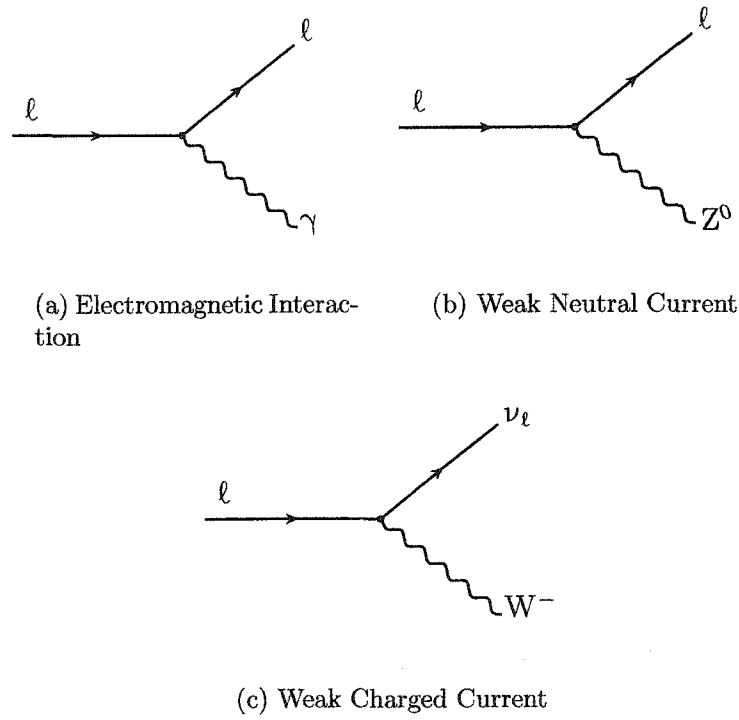


FIG. 2.1: Primitive electro-weak lepton interactions

Quark	Mass	Charge	Properties
u	1 – 5 MeV/c <sup>2</sup>	$\frac{2}{3}e$	$I_z = \frac{1}{2}$
d	3 – 9 MeV/c <sup>2</sup>	$-\frac{1}{3}e$	$I_z = -\frac{1}{2}$
c	1.15 – 1.35 GeV/c <sup>2</sup>	$\frac{2}{3}e$	Charm = +1
s	75 – 170 MeV/c <sup>2</sup>	$-\frac{1}{3}e$	Strangeness = -1
t	$\approx 174$ GeV/c <sup>2</sup>	$\frac{2}{3}e$	Top = +1
b	4.0 – 4.4 GeV/c <sup>2</sup>	$-\frac{1}{3}e$	Bottom = -1

TABLE 2.2: Quark Properties

ter, either in the form of a color neutral three quark bound states that form the common baryons such as the proton and neutron, or in quark-antiquark bound state mesons such as the  $\pi$ ,  $K$ ,  $\eta$ , and  $\rho$ . Free quarks are not accessible due to the requirements of color neutrality and strong force confinement at low energies. Similar to the leptons there exists a generational hierarchy of distinct quark flavor doublets based on the masses of each quark and their associated quantum properties. Each generation consists of two quarks each with fractional electric charges equal to  $-\frac{1}{3}$  and  $\frac{2}{3}$  the charge magnitude of the electron. There exists evidence for three such quark generations whose associated quarks we label as *up*, *down*, *charm*, *strange*, *top*, *bottom*. They are arranged in flavors doublets as:

$$\begin{pmatrix} u \\ d \end{pmatrix} \quad \begin{pmatrix} c \\ s \end{pmatrix} \quad \begin{pmatrix} t \\ b \end{pmatrix} \quad (2.2)$$

The mass hierarchy of the quark doublets is clear from Table 2.2. As with the leptons, each quark flavor has a corresponding anti-particle state leading to a total of 12 distinct particles. These quarks have strong, weak, and electro-magnetic interactions as shown in Fig. 2.2. Unlike the lepton sector the weak interaction vertex can mix quark flavors between generations leading to  $s \rightarrow u$  like processes arising via weak currents.



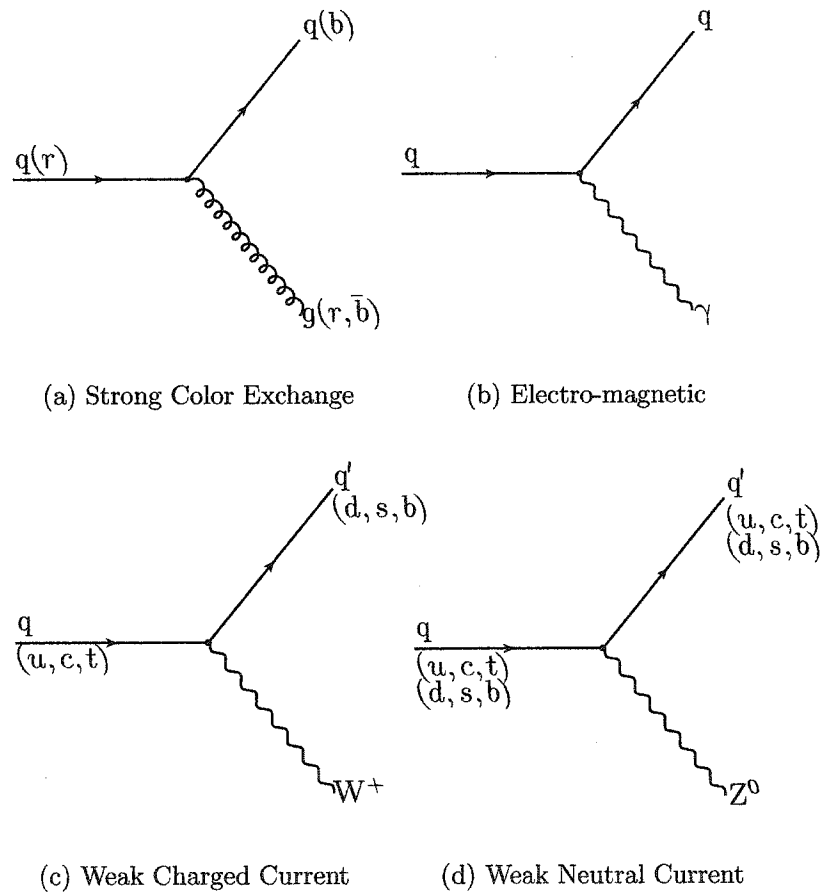


FIG. 2.2: Primitive strong, E&M, and weak quark interactions

### 2.1.1 Weak Flavor Changing Currents

Quark interactions through the weak charged and neutral currents, as shown in Fig. 2.2(c) and 2.2(d) allow for flavor mixing between the quark generations. The strangeness violating decay  $K^+ \rightarrow \mu^+ \nu_\mu$  occurs through a first order interaction of this type as shown in Fig. 2.3(a). For the charged kaon this is the dominant decay, accounting for over 63% of the decays. For the neutral kaon a similar first order weak current would be expected to dominate the allowable decay branches. The decay  $K^0 \rightarrow \mu^+ \mu^-$  follows at leading order the weak neutral current diagram of Fig. 2.3(b) and thus in analogy to the charged kaons would be expected to dominate the system. The two muon decay of  $K^0$  is highly suppressed and only occurs with a branching fraction of  $\approx 7 \times 10^{-9}$ .

To explain the suppression of the weak flavor changing currents, Cabibbo postulated that the quark doublet for the weak interaction consisted of the up quark and an additive mixture of the down and strange quarks rotated through an angle  $\theta_C$ [5].

$$\begin{pmatrix} u \\ d' \end{pmatrix}_L = \begin{pmatrix} u \\ d \cos \theta_C + s \sin \theta_C \end{pmatrix}_L \quad (2.3)$$

The value  $\theta_C \approx 0.26$  or approximately  $12^\circ$ , is obtained through the ratio of the decay rates for  $K^+ \rightarrow \mu \nu$  to  $\pi^+ \rightarrow \mu \nu$ . Using the Cabibbo angle, the strong and weak eigenstates can be connected by a simple rotation matrix:

$$\begin{pmatrix} d' \\ s' \end{pmatrix} = \begin{pmatrix} \cos \theta_C & \sin \theta_C \\ -\sin \theta_C & \cos \theta_C \end{pmatrix} \begin{pmatrix} d \\ s \end{pmatrix} \quad (2.4)$$

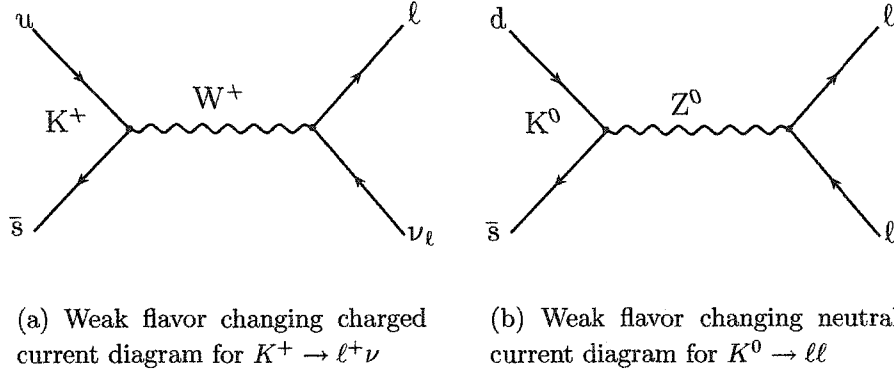


FIG. 2.3: First order weak flavor changing kaon decay processes

The weak charged and neutral currents now can be written as:

$$J_\mu^{CC} = (\bar{d} \cos \theta_C + \bar{s} \sin \theta_C) \gamma_\mu (1 - \gamma_5) u, \quad \text{and} \quad (2.5)$$

$$J_\mu^{NC} = (\bar{d} \cos \theta_C + \bar{s} \sin \theta_C) \gamma_\mu (1 - \gamma_5) (d \cos \theta_C + s \sin \theta_C) \quad (2.6)$$

In this manner taking  $G$  to be the weak coupling constant, the charged current  $\Delta S = 0$  interactions such as  $u \leftrightarrow d$  are coupled via a factor of  $G \cos \theta_C$  while the ( $\Delta S = 1$ )  $u \leftrightarrow s$  transitions are suppressed by a factor of  $G \sin \theta_C$  or roughly a factor of  $\sin^2 \theta_C \sim 1/20$ . For the neutral current processes the coupling will be proportional to the product of the wave functions of the participating states. In this case the neutral processes become:

$$u\bar{u} + d'\bar{d}' = \underbrace{u\bar{u} + (d\bar{d} \cos^2 \theta_C + s\bar{s} \sin^2 \theta_C)}_{\Delta S=0} + \underbrace{(s\bar{d} + d\bar{s}) \cos \theta_C \sin \theta_C}_{\Delta S=1} \quad (2.7)$$

This allows for first order flavor changing weak neutral current processes which are suppressed by  $\cos \theta_C \sin \theta_C$ , but still not suppressed enough to account for the observed rate for  $K^0 \rightarrow \mu^+ \mu^-$ .

### 2.1.2 GIM Mechanism

To explain the observed suppression of the  $K^0 \rightarrow \mu^+ \mu^-$  decay, Glashow, Iliopoulos and Maiani proposed the inclusion of an  $up$  like *charm* quark with  $2/3$  charge, to form a second mixing doublet:

$$\begin{pmatrix} c \\ s' \end{pmatrix} = \begin{pmatrix} c \\ s \cos \theta_C - d \sin \theta_C \end{pmatrix} \quad (2.8)$$

An admixture of the  $s$  and  $d$  quarks is again used to form the weak interaction eigenstates. When we now consider the neutral currents with the inclusion of the charm contribution we find:

$$\begin{aligned} u\bar{u} + d'\bar{d}' + c\bar{c} + s'\bar{s}' &= \underbrace{u\bar{u} + c\bar{c} + (d\bar{d} + s\bar{s}) \cos^2 \theta_C + (d\bar{d} + s\bar{s}) \sin^2 \theta_C}_{\Delta S=0} \\ &+ \underbrace{(s\bar{d} + \bar{s}d - \bar{s}d - s\bar{d}) \sin \theta_C \cos \theta_C}_{\Delta S=1} \end{aligned} \quad (2.9)$$

The  $\Delta S = 1$  contribution exactly cancels leaving no first order flavor changing neutral currents. This can be expressed more generally in terms of the mixing matrix of Eq. (2.4) by denoting the mixing matrix as  $V_{ij}$ . In this manner we can express the mixing of *down* type quarks (d,s,b) in a summation over flavors as:

$$q'_i = \sum_j V_{ij} q_j \quad (2.10)$$

If the mixing matrix is required to be unitary then for  $N$  generations of quarks the GIM identity

$$\begin{aligned} \sum_i^N \bar{q}'_i q'_i &= \sum_i^N \sum_j^N \sum_k^N \bar{q}_i V_{ij}^\dagger V_{jk} q_k \\ &= \sum_i^N \bar{q}_i q_i \end{aligned} \tag{2.11}$$

then regardless of the number of quarks first order flavor changing neutral currents are forbidden. The identity relies only on the unitary nature of mixing matrix  $V_{ij}$ .

The GIM mechanism also explains the suppression of the second order charged current processes of Fig. 2.4 to the  $K_L^0 \rightarrow \mu^+ \mu^-$  amplitude. Through this process the contribution from *up* to *strange* mixing contributes with a coupling proportional to  $\cos \theta_C \sin \theta_C$  and is almost exactly canceled by the contribution from *charm* to *strange* mixing which is nearly proportional to  $-\cos \theta_C \sin \theta_C$ . If the up and charm quarks were degenerate in mass, then the cancellation would be exact. In this manner  $K_L^0$ ,  $K_S^0$  mass splitting  $\Delta m_K$  can be used to place limits on the mass of the charm quark.

$$m_c^2 \simeq \frac{3\pi m_\mu^2 \Delta m_K}{4 \cos^2 \theta_C \Gamma(K^+ \rightarrow \mu^+ \nu)} \tag{2.12}$$

### 2.1.3 CKM Mixing

The inclusion of a third generation of strong mass states containing both *top* and *bottom* quarks leads to the extension of the Cabibbo mixing via a generalized rotation matrix by Kobayashi and Maskawa [6]. The  $3 \times 3$  CKM matrix mixes the

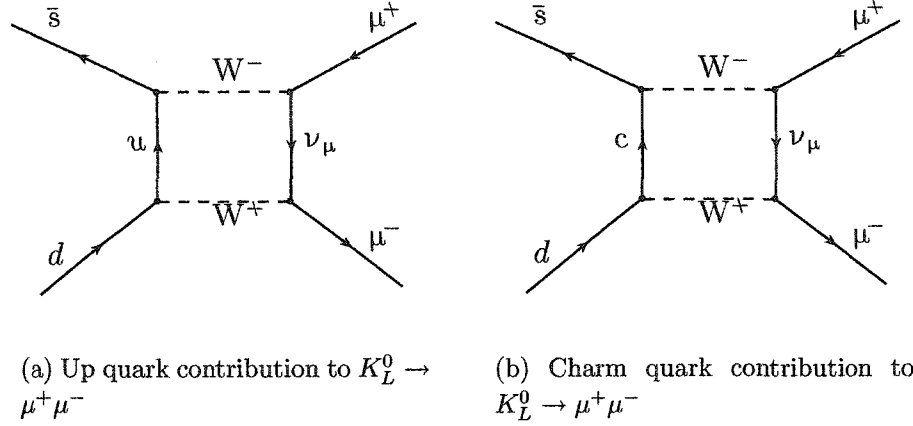


FIG. 2.4: Second order weak  $\Delta S = 1$  contributions to  $\Gamma(K_L^0 \rightarrow \mu^+ \mu^-)$  which approximately cancel through the GIM mechanism

down-like  $-1/3$  charge quarks with their respective weak eigenstates.

$$\begin{pmatrix} d' \\ s' \\ b' \end{pmatrix} = \begin{pmatrix} V_{ud} & V_{us} & V_{ub} \\ V_{cd} & V_{cs} & V_{cb} \\ V_{td} & V_{ts} & V_{tb} \end{pmatrix} \begin{pmatrix} d \\ s \\ b \end{pmatrix} \quad (2.13)$$

Like the Cabibbo matrix the  $3 \times 3$  CKM matrix is unitary such that off diagonal mixing in the *top* and *bottom* rows are near zero.

$$\mathbf{V}^{-1} = \mathbf{V}^\dagger \quad \text{and} \quad \mathbf{V}^{-1} \cdot \mathbf{V} = \mathbf{1} \quad (2.14)$$

The unitary condition preserves the cancellation of first order flavor changing weak neutral currents and preserves the GIM identity:

$$\begin{aligned} \sum_i \bar{d}'_i d'_i &= \sum_{i,j,k} \bar{d}_i V_{ij}^\dagger V_{jk} d_k \\ &= \sum_i \bar{d}_i d_i \end{aligned} \quad (2.15)$$

The unitarity of the matrix restricts the elements to:

$$N^2 - (2N - 1) \quad (2.16)$$

independent degrees of freedom, while the orthogonality of the matrix further restricts the independent real parameters to:

$$\frac{1}{2}N(N - 1) \quad (2.17)$$

Combining the restrictions of Eq. (2.16) and 2.17 results in

$$\frac{1}{2}(N - 1)(N - 2) \quad (2.18)$$

allowable independent phases. For the  $3 \times 3$  mixing of the CKM matrix this results in 3 real parameters and a single phase. Denoting the real parameters as the angles  $(\theta_1, \theta_2, \theta_3)$  and the phase as  $\delta$  we can rewrite the mixing matrix as:

$$V_{CKM} = \begin{pmatrix} c_1 & -s_1 c_3 & -s_1 s_3 \\ s_1 c_2 & c_1 c_2 c_3 - s_2 s_3 e^{i\delta} & c_1 c_2 s_3 + s_2 c_3 e^{i\delta} \\ s_1 s_2 & c_1 s_2 c_3 + c_2 s_3 e^{i\delta} & c_1 s_2 s_3 - c_2 c_3 e^{i\delta} \end{pmatrix} \quad (2.19)$$

where:

$$c_i \equiv \cos \theta_i \quad \text{and} \quad s_i \equiv \sin \theta_i. \quad (2.20)$$

A non-zero value of the phase  $\delta$  leads to off diagonal contributions to  $V_{cb}$  and  $V_{ts}$  that break the CP invariance of the weak interactions.

The CKM matrix can be related to the geometric construct of the unitary triangle by expanding the matrix in powers of the Cabibbo angle  $\lambda = |V_{us}|$  and

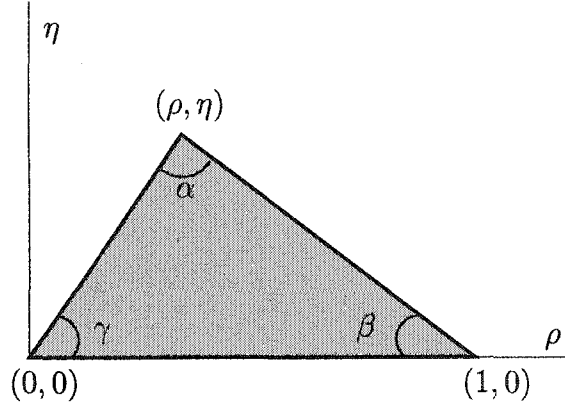


FIG. 2.5: Geometric representation of the unitary triangle

rewriting the matrix in terms of  $(\lambda, A, \rho, \eta)$ . This Wolfenstein parameterization of the CKM matrix becomes[7]:

$$\mathbf{V} = \begin{pmatrix} 1 - \frac{1}{2}\lambda^2 & \lambda & A\lambda^3(\rho - \eta) \\ -\lambda & 1 - \frac{1}{2}\lambda^2 & A\lambda^2 \\ A\lambda^3(1 - \rho - \eta) & -A\lambda^2 & 1 \end{pmatrix} \quad (2.21)$$

The family mixing terms have been approximated as:

$$V_{us} \sim \lambda \quad (2.22)$$

$$V_{ub} \sim A\lambda^3(\rho - \eta) \quad (2.23)$$

$$V_{cb} \sim A\lambda^2 \quad (2.24)$$

$$V_{td} \sim \lambda^3(1 - \rho - \eta) \quad (2.25)$$

More completely the parameterization can be extended to require unitarity of the



imaginary part to  $\mathcal{O}(\lambda^5)$  and the real part to  $\mathcal{O}(\lambda^3)$ :

$$\mathbf{V} = \begin{pmatrix} 1 - \frac{1}{2}\lambda^2 & \lambda & A\lambda^3(\rho - \eta + \frac{1}{2}\eta\lambda^2) \\ -\lambda & 1 - \frac{1}{2}\lambda^2 - \eta A^2\lambda^4 & A\lambda^2(1 + \eta\lambda^2) \\ A\lambda^3(1 - \rho - \eta) & -A\lambda^2 & 1 \end{pmatrix} \quad (2.26)$$

In this manner the CP violating terms all appear to  $\mathcal{O}(\lambda^3)$  and can be directly related to the decays of the charged and neutral kaons.

### 2.1.4 Unitarity Bound

The decay rates for kaon into leptonic pairs can be split into both its real and imaginary components.

$$B(K_L^0 \rightarrow \ell^+\ell^-) = |Re\mathcal{A}|^2 + |Im\mathcal{A}|^2 \quad (2.27)$$

The real component of the decay rate is the dispersive part while the imaginary component is recognized as the absorptive piece, in analogy to the real and imaginary portions of a scattering amplitude. Each of these amplitudes can then further be broken down into the fractions of each amplitude which come from short distance weak interactions and the component of the amplitude arising from the long distance electro-magnetic diagrams. In this manner the total amplitude can be written as:

$$\mathcal{A} = (\mathcal{A}_{disp,weak} + \mathcal{A}_{disp,ld}) + i(\mathcal{A}_{abs,weak} + \mathcal{A}_{abs,ld}) \quad (2.28)$$

where the *weak* and *ld* refer respectively to the electro-weak diagrams involving the exchange of  $W^\pm$  and  $Z^0$  bosons and long distance diagrams involving contributions from photon propagators. The diagrams associated with the weak absorptive amplitude are unphysical due to the mass requirements of the weak bosons, as a result

the contribution from  $\mathcal{A}_{abs,weak}$  is explicitly zero. The branching fraction can thus be rewritten in a simplified form whereby the only contributions from the weak diagrams are manifest in the real part of the decay.

$$\begin{aligned} B(K_L^0 \rightarrow \ell^+ \ell^-) &= |\mathcal{A}_{disp}|^2 + |\mathcal{A}_{abs}|^2 \\ &= |\mathcal{A}_{weak} + \mathcal{A}_{ld}|^2 + |\mathcal{A}_{abs}|^2 \end{aligned} \quad (2.29)$$

The absorptive portion of the amplitude is dominated by a real two photon intermediate state as shown in Fig. 2.6. This diagram can be exactly calculated from QED and is referred to as the unitary diagram. The computation by Sehgal [8][9] gives the unitary limits on the branching fraction for the dilepton decays:

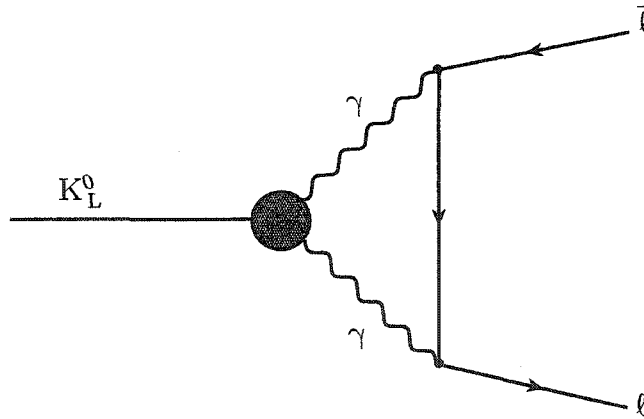
$$\frac{B(K_L^0 \rightarrow \gamma\gamma \rightarrow \ell\bar{\ell})}{B(K_L^0 \rightarrow \gamma\gamma)} = \frac{1}{2} \alpha^2 \left( \frac{m_\ell}{M_K} \right)^2 \frac{1}{\beta} \left( \ln \frac{1+\beta}{1-\beta} \right)^2 \quad (2.30)$$

where  $\alpha$  is the fine structure constant and  $\beta$  is taken as

$$\beta = \left( 1 - \frac{4m_\ell^2}{M_K^2} \right)^{\frac{1}{2}} \quad (2.31)$$

Since no other diagrams interfere with the unitary diagram, the rate obtained from this calculation is taken as a lower bound on the decay rate for  $K_L^0 \rightarrow \ell\bar{\ell}$  and is denoted as the unitary bound. Table 2.3 lists the QED predictions for the unitary limits and current experimental measurements of the branching fractions. It should be noted that the experimental measurement of the dimuon decay branch abuts the unitary bound without consideration of any additional decay paths including contributions from the dispersive weak and long distance decay amplitudes.

Decay Branch	Unitary Bound	Observation
$B(K_L^0 \rightarrow \gamma\gamma)$	$N/A$	$(5.96 \pm 0.15) \times 10^{-4}$
$B(K_L^0 \rightarrow e^+e^-)/B(K_L^0 \rightarrow \gamma\gamma)$	$1.19 \times 10^{-5}$	$N/A$
$B(K_L^0 \rightarrow \mu^+\mu^-)/B(K_L^0 \rightarrow \gamma\gamma)$	$5.32 \times 10^{-9}$	$N/A$
$B(K_L^0 \rightarrow e^+e^-)$	$(3.15 \pm 0.08) \times 10^{-12}$	$(9_{-4}^{+6}) \times 10^{-12}$
$B(K_L^0 \rightarrow \mu^+\mu^-)$	$(7.04 \pm 0.18) \times 10^{-9}$	$(7.25 \pm 0.16) \times 10^{-9}$

TABLE 2.3: Unitary limits on dilepton decays of  $K_L^0$ FIG. 2.6: Leading order absorptive contribution to  $K_L^0 \rightarrow l\bar{l}$  via a real two photon intermediate state

## 2.2 The K Meson

The neutral K meson was first reported to have been observed in 1947 by G. Rochester and C. Butler[10] in a cloud chamber exposed to cosmic rays. The K meson was identified through two charged tracks whose trajectories could be reconstructed to have originated from the decay of a neutral particle approximately 900 times that mass of the electron. Since this first observation of the kaon, the field of strange interactions and kaon physics has revealed key insights into the nature of the fundamental symmetries of the standard model.

The neutral K meson,  $K^0$  and its antiparticle  $\bar{K}^0$  form a classic two state quantum mechanical system whose properties under symmetry transformations and interactions with the standard model Hamiltonian are surprising. The  $K^0$  and  $\bar{K}^0$  both have identical charge, mass, spin and parity. They are distinguishable by the addition of a new quantum number which is denoted as the Strangeness S of the particle. With benefit of hindsight one can appeal to the quark model to assign the S quantum number on the basis of the strange quark content of each meson. Using this model we identify the  $K^0$  as a bound state of the down quark with the anti-strange quark and its anti particle the  $\bar{K}^0$  as a bound state of the strange quark with the anti-down quark.

$$K^0 = |\bar{s}d\rangle \quad \text{and} \quad \bar{K}^0 = |s\bar{d}\rangle \quad (2.32)$$

It is clear from this construction that both states are now definite eigenstates of the strangeness operator  $\hat{S}$ .

$$S |K^0\rangle = + |K^0\rangle \quad S |\bar{K}^0\rangle = - |\bar{K}^0\rangle \quad (2.33)$$

The states are clearly distinguishable now based on their quantum numbers in much

the same manner as the neutron is distinguishable on the basis of isospin and baryon number from the anti-neutron.

$$\begin{aligned} K^0 : T &= \frac{1}{2}, T_3 = -\frac{1}{2}, S = +1 \\ \bar{K}^0 : T &= \frac{1}{2}, T_3 = +\frac{1}{2}, S = -1 \end{aligned} \quad (2.34)$$

Unlike the neutron, the presence of strangeness-changing interactions with the weak force permits an initially pure  $|K^0\rangle$  state to evolve into a  $|\bar{K}^0\rangle$  state. As a result of this mixing of the strong eigenstates under the weak force, kaons exhibit strangeness oscillations and regeneration effects which are unique to the system. A beam of pure  $K^0$  will thus evolve such that at time  $t$  in the future it will develop a non-zero coefficient  $b(t)$  for the overlap of the beam population to exist in the antiparticle state.

$$|K^0(t)\rangle \rightarrow a(t) |K^0\rangle + b(t) |\bar{K}^0\rangle \quad (2.35)$$

Because the strong nuclear force does not contain strangeness-violating processes, and the kaon is the lightest particle species with strange content we find that kaon decay via a strong interaction is kinematically forbidden by strangeness conservation. The process of oscillation is thus not possible within the confines of the strong Hamiltonian since it results in a  $\Delta S = 2$  transition. To describe this phenomena more fully we note that both the  $K^0$  and  $\bar{K}^0$  may decay into a two pion state ( $\pi^+\pi^-$ ) via a weak  $\Delta S = 1$  transition. We can combine two such interactions to form a connecting pion loop between the states as shown in Fig. 2.7. The resulting  $\Delta S = 2$  strangeness-violating interaction is second order in the weak coupling and fully allowed under the standard model.

The process can be broken down further showing the actual exchange of the intermediate  $W^+$  and  $W^-$  bosons. Fig. 2.8 shows explicitly the quark content of the

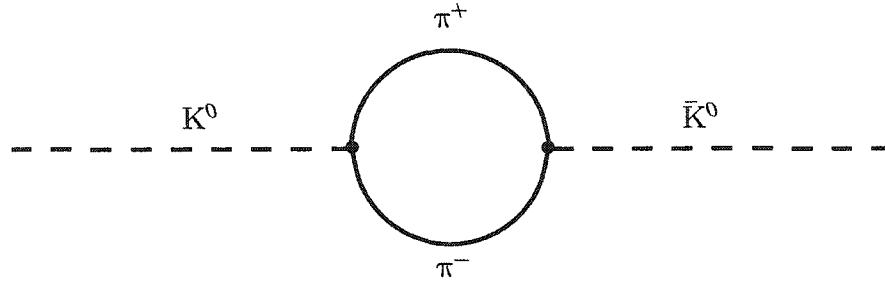


FIG. 2.7:  $K^0$  to  $\bar{K}^0$  mixing via an intermediate pion loop

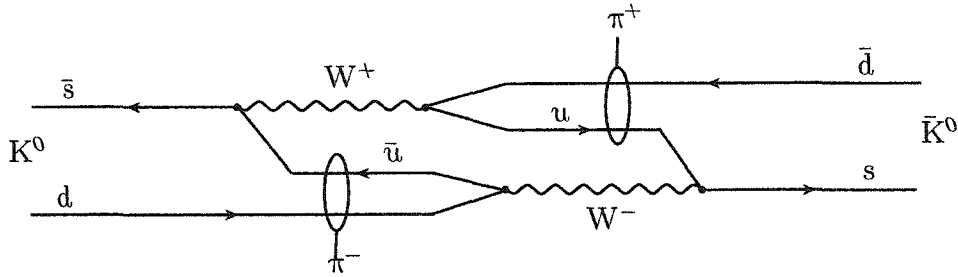


FIG. 2.8:  $K^0$  to  $\bar{K}^0$  mixing via a second order  $\Delta S = 2$  weak interaction

interaction and denotes the effective pion loop. To leading order this transition is just a standard set of box diagrams. The first few terms in the expansion can then be expressed as shown in Fig. 2.9.

The weak perturbation to the Hamiltonian breaks the initial degeneracy of the two kaon states and splits the  $K^0$ ,  $\bar{K}^0$  levels. We can diagonalize this new interaction to produce two new eigenstates  $K_1^0$  and  $K_2^0$  of the system. The perturbation now splits the expectation value of the kaon masses for  $K_1^0$  and  $K_2^0$  in such a way that  $\Delta m_k = |m_1 - m_2|$  is small but non-zero.

The lifting of the degeneracy in the states leads us to rewrite the original strong

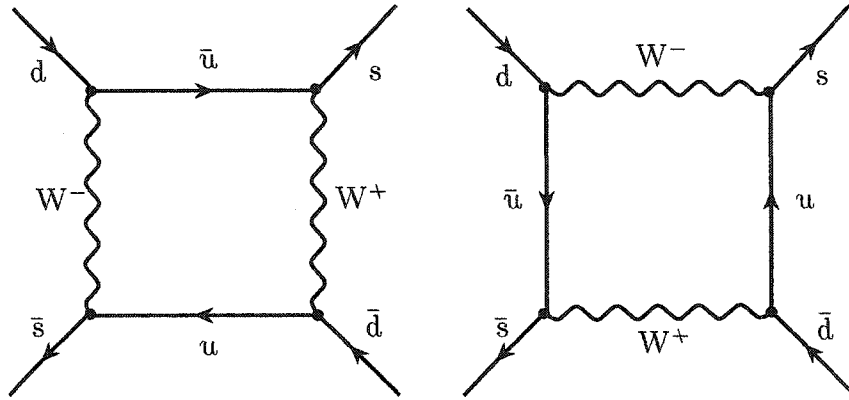


FIG. 2.9: Leading order box diagrams contributing  $K^0$  to  $\bar{K}^0$  mixing

states as a linear combination of the new observable states  $|K_1^0\rangle$  and  $|K_2^0\rangle$ .

$$|K^0\rangle = (a|K_1^0\rangle + b|K_2^0\rangle) / \sqrt{a^2 + b^2} \quad (2.36)$$

$$|\bar{K}^0\rangle = (c|K_1^0\rangle + d|K_2^0\rangle) / \sqrt{c^2 + d^2} \quad (2.37)$$

In this new framework we can examine the consequences of basic symmetry operators on the kaon system as well as describe physical properties of the system which are observable in the lab. Most importantly the new states are now explicitly tied to the effects of the weak interaction and thereby permit the exploration of their allowable standard model decay branches.

## 2.3 Weak Eigenstates and Basic Symmetries

The weak interaction is not invariant under parity transformations due to the explicit  $V - A$  nature of the coupling. If however the charge conjugation operator  $\hat{C}$  is considered in combination with the parity operator then the weak interaction does display at first glance an invariance.

In the case of the kaon system it is natural to examine the transformation of

the two sets of eigenstates that have been developed. The strange eigenstates  $K^0$  and  $\bar{K}^0$  under  $\hat{C}\hat{P}$  transform into one another<sup>1</sup>:

$$\hat{C}\hat{P}|K^0\rangle = -|\bar{K}^0\rangle \quad \hat{C}\hat{P}|\bar{K}^0\rangle = -|K^0\rangle \quad (2.38)$$

As a result  $K^0$  and  $\bar{K}^0$  are clearly not the CP eigenstates. The weak eigenstates  $K_1^0$  and  $K_2^0$  arise from the perturbative breaking of the strong Hamiltonian degeneracy. They can be expressed as an orthonormal linear combination of the original states  $K^0$  and  $\bar{K}^0$ . With a choice of normalization these become:

$$\begin{aligned} |K_1^0\rangle &\equiv \frac{1}{\sqrt{2}} [|K^0\rangle + |\bar{K}^0\rangle] \\ |K_2^0\rangle &\equiv \frac{1}{\sqrt{2}} [|K^0\rangle - |\bar{K}^0\rangle] \end{aligned} \quad (2.39)$$

The weak eigenstates are now states of definite  $\hat{C}\hat{P}$ :

$$\begin{aligned} \hat{C}\hat{P}|K_1^0\rangle &= +|K_1^0\rangle \\ \hat{C}\hat{P}|K_2^0\rangle &= -|K_2^0\rangle \end{aligned} \quad (2.40)$$

Since pions have an intrinsic negative parity and are emitted with an angular momentum  $\ell = 0$  corresponding to a spatial wave function with positive parity, the overall parity of the final state of a decay can be found simply by counting the number of pions. In the case of the kaon system this leads to the prediction that the two eigenstates  $K_1^0$  and  $K_2^0$  should have primarily CP even and CP odd decay

---

<sup>1</sup>We have suppressed the arbitrary phase by choosing the relative phase angle between  $K^0$  and  $\bar{K}^0$  to be  $\pi$ . As a result  $\hat{C}\hat{P}|K^0\rangle = e^{i\theta_{cp}}|\bar{K}^0\rangle = -|\bar{K}^0\rangle$ . Alternatively we could have invoked the observed intrinsic negative parity (pseudoscalar nature) of the kaon to set the phase angle so that  $\hat{C}\hat{P}|K^0\rangle = -\hat{C}|K^0\rangle = -|\bar{K}^0\rangle$ .



Kaon Species	Lifetime $\tau$ (s)	$c\tau$	Spin	$\widehat{CP}$
$K_S^0$	$0.89 \times 10^{-10}$	2.67 cm	0	even
$K_L^0$	$5.17 \times 10^{-8}$	15.51 m	0	odd

TABLE 2.4: Experimentally observed kaon properties

modes:

$$\begin{aligned}
 K_1^0 &\rightarrow \pi^0\pi^0 \\
 K_1^0 &\rightarrow \pi^+\pi^-
 \end{aligned}
 \tag{2.41}$$

$$\begin{aligned}
 K_2^0 &\rightarrow \pi^0\pi^0\pi^0 \\
 K_2^0 &\rightarrow \pi^+\pi^-\pi^0 \\
 K_2^0 &\rightarrow \pi^\pm e^\mp \nu_e \\
 K_2^0 &\rightarrow \pi^\pm \mu^\mp \nu_\mu
 \end{aligned}
 \tag{2.42}$$

Since the kaon has a mass  $m_k \approx 497$  MeV and pion  $m_\pi \approx 140$  MeV the  $2\pi$  decay modes have 215MeV of kinetic energy available to the phase space. In contrast the  $3\pi$  decay modes of the CP odd state have only 78MeV of kinetic energy. This smaller available phase space in addition to the additional factors of  $1/2\pi$  arising from the three body final state, suppresses the decay rate of the CP odd  $K_2^0$  giving it a longer lifetime than the CP even state.

Experimentally the effect of the CP even and CP odd phase spaces are seen through the observation of two distinct neutral kaon species with differing lifetimes and primary decays modes of opposite parity. The two observed kaons are denoted as the short-lived and long-lived neutral kaons,  $K_S^0$  and  $K_L^0$  with lifetimes  $c\tau$  which differ by two orders of magnitude. The properties of these species are listed in Table 2.4.

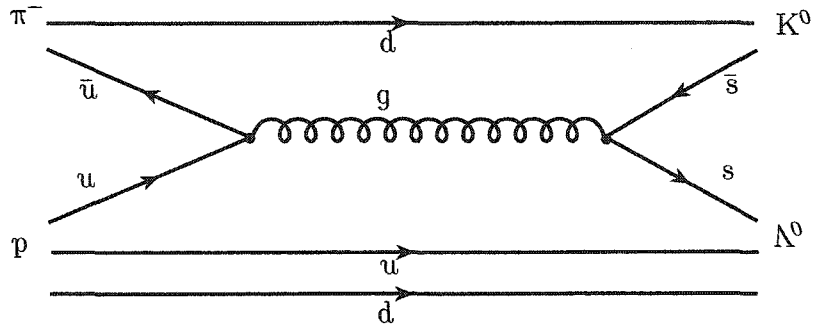


FIG. 2.10: Strong interaction production of a neutral kaon through associated  $\Lambda^0$  hyperon production.

The production of kaons through the strong interaction entails a reaction of the form:

$$\pi^- p \rightarrow K^0 \Lambda \quad (2.43)$$

where strangeness is conserved by the associated production of a lambda hyperon as depicted in Fig. 2.10. From Eq. (2.39) the strong eigenstate can be rewritten as a linear combination of the weak CP eigenstates. If we consider a beam of kaons generated through the strong production mechanism of Eq. (2.43) then each state  $K_S^0$  and  $K_L^0$  is equally prevalent in the initial beam. The large difference in lifetime between  $K_L^0$  and  $K_S^0$  makes it possible to separate the species by allowing the  $K_S^0$  component to decay out leaving only the long lived kaons. A beam of pure  $K_L^0$  is then able to decay only via the weak processes outlined above, specifically accessing only CP odd decay branches.

## 2.4 CP Violation

The experimental observation of the decay of the  $K_L^0$  into a two pion final state in 1964 by Fitch and Cronin[11] demonstrated that the  $\hat{C}\hat{P}$  symmetry of the standard model was not exact. Further measurements have found that in fact  $B(K_L^0 \rightarrow \pi^+\pi^-) = 0.2067 \pm 0.035\%$  [12] or roughly that 1 in 500 decays of the  $K_L^0$  decay into a two pion final state. Since the kaons are spin zero pseudoscalars, the pions in the decay must be emitted in a spin zero state, leaving the intrinsic parity of the final state definitely positive. This leads to the conclusion that while strongly suppressed, the  $\hat{C}\hat{P}$  symmetry is violated in weak decays. As a consequence of CP non-conservation, we note that time reversal invariance must also be violated for the CPT theorem to hold, leading to the conclusion that the transition amplitudes for  $K^0 \leftrightarrow \bar{K}^0$  oscillation are not equal:

$$\langle K^0 | \hat{S} | \bar{K}^0 \rangle \neq \langle \bar{K}^0 | \hat{S} | K^0 \rangle \quad (2.44)$$

To quantify this CP violation we rewrite the weak eigenstates  $K_S^0$  and  $K_L^0$  again in terms of the CP eigenstates  $K_1^0$  and  $K_2^0$  and allow for a slight mixing of the states through a violation parameter  $\epsilon$ :

$$\begin{aligned} |K_S^0\rangle &= \frac{1}{\sqrt{1+|\epsilon|^2}} (|K_1^0\rangle + \epsilon |K_2^0\rangle) \\ |K_L^0\rangle &= \frac{1}{\sqrt{1+|\epsilon|^2}} (|K_2^0\rangle + \epsilon |K_1^0\rangle) \end{aligned} \quad (2.45)$$

where the parameter  $\epsilon \approx 2.3 \times 10^{-3}$ . The actual degree to which CP is violated can then be expressed as a ratio of the decay rates for each of the physically observable

states to decay to a two pion final state.

$$\eta = \frac{\langle 2\pi | K_L^0 \rangle}{\langle 2\pi | K_S^0 \rangle} = \frac{1 - \epsilon}{1 + \epsilon} \approx \frac{1 - \epsilon}{2} \quad (2.46)$$

Experimentally we measure the decay branches for the charged two pion state and the neutral pion state separately:

$$\eta_{\pm} = |\eta_{\pm}| e^{i\phi_{\pm}} = \frac{\langle \pi^+ \pi^- | K_L^0 \rangle}{\langle \pi^+ \pi^- | K_S^0 \rangle} \quad (2.47)$$

In this manner we can now predict the time dependent rate intensity for an initial  $K^0$  state to decay into the  $2\pi$  final state as:

$$I(K^0 \rightarrow \pi^+ \pi^-) \propto e^{-\Gamma_S t} + |\eta_{\pm}|^2 e^{-\Gamma_L t} + 2|\eta_{\pm}| \cos(\Delta m t + \phi_{\pm}) e^{-(\Gamma_S + \Gamma_L)t/2} \quad (2.48)$$

Where  $\Gamma_S$  and  $\Gamma_L$  are the proper decay rates for the short-lived and long-lived weak eigenstates. We note that the first two terms in the expression are the standard exponential decay rates of the states where the rate for contribution from the  $K_L^0$  state is explicitly suppressed by the CP violation parameter  $\eta_{\pm}$ . The last term represents the effect of quantum mechanical interferences between the states and corresponds directly to the degree of strangeness oscillation between the kaons. The phase angle  $\phi_{\pm}$  of the CP violation can be extracted from this term with knowledge of the  $K_S^0/K_L^0$  mass splitting and the lifetimes for each state:

$$\tan(\phi_{\pm}) = 2 \frac{\Delta m}{\Gamma_S - \Gamma_L} \rightarrow \phi_{\pm} = (43.7 \pm 0.6)^{\circ} \quad (2.49)$$

The same treatment can be applied to the neutral pion decays of the  $K_L^0$  and  $K_S^0$  to

obtain:

$$\eta_{00} \equiv |\eta_{00}|e^{i\phi_{00}} = \frac{\langle \pi^0\pi^0 | K_L^0 \rangle}{\langle \pi^0\pi^0 | K_S^0 \rangle} \quad (2.50)$$

$$|\eta_{00}| = (2.275 \pm 0.019) \times 10^{-3} \quad (2.51)$$

$$\phi_{00} = (43.4 \pm 1.0)^\circ \quad (2.52)$$

The quantities  $\eta_{\pm}$  and  $\eta_{00}$  can be re-expressed in terms of the proportions of each amplitude which comes from direct and indirect CP violation[13] to determine the underlying flavor mixing phenomena.

### 2.4.1 Indirect and Direct CP Violation

The origin of CP violation in the kaon system can be explained by noting that two basic reaction types can lead to a final state with CP symmetry different from the original eigenstate that the system was prepared in.

In the case of *indirect* CP violation the initially CP odd  $K_L^0$  state first oscillated through the  $K^0/\bar{K}^0$  mixing process into a large overlap with the  $K_S^0$  eigenstate and then naturally decays through the  $K_S^0$  two pion decay branch. Schematically the process appears as:

$$K_L^0 \rightarrow K_S^0 \rightarrow \pi^+\pi^- \quad (2.53)$$

where the intermediate  $K_S^0$  oscillation process involves the  $\Delta S = 2$  weak current effect of the virtual pion loop as shown previously in Fig. 2.7 and 2.8. This can also be viewed as the overlap of the  $K_L^0$  with the CP even  $K_1^0$  state acting as an approximate eigenstate of the weak interaction and thus decaying to the appropriate two pion final state with a reduced probability related to the overlap coefficient  $\epsilon$ .

In contrast to indirect violation of the symmetry, the underlying quark substructure

ture of the final state mesons can lead to small but non-zero direct violation of CP. Normally weak hadronic interactions obey a  $\Delta I = \frac{1}{2}$  transition rule for the isospin change of the hadrons involved, in this case corresponding to the  $d \rightarrow s$  transition. By way of example the  $\Lambda$  hyperon with an underlying  $uds$  quark substructure has a net isospin  $I = 0$ , and strangeness  $S = -1$ . The normal Clebsch-Gordon coefficients then predict the ratio of the rates for the two primary decay branches:

$$\frac{\Gamma(\Lambda \rightarrow n\pi^0)}{\Gamma(\Lambda \rightarrow p\pi^-)} = \frac{1}{2} \quad (2.54)$$

which is experimentally observed to be correct. What the Clebsch-Gordon coefficients fail to account for are the additional  $\Delta I = \frac{3}{2}$  decays also observed in the  $\Lambda$  system, with a greatly reduced branching fraction.

These same  $\Delta I = 3/2$  transition can also be manifested in the neutral kaon system. The process  $K \rightarrow \pi^+\pi^-$  or  $K \rightarrow \pi^0\pi^0$  can then occur where the final states pions have an isospin  $I = 0$  as well as in a final state of total isospin  $I = 2$ . The resulting transitions then each can be assigned a decay amplitude<sup>2</sup> including a corresponding phase factor for each:

$$\text{Amplitude for } \Delta I = \frac{1}{2} \rightarrow A_0 e^{i\delta_0} \quad (2.55)$$

$$\text{Amplitude for } \Delta I = \frac{3}{2} \rightarrow A_2 e^{i\delta_2} \quad (2.56)$$

The difference between the phase angles  $\delta_0 - \delta_2$  explicitly changes sign under time reversal and thus by the CPT theorem is equivalent to direct violation of the CP symmetry.

The forbidden  $\Delta I = \frac{3}{2}$  is allowed to occur due to the underlying flavor mixing between the quark generations. When the Cabibbo mixing mechanism of section

---

<sup>2</sup>An amplitude for the the case  $I = 0$  is omitted as the final state is forbidden by Bose symmetry.

2.1.2 is extended to a third quark doublet containing the *top* and *bottom* it introduces a complex phase  $\delta$  into the CKM matrix parameterized by the real mixing angles  $\theta_1, \theta_2, \theta_3$ :

$$V_{CKM} = \begin{pmatrix} c_1 & -s_1 c_3 & -s_1 s_3 \\ s_1 c_2 & c_1 c_2 c_3 - s_2 s_3 e^{i\delta} & c_1 c_2 s_3 + s_2 c_3 e^{i\delta} \\ s_1 s_2 & c_1 s_2 c_3 + c_2 s_3 e^{i\delta} & c_1 s_2 s_3 - c_2 c_3 e^{i\delta} \end{pmatrix} \quad (2.57)$$

where

$$c_i \equiv \cos \theta_i \quad \text{and} \quad s_i \equiv \sin \theta_i. \quad (2.58)$$

The non-zero phase then results in an allowable  $\Delta I = 3/2$  transition originating from the non-zero off diagonal elements of the matrix.

To determine the phase we examine the semi-leptonic decays of the  $K_L^0$  system. These two major decay branches allow us to consider the asymmetry that exists between states that are independently conjugates of both parity and charge. In particular:

$$K_L^0 \rightarrow \pi^- \mu^+ \nu_\mu \quad (2.59)$$

$$K_L^0 \rightarrow \pi^+ \mu^- \nu_\mu \quad (2.60)$$

and

$$K_L^0 \rightarrow \pi^- e^+ \nu_e \quad (2.61)$$

$$K_L^0 \rightarrow \pi^+ e^- \nu_e \quad (2.62)$$

Both exhibit a slight asymmetry in their absolute decay fractions. From this asym-

metry we can connect directly to the phase  $\delta$ :

$$\delta = \frac{\Gamma(K_L^0 \rightarrow \pi^- \ell^+ \nu_\ell) - \Gamma(K_L^0 \rightarrow \pi^+ \ell^- \nu_\ell)}{\Gamma(K_L^0 \rightarrow \pi^- \ell^+ \nu_\ell) + \Gamma(K_L^0 \rightarrow \pi^+ \ell^- \nu_\ell)} \quad (2.63)$$

and from the measured value of the semi-leptonic asymmetry of  $(0.327 \pm 0.012)\%$  note that the kaon system provides a unique distinction between particles and anti-particles. Moreover it provides us with an absolute definition of positive charge, as being that flavor of lepton which is preferred in the decay of the neutral kaon.

Since the phase  $\delta$  from Eq. (2.63) is non-zero, we consider the effect now of the forbidden  $\Delta I = 3/2$  transitions on direct CP violation. Taking into account both the  $\pi^0\pi^0$  and  $\pi^+\pi^-$  interference for  $I = 0$  and  $I = 2$  final states it can be shown that the indirect CP violation amplitude  $\varepsilon$  and the direct CP violation amplitude  $\varepsilon'$  can be related to the decay branch ratios[13]:

$$\eta_{\pm} = |\eta_{\pm}| e^{i\phi_{\pm}} \simeq \varepsilon + \varepsilon' \quad (2.64)$$

$$\eta_{00} = |\eta_{00}| e^{i\phi_{00}} \simeq \varepsilon - 2\varepsilon' \quad (2.65)$$

### 2.4.2 Measurement of $\varepsilon'/\varepsilon$

Eq. (2.64) and (2.65) allow for the decay ratios  $\eta_{\pm}$  and  $\eta_{00}$  to be used to extract information on  $\varepsilon$  and  $\varepsilon'$ . In particular it is convenient to extract the parameters as a ratio of the direct to indirect components of the CP violation of the form  $\varepsilon'/\varepsilon$ . Since both effects are small, extraction of the real part of the double ratio preserves the relative magnitudes of the parameters by suppressing systematic uncertainties that appear in each measured branching fraction. Taking only the real part of the



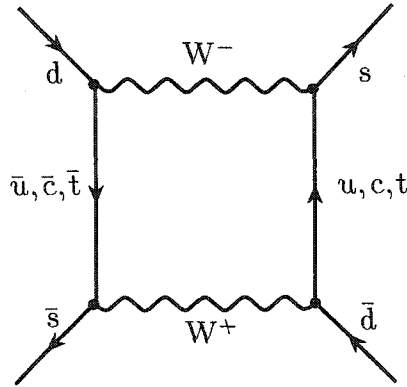


FIG. 2.11: Intermediate quark contributions to  $K^0$  to  $\bar{K}^0$  mixing

ratio, the prescription for obtaining  $Re(\epsilon'/\epsilon)$  becomes:

$$Re(\epsilon'/\epsilon) \simeq \frac{1}{6} \left[ \left| \frac{\eta_{\pm}}{\eta_{00}} \right|^2 - 1 \right] \quad (2.66)$$

Within the confines of the standard model this ratio of  $\epsilon'/\epsilon$  can only be different from zero if there exists a complex non-zero phase in the off diagonal components of the CKM matrix  $V_{ij}$  as stated in Eq. (2.57). These matrix elements describe the weak current mixing between the third generation top quark with the lighter *strange* and *down* quarks. In particular the direct and indirect contributions to CP violation can be related to the coupling of the top quark through the imaginary part of  $\lambda_t$  [14]:

$$\epsilon' \propto \text{Im } \lambda_t = \text{Im}(V_{td}V_{ts}^*) \quad (2.67)$$

which correspond to the dominance of the class of diagrams containing a heavy t-quark propagator, such as primary indirect contribution from  $K^0$  to  $\bar{K}^0$  oscillation shown in Fig. 2.11. We can relate  $\text{Im}\lambda_t$  via the Wolfenstein parameterization of the CKM matrix to the Jarlskog parameter  $J_{CP}$  which is the invariant measure of CP

violation in the standard model. In particular taking the Wolfenstein  $\lambda = 0.221$  we have:

$$J_{CP} = \lambda\sqrt{1 - \lambda^2}\text{Im}\lambda_t \quad (2.68)$$

where  $J_{CP}$  is given more traditionally as an invariant combination of the CKM matrix elements[15]:

$$J_{CP} = \text{Im}(V_{ij}V_{kl}V_{kj}^*V_{il}^*) \quad (2.69)$$

which reduces in all cases to:

$$J_{CP} = s_1^2 s_2 s_3 c_1 c_2 c_3 \sin \delta \quad (2.70)$$

$$c_i \equiv \cos \theta_i \quad \text{and} \quad s_i \equiv \sin \theta_i$$

where  $\theta_1, \theta_2, \theta_3$  are the angles of the unitary triangle. This connection makes  $J_{CP}$  a direct measure of the area of the unitary triangle and proportional to the strength of the CP violation in the standard model.

In particular we notice that  $J_{CP}$  vanishes if any of the conditions are met:

$$\theta_i = 0, \quad \theta_i = \pi/2 \quad (2.71)$$

$$\delta = 0, \quad \delta = \pi$$

resulting in no CP non-conservation within the standard model.

With knowledge of the imaginary phase  $\delta$  and the invariant Jarlskog parameter the formalism still requires a measure of the length of the sides of the unitary triangle, or conversely the location of it's vertices through extraction of the Wolfenstein parameters  $\rho$  and  $\eta$ . This additional information would provide an understanding

of the underlying structure of CP violation in the standard model. To gain this information we examine the rare decays of the neutral kaon system relating to the  $K_{\gamma^*\gamma^*}$  vertex and the extraction of short and long distance information from the decays  $K_L^0 \rightarrow \mu^+\mu^-$  and  $K_L^0 \rightarrow \mu^+\mu^-e^+e^-$ .

# CHAPTER 3

## The Phenomenology of $K_{\gamma^*\gamma^*}$ and the Decay $K_L^0 \rightarrow \mu^+ \mu^- e^+ e^-$

### 3.1 Dispersive Amplitude and $K_L^0 \rightarrow \gamma^* \gamma^*$

In addition to the contributions from the unitary diagram, decays of the form  $K_L^0 \rightarrow \ell^+ \ell^-$  include the dispersive contributions from  $Re\mathcal{A}$  divided into the short distance weak and long distance electromagnetic amplitudes:

$$Re\mathcal{A} = \mathcal{A}_{SD} + \mathcal{A}_{LD} \quad (3.1)$$

The cancellation of flavor-changing neutral currents at tree level via the GIM mechanism leaves the residual rates in the short distance amplitude confined to the second order box diagrams containing the exchange of  $W^\pm$  bosons as well as the second order penguin diagrams involving the exchange of a  $Z^0$  boson as shown in Fig. 3.1. To determine the contribution of these second order processes to the branching fraction  $B(K_L^0 \rightarrow \mu^+ \mu^-)$  the decay can be related to the charged current process  $K^+ \rightarrow \pi^+ \nu \bar{\nu}$ [16]. Only the real part of the amplitude contributes to the second

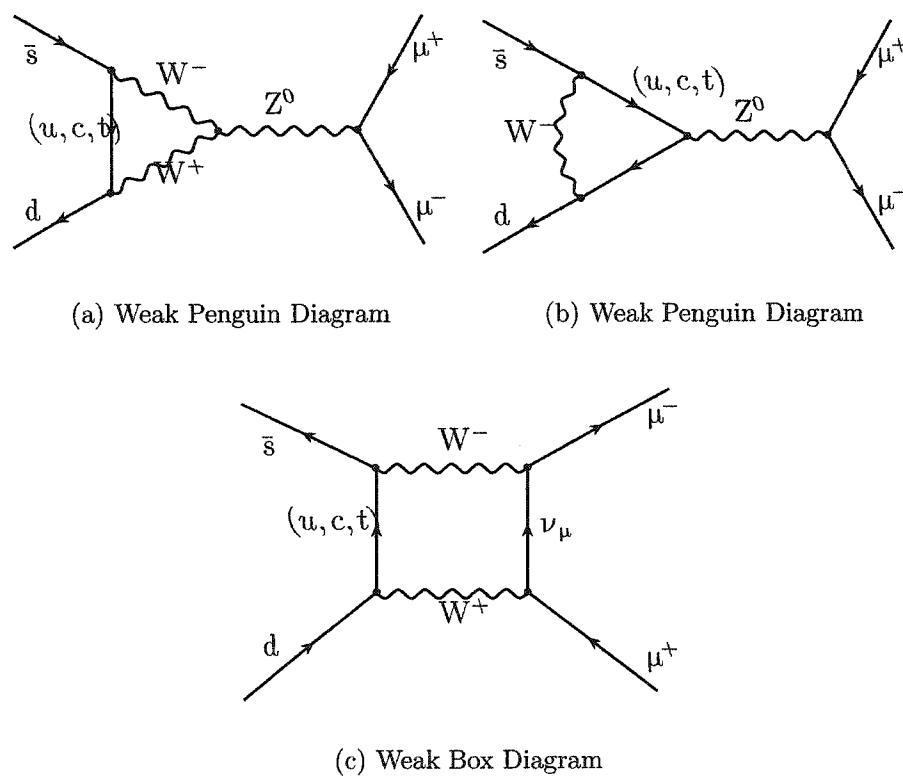


FIG. 3.1: Short distance weak diagrams contributing to  $K_L^0 \rightarrow \mu^+ \mu^-$

order diagrams and again the imaginary portion of the amplitude is dominated by the intermediate two photon state of Fig. 2.6.

$$Re(\mathcal{A})_{SD} = \frac{\alpha^2}{4\pi^2 \sin^4 \theta_W} \frac{(1 - 4m_\mu^2/M_K^2)^{1/2}}{(1 - m_\mu^2/M_K^2)^2} \frac{\left| Re \sum_{i=c,t} \eta_i V_{is}^* V_{id} C_\mu(x_i) \right|^2}{|V_{us}|^2} \quad (3.2)$$

where  $\eta_i$  are the QCD corrections,  $x_i = m_i^2/M_W^2$  such that:

$$C_\mu(x_i) = \frac{4x_i - x_i^2}{4(1 - x_i)} + \frac{3x_i^2 \ln x_i}{4(1 - x_i)^2} \quad (3.3)$$

We find that for the up, charm and top quark:

$$C(x_{up}) \approx 10^{-9} \quad , \quad C(x_{charm}) \approx 3 \times 10^{-3} \quad , \quad C(x_{top}) \approx 2.1 \quad (3.4)$$

This leads to the dominance of the top quark diagrams in the short distance contributions to  $K_L^0 \rightarrow \mu^+ \mu^-$ . From this we relate the matrix elements to the Wolfenstein parameterization:

$$Re(V_{ts}^* V_{td}) = -A^2 \lambda^5 (1 - \rho) \quad (3.5)$$

$$Re(V_{cs}^* V_{cd}) = -\left(\lambda - \frac{1}{2} \lambda^2\right) \quad (3.6)$$

and make the substitutions into Eq. (3.2) to show:

$$|\mathcal{A}_{SD}|^2 = (4.17 \times 10^{-10}) A^4 |\eta_t C(x_t)|^2 \left[ 1 - \rho + \frac{474 \eta_c C(x_c)}{A^2 \eta_t C(x_t)} \right]^2 \quad (3.7)$$

From the relations of Eq. (3.4) it becomes clear that the ratio  $C(x_c)/C(x_t)$  becomes negligible resulting in the real part of the amplitude becoming proportion to the Wolfenstein factor of  $(1 - \rho)^2$ .

In order to properly extract the short distance dispersive amplitude from the

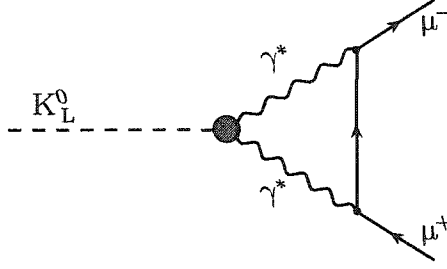


FIG. 3.2: Long distance dispersive diagram for  $K_L^0 \rightarrow \mu^+\mu^-$  involving the exchange of two virtual photons,  $\gamma^*$

dilepton decay branches, thereby obtaining the Wolfenstein parameter  $\rho$ , knowledge of the long distance dispersive amplitude  $\mathcal{A}_{LD}$  as developed in Eq. (2.29) must be obtained. The long distance dispersive amplitude  $\mathcal{A}_{LD}$  results from the class of diagrams involving an intermediate state exchanging two virtual photons. The parent diagram for this amplitude is shown in Fig. 3.2. Difficulty arises from the lack of knowledge of how to compute the effective coupling of the kaon to the virtual two gamma state. Three main model dependent methods need to be considered in this respect, each yielding different results for the momentum dependence of the form factor of the interaction.

### 3.2 Vector Meson Dominance Model (VDM)

The long distance interaction relies on knowledge of the strength of the effective coupling of the K meson to the virtual two gamma state,  $K_{\gamma^*\gamma^*}$ . Use of a vector meson exchange model to describe this coupling results in the series of model dependent terms such as those proposed by Bergstrom, Masso and Singer [17] and shown in Fig. 3.3 that contribute to the transition amplitude. The diagram of Fig. 3.3(a) places the  $\Delta S = 1$  transition on the meson leg and as a result reduces to a process of the type  $P \rightarrow \gamma^*\gamma^*$  where P is an off mass shell pseudoscalar meson. This process

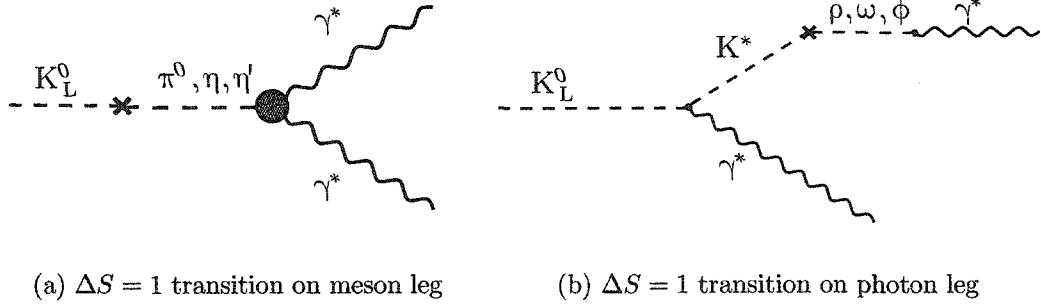


FIG. 3.3: Long distance dispersive pole diagram for  $K_L^0 \rightarrow \gamma^* \gamma^*$  as proposed by Bergstrom, Masso, Singer, et. al. [17]

can be calculated and described using a vector meson dominance model (VDM) resulting in the model dependent amplitude for the long distance coupling  $\mathcal{A}_{LD}$  given by:

$$\mathcal{A}_{\gamma^* \gamma^*, VDM}^1 = -2.3 \times 10^{-2}, \quad \text{Single photon saturation} \quad (3.8)$$

$$\mathcal{A}_{\gamma^* \gamma^*, VDM}^2 = -1.3 \times 10^{-2}, \quad \text{Double photon saturation} \quad (3.9)$$

The diagram of Fig. 3.2 in combination with the intermediate state diagrams of Fig. 3.4 provides the leading order terms for the form-factor for dileptonic decays of the form  $K \rightarrow \ell^+ \ell^-$  with the  $\gamma^* \gamma^*$  intermediate state.

$$F(s)_{VDM} = \alpha \sqrt{2} e G_F f_{K^* K_\gamma} \left( \frac{m_\rho^2}{f_{K^*} f_\rho^2} \right) \left( 1 - \frac{s}{m_{K^*}^2} \right)^{-1} \times \left( \frac{4}{3} - \left( 1 - \frac{s}{m_\rho^2} \right)^{-1} - \frac{1}{9} \left[ \left( 1 - \frac{s}{m_\omega^2} \right)^{-1} + 2 \left( 1 - \frac{s}{m_\phi^2} \right)^{-1} \right] \right) \quad (3.10)$$

where  $s$  is the square of the virtual photon mass and  $\alpha$  is the model dependent factor used in calculating the  $\Delta S = 1$  transition arising on the  $K^* - V$  leg of the diagram. Experimental knowledge of  $\alpha$ , which is essentially a measure of the strength of



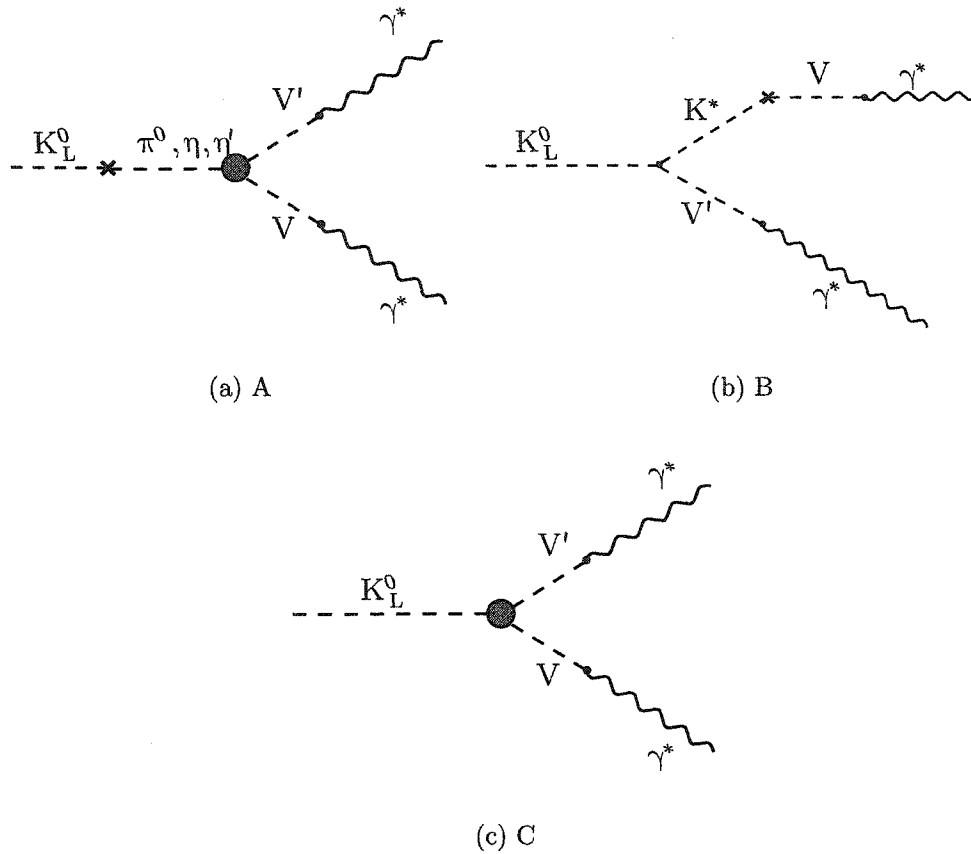


FIG. 3.4: Long distance dispersive diagram for  $K_L^0 \rightarrow \gamma^* \gamma^*$  as proposed by Ko involving vector meson couplings. [18]

the transition between vector mesons, can be found through examination of the Dalitz decay  $K_L^0 \rightarrow \mu^+ \mu^- \gamma$  and the four lepton final state decay  $K_L^0 \rightarrow \mu^+ \mu^- e^+ e^-$ , providing both the single and double virtual photon vertices.

In the vector meson model of Ko [18] the model dependence of the  $K_{\gamma^* \gamma^*}$  amplitude is determined through the set of vector meson exchange diagrams shown in Fig. 3.4. In this model the vector-meson form factors cut off the high momentum behavior of the virtual photons resulting in a convergence for the calculation of the amplitude. The model parameters rely on a knowledge of the behavior of the vertex resulting from the Dalitz decay  $K_L^0 \rightarrow e^+ e^- \gamma$  in analogy to the Bergstrom model's

reliance on knowledge of  $K_L^0 \rightarrow \mu^+\mu^-\gamma$ . The resulting amplitude and form factor from Ko are less sensitive to the dominance of the top quark and the resulting effects on the saturation of the  $K_L^0 \rightarrow \mu^+\mu^-$  amplitude.

### 3.3 QCD model of $K_{\gamma^*\gamma^*}$

The dispersive amplitude  $Re(\mathcal{A}_{LD})$  can be treated in a less model dependent manner by extending the validity of a perturbative QCD down to the energy scale of the  $K_L \rightarrow \gamma^*\gamma^*$  transition. By assuming CP conservation, gauge invariance and Lorentz invariance of the QCD Lagrangian for long distance decay the  $K_{\gamma^*\gamma^*}$  amplitude can be expressed as [19, 20] :

$$\mathcal{A}(K_L \rightarrow \gamma^*(q_1, \epsilon_1)\gamma^*(q_2, \epsilon_2)) = i\varepsilon_{\mu\nu\rho\sigma}\epsilon_1^\mu\epsilon_2^\nu q_1^\rho q_2^\sigma F(q_1^2, q_2^2) \quad (3.11)$$

From this formalism it is clear that the amplitude is again reduced to the evaluation of a form-factor for the decay.  $F(0,0)$ , corresponding to  $q_1^2, q_2^2 = 0$ , can be determined from the  $K \rightarrow \gamma\gamma$  width:

$$|F(0,0)| = \sqrt{\frac{64\pi\Gamma(K_L \rightarrow \gamma\gamma)}{m_K^3}} = (3.51 \pm 0.05) \times 10^{-9} GeV^{-1} \quad (3.12)$$

With knowledge of  $K_{\gamma\gamma}$ , the form-factor can be expressed in a model independent parameterization for the low energy regime ( $q_1^2, q_2^2 < 1GeV$ ) as:

$$f(q_1^2, q_2^2) = \frac{F(q_1^2, q_2^2)}{F(0,0)} = 1 + \alpha \left( \frac{q_1^2}{q_1^2 - m_V^2} + \frac{q_2^2}{q_2^2 - m_V^2} \right) + \beta \frac{q_1^2 q_2^2}{(q_1^2 - m_V^2)(q_2^2 - m_V^2)} \quad (3.13)$$

Here  $\alpha$  and  $\beta$  are chosen as arbitrary real parameters which are accessible through experimental data. The vector meson poles are accounted for by taking  $m_V$  as the

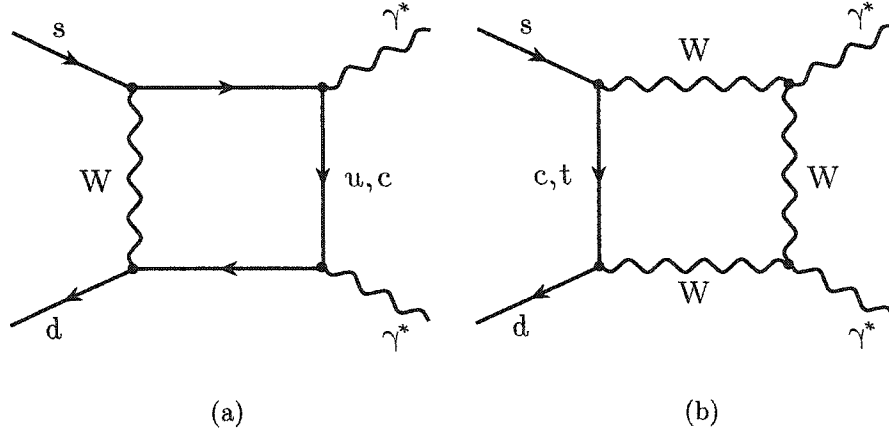


FIG. 3.5: Loop order QCD diagrams contributing to  $K_L^0 \rightarrow \gamma^* \gamma^*$ . [19]

$\rho$  mass.

At high virtual photon momenta the loop structure of Fig. 3.5(a) and 3.5(b) yield operators similar to the short distance box structure of Fig. 3.1 and are dominated by the c-quark. When this structure is included in a  $K_L \rightarrow \gamma^* \gamma^* \rightarrow \mu^+ \mu^-$  two loop decay process the weak contribution cannot be ignored in computing complete short distance amplitude, but can be extracted through use of an ultraviolet cutoff such that for large photon momenta the form factor of Eq. (3.13) yields the relation:

$$f(\ell^2, \ell^2) \xrightarrow{\ell^2 \gg m_V^2} 1 + 2\alpha + \beta \quad (3.14)$$

The parameter  $\alpha$  is accessible experimentally through decays of the form  $K_L \rightarrow \ell \bar{\ell} \gamma$  which are dominated by the  $K_{\gamma^* \gamma}$  form-factor  $F(q^2, 0)$ . The data from the decays  $K_L^0 \rightarrow \mu^+ \mu^- \gamma$  and  $K_L^0 \rightarrow e^+ e^- \gamma$  has been used to fit the parameter  $\alpha_K^*$  from the VDM model of Bergstrom, Masso, Singer [21] as discussed in section 3.2. Expanding

the VDM form-factor in powers of  $q^2/m_\rho^2$  gives:

$$f(q^2, 0)_{VDM} \simeq 1 + (1 - 3.1\alpha_K^*) \frac{q^2}{m_\rho^2} + \mathcal{O}\left(\left(\frac{q^2}{m_\rho^2}\right)^2\right) \quad (3.15)$$

Comparing the VDM form-factor of Eq. (3.15) with the QCD form-factor of Eq. (3.13) gives the relation:

$$\alpha_{QCD} = -1 + (3.1 \pm 0.5)\alpha_K^* \quad (3.16)$$

Extraction of the parameter  $\beta$  is in principle possible through knowledge of the decay  $K_L^0 \rightarrow \mu^+ \mu^- e^+ e^-$  and is dominated by the long distance dispersive form-factor for  $K_L \rightarrow \gamma^* \gamma^*$ . The amount of data available on the four lepton decay prior to this experiment was insufficient to determine  $\beta$ ; as a result a perturbative evaluation of the form-factor at high  $q^2$  can be used in conjunction with the ultraviolet relation of Eq. (3.14) to recover a reasonable estimation of the values of the parameters.

Taking  $q_1^2 = q_2^2 = q^2 \gg m_K^2$  the form-factor evaluated in the framework of perturbative QCD has been found to lowest order from an evaluation of the diagrams in Fig. 3.6. The resulting QCD form factor can be expressed as [20]:

$$f_{QCD}(q^2, q^2) = N_F \left[ g_u \left( \frac{q^2}{4m_u^2} \right) - g_c \left( \frac{q^2}{4m_c^2} \right) \right] \quad (3.17)$$

where

$$g_q(r) = -r \frac{d}{dr} J(r) + \left[ \frac{1+2r}{6r} J(r) + \frac{1}{3} \ln \frac{M_W^2}{m_q^2} \right], \quad \text{and} \quad (3.18)$$

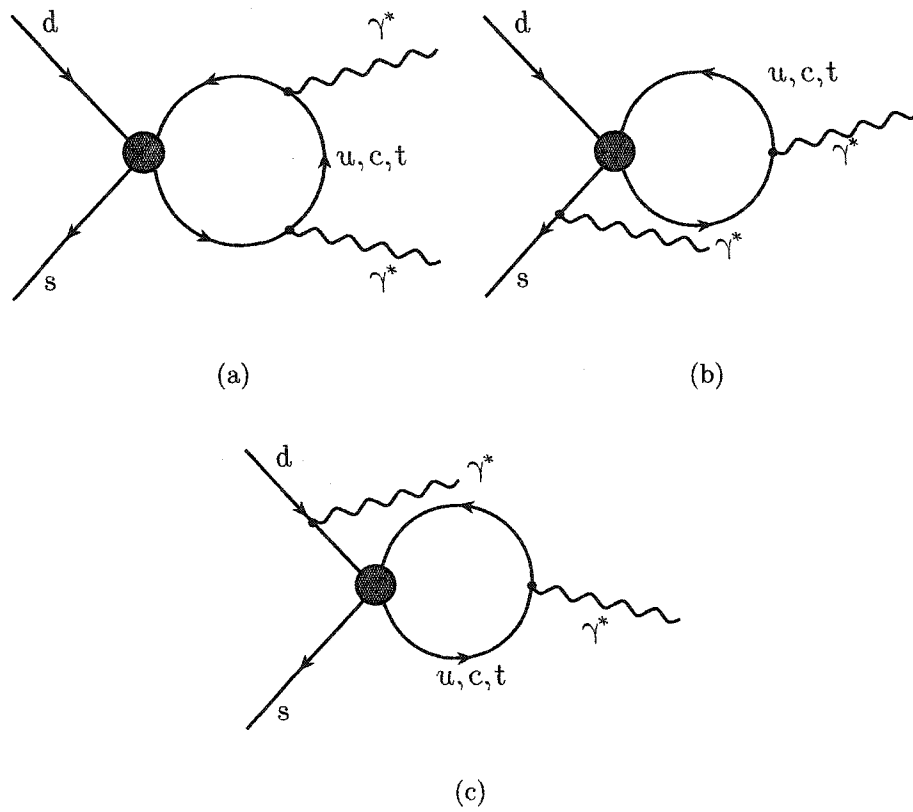


FIG. 3.6: Lowest order effective quark diagrams contributing to  $K_L^0 \rightarrow \gamma^* \gamma^*$  in the framework of a perturbative QCD expansion of  $F(q^2, q^2)$ . [20]

$$J(r) = \begin{cases} -2\sqrt{(1/r)-1} \arctan \sqrt{r/(1-r)} + 2 & 0 < r < 1 \\ \sqrt{1-(1/r)} \left( \ln \frac{1-\sqrt{1-(1/r)}}{1+\sqrt{1-(1/r)}} + i\pi \right) + 2 & r > 1 \end{cases} \quad (3.19)$$

The normalization factor  $N_F$  is given by:

$$|N_F| = \frac{16 G_F F_\pi \alpha_{em} \sin(\theta_C)}{9 \sqrt{2\pi^2} |F(0,0)|} \simeq 0.20 \quad (3.20)$$

where the pion decay constant  $F_\pi = 93 MeV$ . The result is that in a combination of the sum rule of Eq. (3.14) and the ultraviolet cut off constraint introduced by the expansion above we obtain the relation for  $\beta$ :

$$|1 + 2\alpha + \beta| \simeq \frac{14}{9} N_F \simeq 0.3 \quad (3.21)$$

Extracting the  $\beta$  parameter from the VDM model in this manner leads to the constraint:

$$1 + 2\alpha_{VDM} + \beta_{VDM} = -0.01 \quad (3.22)$$

and yields the beta for the form-factor:

$$\beta_{VDM} = \frac{256\pi G_8 \alpha_{em} m_V^2}{3\sqrt{2} F_\pi |F(0,0)|} F_V^3 h_v \eta \simeq 1.43 \quad (3.23)$$

These results allow for the modeling of the form-factor for  $K_L^0 \rightarrow \mu^+ \mu^- e^+ e^-$  as well as providing for the extraction of the short distance amplitude for  $K_L^0 \rightarrow \mu^+ \mu^-$  both in the QCD formalism and in the VDM model dependent approach.

### 3.4 $\chi PT$ model of $K_{\gamma^*\gamma^*}$

In direct analogy to Eq. (3.11) the dispersive amplitude can be calculated using the techniques of chiral perturbation theory to describe the low energy behavior of the form-factor in terms of its momentum dependence on the invariant mass of the virtual photons. In the limit of CP conservation the general form of the amplitude is taken as:

$$\mathcal{A}(K_L \rightarrow \gamma^* \gamma'^*) = \varepsilon_{\mu\nu\rho\sigma} \epsilon_1^\mu q_1^\nu \epsilon_2^\rho q_2^\sigma \mathcal{F}(t, t') \quad (3.24)$$

where the invariant mass of the virtual photons  $\gamma^*$  and  $\gamma'^*$  are taken as  $t = q_1^2$  and  $t' = q_2^2$ .  $\mathcal{F}(t, t')$  represents the form-factor expanded to order  $p^6$  in the framework of chiral perturbation theory. The form factor is split into two parts  $F_1$  and  $F_2(t, t')$ . The first portion of this form factor is taken as being independent of the photon momenta  $t, t'$  and is due to the presence of the  $\pi^0$ ,  $\eta$  and  $\eta'$  poles. It is expressed as [22][23]:

$$\begin{aligned} F_1 &= -\frac{\alpha_{em}}{2\pi F_\pi} C_8 \tilde{F}_1 \\ \tilde{F}_1 &= r_\pi + r_\eta \Theta_1 + r_{\eta'} \Theta_2 \end{aligned} \quad (3.25)$$

In this expression  $C_8 = 3.12 \times 10^{-7}$  is the octet coupling in the effective chiral Lagrangian,  $r_\pi = (1 - m_\pi^2/M_K^2)^{-1}$  and the factors  $\Theta_1, \Theta_2$  are determined from the chiral expansion as:

$$\begin{aligned} \Theta_1 &= \frac{1}{3} ((1 + \delta) \cos \theta + 4\kappa \sin \theta) \times \left( \frac{F_\pi}{F_{\eta 8}} \cos \theta - 2\sqrt{2} \frac{F_\pi}{F_{\eta 1}} \sin \theta \right) \\ \Theta_2 &= \frac{1}{3} ((1 + \delta) \sin \theta + 4\kappa \cos \theta) \times \left( \frac{F_\pi}{F_{\eta 8}} \sin \theta - 2\sqrt{2} \frac{F_\pi}{F_{\eta 1}} \cos \theta \right) \end{aligned} \quad (3.26)$$

The form-factor is heavily dependent on the parameters  $\kappa$  and  $\delta$  and is fit to the  $K_L \rightarrow \gamma\gamma$  decay. In this manner the form factor can be rewritten for the  $K_L \rightarrow \gamma\gamma$  width as:

$$F(0) = \frac{\alpha_{em} C_8}{2\pi F_\pi} L_1 \quad (3.27)$$

where  $L_1 = -\tilde{F}_1 + C_1 \frac{M_K^2 + M_\pi^2}{6\pi^2 F_\pi^2}$

In this expression, the possible values of  $L_1 = \pm 0.89$ , set the  $\tilde{F}_1$  portion of the form factor at either  $-1.2 \pm 0.3$  or  $2.5 \pm 0.3$ .

The momentum dependence of the form factor is written as:

$$F_2(t, t') = \frac{\alpha_{em} C_8}{192\pi^3 F_\pi^3} [-(a_2 + 2a_4)D(t, t', m_V) + C(\mu)(t + t')] \quad (3.28)$$

where  $C(\mu)$  is a counter term and again  $F_\pi = 93MeV$  is the pion decay constant.

The momentum dependence of the form factor is carried in  $D(t, t', \mu)$  given by:

$$D(t, t', m_V) = (t + t') \left[ \frac{10}{3} - \left( \ln \frac{M_K^2}{m_V^2} + \ln \frac{M_\pi^2}{m_V^2} \right) \right] + \quad (3.29)$$

$$4 [F(M_\pi^2, t) + F(M_K^2, t) + F(M_\pi^2, t') + F(M_K^2, t')]$$

The chiral logarithms appear in the functions  $F(m^2, t)$  given by defining  $y = t/m^2$  and taking:

$$F(m^2, t) = \left( \left(1 - \frac{y}{4}\right) \sqrt{\frac{y-4}{y}} \ln \frac{\sqrt{y-4} + \sqrt{y}}{\sqrt{y-4} - \sqrt{y}} - 2 \right) m^2 \quad (3.30)$$

As with the QCD analysis the dominance of the  $\rho$  meson is assumed by taking  $m_V = m_\rho$

The parameters  $a_2$ ,  $a_4$ , and the counter term  $C(m_\rho)$  are fixed from the two possible fits to the  $K_{\gamma\gamma}$  width giving the two possible parameter sets listed in Table 3.1



$F_1$	$a_2 + 2a_4$	$C(m_\rho)$
0.89	$-0.3 \pm 0.3$	$14.2 \pm 7.3$
-0.89	$-1.5 \pm 0.3$	$10.3 \pm 7.3$

TABLE 3.1: Parameter sets for the chiral expansion of  $\mathcal{F}(t, t')$ [24]

For decays of the kaon into a four lepton final state via the virtual two gamma intermediate state, the amplitude and decay widths can be computed. In the case of  $K_L^0 \rightarrow \mu^+ \mu^- e^+ e^-$  the final state particles are all distinguishable. The amplitude can thus be written as:

$$A_1 = e^2 \mathcal{F}(t, t') \varepsilon^{\mu\nu\rho\sigma} \frac{(p_+ + p_-)_\nu (p'_+ + p'_-)_\sigma}{tt'} \times \bar{u}(p_-) \gamma_\mu \nu(p_+) \times \bar{u}(p'_-) \gamma_\rho \nu(p'_+) \quad (3.31)$$

and the total decay width is given by:

$$\Gamma(K_L^0 \rightarrow \mu^+ \mu^- e^+ e^-) = \int \sum_{spins} |A_1|^2 d\Phi \quad (3.32)$$

We compare this rate in standard fashion to the  $K_L \rightarrow \gamma\gamma$  width by defining:

$$\rho = \Gamma(K_L^0 \rightarrow \mu^+ \mu^- e^+ e^-) / \Gamma(K_L^0 \rightarrow \gamma\gamma) \quad (3.33)$$

This is done for both allowable values of  $F_1$  and displayed along with the unmodified prediction for the branching fraction as computed without a model dependent form-factor [25]. The result is a significant enhancement in the total decay branching fraction along with an enhancement in the high momentum portion of the resulting phase space for the muon pair. These enhancements are shown in Table 3.2.

$F_1$	Model	$\rho = \Gamma/\Gamma(K_L^0 \rightarrow \gamma\gamma)$
0.89	Point-like Form Factor	$1.42 \times 10^{-6}$
-0.89	Ref. [25]	$1.71 \times 10^{-6}$
0.89	$\chi PT$ Form Factor	$(2.20 \pm 0.25) \times 10^{-6}$
-0.89	Ref. [24]	$(2.18 \pm 0.25) \times 10^{-6}$

TABLE 3.2: Branching fraction calculations for  $K_L^0 \rightarrow \mu^+\mu^-e^+e^-$  using both a point-like form factor [25] and a  $\chi PT$  form factor [24]

### 3.5 CP violation and $\mathcal{F}(K_{\gamma^*\gamma^*})$

The CP violating amplitude arising in the transition elements of the CKM matrix, as expressed by the non-zero nature of  $\epsilon'$  leads to the examination of the angular distributions of the four lepton decay modes of both  $K_L^0$  and  $K_S^0$ . Since pseudoscalar mesons emit photons with mutually perpendicular polarizations [26], the decay planes defined by the resulting Dalitz pairs in a  $K \rightarrow \gamma^*\gamma^* \rightarrow \ell_1\bar{\ell}_1\ell_2\bar{\ell}_2$  contain the electric field vectors of intermediate state photons, and have an angular distribution function directly related to the  $K_{\gamma^*\gamma^*}$  form factor.

The couplings of  $K_L^0$  and  $K_S^0$  to the photon fields are assumed initially to be such that  $K_L^0$  and  $K_S^0$  are approximate eigenstates of the CP operator. In this manner  $K_L^0 \approx K_2^0$  with CP=-1, and  $K_S^0 \approx K_1^0$  with CP=+1. The mesons couple to the photon field via the  $CP_{even} = \Phi F_{\mu\nu}F_{\mu\nu}$  and the  $CP_{odd} = \Phi\epsilon_{\mu\nu\rho\eta}F_{\mu\nu}F_{\rho\eta}$  interactions. In general the effective Lagrangian for a decay of the form  $K \rightarrow \ell_1\bar{\ell}_1\ell_2\bar{\ell}_2$  can be written as the kaon to photon vertex described by[27]:

$$\mathcal{L}(K_{\gamma\gamma}) = \underbrace{\frac{i\mathcal{F}_{odd}}{4M_k}\Phi\epsilon_{\mu\nu\rho\eta}F_{\mu\nu}F_{\rho\eta}}_{CP=-1} + \underbrace{\frac{i\mathcal{F}_{even}}{4M_k}\Phi F_{\mu\nu}F_{\mu\nu}}_{CP=+1} \quad (3.34)$$

in conjunction with the standard QED couplings for the  $\gamma \rightarrow \ell\bar{\ell}$  vertices. Here  $F_{\mu\nu} = \partial_\mu A_\nu - \partial_\nu A_\mu$  with  $A_\mu$  being the photon field.  $\mathcal{F}_{even}$  and  $\mathcal{F}_{odd}$  the form factors

for the  $K_{\gamma^*\gamma^*}$  vertex characterizing the CP even and CP odd eigenstates.

By defining  $\phi$  as the relative angle between the decay planes as defined by the Dalitz pairs, the differential decay spectrum  $d\Gamma/d\phi$  can be used to determine the relative strength of  $K_L^0$  to the CP eigenstates via the form factors of Eq. (3.34).

Denoting the CP odd form factor as  $\mathcal{F}_{odd} = H$  and the CP even form factor as  $\mathcal{F}_{even} = G$ , the angular dependence of the decay  $K_L^0 \rightarrow \gamma^*\gamma^* \rightarrow \mu^+\mu^-e^+e^-$  can be shown to take the form:

$$\begin{aligned} \frac{d\Gamma}{d\phi} = \frac{4\alpha^2}{2(2\pi)^4(M_K)^5} & \left( |H|^2\sigma_1 \sin^2 \phi + |G|^2\sigma_2 \cos^2 \phi \right. \\ & \left. + \text{Im}(HG^*)\sigma_3 \sin \phi \cos \phi + |H|^2\sigma_4 + |G|^2\sigma_5 \right) \end{aligned} \quad (3.35)$$

The coefficients  $\sigma_i = \{2.694, 2.826, 5.504, 18.807, 9.067\}$  are determined from numerical integration of the matrix element for the four lepton decay mode[28]. The form factors can be re-expressed in terms of their relative phases such that

$$H = he^{i\psi_h}, \quad G = ge^{i\psi_g}, \quad \delta = (\psi_g - \psi_h) \quad (3.36)$$

In this manner the angular distribution and the ratio of the absolute strength of the CP violating and CP conserving contributions can be found from:

$$\begin{aligned} \frac{1}{\Gamma(K \rightarrow \gamma\gamma)} \frac{d\Gamma}{d\phi} = F\sigma_1 & [l_1 \sin^2 \phi + (g/h)^2 l_2 \cos^2 \phi \\ & - (g/h) \sin \delta l_3 \sin \phi \cos \phi + l_4 + (g/h)^2 l_5] / [1 + 2(g/h)^2] \end{aligned} \quad (3.37)$$

Where  $l_i = \sigma_i/\sigma_1$  and  $F = 4 \left( \frac{4\alpha^2}{(2\pi)^3 M_K^5} \right)$ .

To isolate both the ratio of the CP conserving to CP violating strength ( $g/h$ )

and the relative phase  $\delta$  the expressions  $\Sigma(\phi)$  and  $\Delta(\phi)$  are defined as:

$$\Sigma(\phi) = [F\sigma_1\Gamma(K_L^0 \rightarrow \gamma\gamma)]^{-1} \left[ \frac{d\Gamma(\phi)}{d\phi} + \frac{d\Gamma(-\phi)}{d\phi} \right] \quad (3.38)$$

$$= [2l_1 \sin^2 \phi + (g/h)^2 l_2 \cos^2 \phi + l_4 + (g/h)^2 l_5][1 + 2(g/h)^2]^{-1}$$

$$\Delta(\phi) = [F\sigma_1\Gamma(K_L^0 \rightarrow \gamma\gamma)]^{-1} \left[ \frac{d\Gamma(\phi)}{d\phi} - \frac{d\Gamma(-\phi)}{d\phi} \right] \quad (3.39)$$

$$= -2[(g/h) \sin \delta l_3 \cos \phi \sin \phi][1 + 2(g/h)^2]^{-1}$$

For the extreme cases of no CP violating form factor or no CP conserving form factor, the limits on the branching fraction for the decay can be computed as:

$$B(K_L^0 \rightarrow \mu^+\mu^-e^+e^-) = \frac{\Gamma(K_L^0 \rightarrow \mu^+\mu^-e^+e^-)}{\Gamma(K \rightarrow \gamma\gamma)} B(K \rightarrow \gamma\gamma) \quad (3.40)$$

For H=0, CP=+1, 100% CP-Conserving mode:

$$B(K_L^0 \rightarrow \mu^+\mu^-e^+e^-) = (3.67 \pm 0.15) \times 10^{-6} \quad (3.41)$$

For G=0, CP=-1, 100% CP-Violating mode:

$$B(K_L^0 \rightarrow \mu^+\mu^-e^+e^-) = (1.63 \pm 0.15) \times 10^{-9} \quad (3.42)$$

From knowledge of both the actual branching ratio for  $K_L^0 \rightarrow \mu^+\mu^-e^+e^-$  and the angular distribution of the Dalitz pairs as characterized by the angle  $\phi$  it is possible to measure the strength of the CP violation arising from the quark mixing.

# CHAPTER 4

## $K_L^0 \rightarrow \mu^+ \mu^- e^+ e^-$ at E871

### 4.1 Motivation for $K_L^0 \rightarrow \mu^+ \mu^- e^+ e^-$ at E871

Experiment E871 performed at the Brookhaven National Laboratory's Alternating Gradient Synchrotron (AGS) was designed to measure the ultra rare dilepton decays of the long lived neutral kaon to a single event sensitivity approaching  $1 \times 10^{-12}$ . The experimental apparatus shown in Fig. 5.2 was designed to maximize acceptance for two body events with low net transverse momentum and an average transverse momentum per particle  $p_t \approx 225 \text{ MeV}/c$ . The primary decay streams searched for were  $K_L^0 \rightarrow \mu^+ \mu^-$ ,  $K_L^0 \rightarrow e^+ e^-$ , and  $K_L^0 \rightarrow \mu^\pm e^\mp$ . Each of these data sets was normalized to the CP violating two pion decay,  $K_L^0 \rightarrow \pi^+ \pi^-$ .

The resulting analysis of the  $\mu\mu$  data set yielded 6216 candidate events for the decay  $K_L^0 \rightarrow \mu^+ \mu^-$  which leads to a branching ratio of  $7.18 \times 10^{-9}$ [2]. At this level the single event sensitive of the  $\mu\mu$  data set was calculated at  $1.15 \times 10^{-12}$  subject to the restrictions of the trigger and event criteria. From this measurement the dispersive contribution to the decay arising from the diagrams of Fig. 2.1 was computed by subtraction of the unitary bound and the estimate of the long distance

amplitude  $|\Re(A_{LD})|$  as computed by Ambrosio and others [20].

As discussed in chapter 3 the long distance amplitude  $A_{LD}$  arising from the diagram pictured in Fig. 3.2 is highly dependent upon the form of the interaction used to compute the  $K_{\gamma^*\gamma^*}$  vertex. The dependence of the amplitude on the differing form factors arising from the VDM, QCD,  $\chi$ PT, and CP violation models, make the extraction of  $|\Re(A_{LD})|$  in a self consistent manner difficult. Without direct measurement of the parameters described in each of the models, or a measurement of a decay which accesses the long distance amplitude and allows for a direct cancellation of the long distance portions of the amplitude arising from the rate as measured by  $B(K_L^0 \rightarrow \mu^+\mu^-)$ , systematic acceptances and errors are introduced through the experimental analysis.

During the analysis of the  $ee$  data set, evidence for the four lepton decay  $K_L^0 \rightarrow e^+e^-e^+e^-$  was found to exist as a background to the primary data sample in the form of  $e^+e^-$  tracking events which had associated partially reconstructed tracks in the forward straw drift chambers of the spectrometer. The partial tracks were recognized to be additional electrons or positrons which were incident upon the spectrometer in such a manner that either their polarities mismatched the field of the dipole analyzing magnets resulting in the particle trajectory being expelled from the valid region of the detector or the particle's momentum was too low to correctly traverse the spectrometer. These events were removed from the data set by instituting a particle tracking or "stub" requirement that allowed for proper tagging of this event class. While this four lepton decay accesses the  $K_{\gamma^*\gamma^*}$  vertex the final state interchange of indistinguishable particles results in interference terms which reduce the sensitive of the E871 spectrometer to the kinematic distribution of the electron/positron pairs. The decay also suffers from significant contamination from other physics backgrounds making it impractical as a means of extracting the long distance dispersive amplitude.

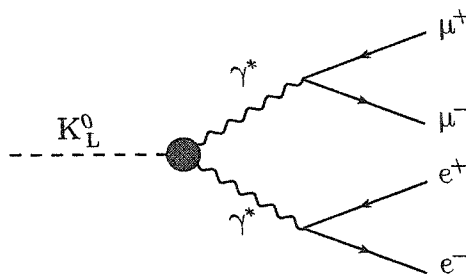


FIG. 4.1: Long distance dispersive diagram for  $K_L^0 \rightarrow \mu^+ \mu^- e^+ e^-$  involving the exchange of two virtual photons,  $\gamma^*$  and directly accessing the  $K_{\gamma^* \gamma^*}$ .

In analogy to the four electron final state, the decay  $K_L^0 \rightarrow \mu^+ \mu^- e^+ e^-$  also accesses the long distance dispersive amplitude through the diagram of Fig. 4.1. Due to the completely distinct final state, there exist no interference terms to suppress the phase space of the decay to which the E871 spectrometer has the greatest acceptance. The form factors of section 3.4, in fact, result in an enhancement of the high invariant mass spectrum for the  $\mu^+ \mu^-$  pair and a softening of the momentum spectrum for the electron pair. This set of kinematics creates a situation where it is favorable for  $K_L^0 \rightarrow \mu^+ \mu^- e^+ e^-$  decays to exist in the  $\mu\mu$  data set at a level sufficient to measure a significant event signal above known physics backgrounds.

Measurement of  $B(K_L^0 \rightarrow \mu^+ \mu^- e^+ e^-)$  from the  $\mu\mu$  data set also serves to give a direct and consistent measurement of the long distance dispersive amplitude which is subject to the same systematic sources of uncertainty. By doing so the measurement can complement the measurement of  $B(K_L^0 \rightarrow \mu^+ \mu^-)$  and allow for extraction of the short distance amplitude without recourse to model dependent approximations. The direct measurement of  $B(K_L^0 \rightarrow \mu^+ \mu^- e^+ e^-)$  from the E871 data sets also permits analysis of the decay rates and momentum spectra to help distinguish between the competing models mentioned in sections 3.2-3.5 as well as provide verification of the model dependent parameters used therein.

## 4.2 Prior Measurements of $K_L^0 \rightarrow \mu^+ \mu^- e^+ e^-$

At the inception of the search for  $K_L^0 \rightarrow \mu^+ \mu^- e^+ e^-$  in the E871 data set, there existed in the world average the observation of a single event from Fermilab experiment E799[1]. The observed branching ratio for the process was quoted as:

$$\Gamma(\mu^+ \mu^- e^+ e^-) / \Gamma_{total} = 2.9_{-2.4}^{+6.7} \times 10^{-9}, \quad (4.1)$$

leading to an effective range in the possible branching fraction extending from  $9.6 \times 10^{-9}$  to  $0.5 \times 10^{-9}$ . This uncertainty spanned almost a full order of magnitude in the allowable range for the process. This indeterminate range did not allow for clear differentiation in the rates arising from a form factor of the type describe by the VDM model of section 3.2 or the more general QCD approach of section 3.3. The size of the observation, being limited to one event, also limited the validity of testing the chiral perturbation theory expansion of the form factor in section 3.4 and the extraction of the parameters  $a_2$  and  $a_4$  from the momentum dependence of the form factor in Eq. (3.28). Enhancement of the phase space in the high muon momentum corner of the Dalitz plot could also not be determined from so limited a set.

The single event nature of the observation also prevented determination of the relative strength of the CP violation in the decay and the examination of the angular dependence of the planes of the Dalitz pairs as in section 3.5. The ratio of the CP-conserving to CP-violating form factors ( $g/h$ ) as expressed in the differential decay rate with respect to the separation angle  $\phi$  as in Eq. (3.37) is not obtainable with the range of variation in the branching fraction or the lack of a statistically meaningful measure of the angle  $\phi$ .

The wide variation in the measurement of the branching ratio also compounds the difficulty in extracting the long distance amplitude for the  $K_{\gamma^* \gamma^*}$  vertex. All



four major models discussed in Chapter 3 rely on the four lepton decay mode as a means of accessing the  $K_{\gamma^*\gamma^*}$  form factors. Proper knowledge of the form factors and coupling of the  $K_{\gamma^*\gamma^*}$  vertex is required to access the long distance dispersive amplitude  $\mathcal{A}_{LD}$  of Eq. (3.1) corresponding to the diagram shown in Fig. 3.2 for the dimuon decay channel of the  $K_L^0$ . The long distance amplitude then serves as the limiting term in extracting the weak flavor changing neutral currents, as shown in Fig. 3.1(c), 3.1(a), and 3.1(b) from the remaining unitary diagram and long distance contributions to the dimuon decay channel. With this knowledge the Wolfenstein factor  $(1 - \rho)^2$  and the real coupling  $Re(V_{ts}^*V_{td})$  are attainable.

During the course of this analysis an additional 43 events were reported by the KTeV collaboration [29]. The events were reported through four body reconstruction of the decay  $K_L^0 \rightarrow \mu^+\mu^-e^+e^-$  in an invariant mass window  $480MeV/c^2 < M_{\mu\mu ee} < 510MeV/c^2$  and with total transverse momentum  $P_T^2 < 0.00025(GeV/c)^2$ . This measurement was reported at a branching ratio of  $2.62 \times 10^{-9}$ .

### 4.3 Event Signature for $K_L^0 \rightarrow \mu^+\mu^-e^+e^-$ at E871

Detection of events of the form  $K_L^0 \rightarrow \mu^+\mu^-e^+e^-$  can be characterized by any one of four general reconstruction methods. The experimental apparatus of E871 was designed originally to search for ultra rare dileptonic decay modes of the neutral kaon, as normalized to the CP violating two pion decay mode. The two body nature of the primary data streams mandates that all decay modes with larger numbers of final state particles also fulfill tracking requirements imposed by the dilepton triggers. In this manner, candidate event signatures for the  $K_L^0 \rightarrow \mu^+\mu^-e^+e^-$  data stream are mandated to include two charged tracks of opposite polarity. These tracks must satisfy spectrometer tracking reconstruction and a parallelism requirement after emerging from the second dipole analyzing magnet. Additionally the

reconstructed tracks must reconstruct under a dilepton or, for normalization, a two pion hypothesis<sup>1</sup> to an invariant mass greater than  $460\text{MeV}/c^2$ . Each of these data streams was recorded during experimental running. The data streams were referred to as the  $\mu\mu$ ,  $ee$  and  $\mu e$  data sets.

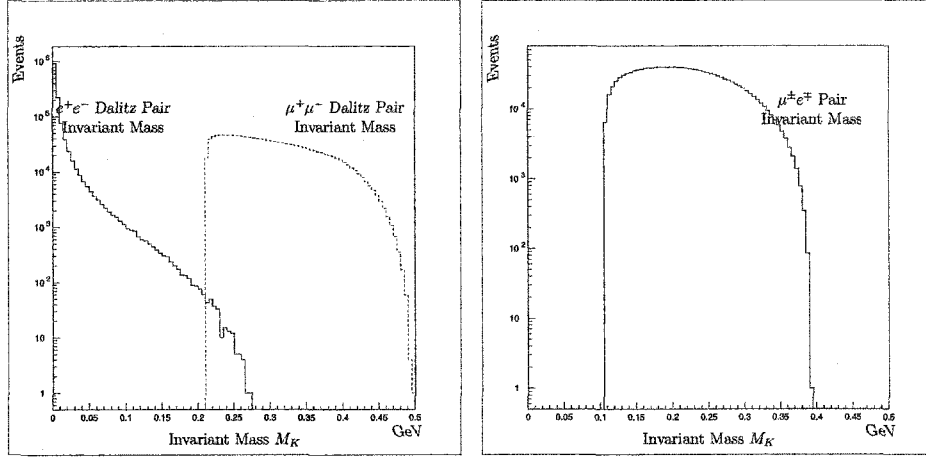
In the case of the  $K_L^0 \rightarrow \mu^+\mu^-e^+e^-$  event signature, form factors discussed in Chapter 3 impart to the muonic Dalitz pair the majority of the invariant mass and momentum of the parent kaon. The electron-positron Dalitz pair correspondingly receives little of the total momentum and results in the pair's having a substantially lower reconstructed invariant mass which does not exceed the trigger threshold value of  $460\text{MeV}/c^2$ . The reconstructions for both the  $\mu^+\mu^-$  and  $e^+e^-$  pairs are shown in Fig. 4.2(a). Events with mixed lepton tracks result in reconstruction of  $\mu^\pm e^\mp$  events for which the reconstructed invariant mass spectrum is shown in Fig. 4.2(b).

The limitations of the  $460\text{MeV}/c^2$  trigger threshold preclude the use of  $e^+e^-$  data stream events for the  $\mu^+\mu^-e^+e^-$  candidates of interest. The limited phase space overlap of the invariant mass reconstruction of events with mixed particle identification tracks with the region of interest above the  $460\text{MeV}/c^2$  threshold results in a minimal acceptance for such track combinations. The  $\mu e$  data stream is therefore omitted from the viable candidate event signatures for  $K_L^0 \rightarrow \mu^+\mu^-e^+e^-$ .

Basic two-body invariant mass reconstruction of events using  $\mu^+\mu^-$  tracks results in an event signature above the  $460\text{MeV}/c^2$  threshold, extending up to the kaon mass of  $497.7\text{MeV}/c^2$ . The E871  $\mu\mu$  data stream maximizes the acceptance of tracks of this nature as it was tuned to accept well defined pairs of muon tracks in the high invariant mass and low transverse momentum region of the allowed phase space.

---

<sup>1</sup>Invariant mass reconstructions assumes the available combinations of  $(\mu^+, \mu^-), (e^+, e^-), (\mu^\pm, e^\mp)$  or  $(\pi^+, \pi^-)$  prior to formal particle identification, based on triggered particle identification detectors



(a) Invariant mass reconstruction of  $e^+e^-$  and  $\mu^+\mu^-$  Dalitz pairs

(b) Invariant mass reconstruction of  $\mu^\pm e^\mp$  tracking pairs

FIG. 4.2: Monte Carlo simulations of invariant mass reconstructions for  $K_L^0 \rightarrow \mu^+\mu^-e^+e^-$  using (a)  $(e^+e^-)$ ,  $(\mu^+\mu^-)$  and (b)  $(\mu^\pm e^\mp)$  tracking pairs

In addition to the identification and reconstruction of a pair of muon tracks, the electron/positron Dalitz pair for the  $K_L^0 \rightarrow \mu^+\mu^-e^+e^-$  decay is required to be registered within the forward spectrometer. Due to the kinematics of the decay process the resulting  $e^+e^-$  signatures fall into four general classification signatures based upon the degree to which each of the particle's trajectories progress through the spectrometer.

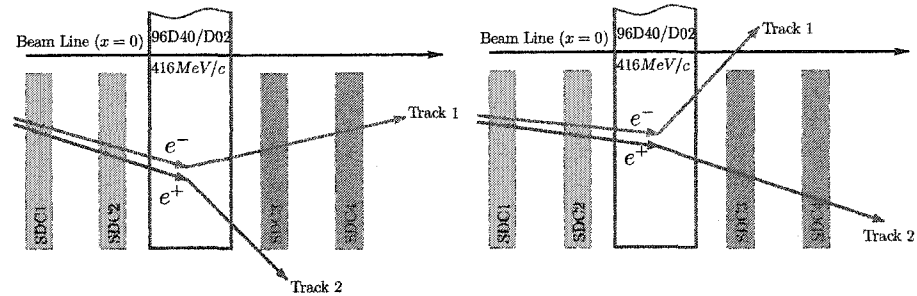
1. Full four track vertex reconstruction of  $\mu^+\mu^-e^+e^-$  with invariant mass at  $M_{K_L}$  and low  $p_T^2$ .
2. Three track vertex reconstruction with one missing  $e^+$  or  $e^-$  with invariant mass greater than  $460MeV/c^2$ .
3. Two track vertex reconstruction with invariant mass greater than  $460MeV/c^2$  and two correlated  $e^+e^-$  tracking stubs projecting back to an associated  $\mu^+\mu^-$  event vertex.
4. Two track vertex reconstruction with invariant mass greater than  $460MeV/c^2$ , and a single  $e^+$  or  $e^-$  tracking stub projecting back to the primary  $\mu^+\mu^-$  event vertex.

### 4.3.1 Decay Vertex

Valid vertex reconstruction is accomplished by projection of charged particle tracks upstream into the decay volume. The tracks must be projected to intersect at a point within the fiducial volume of the decay tank and within the known beam profile. Track intersection is defined by the distance of closest approach (DOCA) of the projected trajectories. The valid vertex DOCA thresholds are determined through detector resolution, particle track deflection in the magnetic fringe field, multiple scattering effects, and other known sources of systematic uncertainties. Vertex reconstruction is discussed fully in chapter 8.

### 4.3.2 Tracking Stubs

Due to the kinematics of the four-body decay and the form factors discussed in sections 3.2, 3.3, 3.4, and 3.5 the electron/positron Dalitz pair emerges from the decay with only a small fraction of the total available invariant mass of the parent kaon, and with only a small fraction of the available momentum when properly boosted into the laboratory reference frame. Additionally the form factor results in a high angular correlation between the  $e^+e^-$  trajectories resulting in little separation of the pair's tracks with respect to each other. Tightly correlated track pairs entering the forward spectrometer are subjected to the dipole field of the analyzing magnets in such a manner as to impart a 416MeV/c transverse (inbend) momentum kick in the x coordinate direction towards the beamline to negatively charged particles incident on the beam right side of the spectrometer and similarly a 416MeV/c transverse momentum kick to positively charged particles incident upon the beam left side of the spectrometer. Due to the low energy nature of the  $e^+e^-$  pairs the trajectory of the member particle whose polarity does not correspond to the dipole field orientation receives a transverse momentum kick away from the central axis



(a) Ejection of positron track from active spectrometer volume based on polarity mismatch with analyzing magnet 96D40/D02

(b) Loss of particle tracking due to excessive inbend of extremely low momentum electron track

FIG. 4.3: Examples of low momentum  $e^+e^-$  Dalitz pair trajectories leaving partial (stub) tracks in straw drift chambers SDC1/SDC2

of the apparatus which most often is sufficient to eject the particle from the active regions of the spectrometer. Similarly tracks with the correct polarity but low incident transverse momentum can be bent towards the central axis on an excessively steep trajectory such that they cross the  $x=0$  position or are unable to enter the second (outbend) analyzing magnet and register in the straw and wire drift chambers SDC3, SDC4, DC5 and DC6. Diagrammatic examples of these situations are shown in Fig. 4.3(a) and 4.3(b). Low momentum  $e^+e^-$  tracks of this kind leave only partial tracking information in the forward straw drift chambers. These partial tracking hits are used to construct tracking “stubs” which are used for vertex correlation and event determination. Detailed discussion of the analysis of partial track and stub reconstruction is discussed in chapter 8.

## 4.4 Physics Backgrounds

The event signatures proposed in Section 4.3 can in some cases be mimicked by other real physics events which undergo decays in flight, electromagnetic pair production, particle misidentification or multi-event pile-up. The primary sources of concern with respect to the aforementioned events signatures are the real decays  $K_L^0 \rightarrow \mu^+\mu^-\gamma$ ,  $K_L^0 \rightarrow \pi^+\pi^-\gamma$ ,  $K_L^0 \rightarrow \pi^+\pi^-\pi^0$ ,  $K_L^0 \rightarrow \pi^+\pi^-e^+e^-$ , as well as  $K_L^0 \rightarrow \pi^\pm e^\mp \nu_e$  and  $K_L^0 \rightarrow \pi^\pm \mu^\mp \nu_\mu$  pile-up. The background contributions of each of these decays are of importance and serve as one of the primary systematic limitations of the experiment. The decay channel  $\pi^0\mu^+\mu^-$  is dismissed from the background analysis because it is known to have a branching fraction less than  $3.8 \times 10^{-10}$ [12].

The background decays of interest have been calculated through the known branching fractions of each decay, detailed Monte Carlo modeling as described in Chapter 7, and through the calculations provided herein.

### 4.4.1 $K_L^0 \rightarrow \mu^+\mu^-\gamma$

The Dalitz decay  $K_L^0 \rightarrow \mu^+\mu^-\gamma$  has a well measured branching fraction of  $3.59 \pm 0.11 \times 10^{-7}$ [12] and is the primary physics background to the measurement of  $K_L^0 \rightarrow \mu^+\mu^-e^+e^-$ . The decay proceeds from a  $K_L^0 \rightarrow \gamma\gamma^*$  intermediate state and follows a high  $q^2$  momentum profile similar to that of  $K_L^0 \rightarrow \mu^+\mu^-e^+e^-$ . This Dalitz decay has the ability to contribute a real signal mimicking background. This occurs when the two muon tracks are stiff enough to satisfy the parallel trigger and the associated gamma-ray converts to a  $e^+e^-$  pair in the front window of the decay volume or in the first two layers of the straw drift chambers. Due to this possibility the probabilities for pair production are calculated for the interaction regions prior to the third layer of straw tubes in straw drift chamber SDC1 in order to register a valid hit cluster for track reconstruction or stub identification. Table 4.1 details the

interaction materials that contribute to the possible pair production cross section for electromagnetic conversion of the daughter photon. The total effective interaction lengths of material that can contribute to this process are divided into those planes prior to the sensitive volume and the first three layers of the first sensitive volume. This allows for additional calculation of additional interaction processes of concern in the vacuum decay region. These are summarized in Table 4.2

The probability for a single interaction can then be computed from the fraction of total interaction lengths  $F_{\lambda_t}$  of material present as:

$$\mathcal{P}(F_{\lambda_t}) = 1 - e^0 = 1 - e^{-f_{\lambda_t}} \quad (4.2)$$

When the results for the materials listed in Table 4.1 and Table 4.2 are calculated they yield the total pair production interaction probabilities listed in Table 4.3.

To compute the maximum total rate for pair production arising via the real photon in decays of the form  $K_L^0 \rightarrow \mu^+ \mu^- \gamma$ , we first compute the effective branching ratio for the decay into the mass region of interest. We take the limits on the invariant mass of the muon pair such that  $460 \text{ MeV}/c < M_{\mu^+ \mu^-} < M_{K_L}$ . Integration of the differential decay rate follows the prescription of Goity and Zhang[22] utilizing a chiral expansion for the effective  $K_{\gamma^* \gamma}$  interaction. The differential decay rate is expressed in terms of the momentum transfer,  $t$ , of the virtual photon:

$$\begin{aligned} \frac{d\Gamma}{dt} &= \Gamma_{K_{\gamma\gamma}} \Phi(t) |F(t)|^2 \\ &= \Gamma_{K \rightarrow \gamma\gamma} \frac{\alpha_{em}}{3\pi} \frac{2}{t} \left(1 - \frac{t}{M_K^2}\right)^3 \left(1 + \frac{2m_\ell^2}{t}\right) \sqrt{1 - 4\frac{m_\ell^2}{t}} |F(t)|^2 \end{aligned} \quad (4.3)$$

Material	Thickness (mm)	Total Pair Production Cross Section $\lambda_0$ ( $g/cm^2$ )	Total Interaction Lengths $\lambda/\lambda_0$
Kevlar 29	0.381 (15 mil)	229.52 10 MeV	$2.39 \times 10^{-4}$
		79.87 100 MeV	$6.87 \times 10^{-4}$
		58.04 1 GeV	$9.45 \times 10^{-4}$
	0.4318 (17 mil)	229.52 10 MeV	$2.71 \times 10^{-4}$
		79.87 100 MeV	$7.79 \times 10^{-4}$
		58.04 1 GeV	$1.07 \times 10^{-3}$
Mylar	0.127 (5 mil)	220.38 10 MeV	$8.01 \times 10^{-5}$
		76.98 100 MeV	$3.15 \times 10^{-4}$
		56.03 1 GeV	$2.29 \times 10^{-4}$
Polyethylene	0.0254 (1 mil)	231.69 10 MeV	$1.04 \times 10^{-5}$
		80.28 100 MeV	$3.00 \times 10^{-5}$
		58.07 1 GeV	$4.15 \times 10^{-5}$
Helium	183	610.17 10 MeV	$4.99 \times 10^{-6}$
		189.14 100 MeV	$1.61 \times 10^{-5}$
		131.67 1 GeV	$2.31 \times 10^{-5}$
Mylar (straw wall)	0.7975 (3.14 mil)	220.38 10 MeV	$5.03 \times 10^{-5}$
		76.98 100 MeV	$1.44 \times 10^{-4}$
		56.03 1 GeV	$1.98 \times 10^{-4}$
Copper	$3.14 \times 10^{-4}$	59.00 10 MeV	$4.77 \times 10^{-6}$
		22.57 100 MeV	$1.25 \times 10^{-5}$
		17.59 1 GeV	$1.60 \times 10^{-5}$
$CF_4C_2H_6$ (gas)	4.0	213.68 10 MeV	$4.65 \times 10^{-6}$
		74.91 100 MeV	$1.33 \times 10^{-5}$
		54.67 1 GeV	$1.82 \times 10^{-5}$
Tungsten Wire	$6.16 \times 10^{-5}$	28.84 10 MeV	$6.39 \times 10^{-5}$
		11.64 100 MeV	$1.80 \times 10^{-4}$
		9.26 1 GeV	$2.45 \times 10^{-4}$

TABLE 4.1: Material properties related to pair production interactions at or forward of SDC1



Region	Total Interaction Lengths $\lambda/\lambda_0$
Material Prior to SDC1	$3.66 \times 10^{-4}$ 10 MeV
	$1.05 \times 10^{-3}$ 100 MeV
	$1.45 \times 10^{-3}$ 1 GeV
Effective Length of 3 Straw Layers	$1.92 \times 10^{-4}$ 10 MeV
	$5.40 \times 10^{-4}$ 100 MeV
	$7.35 \times 10^{-4}$ 1 GeV
Total Effective Interaction Lengths	$5.58 \times 10^{-4}$ 10 MeV
	$1.59 \times 10^{-3}$ 100 MeV
	$2.19 \times 10^{-3}$ 1 GeV

TABLE 4.2: Effective pair production interaction lengths computed at and forward of SDC1

$\gamma$ energy	Total Pair Production Probability
10 MeV	$5.58 \times 10^{-4}$
100 MeV	$1.59 \times 10^{-3}$
1 GeV	$2.18 \times 10^{-3}$

TABLE 4.3: Total probabilities for pair production interactions

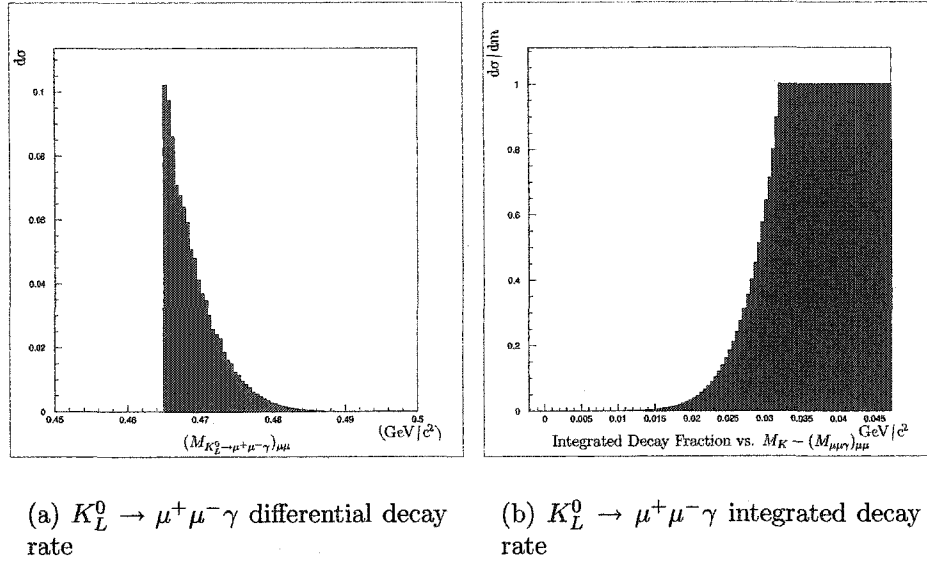


FIG. 4.4: Differential decay rate as a function of invariant mass of the muon pair and effective integrated decay rate as a function of  $M_K - m_{\mu^+ \mu^-}$  for  $K_L^0 \rightarrow \mu^+ \mu^- \gamma$

The form factor is expanded in  $\chi PT$  as:

$$F(t) = 1 + \alpha_{\chi PT} \left( \frac{t}{t - m_\rho^2} \right) \quad (4.4)$$

This integrated decay rate yields

$$\begin{aligned} \Gamma &= \Gamma_{K\gamma\gamma} \int_{m_{low}^2}^{M_K^2} \Phi(t) |F(t)|^2 dt \\ &= 4.39 \times 10^{-10} \end{aligned} \quad (4.5)$$

for  $m_{low} = 460 \text{ MeV}/c^2$  and  $M_K = 497 \text{ MeV}/c^2$ . This is then the effective branching fraction for the background decay, subject only to the requirements of the mass window. We calculate both the decay rate and the integrated decay fraction. These are shown in the plots of Fig. 4.4 as functions of the invariant mass and of the difference between the kaon mass and the lower bound on the invariant mass cut.

$\gamma$ Energy	Effective $B(K_L^0 \rightarrow \mu^+\mu^-(\gamma \rightarrow e^+e^-))$	Expected Background Events
10 MeV	$2.45 \times 10^{-13}$	0.20 events
100 MeV	$6.97 \times 10^{-13}$	0.59 events
1 GeV	$9.56 \times 10^{-13}$	0.82 events

TABLE 4.4: Expected background events of the form  $K_L^0 \rightarrow \mu^+\mu^-\gamma$  in the signal stream at varying energies

The effective decay rate for  $K_L^0 \rightarrow \mu^+\mu^-\gamma$  with ( $M_{\mu\mu} > 460 \text{ MeV}/c^2$ ) can now be multiplied by the pair production probability to calculate the effective rate for the  $K_L^0 \rightarrow \mu^+\mu^-\gamma$  decay branch to mimic the primary decay  $K_L^0 \rightarrow \mu^+\mu^-e^+e^-$ . The resulting rate is taken to be the highest level at which this decay branch can contribute. For the observed number of  $K_L^0 \rightarrow \mu^+\mu^-$  events observed the maximum number of background events is tabulated. These rates are given as a function of photon energy in Table 4.4.

It should be noted that these rates represent the theoretical maxima which can occur due to interactions in the front chambers by assuming identical geometric acceptance factors for both decay modes. Since in the limit as  $p_\gamma \rightarrow 0$  the acceptance for the Dalitz decay must be bounded from above by the acceptance for  $K_L^0 \rightarrow \mu^+\mu^-$ , we can further strengthen our upper bound on the background by replacing the unity assumption for the acceptance ratio  $A_{\mu\mu\gamma}/A_{\mu\mu}$  by the Monte Carlo estimate for the geometric acceptance of the decay  $K_L^0 \rightarrow \mu^+\mu^-\gamma$ . In this case we find that from both E871 and Geant models that the acceptance ratio  $A_{\mu\mu\gamma}/A_{\mu\mu} \ll 1$ . The Monte Carlo models find that the ratio is on the order of 0.05 and is subject to further reduction by the  $K_L^0 \rightarrow \mu^+\mu^-\gamma$  form factor. By including the weighting of this acceptance factor we arrive at the stronger upper bound on the background contribution attributed to  $K_L^0 \rightarrow \mu^+\mu^-\gamma$  in the  $K_L^0 \rightarrow \mu^+\mu^-e^+e^-$  data stream as a function of photon energy. This set of bounds is shown in Table 4.5.

Energy	Expected Background Events
10 MeV	< 0.01 events
100 MeV	< 0.03 events
1 GeV	< 0.04 events

TABLE 4.5: Expected background events of the form  $K_L^0 \rightarrow \mu^+\mu^-\gamma$  including geometric acceptance weights for the E871 apparatus

#### 4.4.2 $K_L^0 \rightarrow \pi^+\pi^-\gamma$

The decay  $K_L^0 \rightarrow \pi^+\pi^-\gamma$  occurs at a branching fraction of  $4.38 \times 10^{-5}$ , roughly two orders of magnitude higher than the  $\mu^+\mu^-\gamma$  decay discussed in section 4.4.1. The cross section for the decay is dominated by the direct emission of the photon as shown in diagram 4.5(b) while the contribution from the inner Bremsstrahlung process of Fig. 4.5(a) is highly suppressed by the CP violating nature of the  $K_L^0 \rightarrow \pi^+\pi^-$  decay process. The direct emission dominance of the decay leads to the use of a  $\rho$ -propagator in the form factor of the decay[30].

$$\mathcal{F} = \frac{a_1}{(m_\rho^2 - m_K^2) + 2m_K E_\gamma^*} + a_2 \quad (4.6)$$

The parameters  $a_1$  and  $a_2$  come from the chiral expansions of the vertex[31]. The result of the form factor is to soften the momentum spectrum of the photon again leading to a condition where the kinematics of the resulting pion pair are favorable to the acceptance range of the E871 spectrometer.

For the decay to mimic the  $\mu^+\mu^-e^+e^-$  signal criteria a series of two processes must occur. To obtain the proper electron tracks or stubs the photon must pair produce in a manner similar to the  $K_L^0 \rightarrow \mu^+\mu^-\gamma$  decay prior to the third layer of straw tubes in the first straw drift chamber (SDC1). The calculation of this process follows from the same interaction cross sections listed in Table 4.1 and 4.2. The dimuon trigger is satisfied only if the pion tracks are both misidentified and incor-

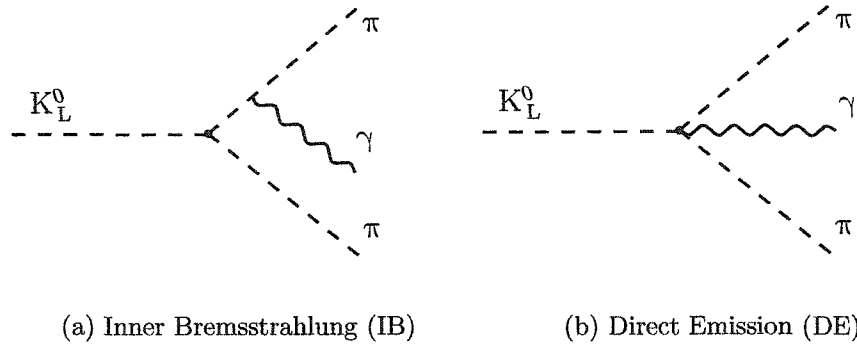


FIG. 4.5: Inner Bremsstrahlung and Direct Emission contributions to  $K_L^0 \rightarrow \pi^+\pi^-\gamma$

rectly flagged as muons, or decay in flight prior to the first momentum measurement in the spectrometer. Particles that decay in flight within the spectrometer result in poorly reconstructed or inconsistent tracks and fail momentum matching during the particle identification requirements for muons.

In the event of particle misidentification of a pion as a muon, or in the event of pion decay in flight within the tolerances of particle tracking a series of incorrect particle mass substitutions are made during the invariant mass reconstruction of the primary vertex. The original pion four vector  $(E_\pi, \vec{p}_\pi)$  in the event of pion decay in flight obeys conservation of momentum such that for  $\pi \rightarrow \mu + \nu_\mu$  where  $(E_\nu, \vec{p}_\nu)$  is the neutrino four vector, then  $\vec{p}_\pi = \vec{p}_\mu + \vec{p}_\nu$ . The momentum  $p_\mu$  is measured in the spectrometer. Because the invariant mass reconstruction also relies upon the energy of the particles the substitution of  $m_\mu$  for  $m_\pi$  occurs when the pion track is incorrectly identified as a muon track. This results in the square of the original pion track's energy being calculated as:

$$E_\pi^2 = p_\pi^2 + m_\mu^2 \quad (4.7)$$

In the relativistic limit the pion momentum then becomes:

$$\begin{aligned}
p_\pi &= \sqrt{(E_\mu + E_\nu)^2 - m_\pi^2} \\
&\approx E_\mu + E_\nu - \frac{m_\pi^2}{2(E_\mu + E_\nu)} \\
&\approx p_\mu + p_\nu + \frac{m_\mu^2 p_\nu - (m_\pi^2 - m_\mu^2) p_\mu}{2p_\mu(p_\mu + p_\nu)}
\end{aligned} \tag{4.8}$$

The reconstructed mass of the  $\mu\mu$  decay vertex under the double pion misidentification or decay in flight becomes:

$$(M_{\mu\mu}^2)_{\pi\pi} = (E_\pi + E_{\pi'})^2 - (\vec{p}_\pi + \vec{p}_{\pi'})^2 \tag{4.9}$$

We expand this in the relativistic limit where  $p_\pi \gg m_\mu$  and in terms of the substitutions above:

$$\begin{aligned}
(M_{\mu\mu}^2)_{\pi\pi} &= E_\pi^2 + E_{\pi'}^2 + 2E_\pi E_{\pi'} - (p_\pi^2 + p_{\pi'}^2 + 2\vec{p}_\pi \cdot \vec{p}_{\pi'}) \\
&\approx (p_\pi^2 + m_\mu^2) + (p_{\pi'}^2 + m_\mu^2) + 2 \left( p_\pi + \frac{m_\mu^2}{2p_\pi} \right) \left( p_{\pi'} + \frac{m_\mu^2}{2p_{\pi'}} \right) \\
&\quad - (p_\pi^2 + p_{\pi'}^2 + 2(\vec{p}_\pi \cdot \vec{p}_{\pi'})) \\
&\approx 2m_\mu^2 + 2 \left[ p_\pi p_{\pi'} + \frac{m_\mu^4}{4p_\pi p_{\pi'}} + \frac{(p_\pi^2 + p_{\pi'}^2)}{2p_\pi p_{\pi'}} m_\mu^2 \right] - 2(\vec{p}_\pi \cdot \vec{p}_{\pi'})
\end{aligned} \tag{4.10}$$

In contrast to the misidentification scenario, had the invariant mass vertex been reconstructed from a properly identified set of pions then the invariant mass would have appeared as:

$$\begin{aligned}
M_{\pi\pi}^2 &= (E_\pi + E_{\pi'})^2 - (\vec{p}_\pi + \vec{p}_{\pi'})^2 \\
&= p_\pi^2 + m_\pi^2 + p_{\pi'}^2 + m_{\pi'}^2 + 2E_\pi E_{\pi'} - (p_\pi^2 + p_{\pi'}^2 + 2\vec{p}_\pi \cdot \vec{p}_{\pi'}) \\
&= 2m_\pi^2 + 2E_\pi E_{\pi'} - 2(\vec{p}_\pi \cdot \vec{p}_{\pi'})
\end{aligned} \tag{4.11}$$

Again we expand the energy in the relativistic limit to find:

$$M_{\pi\pi}^2 \approx 2m_\pi^2 + 2 \left( p_\pi + \frac{m_\pi^2}{2p_\pi} \right) \left( p_{\pi'} + \frac{m_\pi^2}{2p_{\pi'}} \right) - 2(\vec{p}_\pi \cdot \vec{p}_{\pi'}) \quad (4.12)$$

In the event of pure misidentification where there is no decay in flight of the pion, the true momenta  $\vec{p}_\pi$  are taken as measured momenta  $\vec{p}_\mu$ . The difference in the invariant mass as calculated between Eq. (4.12) and (4.10) then becomes:

$$M_{\pi\pi}^2 - (M_{\mu\mu}^2)_{\pi\pi} = 2(m_\pi^2 - m_\mu^2) + (m_\pi^2 - m_\mu^2) \left( \frac{p_\pi^2 + p_{\pi'}^2}{p_\pi p_{\pi'}} \right) + \frac{(m_\pi^4 - m_\mu^4)}{2p_\pi p_{\pi'}} \quad (4.13)$$

It is clear from Eq. (4.13) that the minimum difference between the true invariant mass and the double misidentified invariant mass under a false  $\mu\mu$  hypothesis occurs for symmetric decays where  $p_\pi^2 = p_{\pi'}^2$ .

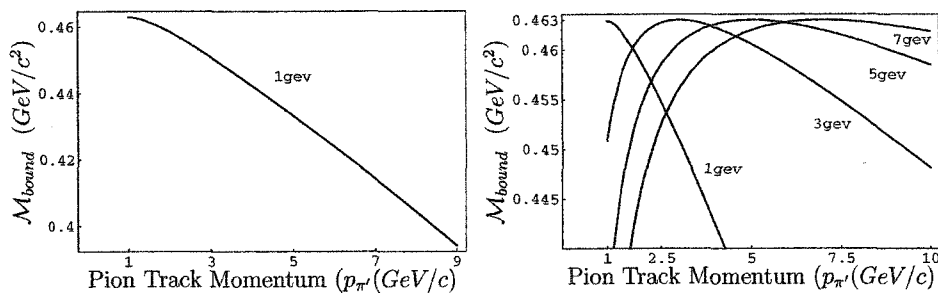
For the decay  $K_L^0 \rightarrow \pi^+\pi^-\gamma$ , the  $\pi\pi$  invariant mass reconstruction for the endpoint of the decay where the photon momentum  $p_\gamma \approx 0$  approaches the invariant mass of the kaon such that  $M_{\pi\pi}^2 \approx M_K^2$ . The difference between the kaon mass and the error induced through double misidentification of the  $\pi\pi$  pair being reconstructed as a  $\mu\mu$  pair results in an upper bound on the possible invariant mass reconstructions of  $K_L^0 \rightarrow \pi^+\pi^-\gamma$  events. The bound is found by considering:

$$\mathcal{M}_{bound}^2 = M_K^2 - (M_{\pi\pi}^2 - (M_{\pi\pi}^2)_{\mu\mu}) \quad (4.14)$$

The upper bound on the invariant mass as measured at the endpoint of the decay is then:

$$\mathcal{M}_{bound} = \sqrt{M_K^2 - (M_{\pi\pi}^2 - (M_{\pi\pi}^2)_{\mu\mu})} \quad (4.15)$$

Fig. 4.6(a) and 4.6(b) show the bounding curves on the invariant mass of the



(a) Maximum invariant mass reconstruction of a  $K_L^0 \rightarrow \pi^+\pi^-\gamma$  event with  $p_\pi = 1\text{GeV}/c$  and  $p_{\pi'}$  varying from 1 to 10  $\text{GeV}/c$

(b) Maximum invariant mass reconstruction curves for  $K_L^0 \rightarrow \pi^+\pi^-\gamma$  events with  $p_\pi = 1, 3, 5, 7\text{GeV}/c$  and  $p_{\pi'}$  varying from 1 to 10  $\text{GeV}/c$

FIG. 4.6: Maximum invariant mass reconstructions for  $K_L^0 \rightarrow \pi^+\pi^-\gamma$  events with both members of the  $\pi^+\pi^-$  pair being misidentified as a  $\mu^+\mu^-$  pair. The event is taken at the end point of the  $K_L^0 \rightarrow \pi^+\pi^-\gamma$  spectrum with  $p_\gamma = 0$ .

kaon as reconstructed from a  $K_L^0 \rightarrow \pi^+\pi^-\gamma$  event where the  $\pi^+\pi^-$  pair is misidentified and the vertex subsequently reconstructed under the  $\mu^+\mu^-$  hypothesis. The curves are plotted from the minimum accepted muon/pion track momentum of 1  $\text{GeV}/c$  to the upper end of the decay spectrum at 10  $\text{GeV}/c$ . From the plots it is easy to see that the effect of the momentum dependence is to push down the reconstructed mass of events with asymmetric tracks. This results in an upper bound on the invariant mass of double misidentified events which occurs at  $p_\pi = p_{\pi'}$ . The maximum value of improperly reconstructed kaon mass  $(\mathcal{M}_K^{\pi\pi\gamma})_{\mu\mu}$  is found to quickly reach its asymptotic limit for relativistic tracks such that for  $p_\pi \gg m_\mu$  the resulting upper bound for background decay reconstruction is given by:

$$(\mathcal{M}_K^{\pi\pi\gamma})_{\mu\mu} = 463.048 \text{ MeV}/c^2 \quad (4.16)$$

As a result of this bound, all contamination of the  $K_L^0 \rightarrow \mu^+\mu^-e^+e^-$  data stream by misidentified  $K_L^0 \rightarrow \pi^+\pi^-\gamma$  events with associated pair production can



be eliminated by extending the lower bound on the invariant mass window from the original value of  $460\text{MeV}/c^2$  up to the limit set by double pion misidentification or decay in flight of  $463\text{MeV}/c^2$ . In this manner the phase space for the decay is eliminated. Any overlap contamination of the signal region with this class of events due to the tracking resolution of the spectrometer is highly suppressed by the additional requirement of electromagnetic pair production from the associated gamma as detailed in section 4.4.1. In this manner the real background expected from  $K_L^0 \rightarrow \pi^+\pi^-\gamma$  is essentially zero.

#### 4.4.3 $K_L^0 \rightarrow \pi^+\pi^-\pi^0$

Decays of the form  $K_L^0 \rightarrow \pi^+\pi^-\pi^0$  can in analogy to the decays of section 4.4.1 and 4.4.2 contribute a signal mimicking that of the  $K_L^0 \rightarrow \mu^+\mu^-e^+e^-$  data criterion of section 4.3 when one of the photons from the  $\pi^0$  produces an electron-positron pair on the material forward of the straw tracking chambers, and the  $\pi^+\pi^-$  is double misidentified as a  $\mu^+\mu^-$  pair or decays in flight to a  $\mu^+\mu^-$  pair. Because the  $K_L^0 \rightarrow \pi^+\pi^-\pi^0$  decay stream encompasses 12.58% of the  $K_L^0$  decay branches it is of concern in computing the background to the event signal.

Because a  $K_L^0 \rightarrow \pi^+\pi^-\pi^0$  event must be subjected to a double misidentification of the charged pions, the same analysis of the invariant mass reconstruction as detailed in section 4.4.2 can be applied again to compute the upper bound on the invariant mass of  $K_L^0$  vertex under improper track identification and reconstruction. Because the neutral  $\pi^0$  is on shell the final state momentum and invariant mass available to the reconstructed vertex at the end point of the decay where  $p_{\pi^0} = 0$  is shifted off the kaon mass. In analogy to Eq. (4.14) and (4.15) the upper bound on

the reconstructed invariant mass from double pion misidentification become:

$$\mathcal{M}_{id}^2 = (M_K^2 - m_{\pi^0}^2) - (M_{\pi\pi}^2 - (M_{\pi\pi}^2)_{\mu\mu}) \quad (4.17)$$

$$\mathcal{M}_{bound} = \sqrt{(M_K^2 - m_{\pi^0}^2) - (M_{\pi\pi}^2 - (M_{\pi\pi}^2)_{\mu\mu})} \quad (4.18)$$

The analysis of these equations proceeds in the same manner as given in Section 4.4.2. Through these calculations we derive a strict upper bound on the possible invariant mass of a  $K_L^0 \rightarrow \pi^+\pi^-\pi^0$  vertex under the  $\mu\mu$  hypothesis of  $442.9\text{MeV}/c^2$ . This value lies substantially under the the lower edge of the established signal box for  $K_L^0 \rightarrow \mu^+\mu^-e^+e^-$  and is not considered to contribute to the background of the data set.

#### 4.4.4 $K_L^0 \rightarrow \pi^+\pi^-e^+e^-$

The four body decay  $K_L^0 \rightarrow \pi^+\pi^-e^+e^-$  has been observed with a branching fraction of  $3.5 \pm 0.6 \times 10^{-7}$ [12], roughly two orders of magnitude higher than the expected level of the signal for  $K_L^0 \rightarrow \mu^+\mu^-e^+e^-$ . While similar in structure to the four body final state of interest in this analysis, the presence of the two final state pions and the hadronic nature of the interactions involved result in a form factor of the form[32]:

$$\mathcal{F} = \tilde{g}_{M1} \left[ 1 + \frac{a_1/a_2}{(M_\rho^2 - M_K^2) + 2M_K(E_{e^+} + E_{e^-})} \right] \quad (4.19)$$

This form factor leads to a kinematic acceptance which again favors low momentum electron pairs in a fashion similar to  $K_L^0 \rightarrow \mu^+\mu^-e^+e^-$ . The Monte Carlo models used to simulate this decay process also indicate  $\pi^+\pi^-$  track momentum distributions similar to the expected  $\mu^+\mu^-$  track distributions for the event signal.

For a  $K_L^0 \rightarrow \pi^+\pi^-e^+e^-$  event to mimic the event signature described in Section

4.3 a situation of double pion misidentification like that described for the  $K_L^0 \rightarrow \pi^+\pi^-\gamma$  decays of section 4.4.2 or decay in flight of both pions would have to occur. Since the decay process involves results from diagrams dominated by virtual photon production resulting from direct emission or internal Bremsstrahlung similar to the  $K_L^0 \rightarrow \pi^+\pi^-\gamma$  diagrams of Fig. 4.5, the analysis of the invariant mass reconstruction of the decay vertex based on the pion tracks is analogous to that described in sections 4.4.2 and 4.4.3. The presence of the on shell  $e^-e^+$  pair again has the effect of slightly shifting the maximum invariant mass reconstruction off the true kaon mass. The analysis of the effect of double misidentification follows in an identical fashion to that given in section 4.4.3 resulting in an endpoint bound on the improperly reconstructed invariant kaon mass of  $463.047\text{MeV}/c^2$ .

The invariant mass cut at 463.048 which eliminates the background contamination from  $K_L^0 \rightarrow \pi^+\pi^-\gamma$  thus also has the effect of eliminating contamination from  $K_L^0 \rightarrow \pi^+\pi^-e^+e^-$  from the data set.

#### 4.4.5 $K_{e3}$ and $K_{\mu3}$ Pileup

The semi-leptonic decays  $K_L^0 \rightarrow \pi^\pm e^\mp \nu_e$  and  $K_L^0 \rightarrow \pi^\pm \mu^\mp \nu_\mu$  account for 38.79 and 27.18 percent respectively of the allowed decay branches for  $K_L^0$ . Together they are responsible for 65.97% of the events occurring in the forward decay tank, and as such present a difficult problem regarding vertex resolution and event overlap. Event pileup occurs when two separate kaons decay in the evacuated decay region at or near the same spatial coordinates and with tracks triggering the hardware and software criterion for a level 3 event trigger within the same 200ns event window. This overlap of distinct events combining to form a valid detector trigger can lead to an event signature similar to that discussed in section 4.3 and result in background noise in the signal region for  $K_L^0 \rightarrow \mu^+\mu^-e^+e^-$ .

For semi-leptonic decay pileup to mimic the  $K_L^0 \rightarrow \mu^+ \mu^- e^+ e^-$  trigger, multiple variants on the possible track combinations and decays in flight can contribute. The background resulting from these combinatorial arrangements requires Monte Carlo modeling and background subtraction in the final analysis. The primary modes that are thought to contribute to the background signal are double  $K_{\mu 3}$  events, and mixed  $K_{\mu 3}/K_{e 3}$  events.

Double  $K_{\mu 3}$  events are found to mimic the trigger criterion when a positive muon from  $K_L^0 \rightarrow \mu^+ \pi^- \nu_\mu$  and a negative muon from the charge conjugate decay  $K_L^0 \rightarrow \pi^+ \mu^- \nu_\mu$  enter the spectrometer and satisfy the parallel trigger requirements of the dimuon event trigger. The remaining  $\pi^-$  and  $\pi^+$  can then enter the forward tracking chambers leaving partial tracking stubs as discussed in section 4.3.2. Because no momentum measurement or particle identification is performed on the partial track stub the charged pions can appear to mimic the signature of a soft  $e^+ e^-$  pair.

The second type of pile up events involves a  $K_{\mu 3}$  event in coincidence with a  $K_{e 3}$  event. In this case the muon from the  $K_{\mu 3}$  decay in combination with a misidentified pion, or pion decay in flight from either the same  $K_{\mu 3}$  or from the companion  $K_{e 3}$  satisfy the trigger criterion for the  $\mu^+ \mu^-$  event trigger. The remaining electron and charged pion then leave partial tracking stubs in the forward regions of the spectrometer thereby mimicking the event signature for  $K_L^0 \rightarrow \mu^+ \mu^- e^+ e^-$ .

Pileup events of this sort do suffer from a number of factors which diminish their acceptance into the detector regions or distinguish them from the four body event of interest. The foremost limitation on the event acceptance is the allowed phase space and kinematics for each of the semileptonic decays. These decays by their three body nature have the Dalitz plots shown in Fig. 4.7. The transverse momentum kick imparted by the spectrometer magnets favor the high momentum, high invariant mass region of the  $\pi/\mu$  decay-pair phase space to maximize acceptance for the decay. This requirement forces the decay to occur near its endpoint where

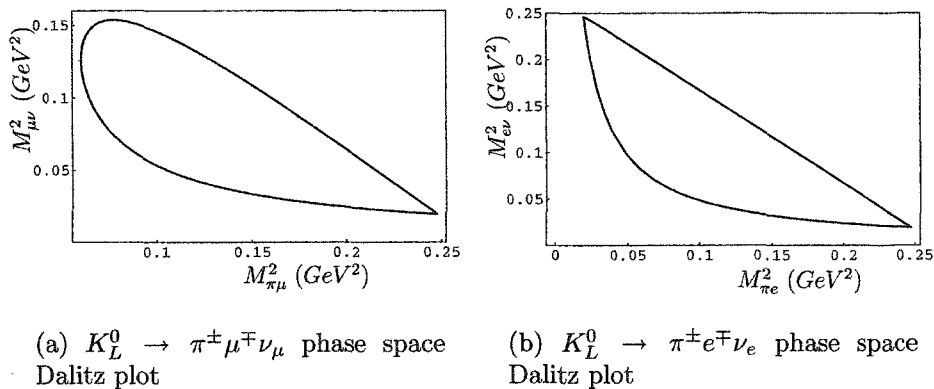


FIG. 4.7:  $K_{\mu 3}$  and  $K_{e 3}$  Dalitz plots representing the available three body phase space in the center of momentum frame such that  $p_K = 0$ . Only the high mass  $M_{\pi\mu}$  and  $M_{\pi e}$  near the  $p_\nu = 0$  endpoint contribute to the events accepted into the E871 spectrometer.

the neutrino comes off at rest in the center of momentum frame, such that  $p_\nu \approx 0$ . By limiting the effective acceptance of the decay to the corner of the Dalitz plot, the probability of event overlap satisfying the requirements of the trigger are diminished. Integrating the phase space results in an effective branching ratio for decays with kinematics favorable to the E871 detector geometry and acceptances. In addition to the limited phase space available to the acceptance of the decays, the pile up events show no tight angular correlation in the particle trajectories which leave partial tracking stubs in the forward spectrometer. In contrast, the  $e^+e^-$  pairs from  $K_L^0 \rightarrow \mu^+\mu^-e^+e^-$  decays are not only extremely soft in terms of their momentum spectrum, but have an extreme degree of angular correlation which creates a tight clustering in the resultant tracking stubs. Moreover the soft nature of the  $e^+e^-$  pair also creates a high degree of correlation between the tracking stubs and the primary laboratory decay plane as defined by the  $\mu^+\mu^-$  pair reconstruction vertex and the trajectories through SDC1 and SDC2. Event pileup does not exhibit this type of planar correlation and as such can be minimized through cuts on the decay plane angles.

The difficulty in determining the exact rate of event overlap is based upon Monte Carlo simulations of the decay vertex distributions. To fully determine the rate at which this process creates a significant background, the invariant mass distribution for decays exceeding the kaon mass is retained and used to provide a flat background subtraction in the signal region.

# CHAPTER 5

## Experiment E871 Detector

### 5.1 E871 Detector System

The E871 detector system was designed to reach a single event sensitivity of  $10^{-12}$  for the  $\mu e$  decay channel in a designated running period of 5600 hours using the 24 GeV/c high intensity proton beam at the BNL AGS. To achieve this sensitivity goal the tracking chambers, particle identification detectors, and data acquisition systems were designed and constructed under the following general criteria:

- Neutral kaon flux at the production target and decay products accepted by the detector systems should be maximized.
- Neutral beam production size should be minimized
- Minimal acceptance of neutral kaon background events
- High resolution tracking, momentum measurement, vertex and invariant mass reconstruction and accurate particle identification of electrons, muons and pions.

The experimental apparatus was assembled at BNL and situated in the B5 secondary beam line of the AGS as shown in Fig. 5.1. To achieve the goals outlined

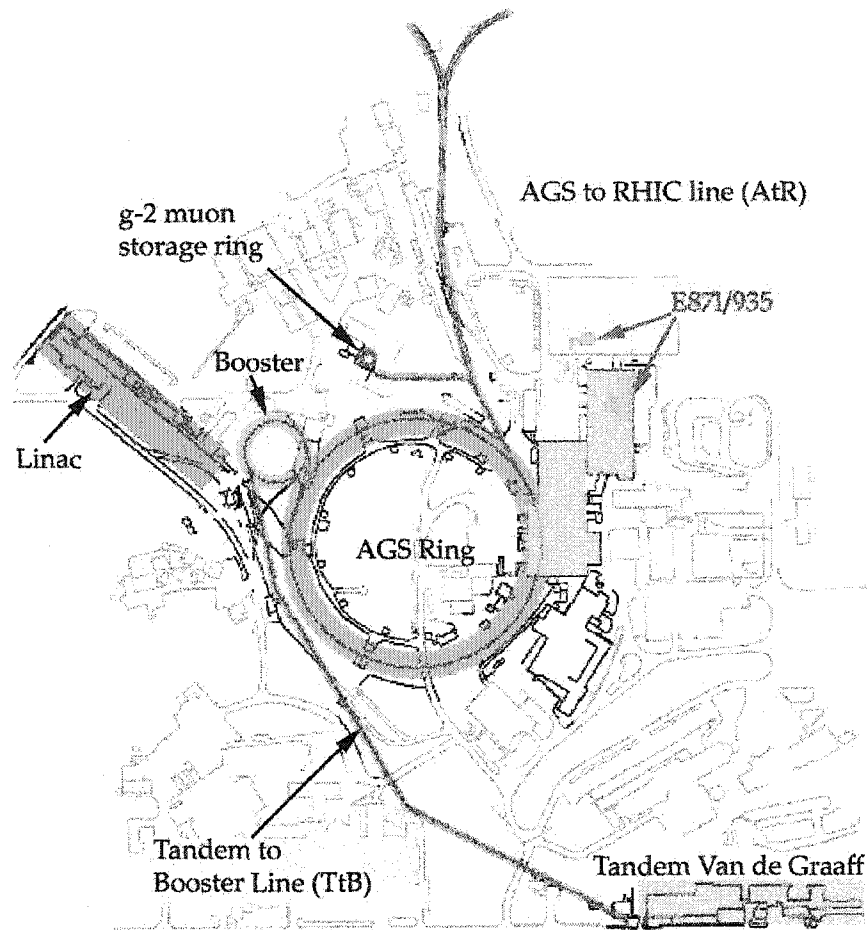


FIG. 5.1: Brookhaven National Labs AGS

above, the experimental apparatus was designed as a follow up and upgrade to the E791 experiment [33]. The E791 double arm spectrometer was redesigned into a single unit with symmetric beam left and right components. The apparatus was arrayed in linear fashion consisting of first beam transport and decay volume, then tracking and momentum analyzing units, followed by particle identification detectors and a muon range stack. Key to the success of this design was the introduction of a neutral beam stop within the first analyzing magnet. The overall layout of these systems is shown in Fig. 5.2, 5.3 and 5.4.



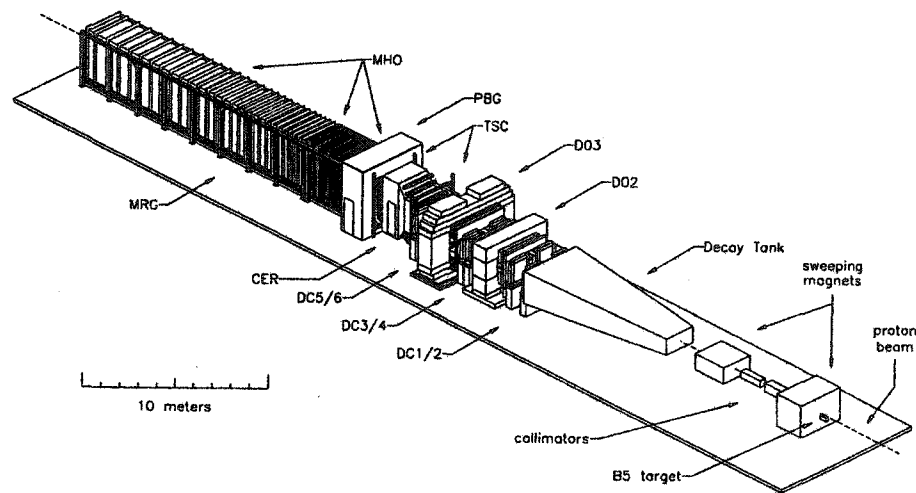


FIG. 5.2: E871 Experimental apparatus

To achieve the stated design goals redundancy was built into all the systems providing multiple distinct tracking and momentum measurements as well as redundant particle identification of electrons and muons. The experimental apparatus started with production target and beam transport systems. A platinum target mounted to a water cooled beryllium support defining the  $z=0$  origin of the experiment created a high intensity secondary beam from the incident 24 GeV primary proton beam delivered by the AGS. Dipole sweeping magnets, lead foils and precision collimators immediately downstream of the target removed charged particles and photons from the secondary beam and shaped the beam transported to the primary decay volume. Long-lived neutral kaons which decayed in the primary volume had their products enter the tracking spectrometer through a downstream Kevlar and Mylar window in the decay tank.

Tracking position measurements for charged decay products were made using four sets of beam left and right, fast gas straw tube drift chambers and two sets of hexagonal cell wire drift chambers. Two dipole spectrometer magnets inbetween sets of tracking chambers provided independent momentum measurements of the

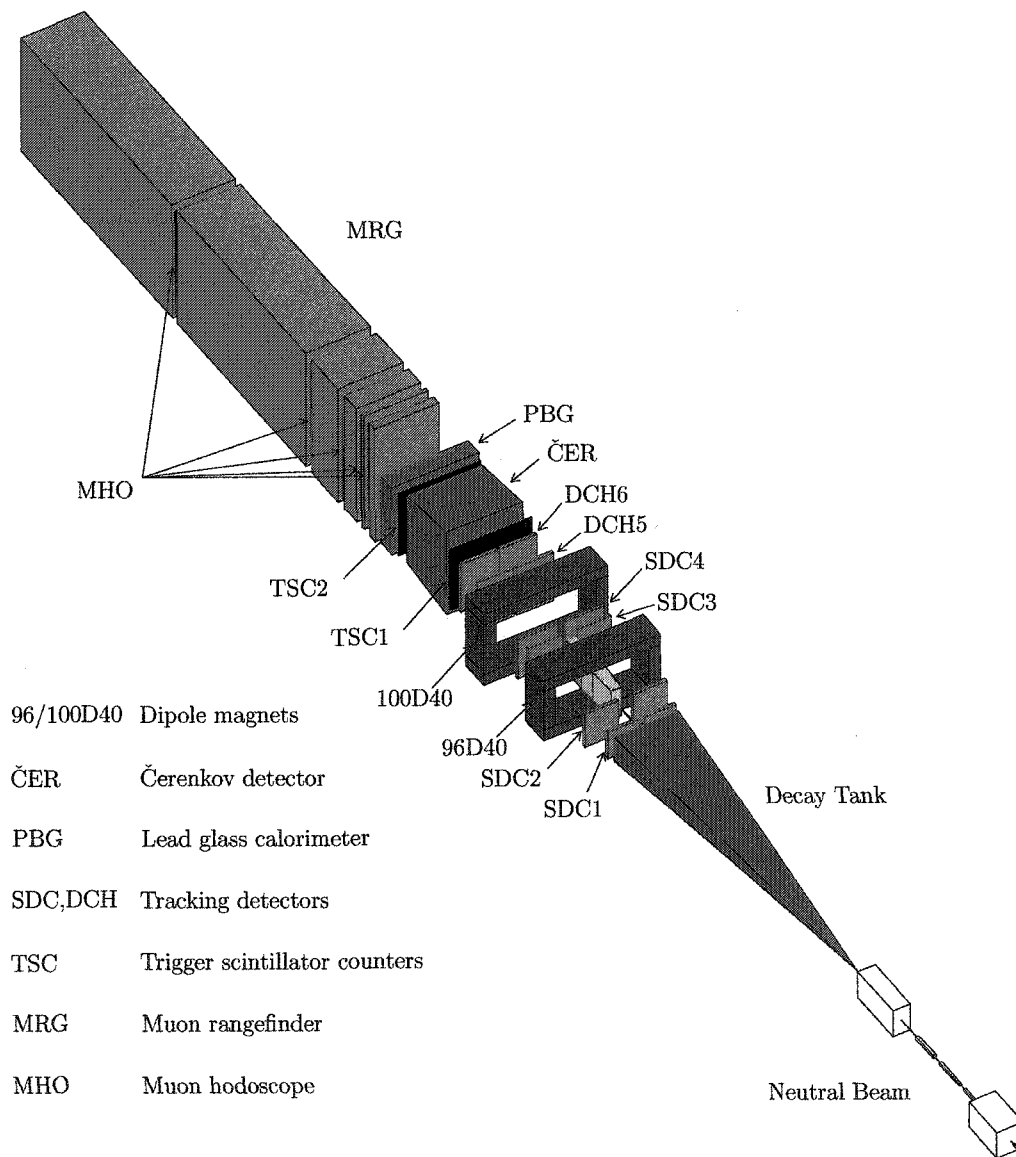


FIG. 5.3: E871 Experimental apparatus

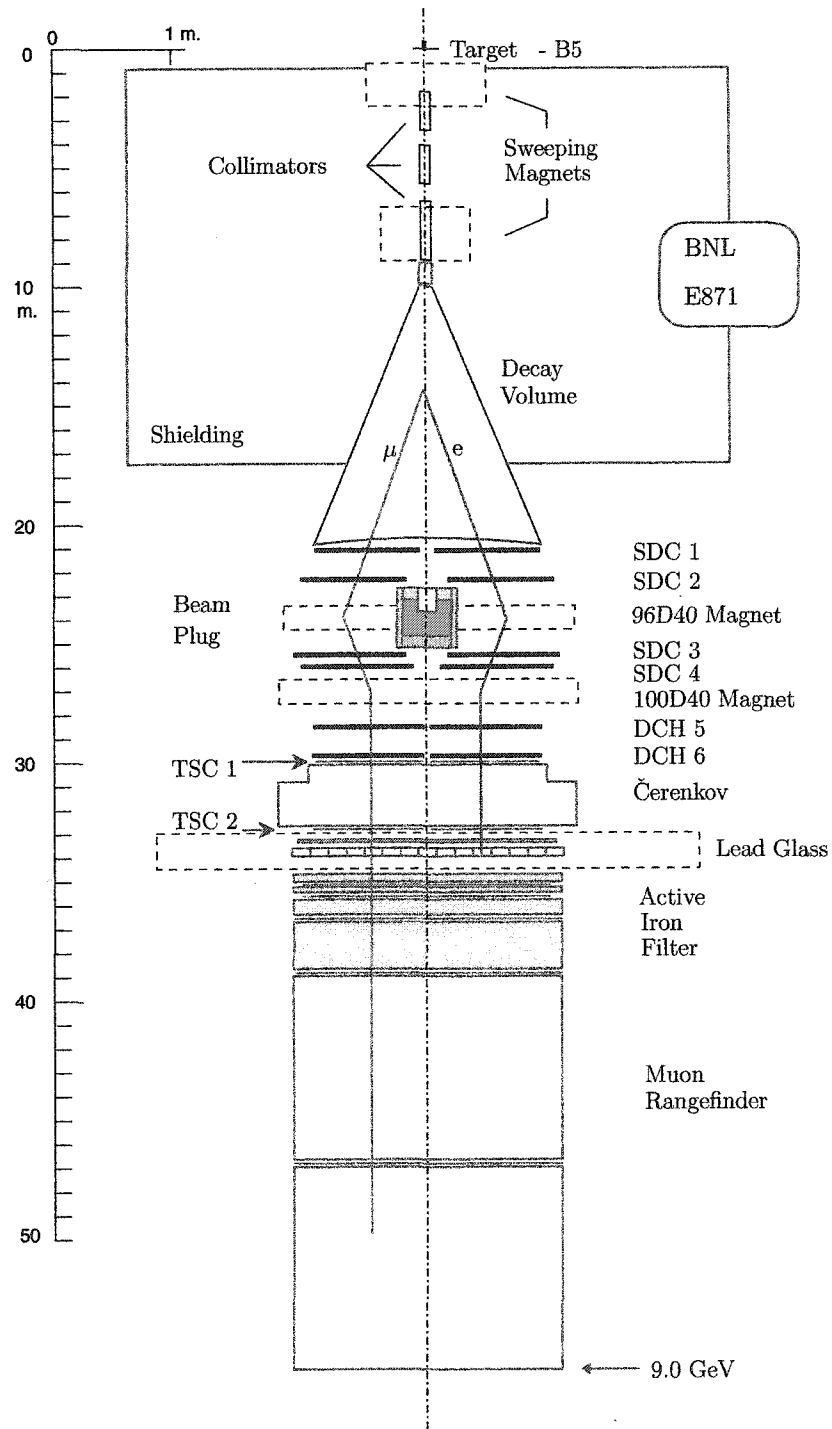


FIG. 5.4: E871 Spectrometer and particle identification

particle trajectories. The magnetic fields of the spectrometer magnets were tuned to impart a net 200MeV/c in-bend momentum kick, resulting in charged particles from 2-body kaon decays with low transverse momentum that emerged roughly parallel to the beam axis.

Triggering of the experiment and particle identification were provided by a series of detectors downstream of the final spectrometer aperture. General charged particle triggering was performed by a series of fast response scintillator hodoscopes. Electron triggering and identification were performed by a large volume hydrogen gas threshold Čerenkov counter and a segmented lead glass array. Muon identification was provided by a scintillator hodoscope and a 10GeV/c momentum range counter consisting of iron, marble and aluminum plates interspersed with an array of scintillator hodoscopes and planes of proportional tube counters. Pion discrimination was performed using the Čerenkov counter as a veto, lead glass array hadronic shower energy deposition, and veto from the muon rangefinder elements.

## 5.2 Kaon Production Target

K mesons are generated from the strong interaction via a standard  $\Delta S = 0$  hadronic interaction as previously discussed. A beam of kaons can thus be produced through the use of an intense proton beam which is incident upon a stationary hadronic target. If the incident proton beam energy exceeds the threshold for inclusive production then kaons are produced primarily from the  $\pi^- p^- \rightarrow K^0 \Lambda$  mechanism[34]. Over the experimental run three production targets were used in this manner.

To highly localize the production origin a platinum strip of 127.0mm length, 3.15mm width and 2.540mm height was thermally mounted to a water cooled beryllium heat sink. Platinum has a density of  $21.45g/cm^3$  and hadronic interaction

length of  $189.7g/cm^2$  thus corresponding to 1.44 hadronic interaction lengths for the 24GeV proton beam . The low mass, low Z beryllium base reduced contamination of the neutral beam from proton interactions off the heat sink and base stem.

The thermal interface between the platinum and beryllium was facilitated on the first two targets using a Ag-Cu-Sn alloy<sup>1</sup> braze. To reduce thermal stress to the material due to non-uniform energy deposition over the 127.0mm interaction path, the platinum strip was divided into five equal length segments along the z-axis.

The target assembly was mounted in the AGS B5 beam line at an angle of  $-3.75^\circ$  to the horizontal. This production angle was chosen to produce a high neutral kaon flux and low neutron production in the resulting beam. At a nominal incident flux of  $20 \times 10^{12}$  protons per spill the resulting neutral beam composition was expected to consist of  $10^8$  kaons and  $2 \times 10^9$  neutrons per spill.

During a high intensity test of the target at  $25 \times 10^{12}$  protons per pulse during March 1995, the thermal braze on the first two segments of the production target failed resulting in the loss of the upstream segments of the unit. The target was replaced with a spare target of identical design for the remainder of the 1995 and first part of the 1996 production run. In May of 1996 a new target was installed consisting of a 150mm long platinum strip divided into 15 equal length segments. The platinum was bonded to a larger heat sink using a Ag-Cu-Li alloy<sup>2</sup> braze designed to withstand a higher temperature environment.

### 5.3 Neutral Beam Collimation

The neutral beam was extracted horizontally at  $3.75^\circ$  from the proton target axis to maximize kaon to neutron flux. The beam first passed through a pair of dipole

---

<sup>1</sup>60% Ag, 30% Cu, 10% Sn

<sup>2</sup>92% Ag, 7.5% Cu, 0.025% Li

sweeping magnets (B5P4/B5P5) to remove charged particles from the stream. The first dipole B5P4 removed both the primary proton beam and positively charged secondary particles from the beam line by redirection to the concrete and steel beam dump located immediately down stream of the primary target below the neutral beam line. The second sweeping magnet, B5P5, removed remaining charged particles from the beamline. Photons were removed from the beam line through a series of 17 2.5mm thick lead foils placed in the upstream dipole magnet. The foils were designed to convert the incident photons to  $e^+e^-$  pairs which were then subsequently swept from the line by B5P4/B5P5. Neutral pions were eliminated by their rapid decay to a  $\gamma\gamma$  prior to the lead foils, and the resulting photons removed as described above.

The neutral beam was collimated using a series of precision lead lined brass collimators as shown in Fig. 5.5. The collimators provided an opening angle of 5mrad in the x direction and 20mrad in the y direction. This opening permitted a well defined 100  $\mu$ steradian neutral beam to enter the decay region.

## 5.4 Decay Tank

The lifetime for the  $K_L^0$  component of the neutral kaon results in a  $c\tau = 15.51m$ . In order to permit a sufficient proportion of the incident particles to decay upstream of the first detector elements a 10.9m long evacuated decay tank was situated after the second sweeping magnet and brass collimators. The tank extended from beam position  $z=10m$ , down to  $z=20.9$  using a trapezoidal geometry to expand from an upstream dimension of 10cm in X by 16cm in Y, to the downstream aperture measuring 193cm in X by 86.4cm in Y as shown in Fig. 5.6. The tank was constructed of welded 5cm thick steel plates embedded in concrete to provide structural support and radiation shielding. The concrete used was borated to capture neutrons from

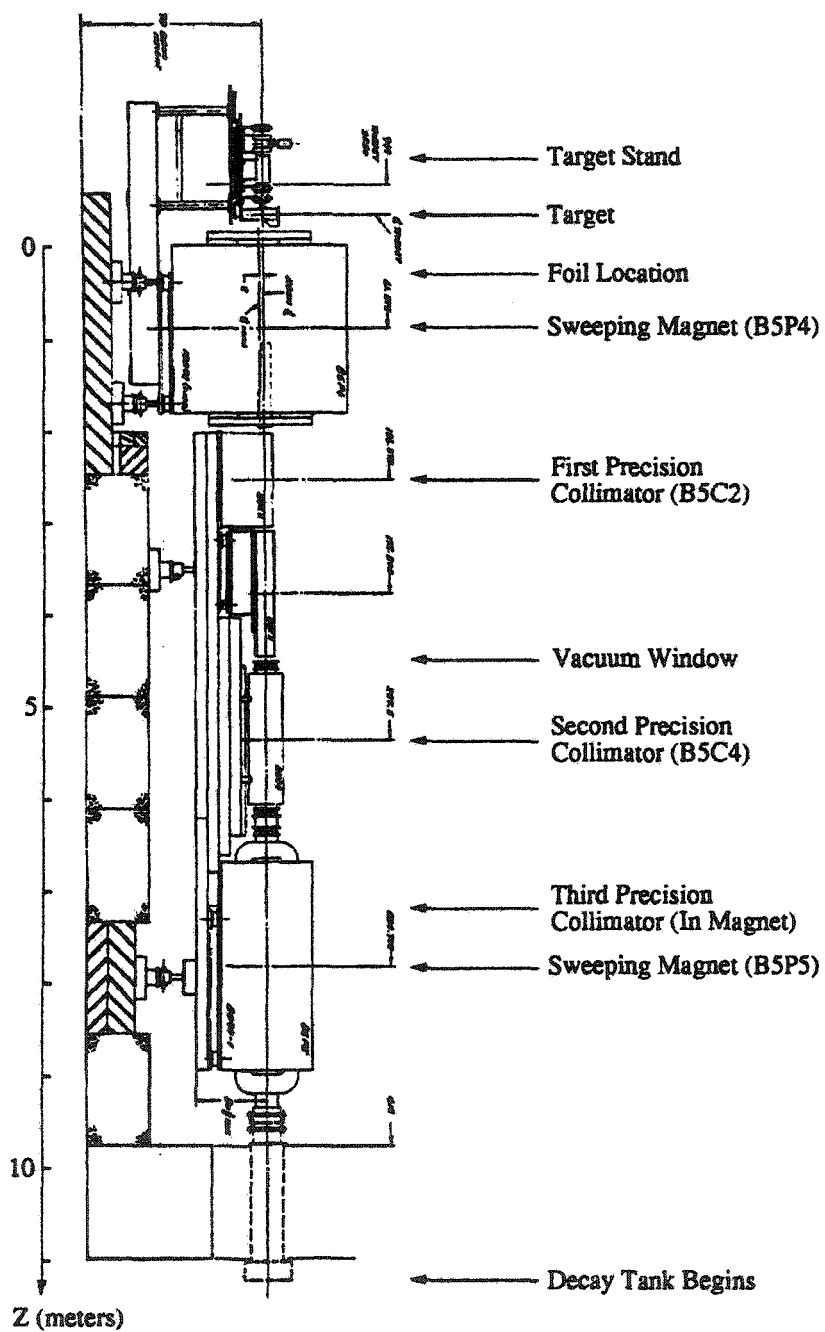


FIG. 5.5: AGS B5 neutral beamline for experiment E871

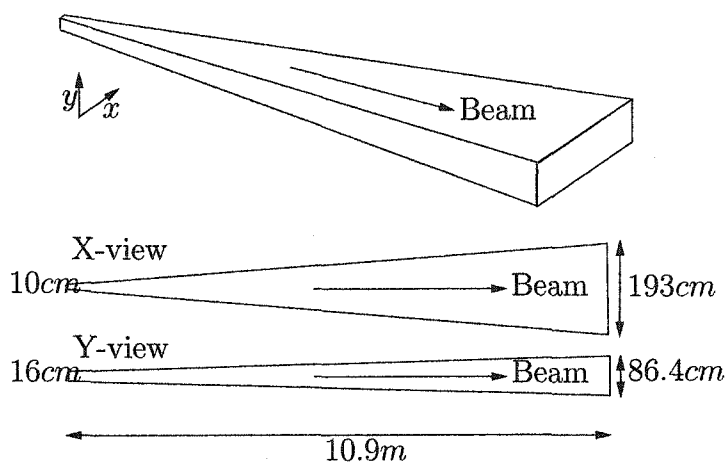


FIG. 5.6: E871 primary decay region geometry

the target area which were moderated to thermal energies by the concrete shielding. The large downstream opening of the tank was sealed by a 0.127mm thick Mylar window. The Mylar window alone was not structurally strong enough to maintain an operating pressure differential between the evacuated tank and atmosphere. At the target operating vacuum level of  $2 \times 10^{-4}$  torr the pressure exerted on the front window was approximately  $15 \text{ lbs/in}^2$  resulting in over 20tons of force on the front aperture. To provide structural support a secondary vacuum window of 0.381mm (15mil) thick Kevlar was used. During the final week of the 1995 run period the outer Kevlar window failed resulting in implosion of the  $640 \text{ ft}^3$  decay region. The vacuum region was reconstructed using a thicker 0.4318mm (17mil) ballistic grade Kevlar windows to prevent catastrophic failure of the region.

The interior region was evacuated to pressure of  $2 \times 10^{-5}$  torr and maintained at that level by a mechanical turbo pump. Residual gas species present in the decay volume were not measured during the initial experimental runs. During the testing of the E935 upgrade a residual gas analyzer was installed on the vacuum system to monitor both pressure and gas species. From these spectra as shown in Fig. 5.7 it was possible to determine that water vapor from the out-gassing of



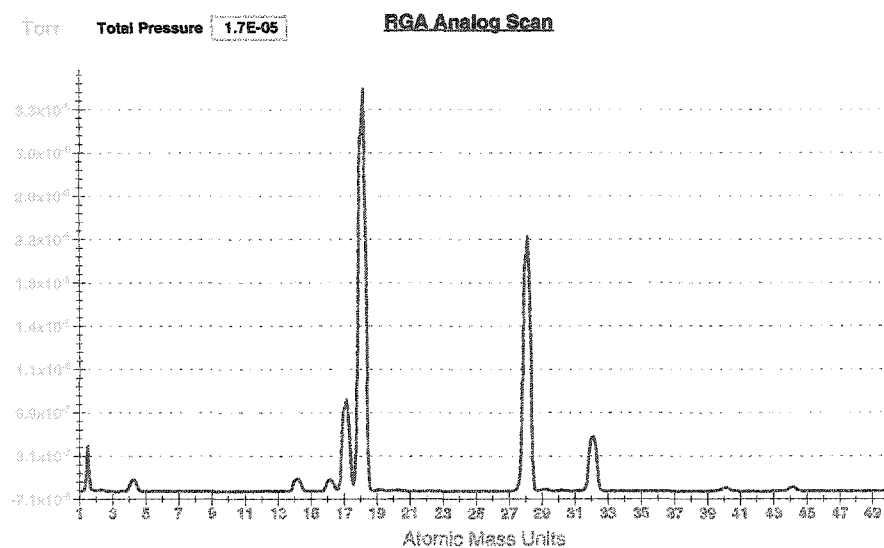


FIG. 5.7: Sample spectrum of residual gas present in the primary decay tank under evacuation via mechanical turbo pump at  $1.7 \times 10^{-5}$  torr

the steel, nitrogen from the surrounding environment and helium diffusing from the downstream helium bags were responsible for the primary species of residual gas in the region.

## 5.5 Spectrometer

Reconstruction of a valid kaon decay required precision tracking and accurate momentum measurements of the charged particles. The upstream half of the E871 experimental apparatus consisted of a spectrometer to provide track identification and to perform two independent momentum measurements of each candidate track. An overview of the forward spectrometer is shown in Fig. 5.9 and Fig. 5.8

The spectrometer consisted of 22 planes of straw tube-based wire chambers

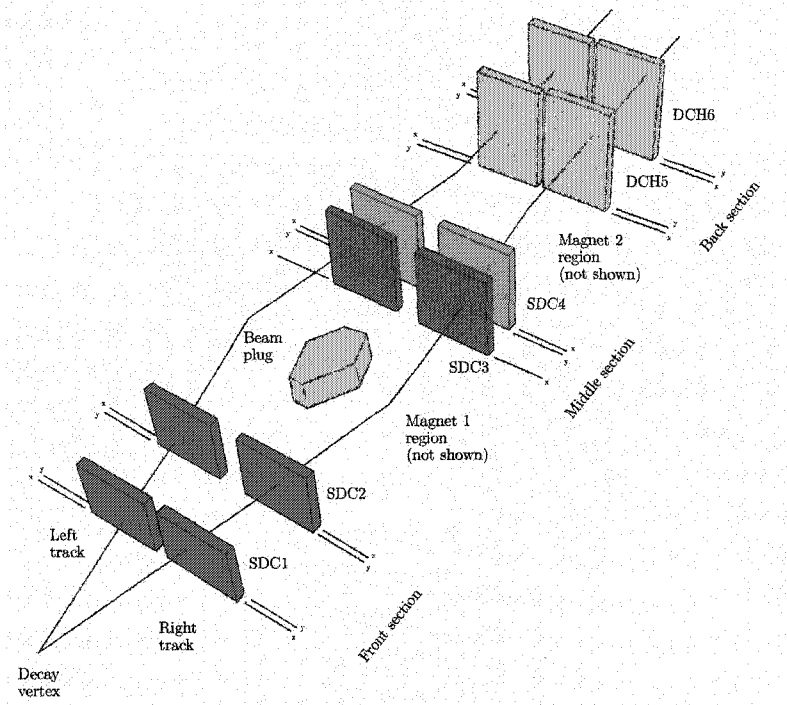


FIG. 5.8: E871 spectrometer overview

arrayed in x coordinate measuring and y coordinate measuring views followed by 8 planes of hexagonal cell wire drift chambers. Each detector plane was segmented to provide independent beam left and beam right elements. Two high field dipole magnets were situated between detector planes to provide momentum measurements transverse to the beam axis in the x-direction.

The spectrometer was required to be highly segmented to provide low single channel occupancy, even in the high rate forward chambers. A low material cross section design was employed to prevent particle interactions and scatter which could distort vertex reconstruction or momentum resolution.

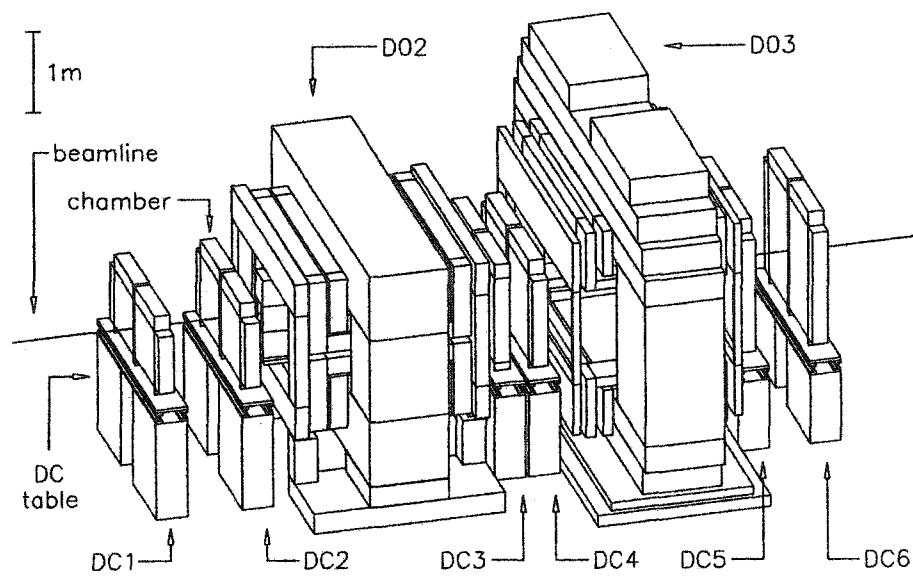


FIG. 5.9: E871 forward spectrometer detailed schematic

## 5.6 Straw Drift Chambers

The high intensity of the neutral beam results in extremely high rates of charged particles in the forward region of the spectrometer resulting from interactions in the decay region and with the beam plug material. The rate is high enough that standard wire proportional counters cannot be used for tracking in these regions. Both the channel occupancy and the recycle times would not be sufficient to accurately measure the environment present. Straw drift chambers using an exotic fast gas mixture and a dense channel geometry were used to provide both the refresh time and single channel luminosities which were required.

Straw drift chambers (SDCs) operate on the same principles as most proportional wire counters. When a charged particle traverses a medium the energy that it deposits can lead to ionization of the material. If the resulting free ions are placed in a strong electric potential then they will accelerate and cause secondary ionization as they pass through more material. The resulting avalanche of ions can then be

registered. In the case of the straw drift chambers, a small cylindrical tube is placed at a ground potential and filled with an easily ionized gas. A wire is positioned under tension along the central axis of the tube and held at a positive high voltage, creating a potential difference between the outer wall of the cell and the sense wire. When a charged particle traverses the cell it ionizes the gas, resulting in an secondary ionization avalanche that drifts under the influence of the radial potential towards the central axis where the ions are registered as current on the sense wire. The resulting current is amplified and read out as a signal pulse.

The straw drift chambers used in E871 were constructed from 5mm diameter cylindrical straws made of  $25\mu\text{m}$  copper-coated Mylar. The straw tube cathodes were constructed with lengths of 80cm for the upstream chambers and 120cm for the downstream chambers. The sense wires for each straw consisted of a  $20\mu\text{m}$  diameter gold-plated tungsten wire which extended down the length of each tube. The choice of copper-oxide as the straw coating was made to shield cathode field emissions and absorb soft photons owing to the high work function for the material.

To provide a fast ionization environment, each tube was filled with a mixture of carbontetrafluoride ( $CF_4$ ) and ethane ( $C_2H_6$ ) in a 50/50 mixture. The inert  $CF_4$  has a low threshold for ionization and is quenched by the presence of the ethane which readily absorbs the de-excitation photons emitted when the molecule returns to the ground state. As a result, the  $CF_4/C_2H_6$  mixture used exhibited a  $100\mu\text{m}/\text{ns}$  drift time at an operating potential of 1950V. Single channel rates of approximately 300kHz per straw in the upstream chambers were manageable with this drift time.

Straw tubes were packed into x-measuring and y-measuring layers using a standard cylindrical packing geometry as shown in Fig. 5.10. Straw chambers SDC1, SDC2 and SDC4 contained both x and y measuring plans while SDC3 consisted of only x measuring straws. Straw planes were arranged as shown in Fig. 5.11 for SDC1 L/R while for chambers SDC2 and SDC4 the y measuring planes were placed

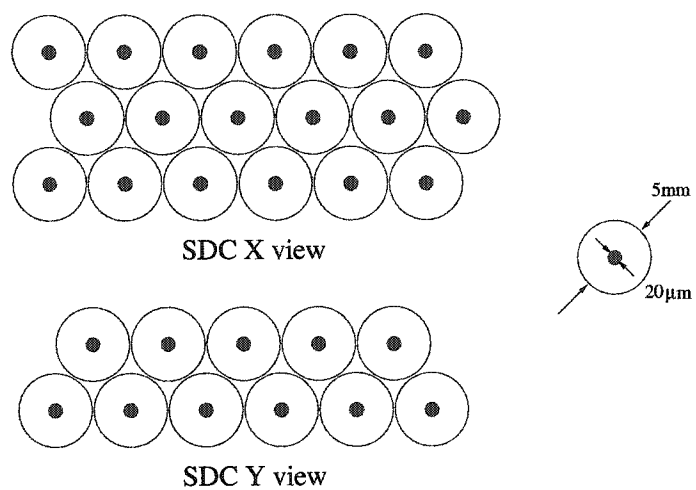


FIG. 5.10: Straw drift chamber layer geometry

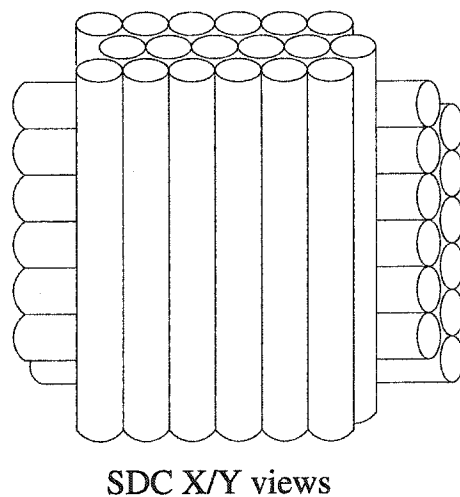


FIG. 5.11: Straw drift chamber X/Y layer arrangement

upstream of the x planes. The overall ordering of measuring planes was SDC1(XY), SDC2(YX), SDC3(X), SDC4(YX) providing seven measuring planes on both beam left and right. Each chamber contained 400 to 500 channels arranged in this manner for a total of over 6400 active straw tubes. Each straw tube channel was equipped with an amplifier card and the resulting signal was readout via a capacitive coupling which discriminated the signal at a  $1.5\mu\text{A}$  threshold. A 30ns wide digital signal was generated by the electronics and sent via 32channel Ansley cabling to a fast TDC for signal processing. High voltage to the chambers was provided by a CAEN SY127 power supply. The voltage was varied on the beam gate between 1850V and 1950V corresponding to out of spill and in spill conditions. The resulting voltage change prevents charge accumulation on the wires out of spill and reduces overall current load on the system.

## 5.7 Spectrometer Magnets

Two large aperture electromagnetic dipole magnets were used to facilitate the momentum measurement of tracks in the forward spectrometer. Each magnet consisted of a conventional iron yoke and two concentric water cooled wire coils. The coils were oriented parallel to each other to produce a uniform magnetic field in the vertical direction. The magnets were situated on concrete pedestals so that the central axis of the magnets and the beam line axis coincided. To prevent excessive fringe fields, mirror plates were installed on the upstream and downstream ends of the yokes. These plates consisted of iron blocks arranged to saturate the field emerging from the aperture. The layout of both magnets can be seen in Fig. 5.12 labeled as D02 and D03 corresponding to the upstream and downstream units.

The upstream magnet, D02, when energized with a nominal current of 3600A provided uniform field strength with magnetic flux per meter of  $1.4 T \cdot m$  which extended over its 96 inch wide (x) by 44 inch tall (y) aperture. The magnetic field orientation in D02 was such that negatively charged particles incident on beam left, and positively charged particles incident on beam right receive a momentum kick of 416MeV/c towards the beam line. Additionally the compact beam stop, as described in Section 5.8 was located within the 96D40 preventing the passage of neutral beam beyond the first magnet aperture.

The downstream magnet, D03 operated at a nominal current of 1900A and provided a dipole field with magnetic flux per meter of  $0.7T \cdot m$  in the orientation opposite that of D02. The magnet aperture spanned 100 inches in the x direction and 58 inches vertically. Positively charged particles incident on beam right and negatively charged particles on beam left consequentially received a momentum kick of 216MeV/c in a horizontal direction away from the beam line.

The net momentum kick imparted to charged particles properly entering the

spectrometer on beam left (negatively charged) or beam right (positively charged) was 200MeV/c towards the beam axis. This inbend was chosen to effectively cancel the net transfer momentum available to the decay streams of interest and thus to render such tracks parallel as they emerge from D03.

Contamination to the primary decay branches of interest in E871 stemmed from background induced by the semi-leptonic  $K_{e3}$  and  $K_{\mu3}$  decays. Each of these three-body decays exhibits a maximum transverse momentum as shown in Table 5.1 corresponding to the endpoint decay where the neutrino is at rest in the center of mass frame. Similarly the two-body decays of interest exhibit net  $p_T$  peaks between 206-249MeV/c creating a signal overlap between the three-body decay endpoint and the two-body phase space. The four-body decay  $K_L^0 \rightarrow \mu^+ \mu^- e^+ e^-$  is unique in that the form factor for the decay enhances the high momentum region of the decay spectrum favoring those events where the electron Dalitz pair emerge soft. This high momentum enhancement leads the muon tracks from the decay to retain a transverse momentum similar to that of the  $K_L^0 \rightarrow \mu^+ \mu^-$  channel. Due to this similarity in muon momentum spectra the spectrometer settings that favor the dilepton decay channels that E871 was designed to measure are also favorable to the measurement of  $K_L^0 \rightarrow \mu^+ \mu^- e^+ e^-$ .

The overall choice of  $p_T$  kick was chosen to provide decays of interest with a slight outbend profile in the trigger scintillation counters, and to maximize acceptance to the  $K_L^0 \rightarrow \pi^+ \pi^-$  decay mode used for overall normalization of experimental data.

## 5.8 Neutral Beam Stop

In the predecessor to this experiment, E791 [35] an optimal beam intensity of  $5.5 \times 10^{12}$  protons per spill was achieved using a two armed spectrometer with wide



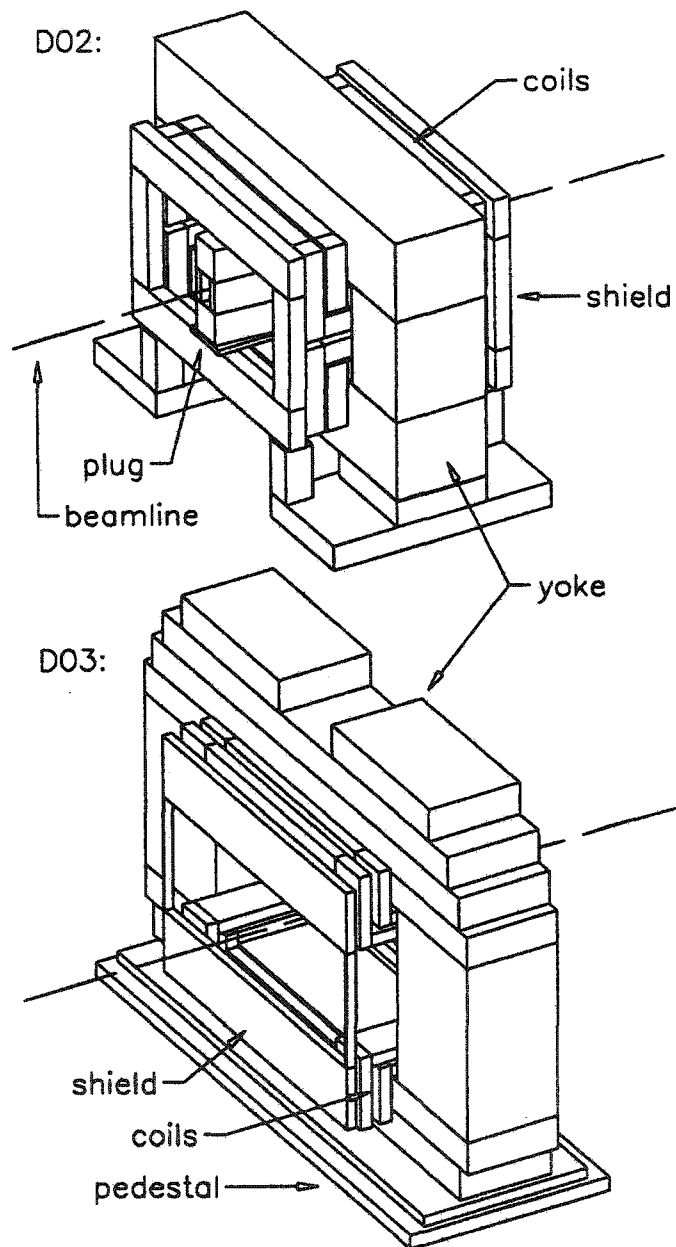


FIG. 5.12: B5 Beamline line analyzing magnets 96D40/D02 (upstream) and 100D40/D03 (downstream)

Decay Branch	Fraction	Decay $p_t$ (MeV/c)
$K_L^0 \rightarrow \pi^\pm e^\mp \nu_e$	$(38.78 \pm 0.27)\%$	229
$K_L^0 \rightarrow \pi^\pm \mu^\mp \nu_\mu$	$(27.17 \pm 0.25)\%$	216
$K_L^0 \rightarrow \pi^+ \pi^-$	$(2.067 \pm 0.035) \times 10^{-3}$	206
$K_L^0 \rightarrow e^+ e^-$	$(9.4_{-4.6}^{+5.9}) \times 10^{-12}$	249
$K_L^0 \rightarrow \mu^+ \mu^-$	$(7.2 \pm 0.5) \times 10^{-9}$	225
$K_L^0 \rightarrow \mu^\pm e^\mp$	$< 4.7 \times 10^{-12}$	238
$K_L^0 \rightarrow \mu^+ \mu^- e^+ e^-$	$\approx 2.9 \times 10^{-9}$	225

TABLE 5.1: Transverse momentum for  $K_L$  decay modes [12]

separation between the detector branches. This allowed passage of neutral beam through the non-active region of the experimental setup without adversely affecting rates in the spectrometer and detector systems. To achieve a targeted running intensity four times that of the prior experiment, and with increased geometric acceptance for the decay streams of interest, the E871 detector was designed with minimal separation between the left and right branches of the apparatus. This design required the use of a stopping mechanism downstream of the primary decay tank which would mitigate the effects of a high rate neutral beam with a momentum distribution peaked close to 9 GeV [36].

To achieve the targeted run intensity of  $20 \times 10^{12}$  protons per spill with a factor of 20 improvement in sensitivity, the decision was made to place a highly efficient neutron absorber inside of the first analyzing magnet. The beam stop would subtend a minimal solid angle for the purposes of geometric acceptance of two-body events, and remain physically compact in relation to the scale of the remaining detectors. A tungsten-nickel alloy (Heavimet) 112cm long with a total mass of 5000 kg was used as the central core of the beam stop. At a material concentration of 97%, the tungsten provided 12 hadronic absorption lengths. To augment this core at a reduced cost, 1880kg of additional copper were inserted after the tungsten blocks. The core geometry used is shown in cross section in Fig. 5.13. The entrance tunnel to the

core material is designed to absorb secondary emissions and to prevent backscattered neutrals from re-entering the upstream elements of the spectrometer. The entrance tunnel is continued vertically 107cm in such a manner that it spans almost entirely the central aperture of the 96D40 analyzing magnet.

To moderate the high neutron flux emerging from the central plug, the core material was surrounded by a layer of borated polyethylene. The hydrogen-rich material served to slow the incident neutrons through elastic collisional processes whereby the light hydrogen nucleus carries off a significant portion of recoil energy. The polyethylene was doped with boron, or borated zirconium hydride powder was used to then further facilitate fast neutron capture. Each polyethylene block was wrapped in a borated silicone sheeting to further mitigate the neutron flux, and any resulting gaps on the plug geometry were filled using silicone. The final layer of the beam stop was composed of a series of 1 inch thick lead sheets. The lead was designed to absorb all the gamma radiation produced in the back regions of the device from the process of neutron capture on boron. In the upstream portion of the beam stop where secondary emissions into the upstream geometry had to be highly suppressed, similar polyethylene blocks were used, but were doped with lithium as the capture material. This choice of dopant was chosen to eliminate the gamma ray spectrum which results from neutron capture on boron, as in the later stages of the plug. The extreme effectiveness of the beam plug can be seen most noticeably in the reduction of signal rates between the straw drift chambers immediately upstream and downstream of the beam stop. Fig. 5.14 shows a comparison of the rates in SDC2L and SDC3L. At small  $x$  there is a noticeable increase in the chamber illuminations prior to the beam plug owing to the halo of the neutral beam. In the same region downstream of the compact beam stop, the sharp spike in interior chamber illuminations is reduced to a level consistent with the more uniform distribution which is predicted from events originating in the primary decay tank.

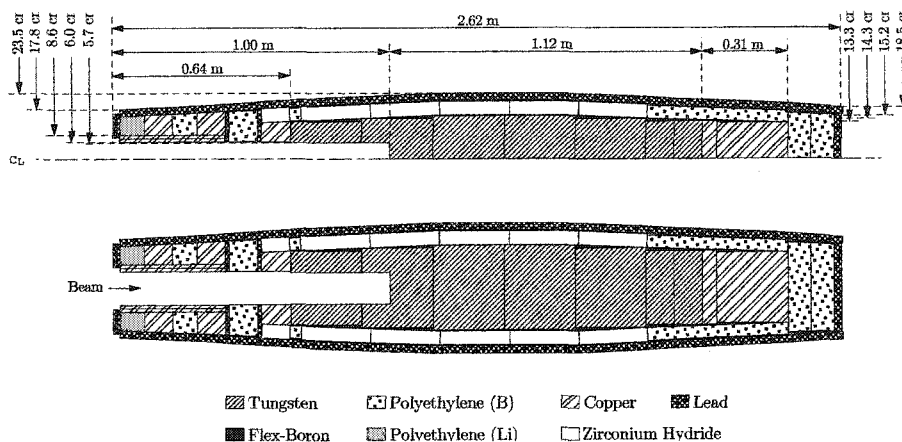


FIG. 5.13: Cross sectional view of E871 compact beam stop

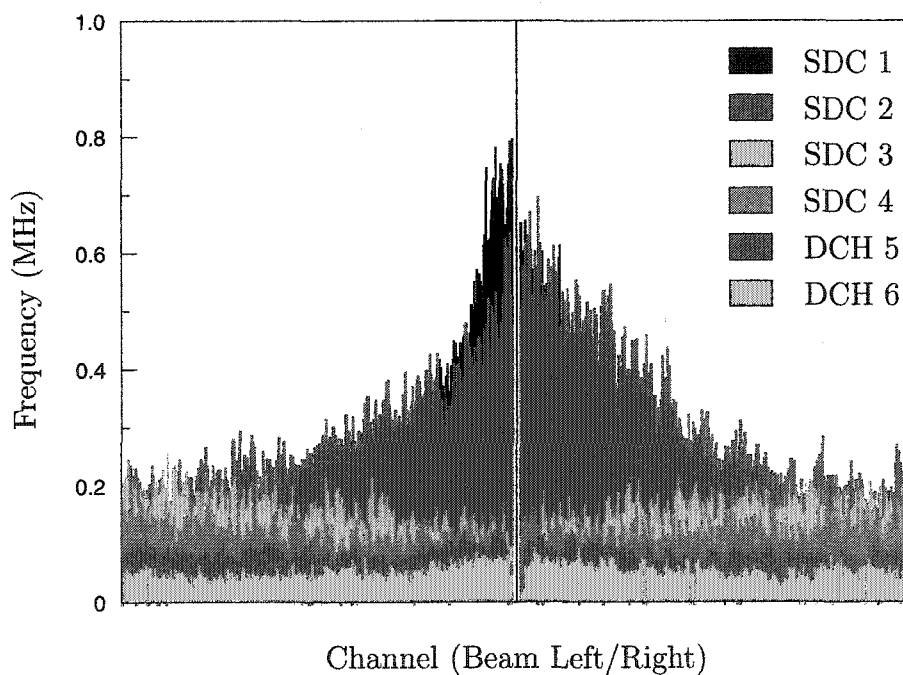


FIG. 5.14: Signal rate comparison between straw drift chambers and hexagonal drift chambers before and after the neutral beam stop

The resulting elimination of the neutral beam within the first analyzing magnet allowed for the subsequent placement of particle triggering and identification detector systems along the  $x=0$  origin of the experiment. By spanning the zero point with active detector elements, the geometric acceptance for the decays in question were maximized without adverse trigger rates along the small  $x$  coordinate. The overall sensitivity of the E871 system was enhanced over the previous two-armed design of E791 even at beam intensities exceeding  $20 \times 10^{12}$  protons per spill owing to the unique design of the compact beam stop.

A more detailed treatment of the Monte Carlo calculations and design specifications, as well as testing procedures and rate calculations are given in [36].

## 5.9 Helium Balloons

Spacing between active spectrometer elements was not evacuated, presenting an incident particle trajectory with regions of possible interaction. To reduce the interaction cross sections for multiple scattering and electromagnetic pair-production in these regions, the air was displaced with helium gas at a slight over-pressure to atmosphere.

The helium gas was contained in thin wall Mylar bags. Each bag contributed an addition 0.00635cm of material per membrane in the beam line. This additional material was taken into consideration in the calculations for multiple scatter and pair production. The Mylar bags were inserted between the detector regions and spectrometer magnets and then inflated via a centralized gas distribution system. Additionally a single Mylar wall was attached to the front face of the primary decay volume and inflated to fill the 10cm gap between the Kevlar window and front face of the first set of straw drift chambers. This configuration is shown in Fig. 5.15

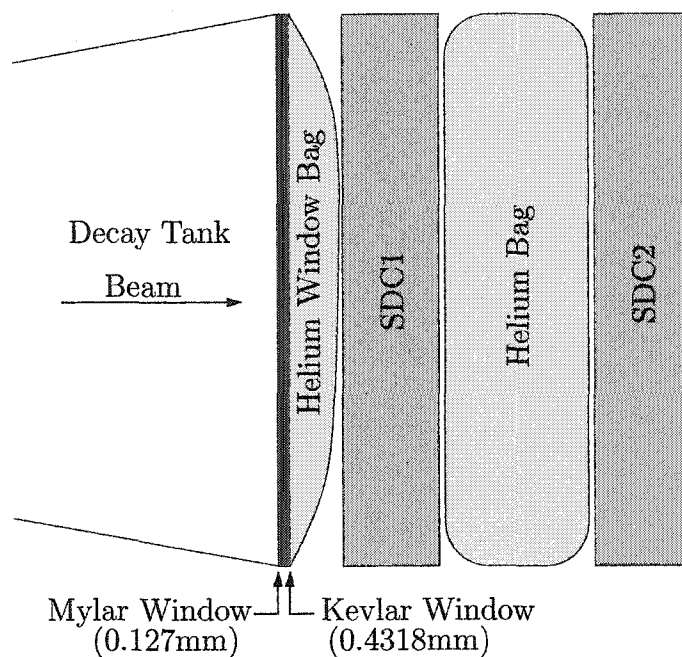


FIG. 5.15: E871 primary decay tank window including He filled Mylar bag

## 5.10 Drift Chambers

The presence of the compact beam stop in the first analyzing magnet reduced the observed particle rates to a level where large cell drift chambers could be utilized downstream of the 100D40 analyzing magnet. Two sets of drift chambers, DC5 and DC6 were used each consisting of over 600, 1cm diameter drift cells. The x-measuring cells extended 152cm in length with similar y-measuring cells 92cm long. Single channel occupancy of the cells approached 100kHz.

Unlike the straw chamber cells based on a cylindrical straw tube cathode, the drift cells utilized a hexagonal field geometry provided by a series of field wires with a single sense wire at the center of each cell. The sense wires were  $20\mu\text{m}$  gold plated tungsten, similar to the straw chambers, and held at ground potential. Each sense wire was surrounded by six gold-plated  $109\mu\text{m}$  aluminum alloy wires held at a nominal negative high voltage of 2300V. The electrostatic field was further shaped

by  $109\mu\text{m}$  gold-plated aluminum guard wires placed on the periphery of the cells and held at ground potential. Analogous to the straw chambers each drift chamber contained three planes of staggered x-measuring cells followed by two planes of y-measuring cells. Field and guard wires were shared between adjacent planes creating an extremely low mass cross section to incident particles. This configuration is shown in Fig. 5.16.

The chambers were filled with a 49%/49% argon-ethane gas mixture to provide an appropriate low ionization threshold medium. To prevent polymerization of the gas mixture building up on the wires, ethanol vapor was added at a level of 2% to quench the process. The resulting environment exhibited a drift time of  $50\mu\text{m}/\text{ns}$  at the nominal field gradient, corresponding to a position resolution of  $150\mu\text{m}$ .

Drift chamber output was first routed to pre-amplifier boards located on the ends of the chambers which provided a signal gain of 20. The resulting signal was then sent to additional amplifier, discriminator and mean timer (ADM) boards where the signals were digitized. Output from the ADM boards was passed to the counting house via 500 ns of Ansley delay cable before being input to custom built time-to-digital converters (TDCs) gated by the level 1 trigger signal. The TDCs provided a 160 ns dynamic range with least count resolution of 2.5 ns and rms error of 0.8 ns.

## 5.11 Trigger Scintillation Counters

Due to the high rate of decay events passing through the experimental apparatus during each beam gate a detector system was required to provide a fast trigger indicator as to the base event quality for data module readouts and event acquisition. The trigger scintillation counter (TSC) provides the first of the hardware trigger systems by providing fast charged particle tracking and determination of

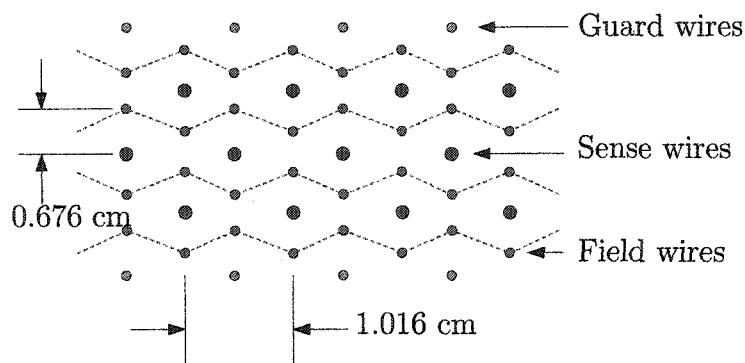


FIG. 5.16: X-measuring hexagonal drift cells cross section

event quality based on track parallelism.

Organic based scintillation detectors such as the type used in E871 operate on the basis of converting energy loss in matter to visible light emissions. When a charged particle traverses a medium there are predictable interactions and energy loss that occur due to ionization events. The mean energy loss due to a charged particle traversing a medium can be expressed by the Bethe-Bloch formula:

$$\frac{dE}{dx} = \frac{4\pi N_a z^2 \alpha^2 Z}{mv^2 A} \left\{ \ln \left[ \frac{2mv^2}{I(1-\beta^2)} \right] - \beta^2 \right\}, \quad (5.1)$$

where  $N_a$  is Avogadro's number,  $m$  is the electron mass,  $z$  the charge of the particle,  $v$  and  $\beta$  are the velocity parameters, and  $Z$  and  $A$  are the atomic and mass numbers of the medium. The quantity  $I$  is taken to be the effective ionization potential averaged over the material. The energy loss  $dE/dx$  is thus independent of the mass  $M$  of the incident particle and varies logarithmically with the velocity parameter for relativistic particles.

In the case of a plastic scintillating material, the energy loss experienced by the incident particle is imparted to the hydrocarbon dopant which experiences ionization and then a series of atomic de-excitations. The transitions primarily occur in the vibrational band of the ground state and result in a series of radiative emissions on



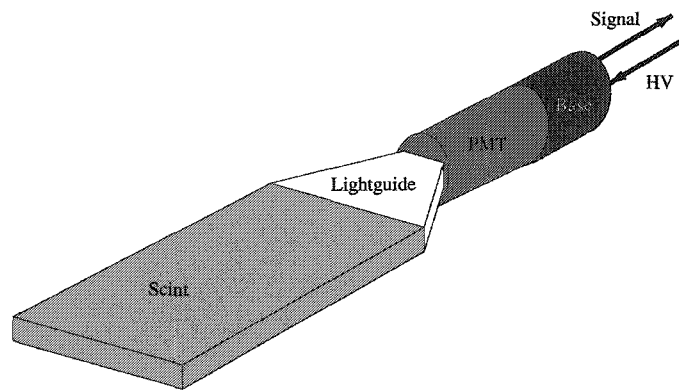


FIG. 5.17: Simple single edge readout scintillator and phototube readout system

the order of a few nanoseconds after the initial ionization as the system decays. By careful choice of the chemical dopant, the efficiency with which the ionization energy as expressed in Eq. (5.1) is converted to radiative emissions can be tuned to match the region to which the base plastic of the scintillator is optically transparent. In general this conversion efficiency is on the order of 1% of the total ionization energy lost by the incident particle.

The resulting light emission then propagate through the length of the scintillator at the local speed of light. The resulting light pulse can then be collected and amplified in a multi stage photomultiplier tube and the resulting current read out and recorded. Due to the fast nature of the atomic excitations, propagation of light in the transparent medium, and photoelectron cascade in a phototube, these types of detectors have the ability to handle high signal rates as seen in E871. Two types of plastic scintillation counters were utilized in creating the fast level 1 trigger system.

The first trigger scintillation system consisted of two planar arrays of thin detector units divided into four x-measuring modules and two y-measuring modules. The first planes (T1L/T1R) of x-measuring modules were located at z-position 29.94m immediately after the last set of proportional wire drift chambers and immediately

preceding the front aperture of the hydrogen Čerenkov counter. The second set of x-measuring planes (T2L/T2R) immediately followed the rear surface of the Čerenkov counter at  $z=32.85\text{m}$  and were arranged in a mesh configuration on both beam left and right with an associated y-measuring module (TYL/TYR).

Each forward x-measuring detector module consisted of 32 5mm-thick scintillator slats measuring 32mm in width by 1.653 m in total length. Each scintillator bar was enclosed first in an aluminized reflective foil to facilitate maximum internal light collection, and then encased in a black wrap to ensure channel isolation and prevent outside light contamination. A small Hamamatsu R1398 photomultiplier tube was connected to each end of these scintillator slats and brought in optical contact with the readout surface via a pressure lock system and optical interface cookie [37]. The units were then aligned vertically in two subplanes with low mass intra-unit *Rohacell* spacers to provide unit to unit ridge support. These two vertical sub planes were mounted flush to a series of carbon steel tubes welded into a “C” configuration, and staggered by an offset of 1.905 cm to provide a unit-to-unit overlap of 3 mm. As a result of the overlapping slats the center to center distance between two adjacent channels was 27.5 mm. The overlap in adjacent bars eliminated any insensitive regions near the edges of physical paddle boundaries which would have been present if the bars had been mounted edge to edge. This design produced then a single module measuring 1.65m vertical by 1.01m in the horizontal coordinate with full active coverage of the region.

The downstream x-measuring modules T2L/T2R were constructed and aligned in the manner identical to the modules T1L/T1R. These modules did however differ from their counterparts in the vertical dimensions of their scintillator bars. To provide full coverage for the active area the length of the scintillator bars was increased to 1.897 cm producing a sensitive x-position measuring plane 1.90 m vertical by 1.01 m wide. To complement the x-measuring module, a set of two y-measuring

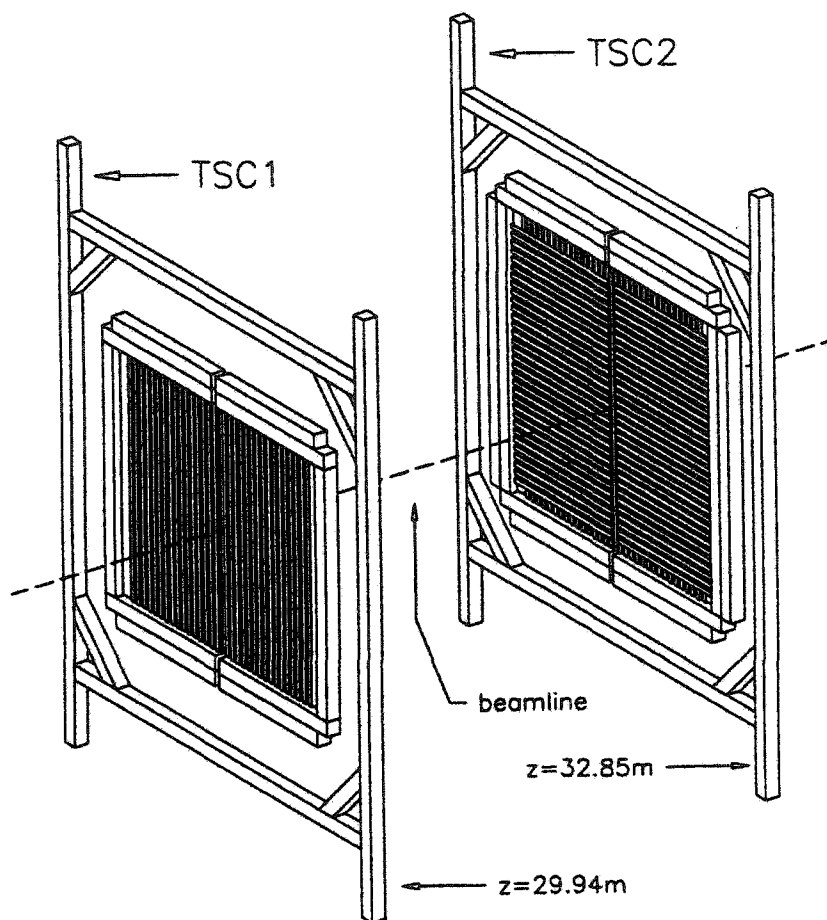


FIG. 5.18: Trigger Scintillation Counters in modules TSC1 and TSC2

TSC planes were placed immediately behind T2L/T2R to form a meshed grid as shown in Fig. 5.18. The y-measuring modules consisted of 64 thinner scintillator slates measuring 3.0 cm wide by 100.9cm long with a phototube readout only on the outside edge of the module. These bars were mounted in the same staggered manner as their x-measuring counterparts but with an overlap coverage of only 2.8mm between adjacent slats. The resulting module was attached to the same “C” support structure as T2L and T2R.

To maintain fast response and recovery, polyvinyltoluene-based Bicron BC-408 scintillator was used. This material exhibits a decay time of 2ns and a maximum

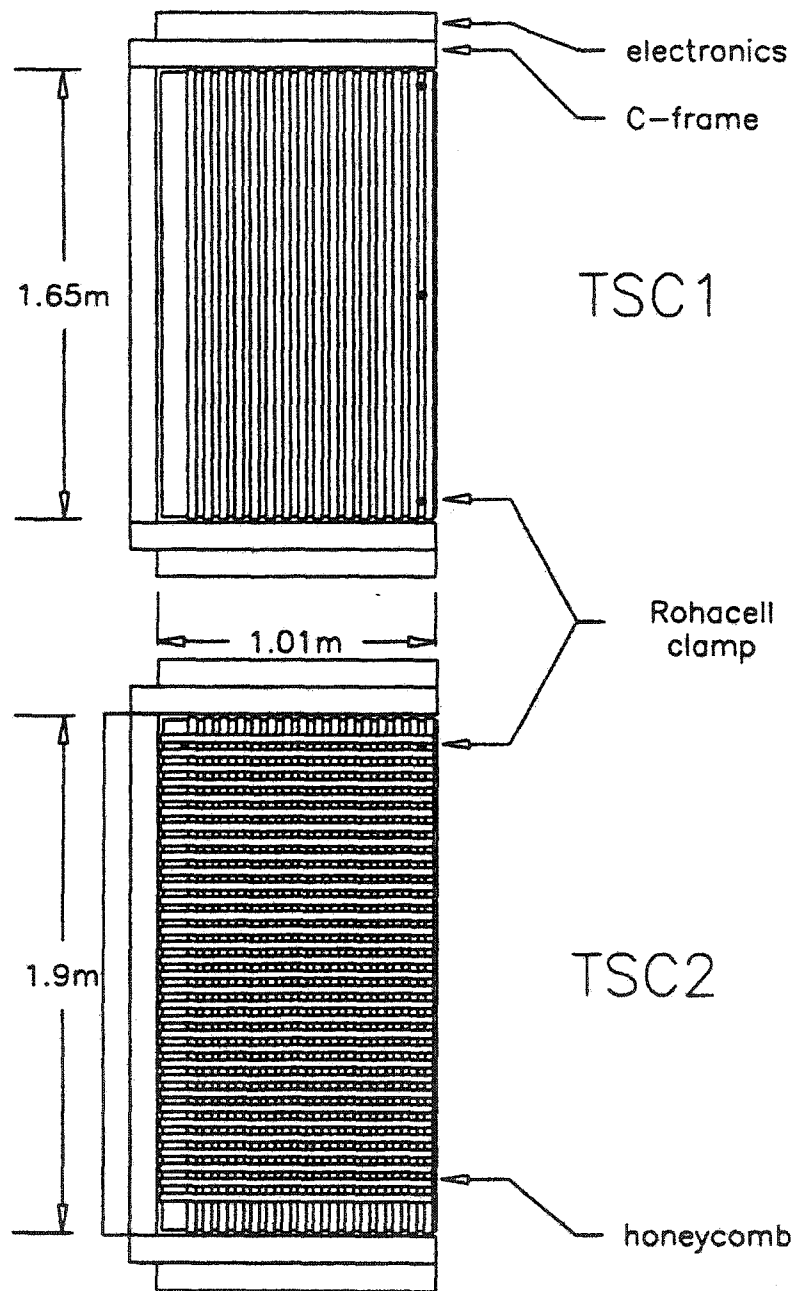


FIG. 5.19: Trigger Scintillation Counter slat plane designs for TSC1 and TSC2

blue light emission peak at 430nm. The Hamamatsu R1398 phototubes used to perform the readout on the scintillator had a 1.9cm diameter photocathode with peak sensitivity at 420nm. The rise time of these ten stage tubes was 1.8ns with a transit time of 19ns. The phototubes were negatively biased to a nominal operating voltage of 1500V. The tubes received power through standard SHV cabling connected to a LeCroy 1440 Mainframe high voltage supply. Channels were tuned individually and maintained via the online monitoring system. Readout for all the units was achieved through a standard low-loss 135ns RG-8 signal cable and were transported to the main counting house where the signals were coupled to Lemo signal cables and fed into 16 channel LeCroy 4413 dual output discriminators. Each discriminator channel produces two standard ECL logic signals. The first signal was routed to the Level 1 electronics to form the base event trigger, while the second signal passed through a 100ns delay line to form the stop pulse for the time-to-digital converters (TDC) which measure the timing of the scintillator signals.

With an upstream to downstream module separation of 2.91m, the vertical counters were able to determine track parallelism to a resolution of 0.54 degrees prior to offline analysis. This information was used in turn as the basis of the Level 1 trigger system to limit event readout to those event classes that exhibited a high degree of parallelism consistent with the decay streams of interest.

## 5.12 Threshold Čerenkov Counter

Positioned at  $z=30.49\text{m}$ , immediately behind the first trigger scintillation counter bank, was the first of two electron identification detectors. The E871 threshold Čerenkov counter consisted of a 2.5 meter deep aluminum enclosure encompassing  $18\text{m}^3$  of hydrogen gas. The active volume was divided into 32 readout cells by banks of 2.9 m radius of curvature spherical mirrors with associated 5inch phototube as-

semblies. These readout channels were incorporated both in the trigger system and read out, and recorded for further analysis in the production data stream.

The threshold Čerenkov counter was designed to distinguish electrons from low momentum pions and muons traversing the volume. The counter relies on the detection of the coherent light cone that is generated whenever a charged particle travels through a dielectric medium with a velocity that exceeds the local speed of light in the medium. This condition can be expressed as  $\beta > 1/n$  where  $n$  is taken to be index of refraction of the material and  $\beta$  is the standard relativistic velocity parameter:

$$\beta = \frac{v}{c} = \frac{p}{\sqrt{p^2 + m^2c^2}} \quad (5.2)$$

From this expression we see it is clear that low mass particles will have correspondingly higher  $\beta$  than heavier ones at similar momenta, and hence will begin the process of producing Čerenkov radiation at a low threshold momentum. From this observation we can then calculate the number of radiated photons in the interval  $dE = h d\nu$  by a particle of charge  $z$  over a path length  $dx$  as:

$$\frac{d^2 N_\gamma}{dx dE} = \frac{\alpha z^2}{\hbar c} \left( 1 - \frac{1}{\beta^2 n^2} \right) \quad (5.3)$$

We now turn to the Huygen's construct of Fig. 5.20. From this diagram we can determine the opening angle of the light cone created by a charged particle as it traverses the medium.

$$\cos \theta_c = \frac{ct/n}{\beta ct} = \frac{1}{\beta n} \quad \text{if } \beta > \frac{1}{n} \quad (5.4)$$

Using this expression we can now rewrite Eq. (5.3) in a more compact form showing

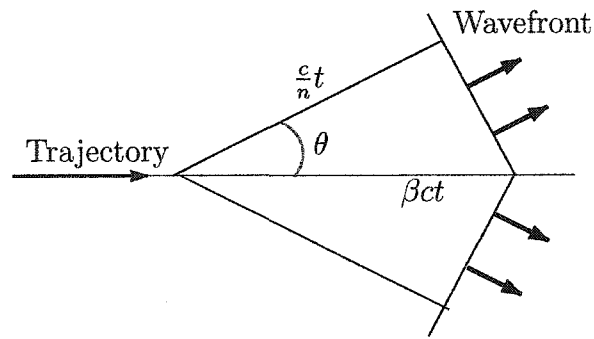


FIG. 5.20: Construction of the conical Čerenkov light cone arising from a charged particle moving through a dielectric medium

the explicit dependence of the light output on the wavelength:

$$\frac{d^2 N_\gamma}{d\lambda dx} = 2\pi\alpha \frac{\sin^2 \theta_c}{\lambda^2} \quad (5.5)$$

From this we can see that the number of photons of a given frequency is proportional to  $d\nu$  or alternatively  $d\lambda/\lambda^2$ . Hence the blue region of the spectrum dominates the Čerenkov effect. For this reason both the mirror and phototubes must be specifically tuned to maximize efficiency in this region.

For this detector the dielectric medium chosen was hydrogen gas at 7.6cm  $H_2O$  of overpressure to atmosphere. For diatomic hydrogen at this pressure the index of refraction is taken as:

$$(n - 1) \times 10^6 = 139.2 \quad (5.6)$$

From this we can calculate the threshold momentum required for the particle species of interest to undergo the Čerenkov process:

$$P_{threshold} = \frac{mc}{\sqrt{n^2 - 1}} \quad (5.7)$$

Particle	Mass ( $MeV/c^2$ )	Threshold ( $GeV/c$ )
$e^\pm$	0.511	0.031
$\mu^\pm$	105.6	6.357
$\pi^\pm$	139.6	8.396
p	938.3	56.233

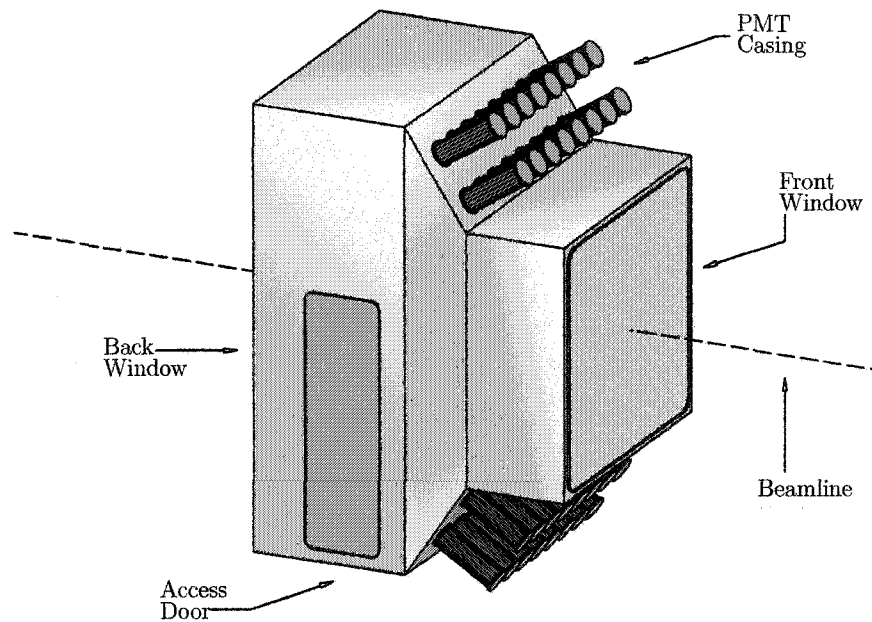
TABLE 5.2: Threshold momenta for Čerenkov radiation in Hydrogen ( $H_2$ )

FIG. 5.21: E871 Čerenkov counter exterior geometry

In the case of the particle species of interest we find that the large gap in Čerenkov threshold momenta between electrons and the heavier muons and pions as shown in Table 5.2, allows for high efficiency differentiation between low momentum electrons and all other charged particles of interest. In the momentum region bordering on and above 6GeV a secondary identification system in the form of an electromagnetic shower calorimeter is used as discussed in Section 5.13.

The exterior volume of the Čerenkov counter was constructed of 2.5cm thick aluminum plate welded to form the geometry shown in Fig. 5.21. To minimize the



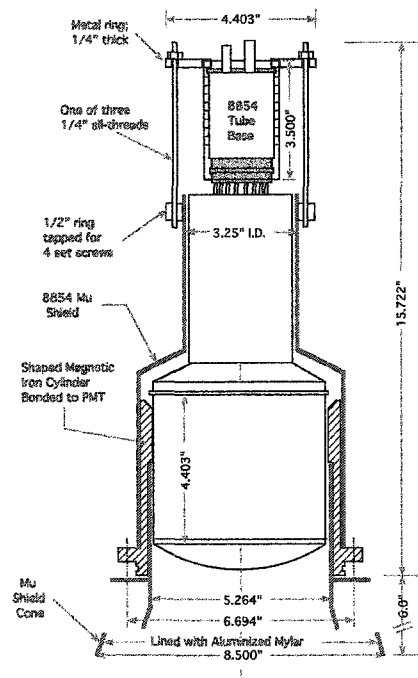


FIG. 5.22: Burle 8854 phototube with mu shielding and collar assembly as used on the E871 Čerenkov counter

amount of high Z material in the average particle trajectory, the upstream face of the detector was designed as a 0.125mm mylar window followed by a 0.0381mm black Tedlar covering to prevent ambient light leakage into the detector volume.

The interior of the volume was segmented along the beam axis to form the active regions of the detector. To prevent light leakage and signal contamination between the beam left and beam right sides of the detector, a black Tedlar curtain was positioned at  $x=0$  to serve as a light barrier and symmetry plane. This plane was further marked externally with survey points to allow for proper detector alignment. The  $x=0$  beam axis serves as a symmetry mirror plane with respect to further detector division. Each side of the detector was then divided into an array of 16 active detector cells consisting of 2.9 m radius of curvature spherical mirrors cut into rectangular mirror blanks. These mirrors were aligned along the x-axis coordinate to form the mirror columns. The physical width of the mirrors differer depending upon column placement. Mirror columns 1 and 4 (outermost and innermost) mirrors measured 0.258m in the x by 0.457m in y, while the inner columns 2 and 3 were narrower measuring 0.231m in x by 0.457m in y. This slight difference in horizontal width is necessary to provide overlap coverage of the vertical slats that compose TSC2-X. This overlap geometry is shown in Fig. 5.23. In this manner the active regions of the Čerenkov counter extend 3cm beyond the active region of the TSCs to accurately capture the light cone of edge triggered events. The interior arrangement of the Čerenkov counter is shown in Fig. 5.24.

Associated with each mirror cell is a single 12cm diameter phototube. Burle 8854 Quanticon photomultiplier tubes were chosen for their short wavelength sensitivity down to 220nm and their single photoelectron response of 22.5% at 385nm. From the geometry of the detector, the front faces of the photomultiplier tubes were in constant contact with the hydrogen gas environment of the Čerenkov detector. As a result of the atmospheric conditions the photocathodes of the tubes were placed

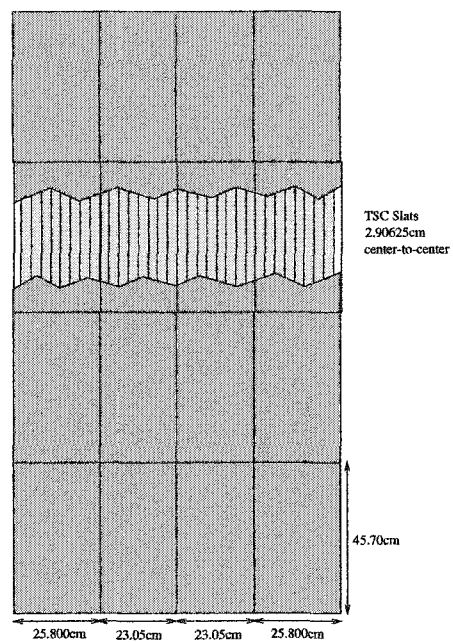


FIG. 5.23: Overlap of Čerenkov mirrors with X measuring TSC slats

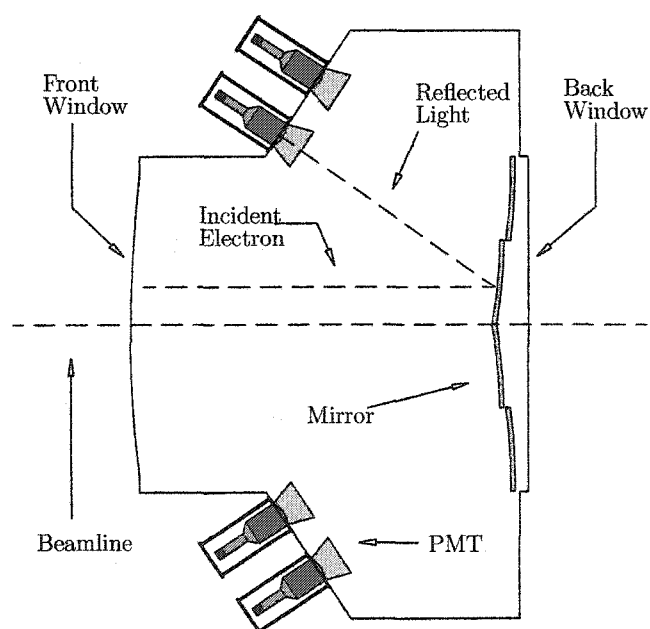


FIG. 5.24: E871 Čerenkov counter interior geometry

at a ground potential and the dynode stages biased with positive high voltage. This presents the obvious problem of possible baseline shifts at high signal rate as well as voltage sagging in the later dynode stages. To combat these two effects custom high voltage bases were designed and built with high voltage Zener diodes to prevent base current effects.

Due to the proximity of the phototube/base assemblies to the second analyzing magnet, a 17 Gauss magnetic fringe field was present at the phototube positions. For the 8854 phototubes to operate correctly, the magnetic field in the assembly region was required not to exceed 0.5 Gauss in either a transverse or an axial orientation. In order to dampen the magnetic field, the 8854 phototubes were first placed inside an iron collar as shown in Fig. 5.22 and cemented into the adapter using a low vapor pressure black silicone base epoxy. The Sylgard 170 epoxy served to structurally secure the phototube and form a gas seal between the tube and collar. The collared phototube assembly was then mounted to the detector inside of an additional iron housing with standard O-rings serving to gas seal the assembly. In the space between the outer housing and the assembly an additional high mu metal<sup>3</sup> layer of shielding was fitted around the PMT adapter. On the interior of the detector the front faces of the phototubes were also fitted with CoNetic shielding in a conical geometry to reduce the local field. The interior surface of the conical shield was then lined with aluminized Mylar to enhance the acceptance of photons from the events.

### 5.13 Lead Glass Array (PBG)

Situated immediately downstream of the second plane of trigger scintillation counters at survey positions 33.2m and 33.4m was the lead glass array (PBG). The

---

<sup>3</sup>CoNetic alloy was used for its ability to readily absorb the magnetic field

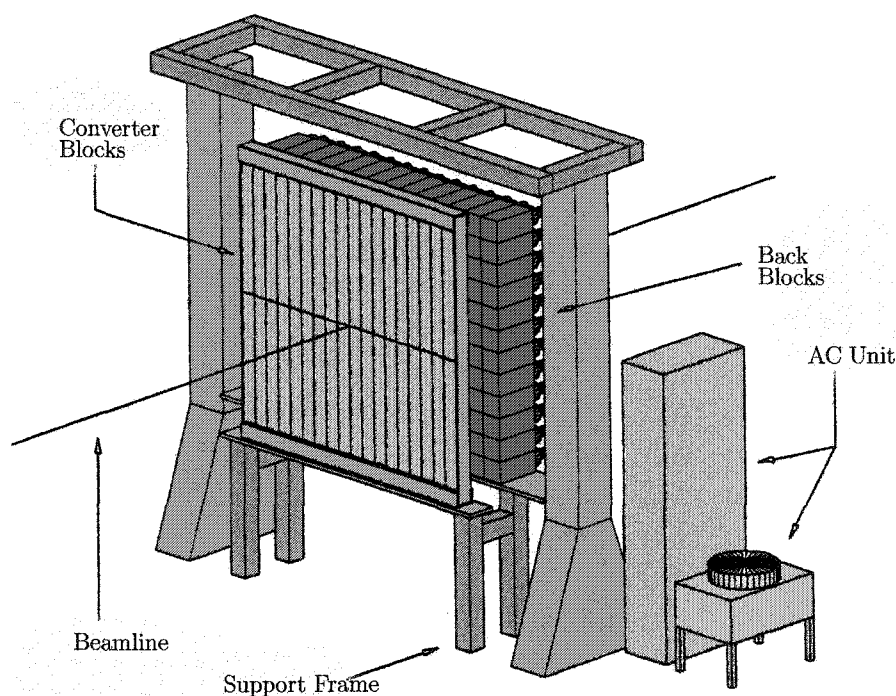


FIG. 5.25: E871 lead glass array with external cooling system

full array consists of two planes of lead glass crystals<sup>4</sup> weighing 6.4 tons. The crystals along with their support structure were contained within a light tight, temperature controlled enclosure<sup>5</sup> constructed from Unistrut and heavy plastic sheeting. This design is shown in Fig. 5.25.

The first or “converter” plane was segmented into two rows of 18 blocks, each measuring  $10.9 \times 90 \times 10\text{cm}$  in the x, y, and z directions, respectively. This depth provided 3.5 radiation lengths of material along the beam direction. Each block was affixed with a 3 inch diameter phototube<sup>6</sup> and base providing both an unamplified signal and a secondary 40 gain amplified copy of the signal. The tubes were mounted vertically to the forward block, aligned along either the positive or negative y-

<sup>4</sup>Schott F2 lead.  $46\%SiO_2, 45\%PbO, 5\%Na_2O, 4\%K_2O$ . Material density  $3.6\text{g/cm}^3$

<sup>5</sup>Enclosure temperature maintained at  $72^\circ F$

<sup>6</sup>Amperex 3462

axis. The second plane of crystals, denoted as the absorber region, consisted of 164 active<sup>7</sup> blocks aligned in 12 rows of 14 crystals. Each crystal had a square front face measuring 15.3cm on a side. The depth of the crystals along the beam axis is 32.2cm corresponding to 10.5 radiation lengths. A single 5 inch diameter phototube<sup>8</sup> was affixed to the downstream end of each of the blocks in a horizontal orientation. As with the converter readouts, photomultipliers provided both raw and amplified signals.

The index of refraction of the glass was 1.62 and had a hadronic interaction length of 35.0cm. This yields a minimum of 1.2 hadronic interaction lengths that a valid<sup>9</sup> particle track must pass through before exiting the downstream face of the detector, in comparison to the total electromagnetic interaction path for the same track of 13.8 radiation lengths. As a result of this difference and the segmentation of the array, electromagnetic showers are initiated in the forward converter block and fully developed and absorbed in the secondary blocks. For electron and positron initiated electromagnetic showers, the total energy deposited in the array should reflect the measured momentum of the charged tracks. Photon initiated showers are identical in their shower nature but are distinguished through the absence of charged particle tracking information correlated to the hit cluster.

Hadronic showers initiated primarily by charged pions develop slower in the beam axis direction resulting in a converter to back block energy energy deposition substantially lower than a corresponding electromagnetic shower. Full absorption of the hadronic shower does not occur within active region of the lead glass array resulting additionally in a total energy deposition to track momentum ratio much

---

<sup>7</sup>Four blocks in the array were considered inactive regions during the experimental run owing to insufficient signal response

<sup>8</sup>EMI 9618R

<sup>9</sup>Tracks or showers prematurely exiting the active region of the array along the x or y planes are not considered in the analysis

less than 1. Pion initiated hadronic showers exiting the lead glass array in this manner are largely absorbed by a 12 inch iron block situated downstream of the PBG array and prior to the first active planes of the muon range finder and muon hodoscope.

## 5.14 The Muon Hodoscope

The base Level 1 trigger requirements for E871 included the ability to identify event candidates which included two parallel muon tracks both for the dilepton decay  $K_L^0 \rightarrow \mu^+ \mu^-$  and for the four lepton decay  $K_L^0 \rightarrow \mu^+ \mu^- e^+ e^-$ . Due to the high beam rates present in the E871 experiment, a system similar in nature to the fast trigger scintillation counters was employed. The muon hodoscope (MHO) consisted of 3 x-measuring and 3 y-measuring plastic slat based scintillator planes situated at z positions in an energy loss range stack consisting of slabs of iron and marble as described in Section 5.15. Table 5.3 lists the lab Z-position of each counter plane along with its corresponding momentum gap placement in the stack. This ordered positioning is shown in Fig. 5.26. Of particular note is that the plane designated X1 is indeed situated upstream of the initial X0/Y0 primary trigger planes. This placement reflects the importance of the 1.0GeV threshold that was imposed on the experiment to prevent contamination of the muon data set by pions creating hadronic shower punch through in the forward region of the range stack.

Each MHO detector plane consisted of a series of long organic scintillator slats fitted with clear acrylic lightguides. For the E871 experimental run the trigger planes MX0/MY0 were custom built to satisfy the requirements of the higher rate trigger. The remaining four detector planes were recycled from the prior E791 experimental run. As a result minor differences existed in both their designs and operating efficiencies. Optical interface between the lightguides and photomultiplier tube

Muon Hodoscope Planes		
Plane	Z Position	Momentum Gap (GeV/c)
MX1	34.945	0.85
MX0	35.265	1.0
MY0	35.265	1.0
MY1	36.345	1.6
MX2	38.195	3.25
MY2	45.915	7.0

TABLE 5.3: Lab Placement and corresponding momentum gap of MHO elements

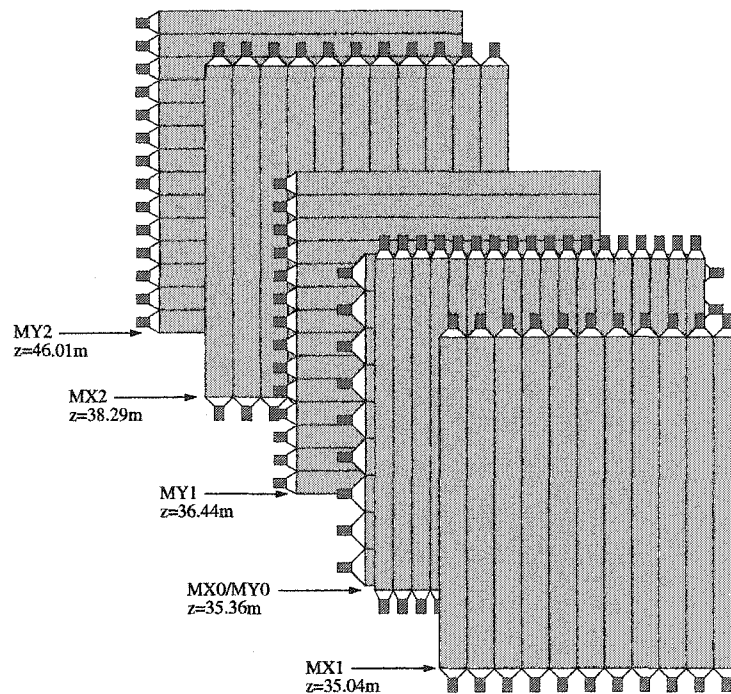


FIG. 5.26: Muon Hodoscope detector plane layout



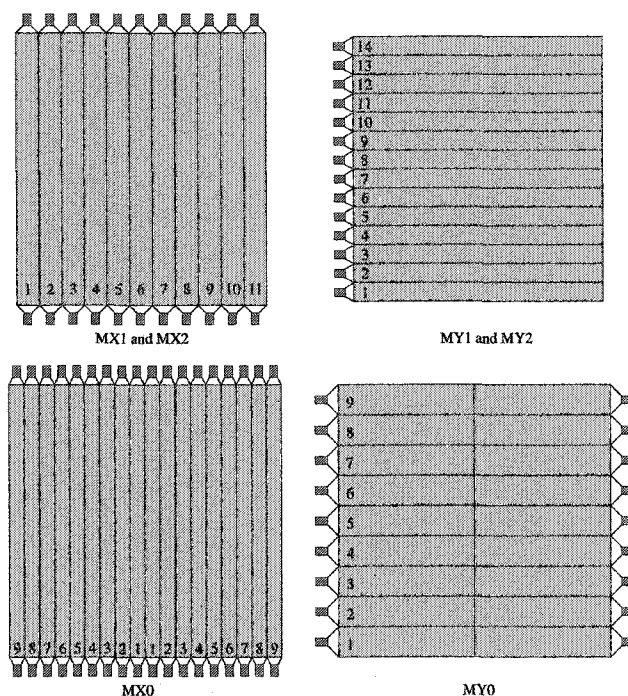


FIG. 5.27: Muon Hodoscope detector plane design

readouts for MX0/MY0 was maintained by an optical “cookie”<sup>10</sup> similar to those used in the TSC system. Contact was maintained by a pressure locked spring system again analogous to the method used for the trigger scintillator counts. Hodoscope counters MX1/MY1 and MX2/MY2 used optical epoxy to permanently affix the photomultiplier tube to the lightguide. The photomultiplier tubes used on counters MX0/MY0 were the 44mm diameter bialkline photocathode model XP2262 from Phillips. The tubes exhibited a peak sensitivity near 400nm and a transit time of 30ns. The Philips tubes were biased with nominal negative high voltage of 1850V as supplied by a LeCroy 1440 HV mainframe. The older modules used similar 44mm diameter 12 stage phototubes from Amperex. The Amperex model XP2230 phototubes also exhibited a peak sensitivity of 400nm but were required to be biased at higher nominal voltage of approximate 2300V. All x-measuring slats were fitted with

<sup>10</sup>Bircon BC-634 1/8in wafer bushing

Muon Hodoscope Scintillator Dimesions				
Plane	Slats	Length (cm)	Width (cm)	Thickness (cm)
MX1	11	267	18.8	2.54
MX2	11	267	18.8	2.54
MX0	18	229	12.7	1.27
MY0	18	104	25.4	1.27
MY1	14	229	18.8	2.54
MY2	14	229	18.8	2.54

TABLE 5.4: Dimensions of muon hodoscope scintillator slats

dual readout on both top and bottom edges of the scintillator while the y-measuring bars were equipped with phototube readouts only on the outer edge away from the beam line axis. Muon hodoscope planes MX0/MX1 were both constructed from a total of 18 scintillator slats each with dimensions as listed in Table 5.4. Each plane was subdivided into a beam left and right half consisting of 9 bars each in a mirror configuration along  $x=0$ . In a manner identical to the staggering of the TSC detector slats to provide edge region overlap, the MHO trigger plane scintillators were staggered to provide a  $1/8$ in overlap between neighboring channels. This overlap was performed in both the x and y measuring counters to ensure maximum sensitivity in the active region. Detector planes MX1/MX2 as shown in Fig. 5.27, both consisted of a total of 11 Polycast Corp PS-10 organic scintillator with a 3.9ns decay time and peak emission spectrum at 415nm [38]. The bars were arranged in a standard edge to edge configuration without division into beam left and beam right channels as shown in Fig. 5.27. Owing to the odd number of slats in the plane's design there is no edge boundary supported mirror symmetry along the  $x=0$  beam line, creating an ambiguity in the center channel designation for left/right tracking. The older y-measuring planes MY1 and MY2 both contain a total of 14 counter slats, 2.29meters in length which span the  $x=0$  beam line position, and are thus not segmented into a beam left/right designation. Owing to this configuration of the

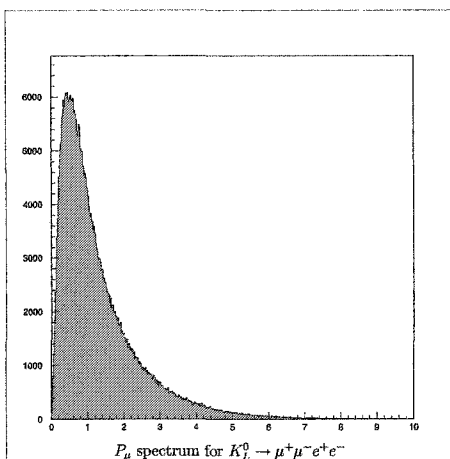


FIG. 5.28: Laboratory frame muon momenta for  $K_L^0 \rightarrow \mu^+ \mu^- e^+ e^-$

y-measuring planes as not associated with a beam axis side, channels are equipped with only a single readout each. The phototube equipped ends were situated on the beam left side of the experiment.

Each planar unit was internally mounted to  $1.25\text{cm} \times 7.62\text{cm}$  aluminum struts and housed in an aluminum box consisting of a 1/16in front and back protective skin and supported by 2 1/2in edge frame. This box ensured additional structural support for the units as well as a secondary light shield in addition to the protective wrappings of each channel.

Signal readout for the individual units was provided via standard RG-8 low loss signal cable and routed to the Level 1 trigger electronics. Channels were read to a threshold discriminator and combined with the TSC output to form the appropriate parallel trigger Level 1 muon trigger.

## 5.15 Muon Range Stack

Muons from the decay process  $K_L^0 \rightarrow \mu^+ \mu^- e^+ e^-$  at E871, exhibit a relativistic laboratory momentum spectrum as shown in Fig. 5.28. In this momentum regime the

muons interact with matter as minimum ionizing particles. The collisional processes that occur between the incident muon and the charge distribution of the material substance are well described by a series of elastic collisions of relativistic charged particles. The energy loss incurred through these interactions is dominated solely in this energy regime by ionization of the target material and as such is well described by the Bethe-Bloch formula for the fractional energy loss  $dE/dx$ [39].

$$\frac{dE}{dx} = \frac{4\pi N_a z^2 \alpha^2 Z}{mv^2} \frac{Z}{A} \left\{ \ln \left[ \frac{2mv^2}{I(1-\beta^2)} \right] - 2\beta^2 \right\} \quad (5.8)$$

This form can be modified to include both the density effect correction  $\delta$  and the shell correction  $C$  so the more appropriate form of the Bethe-Bloch formula used to compute energy loss in matter becomes:

$$\frac{dE}{dx} = \frac{4\pi N_a z^2 \alpha^2 Z}{mv^2} \frac{Z}{A} \left\{ \ln \left[ \frac{2mv^2 W_{max}}{I(1-\beta^2)} \right] - 2\beta^2 - \delta - 2\frac{C}{Z} \right\} \quad (5.9)$$

We take  $W_{max}$  to be the maximum energy transfer to an electron, allowed in a single collision by an incident particle of mass  $M$ :

$$W_{max} = \frac{2m_e c^2 \eta^2}{1 + 2s\sqrt{1 + \eta^2 + s^2}}, \quad (5.10)$$

where  $s = m_e/M$  and  $\eta = \beta\gamma$ . In the event that  $M \gg m_e$  then the limiting form of the maximum energy transfer becomes:

$$W_{max} \simeq 2m_e c^2 \eta^2 \quad (5.11)$$

Equation (5.11) proves to be a fair approximation for the case of muons in E871.

At incident energies below approximately 0.3GeV/c the  $1/\beta$  behavior of the Bethe-Bloch formula dominates the energy loss of the muons in iron. At 0.3GeV/c

a minimum is reached and the relativistic correction to the Bethe-Bloch equation leads to a logarithmic rise in the ionization loss. If the modified Bethe-Bloch as shown in Eq. (5.9) is used then the density correction term damps the rising logarithmic divergence leading to a flatter tail to the differential energy loss as a function of particle momentum. Particles exhibiting this relatively constant minimum rate of differential energy loss,  $dE/dx$ , over the appropriate momentum range can be termed “minimum ionizing”. As such the integrated energy loss over an effective range  $R$  can be calculated as a function of the incident momentum. Taking the process as a series of independent collisional events, we can show that the statistical variation in the expected distance that an incident particle will travel is a Gaussian distribution with fractional width given by [40].

$$\frac{\sigma_R}{R} = \frac{1}{2} \sqrt{\frac{m_e}{M}} \quad (5.12)$$

For muons the fractional variance is computed as:

$$\frac{\sigma_R}{R} = 0.035 \quad (5.13)$$

This 3.5% statistical variation in the particle range becomes the systematic limit on the design resolution of the detector system based upon the ionization energy loss measurement.

In contrast to the minimum ionizing nature of relativistic muons, the energy loss of charged pions in the accessible momentum regions are dominated by strong interactions rapidly producing hadronic showering in the path of the charged particle. The energy loss dynamic and shower characteristics are discussed in section 5.13. The characteristic range for a pion induced hadronic shower as compared to that of the minimum ionizing energy loss of a muon provides a method of accurate

particle differentiation. The muon range stack of E871 exploited this characteristic difference between muons and pions to eliminate background contamination from the  $K_L^0 \rightarrow \mu^+\mu^-$ ,  $K_L^0 \rightarrow \mu^\pm e^\mp$  and  $K_L^0 \rightarrow \mu^+\mu^-e^+e^-$  data stream arising from semileptonic decays of the form  $K_L^0 \rightarrow \pi^\pm \ell^\mp \nu$  with pion misidentification and invariant mass reconstruction in the primary signal region.

Pions were induced to undergo a hadronic shower by the placement of high material with high hadronic cross sections in the particle's path after it emerged from the lead glass calorimeter. The first hadronic filter plane consisted of a 30.5cm thick iron (Fe) slab. The material exhibited a nuclear interaction length  $\lambda_I = 16.76$  and provided a total of 1.82 interaction lengths for pions traversing the first medium. Subsequent iron, aluminum and marble filter planes were then interspersed with detector planes forming the muon hodoscope (MHO) and muon range finder (MRG) at 5% incremental momentum gaps. To reach the fourth detector plane, MX0, in this range stack the incident pion traversed over 4 interaction nuclear lengths of material. At this level 95% of the particles will have undergone the process of hadronic showering and have been absorbed by the filter material. In contrast the material prior to the fourth detector plane represents a momentum range value of only 1GeV/c for a minimum ionizing muon.

Table 5.5 displays the hadronic interaction lengths for the materials used in construction of the range stack along with the material densities used to compute the minimum ionizing energy loss for muons via the Bethe-Bloch prescription. Table 5.6 displays the ordering and positions of the elements included in the muon range stack.

The iron blocks used in the construction of the range finder measure  $88in \times 188in$  and were used in thicknesses of either  $2in$ ,  $3in$  or  $4in$ . Starting at momentum gap 24, marble and aluminum slabs are used in place of iron. The marble consists of  $3in \times 44in \times 59in$  pieces banded and glued together to form  $3in$  thick,  $88in$  wide,  $118in$  high slabs and grouped with  $1\frac{1}{2}in$  and  $\frac{7}{8}in$  aluminum plate to form

Material	$\rho(g/cm^3)$	$\lambda_I(cm)$
Lead Glass	3.60	35.0
Iron (Fe)	7.87	16.76
Aluminum	2.70	39.41
Carrera Marble	2.75	-

TABLE 5.5: Muon range finder material densities and hadronic interaction lengths

the successive 5% momentum gap intervals. Fig. 5.29(a) shows the arrangement of material blocks and Fig. 5.29(b) shows active detector elements which form the detector units. In total the weight of material used in the muon range stack exceeds 420tons and extends over 20 meters of the experimental floor.

## 5.16 Muon Range Finder

In addition to the muon hodoscope trigger planes, the range measurement of muon tracks was performed by 52 planes of proportional wire counters arrayed in x and y measuring planes and spaced sequentially at 5% momentum gaps extending out to a maximum momentum range of 10.258 GeV/c. The design of the range stack allowed for a comparison between the actual stopping point of the charged particle and that predicted based upon the momentum measurement in the forward spectrometer and the assumed particle identification.

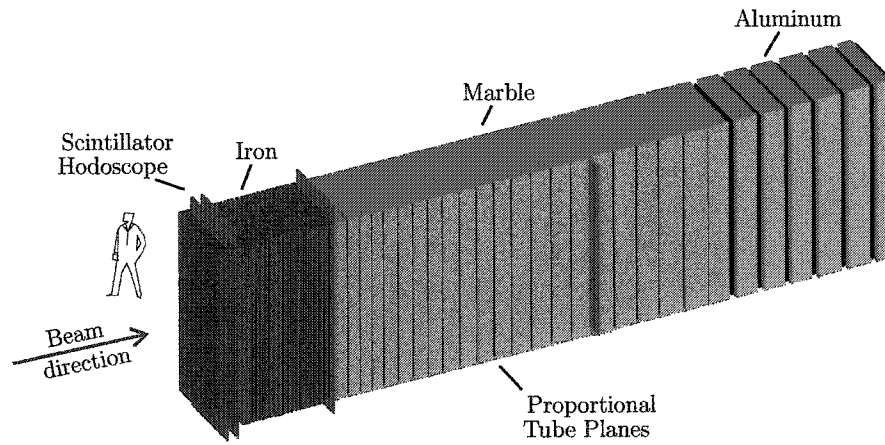
Calculations of the energy loss in matter of the charged muons as they passed through the iron, marble and aluminum of the range stack were computed to determine that stopping gap of each detector plane. Table 5.7 lists the values for the ranger finder in terms of the incident momentum of a muon-like, minimum ionizing particle.

Each plane of the Muon Range Finder (MRG) was constructed by bonding a series of extruded aluminum honeycombs together in an edge to edge configuration

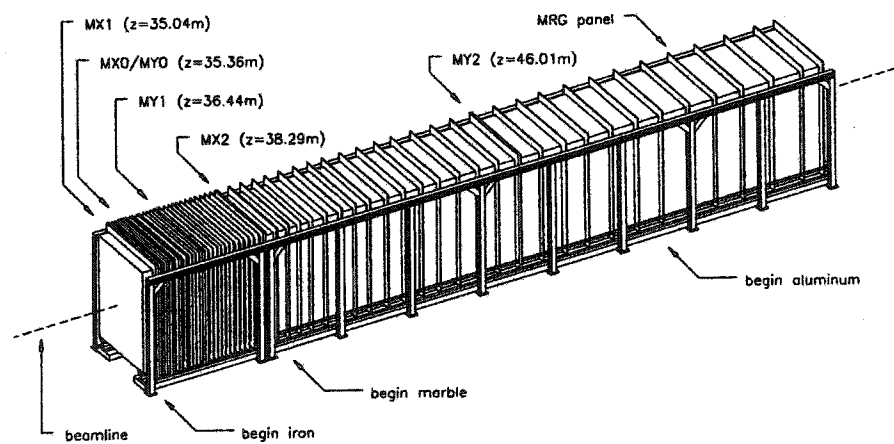
Z(cm)	Material	Gap	Z(cm)	Material	Gap	Z(cm)	Material	Gap
0	12" Fe	-	256	3" Fe	-	954	21" Marble	-
32	MX1	1	267	MRG 19 X	20	1010	MRG 39 X	40
41	2" Fe	-	270	4" Fe	-	1013	21" Marble	-
47	MRG 01 Y	2	282	MRG 20 Y	21	1069	MRG 40 Y	41
49	2" Fe	-	285	4" Fe	-	1072	21" Marble	-
55	MRG 02 X	3	297	MRG 21 X	22	1129	MY2	42
59	2" Fe	-	300	4" Fe	-	1138	24" Marble	-
64	MX0	4	312	MRG 22 Y	23	1201	MRG 41 X	43
73	MY0	4	315	4" Fe	-	1205	24" Marble	-
82	2" Fe	-	327	MRG 23 X	24	1271	MRG 42 Y	44
87	MRG 03 X	5	330	4" Fe	-	1274	24" Marble	-
90	MRG 04 Y	5	343	MRG 24 Y	25	1338	MRG 43 X	45
92	2" Fe	-	346	4" Fe	-	1341	27" Marble	-
100	MRG 05 Y	6	357	MX2	26	1413	MRG 44 Y	46
103	2" Fe	-	366	12" Marble	-	1417	27" Marble	-
108	MRG 06 X	7	398	MRG 25 X	27	1490	MRG 45 X	47
110	MRG 07 Y	7	401	MRG 26 Y	27	1493	27" Marble/Al	-
113	2" Fe	-	403	12" Marble	-	1565	MRG 46 Y	48
120	MRG 08 X	8	435	MRG 27 X	28	1569	30" Marble/Al	-
123	2" Fe	-	438	12" Marble	-	1647	MRG 47 X	49
129	MRG 09 Y	9	471	MRG 28 Y	29	1651	30" Marble/Al	-
134	2" Fe	-	474	12" Marble	-	1729	MRG 48 Y	50
141	MRG 10 X	10	507	MRG 29 X	30	1733	30" Marble/Al	-
144	2" Fe	-	510	15" Marble	-	1811	MRG 49 X	51
151	MRG 11 Y	11	551	MRG 30 Y	31	1815	33" Marble/Al	-
155	2" Fe	-	554	15" Marble	-	1902	MRG 50 Y	52
162	MRG 12 X	12	596	MRG 31 X	32	1906	33" Marble/Al	-
164	2" Fe	-	599	15" Marble	-	1992	MRG 51 X	53
172	MY1	13	639	MRG 32 Y	33	1995	21" Marble/Al	-
180	3" Fe	-	642	15" Marble	-	2052	MRG 52 Y	54
189	MRG 13 X	14	682	MRG 33 X	34	2055	3" Marble	-
194	3" Fe	-	686	18" Marble	-			
203	MRG 14 Y	15	735	MRG 34 Y	35			
206	3" Fe	-	738	18" Marble	-			
216	MRG 15 X	16	787	MRG 35 X	36			
219	3" Fe	-	791	18" Marble	-			
228	MRG 16 Y	17	840	MRG 36 Y	37			
231	3" Fe	-	843	18" Marble	-			
240	MRG 17 X	18	891	MRG 37 X	38			
244	3" Fe	-	895	21" Marble	-			
253	MRG 18 Y	19	950	MRG 38 Y	39			

TABLE 5.6: Muon range stack material placement





(a) Muon range stack material placement



(b) Muon ranger stack active detector placement

FIG. 5.29: E871 muon range stack

Detector Plane	Stopping Momentum (GeV/c)	Detector Plane	Stopping Momentum (GeV/c)
1	0.978	27	3.659
2	1.043	28	3.851
3	1.114	29	4.022
4	1.114	30	4.239
5	1.183	31	4.406
6	1.267	32	4.669
7	1.267	33	4.894
8	1.316	34	5.138
9	1.406	35	5.370
10	1.459	36	5.635
11	1.528	37	5.931
12	1.645	38	6.157
13	1.785	39	6.500
14	1.888	40	6.915
15	1.990	41	7.431
16	2.093	42	7.766
17	2.192	43	8.191
18	2.310	44	8.548
19	2.421	45	8.865
20	2.574	46	9.200
21	2.698	47	9.370
22	2.875	48	9.541
23	3.012	49	9.720
24	3.207	50	9.893
25	3.492	51	10.070
26	3.492	52	10.258

TABLE 5.7: Stopping momenta by detector plane for the muon range finder

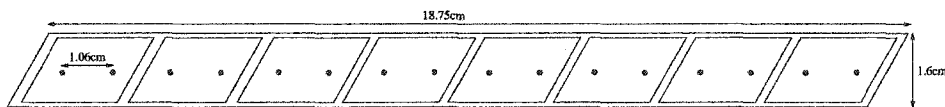


FIG. 5.30: Muon Range Finder extrusion panel

as shown in Fig. 5.30. X view planes consisted of 12 such extrusions each with a length of 301cm, while Y view planes were constructed with 16 extrusion, each 225cm long. The aluminum honeycombs were parallelogram-shaped with a base length of 18.75cm, height of 1.60cm, and a horizontal pitch of 60 degrees. Each unit was further divided into 8 subcells with outer walls measuring 2.0mm and partitioned by a 1.9mm aluminum barrier at the same 60 degree pitch angle as the outer edges. The detection cells each had a 2.1cm base dimension and 1.2cm height. Each cell contained two gold plated tungsten sense wires with a separation distance of 1.06cm. The cells were flushed with an argon and ethane gas mixture in equal parts to provide an environment for the charged particles to create an ionization avalanche between the sense wires and the gas environment. To prevent aging of the wire chambers caused by byproducts from electrical breakdowns building up on the sense wires, a low concentration of ethyl alcohol, on the order of 1.6%, was circulated through the system in addition to the argon/ethane mixture.

The high voltage for the sense wires were disbursed through a high voltage bus system mounted to each plane. The bus for each card was maintained at a nominal positive high voltage of 2600V by a CAEN SY127 high voltage mainframe. Additional low voltage amplifiers and discriminator cards were also mounted on each plane and powered from a series of 5V and 12V supplies located on the beam left of the range stack.

Each proportional counter was designed to detect the passage of charged particles through the interior cell via the ionization of the argon/ethane gas mixture.

When ionization occurred in the field of the sense wires, the negatively charged particles are accelerated towards the high voltage wires. The charge migration induces secondary ionization causing a cascading avalanche effect which deposits a net charge on the sense wire proportional to the initial ionization caused by the incident charged particle. The resulting signal was amplified and passed through a discriminator. The output of the discriminator signals from each cell in a single extrusion were logically ORed to form a single readout for each panel. The composite signals were converted to a differential ECL logic signal approximately 160-200ns in width. These signals were passed over low loss differential Ansley cable to the counting house. Readout was performed for each unit via a FASTBUS latch crate and were gated on the event trigger from the Level 1 electronics.

# CHAPTER 6

## Hardware Trigger and Data Acquisition

### 6.1 Overview

The E871 data acquisition (DAQ) and triggering system was designed to capture and process candidate events for the  $\mu\mu$ ,  $ee$  and  $\mu e$  data streams with normalization to the  $\pi\pi$  data sample. Due to the high rate environment present in the E871 spectrometer and particle identification system, the triggering and data acquisition subsystems were designed to handle an incident raw event rate in excess of  $10^6 Hz$  and filter the resulting data streams down to a level for which the event data could be written to tape at a rate of  $10^2 Hz$ . Due to the required level of online data reduction, the systems were specifically designed to efficiently accept two body  $K_L$  decays of interest while rejecting primary background arising from the semileptonic  $K_{\mu 3}$  and  $K_{e 3}$  decays in order to preserve a high signal to background event ratio in the initial data collection. In order to accomplish a factor of  $10^4$  reduction in the raw event rate, the triggering and DAQ systems were divided into a multi-stage

system with successive reduction at each level.

Events were broken into trigger level tiers denoted at Level 0 (L0), Level 1 (L1) and Level 3 (L3) before final event selection was processed to tape. The tiered event process worked in the following manner, for each event started with a valid single satisfying the L0 trigger. Level 0 events were then passed to the Level 1 systems for basic particle identification checking and tagging for event type. Valid Level 1 triggers notified the Readout Supervisor (RS) to begin processing of the event data. Crate scanners for each of the detector systems were notified by the RS to transfer the event data to the Dual Port Memory (DPM) units for further processing or to internally shift/clear the event from registers. The RS system then notified the L0/L1 trigger units that it was again ready for another event.

Upon filling the available memory of the DPM units, the crate scanners triggered the RS to assign the event block stored in the DPM units to one of eight available high speed processors arrayed in parallel for limited software event reconstruction. Events transferred to the processors were analyzed by the software reconstruction algorithms where tracking quality and invariant mass cuts were performed. Events passing the software reconstruction were denoted at L3 triggers. Events were then uploaded after L3 processing to the main acquisition computer and buffered into 200 megabyte data blocks for output to 4mm data tapes. A schematic overview of this process is shown in Fig. 6.1.

## 6.2 Level 0 Trigger

The Level 0 (L0) trigger forms the basic requirement upon which all events in the E871 data are based. The L0 trigger requires an in-time coincidence set of hits in TSC1L, TSC2L, TSCYL and in TSC1R, TSC2R, TSCYR. The six fold coincidence is interpreted as the basis for the passage of two charged particle trajectories that

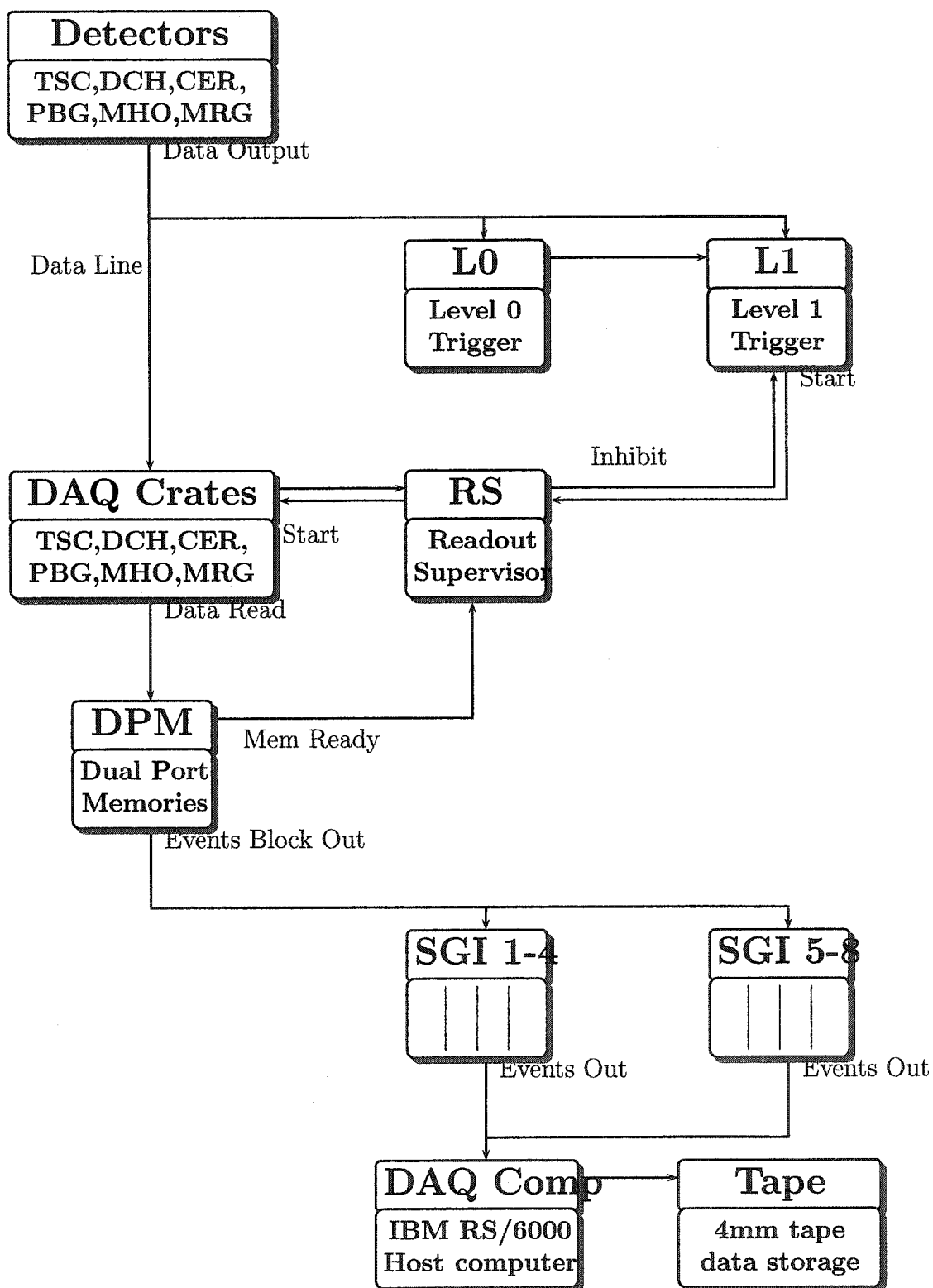


FIG. 6.1: E871 DAQ system overview

have traversed the forward spectrometer and entered into the particle identification elements.

Level 0 triggers are subdivided into two classifications based upon the hit positions of the signals in the x-measuring slats. Non-parallel L0 triggers place no requirement upon the position correlation of hits and TSC1L/TSC2L or TSC1R/TSC2R. This non-parallel trigger is used to determine raw filtering rates and other calibration data requiring an unbiased event trigger. At nominal running the trigger system experienced an average L0 event rate of  $10^6$  hz.

Parallel L0 triggers place an x-slat correlation requirement upon the hits in TSC1L/TSC2L and upon TSC1R/TSC2R. This correlation is set nominally at  $\pm 2$  slats equating to an angular deviation of  $\pm 31$  mrad. The parallelism can be varied to provide lesser or greater correlation, but at its nominal value it corresponds to the expected spread in trajectories of low  $p_t$  two body events passing through the inbend 96D40 and outbend 100D40 analyzing magnets. The coincidence is performed through an electronic AND of T1X with T2X on both left and right, using top and bottom photomultiplier tubes. The result is then put in coincidence with the signal from TY.

$$L0 = (T1X \bullet T2X) \bullet TY \quad (6.1)$$

In order to match the L0 trigger coincidences with additional particle identification detectors, the L0 trigger signals are grouped into a series of spatially correlated blocks. The 32 parallel XX coincidences formed from the initial TSC signals are logically OR'd into a set of 8 trigger "roads" corresponding to the upper and lower left, and upper and lower right quadrants of the detector modules. Similarly the 64 TSC Y measuring counters are divided into 16 signal blocks through a logical OR to produce the TY coincidence signal. The X and Y signal roads are brought into



coincidence forming a grids of 8 upper and 8 lower XY coincidence signal roads for the left and right sides of the detectors. These signals are passed to the subsequent stages of the trigger system. A non-parallel version of these trigger roads is also generated and passed to the subsequent Level 1 trigger systems for calibration.[41]

The parallelism requirement imposed through the XX and XY coincidences and road building results in a factor of four reduction in the base data rate lowering the L0 event rate to approximately 250 kHz at nominal running. This data rate remains too high for software analysis filtering and requires further reduction from the fast particle identification detectors.

### 6.3 Level 1 Trigger

To further reduce the event rate from the parallel L0 triggers, basic particle identification triggers were used to form the Level 1 (L1) trigger set. Five classes of L1 triggers were constructed from basic electron and muon identification information to form the  $\mu\mu$ ,  $ee$ ,  $\mu e$ ,  $e\mu$  and *minimum bias* triggers.

The muon trigger bits were created by requiring an in-time coincidence between the TSC trigger roads described in Section 6.2 and the trigger roads in the muon hodoscope. Since the MH0 x-measuring modules consisted of nine panels, counters 8 and 9 of the MX0 counters were electronically OR'd to produce a single outer road before coincidences were performed with the TSC trigger roads. In addition to the MHO X/Y coincidences  $\mu$  trigger bits required a coincidence with the wire drift chambers DC5 and DC6.

Electron trigger bits for the L1 triggers were created by requiring an in-time and spatially correlated coincidence between the L0 TSC trigger roads described in Section 6.2 and signals in the corresponding Čerenkov counter regions. A minimum signal threshold of 1 photoelectron was imposed upon the single channel Čerenkov

signals through a bank of discriminator boards in the L1 trigger. The output of a Čerenkov discriminator was passed to coincidence logic units for the  $\check{C}er$  signal. The Čerenkov counter regions were defined through a logical OR of the 16 beam left and 16 beam right phototube singles to form 8 upper and 8 lower roads spanning the detector and corresponding spatially to the roads in the TSCs and MHO. In addition to the Čerenkov coincidence, a valid L1 electron bit required corresponding hits in the wire drift chambers DC5 and DC6.

Minimum bias trigger bits were formed by requiring only a coincidence between the L0 TSC trigger roads and hits in the wire drift chambers DC5 and DC6. No additional requirements were imposed upon the event signal thereby allowing for normalization data and pion data to be collected in unison with the primary data paths. Additionally a pion trigger was provided by vetoing on both the Čerenkov and MHO signal in coincidence with the TSC L0 trigger and the drift chambers.

The L1 trigger bits can be summarized as:

$$MinBias(MB) = L0 \cdot DC \quad (6.2)$$

$$\mu = L0 \cdot DC \cdot MHO \quad (6.3)$$

$$e = L0 \cdot DC \cdot \check{C}er \quad (6.4)$$

$$\pi = L0 \cdot DC \cdot \overline{\check{C}er} \cdot \overline{MHO} \quad (6.5)$$

The muon and electron trigger requirements are shown schematically in Fig. 6.2.

The L1 trigger bits for the beam left and right sides of the detector were sent through a programmable coincidence module capable of generating up to eight possible triggers. The two body decay triggers of interest were assigned to these coincidences as shown in Table 6.1.

The L1 two body coincidence triggers are passed through a programmable

Trigger Bit	Type	Trigger Bit	Type
1	$e \cdot \mu$	5	$MB \cdot MB$
2	$\mu \cdot e$	6	
3	$e \cdot e$	7	
4	$\mu \cdot \mu$	8	$L0 \cdot L0$

TABLE 6.1: Level 1 (L1) two body event trigger bits

prescaling module which effects a divide by N prescaling of physics trigger in the range of 1 to  $2^{16} - 1$ . During nominal data collection prescales of 1 were used for the  $e\mu$ ,  $\mu e$ ,  $\mu\mu$  and  $ee$  streams. Minimum bias events were prescaled by a factor of 1000, and L0 triggers by  $10^4$ .

Additional channels of diagnostic and calibration triggers were included in the Level 1 output by means of a separate calibration trigger board providing 16 channels of external triggers, each with an independent prescale. These external triggers controlled ADC pedestal triggers, AGS beam gate veto, standard 50HZ pulsers and other types of calibration signals.

After appropriate prescales the total event rate leaving the L1 trigger systems was 10kHz during nominal operation.

## 6.4 Level 3 Trigger

Events passing the L1 trigger electronics caused the readout supervisor to initiate a read out and record all of the data from the detector electronics crates. These raw event data were stored in custom designed dual port memory units and buffered for event reconstruction and processing. The eight dual port memory units were cycled in such a manner that per beam spill only one half of the processors/DPM queues were used. Cycling the available queues providing each processor a full spill length during which to perform the software reconstruction of its assigned event

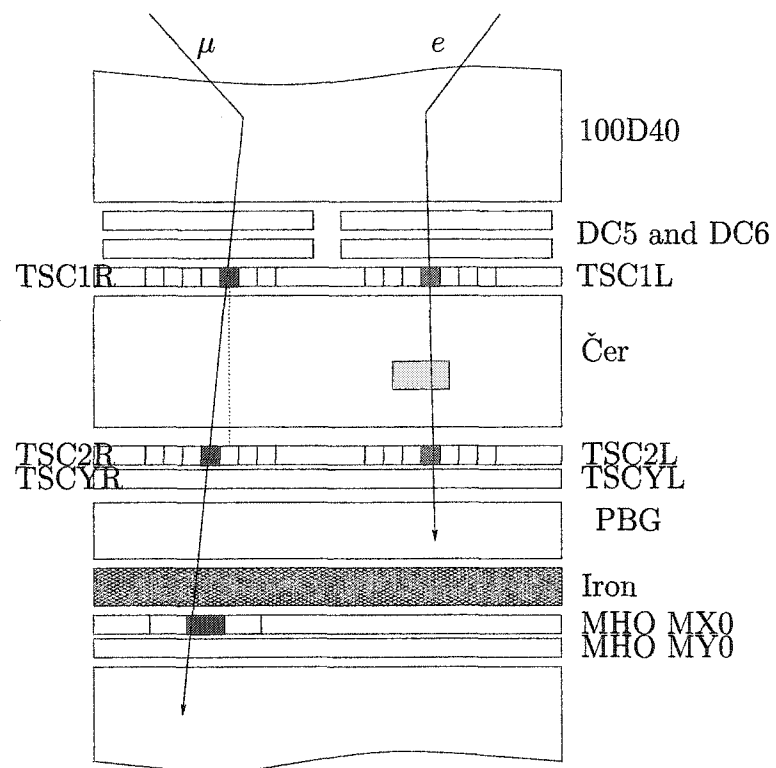


FIG. 6.2: Schematic overview of a level 1 event trigger

block. The size of each data block was set to 3000 events per DPM providing for a nominal sustained L1 event trigger rate of 12,000 events/spill.

The software event reconstruction phase of the trigger system was denoted as the Level 3 (L3) trigger. The L3 software reconstruction was run on a set of eight SGI V35 micro processors arrayed in parallel and housed in a VME crate. Each processor was given access to five of the dual port memory units through the VME backplane and access to the main control computer for data upload through an Ethernet connection.

Level 3 event reconstruction and filtering were designed to further reduce the data set prior to upload by placing loose requirements on the event quality as well as on invariant mass reconstruction and transverse momenta of the events. Track reconstruction was performed by applying a hit and clustering algorithm to the signals in the wire drift chambers and straw chambers. Hit searches were begun in wire drift chambers DC5/DC6 due to the lower hit multiplicities in these chambers as compared to the forward straw chambers. For each chamber the total number of wire events was checked to insure quality. Three layer X-measuring planes were required to have at least two hits and no more than 250 hits, while Y-measuring planes were required to have at least one hit and no more than 150 hits. As in the case of the back drift chambers, the straw chambers were then checked in the same manner in the order of SDC1, SDC2, SDC3. For the fourth set of straw chambers, SDC4, one hit was required in both X and Y views.

Parallelism requirements in the TSC modules were reimposed by requiring at least one and no more than 14 hits in each X module. Each hit in the TSC2X module was then searched against hits in TSC1X for a spatial match conforming to the parallelism requirement and a  $\pm 100$ ns time cut. Hits in the Y measuring module were checked to ensure that at least one and no more than ten slats were illuminated, and that the hits conformed to the same time cut as the X-measuring

pair.

Unpacking of the event data was performed and TDC values in the straw and wire drift chambers were converted to distance of closest approach values (DOCA) through a lookup table. Clusters of illuminated wires were formed. The hit clusters were used to create line segments between adjacent chambers for which the line slope was calculated. Line segments formed by tracking in DC5 and DC6 was used to project upstream and downstream to match tracking in the forward straw chambers and in the trigger scintillators. Line segments in SDC1 and SDC2 were used to compute track slopes and matched on to hits in SDC3.

Pairs of potential tracks found through the clustering algorithm were considered in pairs to form appropriate decay vertex points. For each set of tracks a two dimensional X and Y vertex were formed to determine the z coordinate of the track crossing point. The vertex pairs were sorted according to proximity as determined by their separation. From these two dimensional vertex pairs three dimensional vertices were formed and required to lie within the decay tank boundaries extending from  $z=8\text{m}$  to  $z=21.5\text{m}$ . Additional vertex quality requirements were placed upon the three dimensional vertices. Maximum L3 vertex doca was set at 70cm with the additional positioning requirement that the z position of the vertex be greater than  $z=7\text{m}$ .

Track momentum was determined by calculating the angular deflection of the line segments formed in SDC1/SDC2 with those from the SDC3/SDC4 segments. From a position dependent magnetic field map, the transverse momentum kick was computed through a  $B \cdot dl$  computation. Total event  $p_T$  was required to be less than 60MeV/c.

Reconstruction of the invariant mass of the event was computed using the L1 trigger hypothesis and track momenta as determined from the B-field lookup. Physics event triggers were required to have an invariant mass reconstruction greater

than  $460\text{MeV}/c^2$  to pass the level 3 filter. Events tagged for the  $\pi\pi$  or minimum bias data stream were subjected to an invariant mass reconstruction, but no cut was performed on this quantity and all events in these streams were recorded.

Level 3 data reduction resulted in a 3% pass rate for dilepton physics triggers. At nominal running conditions this resulted in approximately 300 physics events per beam spill uploaded to the host computer for output to data tape. In addition to the physics event triggers, all minimum bias events were passed through Level 3 and resulted in approximately an additional 100 events for calibration and normalization being uploaded per beam spill. With a nominal beam spill length of 3.6 seconds the total upload rate of just over 110Hz was achieved.

# CHAPTER 7

## Monte Carlo Modeling

The complexity of the E871 experimental apparatus creates a series of interdependencies between the key detector systems and subsystems. The interdependencies between these systems are manifest in the systematic responses, acceptances, and efficiencies that the detectors exhibit. The task of calculating these acceptances and normalizing the results is complicated by the additional interdependencies of the initial event state, kinematics and possible intermediate states that can develop through particle interactions in the active regions of the detectors. As a result of these factors no exact analytic expression can be determined for most quantities; instead statistical models are built and response functions determined by parametric fits to simulated data.

### 7.1 Monte Carlo Simulations

The process of Monte Carlo modeling was used to explore the E871 detector responses to both the primary data stream  $K_L^0 \rightarrow \mu^+ \mu^- e^+ e^-$  and to a multitude of potential backgrounds. To ensure model dependent systematics were minimized, two independent simulation systems were employed using different event generation,



transport, tracking and interaction mechanisms.

The first simulation employed the GEANT system for event generation and particle transport to create simulated primary event data for the examination of event kinematics and angular distributions. The second simulation was built upon the actual E871 analysis code and used simulated detector hits together with the actual analysis algorithms to provide accurate simulated detector response.

The strengths of each modeling system are discussed in Sections 7.1.1 and 7.1.2

### 7.1.1 Geant Simulation

The E871 Geant simulation was designed to investigate the characteristics of the  $K_L^0 \rightarrow \mu^+ \mu^- e^+ e^-$  event stream and its associated backgrounds in a manner that allowed for examination of the kinematic properties of the primary vertex and associated daughter particles. The simulation employed a transport mechanism that retained full event data outside of active detector regions. This full particle ID and event tracking allowed for the association of hits in the forward spectrometer with primary track information and particle identification without the necessity for valid downstream particle identification triggers in the Čerenkov, lead glass, muon hodoscope or muon range finder. Due to the increased amount of track associated information that was retained, the Geant models required more processing time per event than similar events in the E871 detector model. While slower in this respect, the resulting body of data allowed for more detailed analysis of the forward spectrometer regions as well as for pair production and multiple scattering in a manner that could not be duplicated with the detector simulations.

The Geant simulation was used primarily to examine the geometric acceptances for partially reconstructed track stubs. Through the use of this simulation, information on the mean angular separation of the electron/positron pair was gathered

along with the angular correlation data connecting the low energy electron Dalitz pair to the primary decay plane as defined by the reconstruction of the muon track pair.

The invariant mass spectra of the decays were computed both with and without detector acceptances to determine the resulting constraints and momentum dependent modifications that the reconstruction software imposes upon the shape of the spectra. In this manner the primary vertex was reconstructed using all available permutations of the track pairs as well as three body and full four body reconstruction of the events. Reconstructions of these types were used to determine the effects of multiple scattering and track deflection in the magnetic fringe field of the 96D40/D02 spectrometer magnets has upon the resolution of the invariant mass spectra.

The Geant Monte Carlo was also used extensively to examine the background decays as discussed in Section 4.4 due to its ability to identify pion decays in flight as well as pair production in the forward regions of the spectrometer. Extensive examination of the opening angle between  $e^+e^-$  pairs resulting from photon conversion in a  $K_L^0 \rightarrow \mu^+\mu^-\gamma$  event was computed and compared to that of the signal pairs as well as the correlation of the resulting pairs with the  $\mu^+\mu^-$  decay plane. In this manner the model was able to determine threshold values to differentiate between pair production events and real events with and without multiple scattering effects.

### 7.1.2 E871 Detector Simulation

The E871 detector simulation was constructed as a full model of the individual detector responses and efficiencies. The simulation was incorporated into the actual analysis code allowing for examination of both real and simulated events. The simulation system generated event data by propagating events through the tracking

and particle identification systems. Within each detector volume hits to sensitive regions were recorded to provide simulated responses. Only detector derived data were recorded in the model and used to create a simulated event block identical in composition to the real event data produced through the data acquisition system. Information on particle interactions, decays in flight and actual flight trajectories were not retained in the model. Instead the model concentrated upon correct derivation of hits in the detector systems using measured efficiencies and accounting for inactive or insensitive regions.

The E871 detector simulation was used extensively to test analysis code and determine figures of merit and cut values for the data. These algorithms were then directly applied to real data sets.

In addition to detector hit derivation, the E871 detector model was used to examine the effects of different theoretical form factors for the decay  $K_L^0 \rightarrow \mu^+ \mu^- e^+ e^-$  upon the event data and acceptance efficiencies for the E871 detectors. From these studies it was found that the enhancements to the decay spectrum were significant in the high invariant mass regions of the  $K_{\mu\mu}$  reconstructions. From both the shape and degree of enhancement present in the data, differentiation between the competing theories should be possible as discussed in Section 7.5.

## 7.2 Blind Analysis

To maintain unbiased procedures as well as algorithm development and determination of threshold “cut” values, a method of pseudo blind analysis was employed in conjunction with the Monte Carlo models. This methodology imposes a blind on all real data falling into the predefined signal region. No analysis routines or derived cut values were permitted to be tested upon the real signal data. Similarly, background calculations and subtractions were not permitted to influence real data

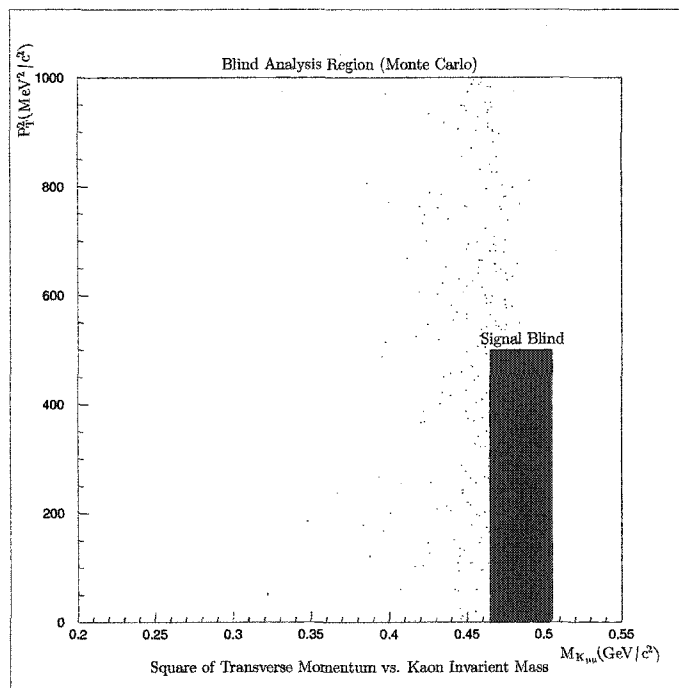


FIG. 7.1: Signal region blackout for development of threshold cuts and algorithm development under the blind analysis

points falling into the signal region. By blacking out the critical signal region in such a manner, the possibility of self consistency errors or of inappropriate cut values is reduced.

For the purposes of the blind procedure the signal region as described in Section 4.3 was removed from the initial analysis. A blind was placed over the data region consisting of events with an invariant mass greater than  $460\text{MeV}/c^2$  and less than  $505\text{MeV}/c^2$  and with a transverse momentum squared,  $p_t^2 < 500\text{MeV}^2/c^2$ . This black out region is shown in Fig. 7.1. No cuts were made upon real data falling into this region. Only event data generated through the Monte Carlo models was used to determine cut values in this region.

In addition to the described blind region, an overall normalization blind was imposed upon the analysis by a random event pre-scale on all Monte Carlo models. The purpose of the pre-scale was to prevent tampering with modeling efficiency and

simulation process that could adversely affect the resulting signal event prediction. Both Monte Carlo simulations were randomly scaled by up to  $\pm 50\%$  of the number of target events that was to be generated. This randomization was recorded but not apparent in the main data output. Initial normalization, efficiencies and event predictions were reported and then the true normalizations and efficiencies computed only after cut values and model dependencies were set.

## 7.3 Monte Carlo Goals

The initial goals of the Monte Carlo models were to determine base sensitivity and acceptance of the E871 detector systems for the four body decay  $K_L^0 \rightarrow \mu^+ \mu^- e^+ e^-$ . Along with this sensitivity, the simulations were designed to identify event characteristics and signatures which could be used to uniquely tag the signal. The event characteristics were used to determine cut values for kinematic quantities as well as to motivate analysis methods unique to the four body final state of interest.

In addition to the base event characteristics and detector sensitivities, the Monte Carlo simulations were adapted to include models of potential backgrounds arising from the decay streams discussed in Section 4.4. The information gained through these simulations was used to compute expected background rates arising from  $K_L^0 \rightarrow \mu^+ \mu^- \gamma$  as well as to exclude backgrounds from the other decay branches as discussed in Sections 4.4.2 - 4.4.4.

### 7.3.1 Event Characteristics

For each of the two Monte Carlo models that were developed, specific event characteristics were studied to determine the parameter set upon which further analysis cuts could be devised. For the decay  $K_L^0 \rightarrow \mu^+ \mu^- e^+ e^-$  the event is char-

acterized by the initial lepton four vectors and the decay point of the original kaon denoted as the primary vertex  $V_K$ . The initial event decay time is indicated by  $v_t$  and included in the vertex four vector to indicate the event timing.

$$p_{\ell_i}^\mu = \begin{pmatrix} p_{x\ell_i} & p_{y\ell_i} & p_{z\ell_i} & E_{\ell_i} \end{pmatrix} \quad (7.1)$$

$$V_K = \begin{pmatrix} v_x & v_y & v_z & v_t \end{pmatrix} \quad (7.2)$$

From the initial vertex and momentum four vector the direction cosines of each particle's trajectory are computed. The event vertex and four lepton trajectories are used to compute primary and secondary decay planes for the event. The primary decay plane is determined by the paths of the two muons and the primary decay vertex. It is denoted by the unit normal to the plane using a right handed convention. The crossproduct is taken from the negatively charged to the positively charged particle such that:

$$\hat{n}_{\mu\mu} = \frac{\vec{p}_{\mu^-} \times \vec{p}_{\mu^+}}{|\vec{p}_{\mu^-} \times \vec{p}_{\mu^+}|} \quad (7.3)$$

$$\hat{n}_{ee} = \frac{\vec{p}_{e^-} \times \vec{p}_{e^+}}{|\vec{p}_{e^-} \times \vec{p}_{e^+}|} \quad (7.4)$$

The full set of kinematic parameters can be used to form the diagram of the primary kaon decay point as shown in figure 7.2. From this diagram the opening angles of the lepton pairs, the relative inclination of the electron to muon planes, decay plane momentum correlation, and solid angle projection are all used to characterize the  $K_L^0 \rightarrow \mu^+ \mu^- e^+ e^-$  events under differing production and transport mechanisms.

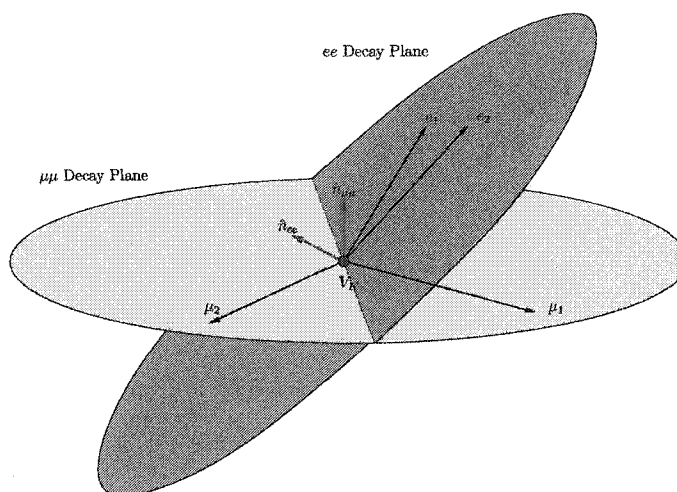


FIG. 7.2: Decay planes as defined by the event vertex and particle momenta  $p_{e_i}$

### 7.3.2 Detector Acceptances

The event characteristics described in Section 7.3.1 produce different kinematic distributions when varied by the introduction of a non-uniform form factor. The opening angle of the muonic pair leads to variable acceptance of the event under the physical geometry of the spectrometer and trigger detectors as well as for propagation of the muon tracks through the magnetic fields of D01 and D02. The angular correlation of the electron pair to the muon decay plane also affects the acceptance of the tracks in the first two straw drift chambers and the creation of a resulting partial tracking stub registering in the detectors.

Monte Carlo modeling of the base acceptances for the muon and electron pairs was created in order to measure the raw sensitivity of the detector geometry to the kaon decay. Acceptance factors and event rates were simulated at the major detector apertures and recorded. These acceptances were varied with different form factor assumptions to refine the expected event signature under each circumstance. The base geometric acceptances were used to make preliminary maximum signal predictions based upon total single event sensitivity and event branching fraction.

Single event rates were normalized to the total number of  $K_L^0 \rightarrow \mu^+\mu^-$  events reported in the E871 analysis of  $6216 \pm 82$  events [2].

In addition to the primary event signature consisting of two muon tracks and a single or tracking stub pair in SDC1/SDC2, other signals were modeled to determine acceptances for fuller event reconstructions. The simulations considered full four track event reconstruction, three track event reconstruction consisting of two muon and one electron tracks,  $\mu e$  event reconstruction with an associated tracking stub,  $\mu\mu$  event reconstruction with an associated single momentum measured partial track in SDC1/SDC2 to SDC3/SDC4, and  $ee$  event reconstruction with partial muon tracks. These event scenarios did not contribute at a level sufficient to serve as primary signal candidates.

### 7.3.3 Physics Background

The aspects of the sources of physics backgrounds discussed in Section 4.4 were examined in the framework of the Monte Carlo simulations due to the complexity of their interactions with the detector apparatus. In particular, Monte Carlo studies were made of the background arising from  $K_L^0 \rightarrow \mu^+\mu^-\gamma$  and  $K_L^0 \rightarrow e^+e^-\gamma$  as well as from event pile-up of semileptonic decays.

The  $K_L^0 \rightarrow \mu^+\mu^-\gamma$  simulations were designed to study the event characteristics of the  $\mu^+\mu^-$  pair in combination with a pair production event upstream of the straw drift chambers as discussed in Section 4.4.1. Of particular interest was the measurement of the geometric acceptance of the two muon tracks at an invariant mass in excess of 460 MeV/c. The presence of the initial three body final state leads to a uniform Dalitz distribution of particle momenta. This distribution is shown in figure 7.3. The invariant mass distribution of the reconstructed kaon mass  $M_{\mu\mu}$  is shown in figure 7.5(a). The resulting kinematic spectrum of the muons when



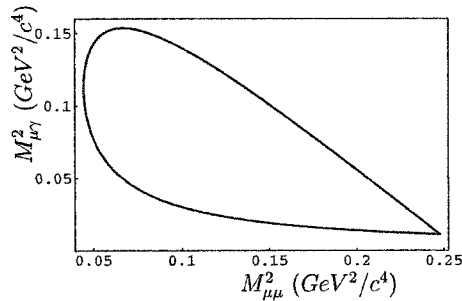


FIG. 7.3: Uniform Dalitz plot for  $K_L^0 \rightarrow \mu^+ \mu^- \gamma$  in the kaon rest frame

boosted into the laboratory frame results in the  $\mu^+$  and  $\mu^-$  momenta curves as shown in figure 7.4.

The geometric acceptance of the spectrometer to the  $K_L^0 \rightarrow \mu^+ \mu^- \gamma$  decay is measured through the valid reconstruction of parallel muon trigger events. The raw invariant mass distribution of accepted parallel trigger events is shown in figure 7.5(b). This distribution is computed prior to analysis cuts including the invariant mass threshold of 465 MeV, and prior to consideration of electron pair production or other stub inducing physics events. Events of this type are then examined in detail to determine acceptance rates based on the known decay branching fraction for  $K_L^0 \rightarrow \mu^+ \mu^- \gamma$  of  $3.59 \pm 0.11 \times 10^{-7}$ . Effects of a non-uniform distribution arising from a single pair conversion of a pseudoscalar meson [25] or from  $\chi PT$  like form factor [22] are considered in the same manner that the possible form factors for  $K_L^0 \rightarrow \mu^+ \mu^- e^+ e^-$  are incorporated into the E871 Monte Carlo code as described in Section 7.5

The analysis of the effects of the background decay stream  $K_L^0 \rightarrow e^+ e^- \gamma$  were examined in the same manner as the  $\mu\mu\gamma$  decay with a consideration of a signal arising from the highly improbable conversion of the photon to a muon pair forward of the spectrometer with subsequent acceptance of the tracks. Additionally the decay was examined for a possible secondary event signature in the form of a  $e^- e^+$

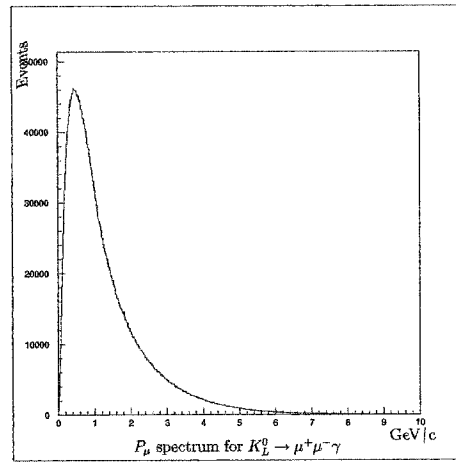
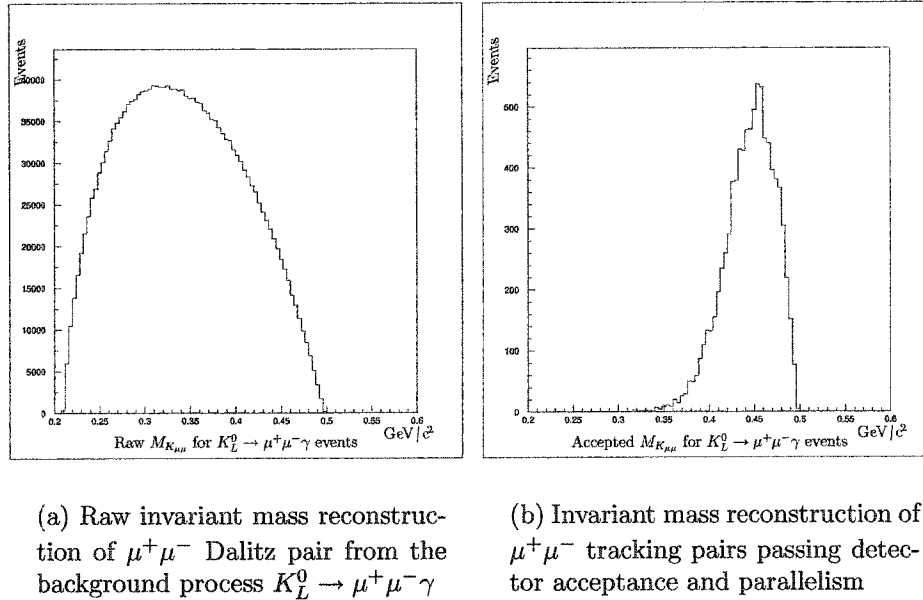


FIG. 7.4: Laboratory frame muon momenta for  $K_L^0 \rightarrow \mu^+ \mu^- \gamma$



(a) Raw invariant mass reconstruction of  $\mu^+ \mu^-$  Dalitz pair from the background process  $K_L^0 \rightarrow \mu^+ \mu^- \gamma$

(b) Invariant mass reconstruction of  $\mu^+ \mu^-$  tracking pairs passing detector acceptance and parallelism

FIG. 7.5: Monte Carlo simulations of invariant mass reconstructions for  $K_L^0 \rightarrow \mu^+ \mu^- \gamma$  using  $\mu^+ \mu^-$  tracking pairs

tracking pair reconstruction with muon tracking stubs. The Monte Carlo showed that this type of signal was not viable due to resulting background from  $K_L^0 \rightarrow e^+e^-\gamma$  with pair production in the decay region and vacuum window, resulting in a four electron final state entering the detectors at a rate higher than the base acceptance for  $K_L^0 \rightarrow \mu^+\mu^-e^+e^-$  events with the  $e^+e^-$  event pair signature above 460 MeV.

Modeling of semileptonic event pile up was attempted using both  $K_L^0 \rightarrow \pi^\pm e^\mp \nu_e$  and  $K_L^0 \rightarrow \pi^\pm \mu^\mp \nu_\mu$  events. Pile up was simulated by modeling a single semileptonic event from its primary decay point. When the primary decay point was determined a secondary event was superimposed and all resulting daughter particles propagated through the detectors. The results were weighted by the decay profile to determine the overlap probability. This method did not include the modeling of decay vertices within the primary beam in close proximity to the primary vertex but not in total overlap. Additionally it did not include any rate dependent or spill structure effects. Alternative methods for determining the background induced through semileptonic pile up were considered outside of Monte Carlo modeling. Flat background subtraction in a manner similar to the method utilized in the  $K_L^0 \rightarrow \mu^+\mu^-$  analysis of the E871 data [41] was determined using reconstructed event data falling above the prescribed kaon mass.

## 7.4 Kaon Modeling

Modeling of the decay  $K_L^0 \rightarrow \mu^+\mu^-e^+e^-$  requires proper treatment of the parent kaon. Generation of the initial energy and momentum distributions as well as the trajectories of the parent kaons are required to allow the Monte Carlo to match the kinematic distributions that are observed experimentally in the E871 apparatus. Due to the two state nature of the kaon system as described earlier in Chapter 2 these processes require knowledge of the strong production mechanism and the weak

decay process. Transport of the beam through the regions upstream of the active detectors requires consideration of additional interaction effects and the probabilities of particle scattering. These topics are addressed in the following sections.

### 7.4.1 Kaon Momentum

Production of the kaon beam within the fixed platinum target involves a reaction of the form:



The pions required for the interaction are produced through the interaction of a beam proton upon the forward end of the target. The resulting pion cloud then interacts with a target proton resulting in the kaon flux. This process is shown in Fig. 2.10.

The momentum spectrum for the kaon beam generated in this manner is not easily determined in an analytical fashion. Modeling of the beam was determined through use of the kaon production data obtained by Skubic et al. [34]. The kaon production data were measured at Fermilab using a 300 GeV/c proton beam incident on beryllium, copper and lead targets at varying production angles. The  $K_S^0$  production cross section was measured in all these experiments. Due to the nature of the kaon system as discussed in Section 2.3 we can relate the observed weak eigenstates  $K_S^0$  and  $K_L^0$  to the strong production states  $K^0$  and  $\bar{K}^0$ . In the absence of CP violation this becomes:

$$|K^0\rangle = \frac{1}{\sqrt{2}} [|K_S^0\rangle + |K_L^0\rangle] \quad (7.6)$$

$$|\bar{K}^0\rangle = \frac{1}{\sqrt{2}} [|K_S^0\rangle - |K_L^0\rangle] \quad (7.7)$$

The strong production mechanism creates an initial beam with a linear combination of strong eigenstates. These can be decomposed into the resulting long lived and short lived weak eigenstates.

$$\begin{aligned}
 K_{beam} &= a |K^0\rangle + b |\bar{K}^0\rangle \\
 &= a \left[ \frac{1}{\sqrt{2}} (|K_S^0\rangle + |K_L^0\rangle) \right] + b \left[ \frac{1}{\sqrt{2}} (|K_S^0\rangle - |K_L^0\rangle) \right] \\
 &= \frac{1}{\sqrt{2}} [(a+b) |K_S^0\rangle + (a-b) |K_L^0\rangle]
 \end{aligned} \tag{7.8}$$

The production mechanism is completely incoherent; thus the sum over all phases results in equal populations of  $|K_S^0\rangle$  and  $|K_L^0\rangle$ . The production cross section for  $K_S^0$  is thus equal to the production cross section for  $K_L^0$ . Because of the equality of the production cross sections, the data of Skubic et al. can be used as a measurement of the  $K_L^0$  production cross section and momentum spectrum. The differential production cross section for the reaction is thus expressed as

$$\frac{d\sigma}{dp d\Omega} = \frac{p_K^2}{E_K} f(x, p_t) \tag{7.9}$$

The form factor  $f(x, p_t)$  is empirically determined and parameterized as

$$f(x, p_t) = \exp(c_1 + c_2 x^2 + c_3 x + c_4 x p_t + c_5 p_t^2) \tag{7.10}$$

$$c_1 = 4.72 \quad c_2 = -2.0 \quad c_3 = -6.5 \quad c_4 = -2.3 \quad c_5 = -1.34 \tag{7.11}$$

The variables  $E_K$  and  $p_K$  are the laboratory energy and momentum of the kaon. The transverse and longitudinal components of the momentum in the center of momentum frame are expressed as  $p_T$  and  $p_L$  with the Feynman scaling variable  $x = p_L/p_L^{max}$ .

The overall production rates are scaled by a normalization factor  $(A_{Pt}/A_{Pb})^\alpha$

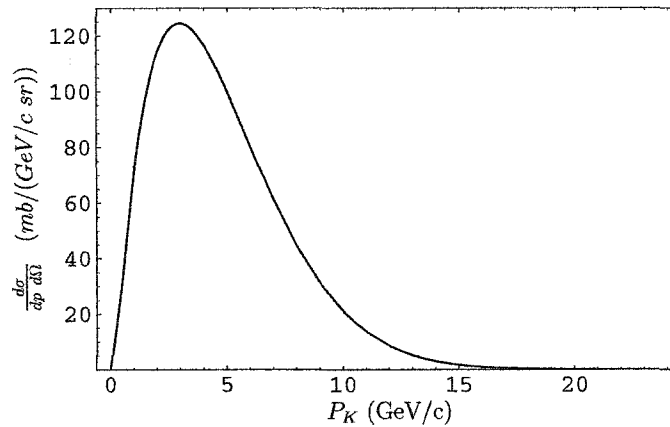


FIG. 7.6:  $K_L^0$  production cross section for 24 GeV protons incident upon a fixed platinum target at a production angle of  $-3.75^\circ$

to compensate for the difference between the parameterization data of Skubic et al. which was taken on a lead target (Pb  $A=207.2$ ), and the E871 production target which was composed of platinum (Pt  $A=195.1$ )

The production cross section at a target angle of  $-3.57^\circ$  is computed from Eq. (7.9) for a 24 GeV incident proton beam on platinum and is shown in Fig. 7.6. The kaon momentum spectrum generated by the Monte Carlo simulations for this production process is shown in Fig. 7.7 where a lower production threshold of  $P_K = 1\text{GeV}$  has been imposed upon the data sample.

#### 7.4.2 Kaon Decay

The simulated kaon beam is transported using the mean  $K_L^0$  lifetime of  $5.17 \times 10^{-8}\text{s}$  to determine the z-axis location of the primary kaon decay. Primary decay vertices determined to occur within the fiducial volume of the decay tank extending from the upstream decay tank window position  $z=10\text{m}$  to the downstream vacuum window at  $z=20.9\text{m}$  were retained for analysis. Decay vertices occurring outside of these boundaries were cut from the Monte Carlo.

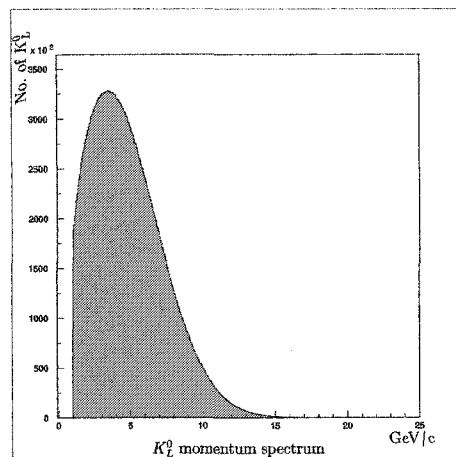


FIG. 7.7:  $K_L^0$  momentum spectrum produced by the E871 Monte Carlo event generator based upon the cross section of Skubic et al.[34]

The distribution of primary kaon decay points is shown in Fig. 7.8 as generated by the Monte Carlo simulations. In addition to the z-axis vertex positions, the decay distributions are tuned to mirror the beam profile in the x and y dimensions.

A defined list of decay models was used for valid vertices. The relative branching fractions for the possible decay modes were simulated by user-defined weighted probability functions. Decay modes of interest were modeled for both primary signal and background signal rates. Subsequent decays of daughter particles were controlled through the standard decay rates for unstable particles.

For three body decay channels the decay kinematics were determined using the standard uniform phase space of the multi-body Dalitz decay spectra. For the decays  $K_L^0 \rightarrow \mu^+ \mu^- \gamma$  and  $K_L^0 \rightarrow e^+ e^- \gamma$  the decay spectra was modified to include the form factor for the decays[25]. The semi-leptonic decays  $K_{e3}$  and  $K_{\mu3}$  were modeled using the known form factors.

Decay into the four body final state  $K_L^0 \rightarrow \mu^+ \mu^- e^+ e^-$  was handled separately using model dependent form factors. The details of these calculations are presented in Section 7.5.

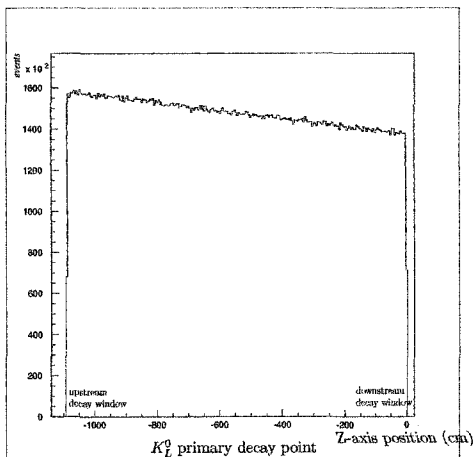


FIG. 7.8: Beam axis  $K_L^0$  primary decay point simulation for  $K_L^0 \rightarrow \mu^+ \mu^- e^+ e^-$  using the E871 kaon momentum distribution.

### 7.4.3 Multiple Coulomb Scattering

In the momentum regime of the soft electron/positron pair resulting from the decay  $K_L^0 \rightarrow \mu^+ \mu^- e^+ e^-$  as shown in Fig. 7.9 multiple Coulomb scattering must be included in the transport of the charged particles to properly account for the low energy trajectories. Multiple scattering is accounted for in the E871 Monte Carlo through a computation of scattering at an aperture and through scattering within a volume prior to an aperture.

Multiple scattering at an aperture is used for transport of charged tracks through thin membranes such as the windows of the vacuum chamber and wire drift chambers. In this approach the incident slope of the particle trajectory is modified by a Gaussian scattering distribution modified by Moliere tails. The probability for scattering through an angle  $\phi$  takes the form

$$P(\phi)d\phi = \frac{2\phi}{\langle \phi^2 \rangle} \exp\left(\frac{-\phi^2}{\langle \phi^2 \rangle}\right) d\phi \quad (7.12)$$



The root mean square deflection angle for a single scatter is given as

$$\phi_{rms} = \langle \phi^2 \rangle^{1/2} = \frac{zE_s}{pv} \sqrt{\frac{x}{X_0}} [1 + 0.038 \ln(x/X_0)] \quad (7.13)$$

For the thin membrane we use the simplified form for the scattering angle in terms of the membrane thickness  $x$  and scattering length  $X_0$ .

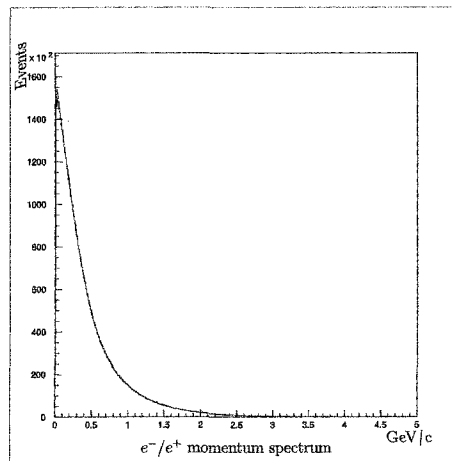
$$\phi_{scat} \approx \frac{21 \text{ MeV}}{\sqrt{2} p \beta c} \sqrt{\frac{x}{X_0}} \quad (7.14)$$

The scattering angle was limited by the parameterization in such a way that  $\Delta\phi < 8\phi_{scat}\sqrt{B}$  where  $B$  was a function of the scattering thickness. In the case of the relativistic regime of the decay electrons the parameter was chosen such that  $B=6$ . The maximum transverse deflection of electrons in the front vacuum windows was thus limited to  $p_t = 7 \text{ MeV}/c$ .

Multiple scattering within a volume was treated in a similar manner to the scattering at an aperture with the additional provision that the track position as well as angle could be modified at each transport step. The effective radiations lengths of materials present between each of the primary apertures is listed in table 7.1. The table details the material between the current aperture and the previous aperture for which the scattering is calculated using the form of Eq. (7.13). Table 7.1 also details the thin membrane material present at the aperture for which the scattering angle is calculated using Eq. (7.14). At each of these positions the transport simulation computes the relevant scattering and modifies the tracking parameters as needed.

Aperture	Position (m)	Prior to Aperture $x/X_0$ ( $\times 10^{-3}$ )	At Aperture $x/X_0$ ( $\times 10^{-3}$ )
Vacuum Window	20.900	1.17	0.0
SDC1	21.083	2.26	0.03
SDC2	22.191	2.26	0.20
96D40	24.000	0.0	0.32
SDC3	25.399	1.46	0.25
SDC4	25.893	2.32	0.09
100D40	27.200	0.0	0.23
DC5	28.485	1.80	0.23
DC6	29.731	1.69	0.22
TSC1	29.941	37.4	0.0
Čer	32.490	11.9	0.0
TSC2	32.854	48.9	0.0

TABLE 7.1: E871 aperture positions and material lengths for multiple scattering

FIG. 7.9: Electron and positron momentum spectra for  $K_L^0 \rightarrow \mu^+ \mu^- e^+ e^-$

## 7.5 Monte Carlo Form Factors

After proper generation of the parent kaon population as described in Section 7.4.1 and transport of the particle to the calculated decay point as discussed in Section 7.4.2 the parent kaon is decayed according to the user defined decay streams. In the case of the primary decay path of interest,  $K_L^0 \rightarrow \mu^+ \mu^- e^+ e^-$ , multiple methods of simulating the decay were used to account for variations in the principal theories. Theory-specific form factors were used to produce the desired decay spectra and angular distribution of particles.

### 7.5.1 Four Body Decay Kinematics

Modeling of the decay  $K_L^0 \rightarrow \mu^+ \mu^- e^+ e^-$  is treated as a double internal conversion of the parent pseudoscalar meson into two distinguishable lepton pairs. Modeling of the four body process was first treated as a generic decay  $Meson \rightarrow \ell^+ \ell^- \ell^+ \ell^-$  and then specialized to the indistinguishable and distinguishable final states. The matrix element for the decay is computed using conventional quantum electrodynamics (QED). The matrix element  $\mathcal{M}$  is broken into two parts  $\mathcal{M}_1$  and  $\mathcal{M}_2$  corresponding to Fig. 7.10(a) and 7.10(b), respectively. The primary matrix element is thus expressed as:

$$\mathcal{M}_1 = \frac{2f}{M_K} \varepsilon_{\mu\nu\rho\sigma} \frac{(p_+ + p_-)^\nu (p'_+ + p'_-)^\sigma}{(p_+ + p_-)^2 (p'_+ + p'_-)^2} \times \bar{u}(p_-) \gamma^\mu \nu(p_+) \bar{u}(p'_-) \gamma^\rho \nu(p'_+) \quad (7.15)$$

The total decay rate for the four lepton decay can be written in terms of the matrix elements for the diagrams of Fig. 7.10.

$$\begin{aligned} \Gamma &= \int |\mathcal{M}_1|^2 d\phi + \int |\mathcal{M}_2|^2 d\phi + \int (\mathcal{M}_1 \mathcal{M}_2^* + \mathcal{M}_2 \mathcal{M}_1^*) d\Phi \\ &= \Gamma_1 + \Gamma_2 + \Gamma_{12} \end{aligned} \quad (7.16)$$

In the case where the final state particles are completely distinguishable the matrix elements of the corresponding contribution from the interchange diagrams cause  $\Gamma_{12}$  to vanish.

$$\begin{aligned}\Gamma_{12} &= \int (\mathcal{M}_1 \mathcal{M}_2^* + \mathcal{M}_2 \mathcal{M}_1^*) d\Phi \\ &= 0 \quad \text{for } K_L^0 \rightarrow \mu^+ \mu^- e^+ e^-\end{aligned}\tag{7.17}$$

As a result, the decay rate expressed in terms of the momenta of the virtual photons  $x_1$  and  $x_2$ , and the variables  $y_1, y_2, \phi$  transformed as per the prescription of appendix B, for the decay  $K_L^0 \rightarrow \mu^+ \mu^- e^+ e^-$  takes the form[25]

$$\begin{aligned}\Gamma &= \frac{1}{\pi} \left( \frac{\alpha}{4\pi} \right)^2 \int \cdots \int dx_1 dx_2 dy_1 dy_2 d\phi \left| \frac{f(x_1^2, x_2^2)}{f(0, 0)} \right|^2 \\ &\times \left[ 1 - \frac{2(x_1^2 + x_2^2)}{M_K^2} + \frac{(x_1^2 - x_2^2)^2}{M_K^4} \right]^{3/2} \\ &\times \left[ \left[ \frac{1}{x_1 x_2} + \left( \frac{y_1^2}{x_1} + \frac{4m_e^2}{x_1^3} \right) \left( \frac{y_2^2}{x_2} + \frac{4m_\mu^2}{x_2^3} \right) \right] \sin^2 \phi \right. \\ &\left. + \left[ \frac{y_1^2 + y_2^2}{x_1 x_2} + \frac{4m_e m_\mu (x_1^2 + x_2^2)}{x_1^3 x_2^3} \right] \cos^2 \phi \right]\end{aligned}\tag{7.18}$$

The form of the decay rate in Eq. (7.18) is used to determine the differential phase space allowed by the Monte Carlo population. In the most basic form the form factor  $f(x_1, x_2)/f(0, 0)$  is taken to be on-shell, reducing the quantity to unity and removing any non-kinematic momentum dependence from the model. This version of the Monte Carlo is referred to as the QED kinematic distribution and serves as a basis for the four body phase space used in further modeling of the decay with non-trivial form factors[25].

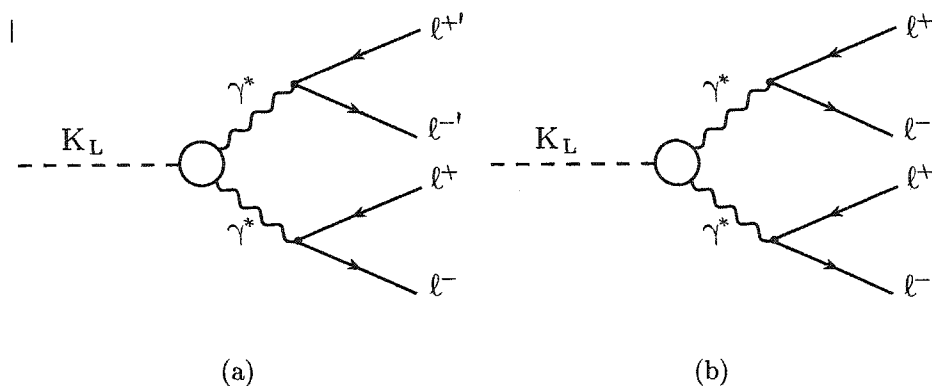


FIG. 7.10: Diagrams contributing to double internal conversion of a pseudoscalar meson into lepton pairs. Matrix element  $\mathcal{M}_1$  corresponds to (a) and the interchange term  $\mathcal{M}_2$  corresponds to (b)

## 7.5.2 Vector Meson Dominance Model Form Factor

The model dependence of the form factors for the decay  $K_L^0 \rightarrow \mu^+ \mu^- e^+ e^-$  involves the use of effective couplings of the kaon to the final state leptons. The effective couplings used in models of vector meson dominance such as that of Ko [42] require knowledge of the coupling strength  $\alpha$  which is obtained through fits to the  $K_L^0 \rightarrow \mu^+ \mu^- \gamma$  data. Since in VDM the form factor for the decay  $K_L^0 \rightarrow \mu^+ \mu^- e^+ e^-$  is dominated by the  $K^* - V$  pole diagrams of Fig. 3.3(b), the corresponding form factor with parameter fits from the  $K_L^0 \rightarrow \ell^+ \ell^- \gamma$  data is used:

$$\begin{aligned}
 F(s)_{VDM} = & \alpha \sqrt{2} e G_F f_{K^*} K_\gamma \left( \frac{m_\rho^2}{f_{K^*} f_\rho^2} \right) \left( 1 - \frac{s}{m_{K^*}^2} \right)^{-1} \\
 & \times \left( \frac{4}{3} - \left( 1 - \frac{s}{m_\rho^2} \right)^{-1} - \frac{1}{9} \left[ \left( 1 - \frac{s}{m_\omega^2} \right)^{-1} + 2 \left( 1 - \frac{s}{m_\phi^2} \right)^{-1} \right] \right) \quad (7.19)
 \end{aligned}$$

The parameter  $\alpha$  is the model dependent coupling strength for the interaction. For the purposes of the Monte Carlo the value of  $\alpha$  is taken from the Bergström

calculation[17] such that:

$$|\alpha_K^*| \simeq 1.2 \sin \theta_C \cos \theta_C \approx 0.2, \quad (7.20)$$

with  $f_{K^*} = f_\rho = 5.09$ . The momentum dependence of the form factor is characterized by the photon mass coupled to the vector meson. For the Monte Carlo generation of the decay this form factor is used in conjunction with the four body kinematics. Overall scaling of the form factor is not necessary since only the kinematics affected by the momentum distribution are relevant in determining the acceptance of the decay.

### 7.5.3 QCD Form Factor

In addition to the model dependent aspects of the VDM form factor the decay was also modeled with the low energy QCD form factor of D'Ambrosio [20] The form factor was modeled with the expansion of the form factor as discussed in Section 3.3 with the vector meson propagator chosen as that of the  $\rho$  mass. In this form the low energy QCD form factor used was:

$$f_{QCD}(q_1^2, q_2^2) = \frac{F(q_1^2, q_2^2)}{F(0, 0)} = 1 + \alpha \left( \frac{q_1^2}{q_1^2 - m_\rho^2} + \frac{q_2^2}{q_2^2 - m_\rho^2} \right) + \beta \frac{q_1^2 q_2^2}{(q_1^2 - m_\rho^2)(q_2^2 - m_\rho^2)} \quad (7.21)$$

The parameter  $\alpha$  is chosen to correspond to the  $K_L^0 \rightarrow \ell^+ \ell^- \gamma$  data and as such is set at:

$$\alpha = -1.63 \quad (7.22)$$

This value can be related to the choice of  $\alpha$  used in the Bergström VDM model in Eq. (7.20) by the relation:

$$\alpha = -1 + (3.1 \pm 0.5)\alpha_K^* \quad (7.23)$$

The problem of determining the parameter  $\beta$  is difficult since in principle it should be empirically determined from the decay  $K_L^0 \rightarrow \mu^+\mu^-e^+e^-$ . In the absence of data on this search decay, the parameter was set using the sum rule for the ultra violet cut off such that for high  $q^2$ ,

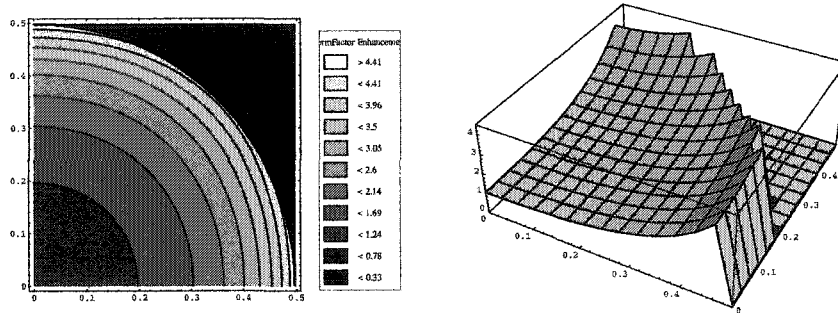
$$1 + 2\alpha + \beta = 0 \quad (7.24)$$

giving  $\beta = 2.26$ . In a similar fashion the parameter  $\beta$  was also determined from the weak sum rule:

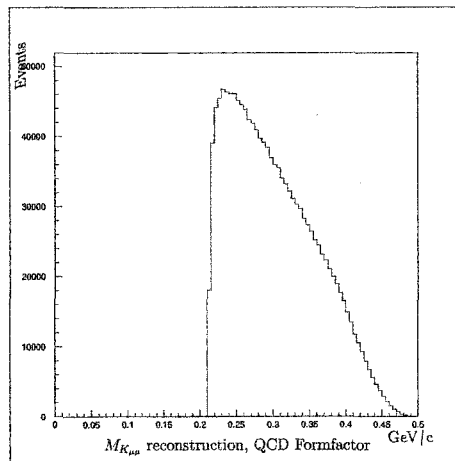
$$1 + 2\alpha + \beta \simeq \frac{14}{9}|N_F| \simeq 0.3 \quad (7.25)$$

yielding  $\beta = 2.56$  or  $\beta = 1.96$ .

In this manner the low energy QCD form factor was combined with the QED kinematic distribution to model the decay  $K_L^0 \rightarrow \mu^+\mu^-e^+e^-$  in the Monte Carlo simulations for both strong and weak bounds on the parameters. The diagrams of Fig. 7.11 show the effect of the QCD form factor on the shape of the resulting  $K_L^0 \rightarrow \mu^+\mu^-e^+e^-$  spectrum. The high invariant mass bands near the kaon mass  $M_K$  show a factor of four enhancement compared to the unmodified QED decay spectrum. This enhancement is also evident in the modified shape of the  $K_{\mu\mu}$  invariant mass reconstruction spectrum above  $M_{\mu\mu} = 460 \text{ MeV}/c^2$  near the kaon endpoint as shown in Fig. 7.11(b). The resulting effect of the high invariant mass enhancement is to increase the efficiency with which the muon pair from  $K_L^0 \rightarrow \mu^+\mu^-e^+e^-$  decays are



(a) QCD form factor [20] with high invariant mass enhancement bands.



(b)  $K_{\mu\mu}$  invariant mass spectrum with the QCD form factor

FIG. 7.11: Model of the QCD form factor for  $\beta = 2.56$  [20] used to simulate the decay  $K_L^0 \rightarrow \mu^+\mu^-e^+e^-$ . Kinematic restraints are placed upon the plot regions to show high mass enhancement of the decay near the kaon endpoint.



accepted by the E871 spectrometer trigger requirements. The increased sensitivity is due to the resulting muon track kinematics that are favorable to the low  $p_T$  required for events to pass the parallelism requirements of the TSC trigger.

#### 7.5.4 $\chi PT$ Form factor

The decay  $K_L^0 \rightarrow \mu^+ \mu^- e^+ e^-$  was also modeled with a form factor derived from a chiral expansion of the decay as discussed in Section 3.4 using the work of Zhang and Goity [24]. The form factor was implemented in the form similar to that of Eq. (3.28) where the momentum dependence was isolated into the  $D(q_1, q_2, M_\rho)$  using again the  $\rho$  mass as the scale for the expansions.

$$F_{\chi PT}(q_1, q_2) = \frac{\alpha_{em} C_8}{192\pi^3 F_\pi^3} [-(a_2 + 2a_4)D(q_1, q_2, M_\rho) + C(M_\rho)(q_1 + q_2)] \quad (7.26)$$

Both parameter sets discussed in section 3.4 involving the sign of the form factor for the Dalitz decays were taken into account. The parameter sets modeled were such that  $F_\pi=93$  MeV,  $C_8 = 3.12 \times 10^{-7}$ , and the values for  $a_2 + a_4$  and the counter term were chosen from the sets  $a_2 + a_4 = \{-0.3, 1.5\}$ ,  $C(M_\rho) = \{14.2, -10.3\}$ .

The momentum dependence of the form factor was expressed in the form similar to Eq. (3.29) with the meson mass set as  $M_\rho$

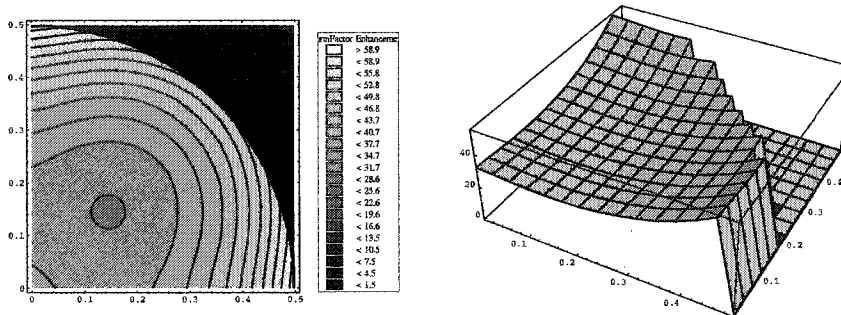
$$D(q_1, q_2, M_\rho) = (q_1 + q_2) \left[ \frac{10}{3} - \left( \ln \frac{M_K^2}{M_\rho^2} + \ln \frac{M_\pi^2}{M_\rho^2} \right) \right] \quad (7.27)$$

$$+ 4 [F(M_\pi^2, q_1) + F(M_K^2, q_1) + F(M_\pi^2, q_2) + F(M_K^2, q_2)]$$

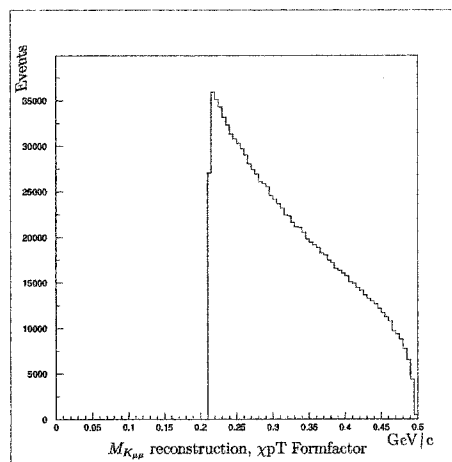
The functions  $F(m^2, q)$  represent the chiral logarithms expressed in terms of  $y = q/m^2$  as:

$$F(m^2, q) = \left( \left( 1 - \frac{y}{4} \right) \sqrt{\frac{y-4}{y}} \ln \frac{\sqrt{y-4} + \sqrt{y}}{\sqrt{y-4} - \sqrt{y}} - 2 \right) m^2 \quad (7.28)$$

The full chiral form factor was combined with the QED kinematic distributions to fully model the decay  $K_L^0 \rightarrow \mu^+\mu^-e^+e^-$ . In analogy to Fig. 7.11 the diagrams of Fig. 7.12 schematically show the effect of the chiral form factor on the shape of the resulting  $K_L^0 \rightarrow \mu^+\mu^-e^+e^-$  spectrum. In contrast to the QCD form factor, the chiral expansion favors enhancement to both the high invariant mass bands near the kaon mass  $M_K$  and to the edge of the kinematic locus. This enhancement is considerably more pronounced than the QCD enhancement as seen by the factor of 100 enhancement compared to the unmodified QED decay spectrum. The enhancement is also seen in the modified shape of the  $K_{\mu\mu}$  invariant mass reconstruction spectrum near the kaon endpoint as shown in Fig. 7.12(b). In the same manner as the QCD enhancement, the effect of the high invariant mass enhancement is to increase the efficiency with which the muon pair from  $K_L^0 \rightarrow \mu^+\mu^-e^+e^-$  decays are accepted into the forward spectrometer. The resulting kinematics are even more favorable to the low  $p_T$  requirements of the E871 experimental apparatus.



(a) Chiral form factor [24] with high invariant mass enhancement bands.



(b)  $K_{\mu\mu}$  invariant mass spectrum with the Chiral form factor

FIG. 7.12: Model of the Chiral form factor [24] used to simulate the decay  $K_L^0 \rightarrow \mu^+\mu^-e^+e^-$ . Kinematic restraints are placed upon the plot regions to show high mass enhancement of the decay near the kaon endpoint.

# CHAPTER 8

## Vertex and Stub Analysis

### 8.1 Event Reconstruction

The kinematics of a relativistic decay from an initial single particle state into a multi body final state can be expressed in terms of the energy and momentum of the initial and final states as well as the spatial coordinates and time at which the decay occurred.

$$\begin{aligned} X &\rightarrow x_1 + x_2 + \cdots + x_n \\ X(E, \vec{p}) &= \sum_{i=1}^n x_i(E_i, \vec{p}_i) \end{aligned} \tag{8.1}$$

Imposing four momentum conservation on the decay products leaves  $4(n - 1)$  independent energy/momentum parameters that determine the event. These parameters are dependent upon the frame of reference in which the event is observed. Reconstruction of the decay event requires that a connection be made between measured quantities in each of the frames of reference. In general transformations from the rest frame of the parent particle to the laboratory frame in which the daughter par-

ticles are observed and measured can be represented by a series of boosts from the initial frame to another Lorentz frame by infinitesimal transformations of the form:

$$A_{boost}(\beta) = \begin{pmatrix} \gamma & -\gamma\beta & 0 & 0 \\ -\gamma\beta & \gamma & 0 & 0 \\ 0 & 0 & 1 & 0 \\ 0 & 0 & 0 & 1 \end{pmatrix} \quad (8.2)$$

where the boost here is taken along the  $x_1$  direction, followed by an appropriate infinitesimal rotation of the spatial coordinates through a small angle  $\Delta\psi$  of the form:

$$\begin{pmatrix} 0 & -\kappa_1\Delta\psi & -\kappa_2\Delta\psi & -\kappa_3\Delta\psi \\ -\kappa_1\Delta\psi & 0 & 0 & 0 \\ -\kappa_2\Delta\psi & 0 & 0 & 0 \\ -\kappa_3\Delta\psi & 0 & 0 & 0 \end{pmatrix} \quad (8.3)$$

The difficulty in using this approach in the case of E871 is that initial momentum of the parent kaon is not measured, making it impossible to directly back transform from the laboratory frame to the rest frame of the parent particle. As an alternative to full event reconstruction through Lorentz transform a series of Lorentz invariants is used to characterize the event and serve as the reconstruction parameters. Since the  $4(n - 1)$  energy/momentum parameters which describe the decay process transform under these matrices as four-vectors, it is possible to choose a linear combination of them which forms a Lorentz scalar under the appropriate transformations and as such characterizes the decay independent of chosen reference frame. The first Lorentz scalar that is analyzed is the invariant mass of the parent particle.

### 8.1.1 Invariant Mass

In constructing the invariant mass of the parent particle it is first necessary to transform to a reference frame in which the parameters set by Eq. (8.1) are further constrained. In particular there always exists the center of momentum (CM) frame and a transformation to it (see Goldstien [43]) such that in that frame, the spatial components of the total four momentum of the initial particle are zero:

$$P_{total}^{\mu} = \begin{pmatrix} E \\ \vec{P} \end{pmatrix} = \begin{pmatrix} E \\ 0 \end{pmatrix} \quad (8.4)$$

Since the internal processes of the multi-body decay are independent of the chosen reference frame, the total momentum four vector of any process taking the form of Eq. (8.1) can be expressed in the CM frame as:

$$P_{init}^{\mu} = \begin{pmatrix} E \\ \vec{P} \end{pmatrix} = \begin{pmatrix} \sqrt{P^2 + M^2} \\ 0 \end{pmatrix} = \begin{pmatrix} M \\ 0 \end{pmatrix} \quad (8.5)$$

$$\sum_{i=1}^n \vec{p}_i^{\mu} = \sum_{i=1}^n \begin{pmatrix} E_i \\ \vec{p}_i \end{pmatrix} = \begin{pmatrix} \sum_i m_i^2 \\ 0 \end{pmatrix} \quad (8.6)$$

In this formulation it is evident that the total momentum four vector is a function only of the mass of the decay products. Under an infinitesimal Lorentz boost the total momentum four vector transforms as:

$$P^{\mu} = A^{\mu}_{\nu}(\beta) P^{\nu} = \begin{pmatrix} \gamma M \\ -\gamma\beta M \\ 0 \\ 0 \end{pmatrix} \quad (8.7)$$

The norm of the total four momentum is clearly left invariant:

$$\begin{aligned}
 P_\mu P^\mu &= g_{\mu\nu} P^{\nu'} P^{\mu'} = g_{\mu\nu} A^\nu P^\alpha A^\mu P^\beta \\
 &= g_{\mu\nu} A^\nu A^\mu P^\alpha P^\beta = g_{\alpha\beta} P^\alpha P^\beta \\
 &= P_\alpha P^\alpha
 \end{aligned} \tag{8.8}$$

As a result the quantity  $P_\mu P^\mu$  transforms as a Lorentz scalar with the single particle value:

$$\begin{aligned}
 P_\mu P^\mu &= (E, -\vec{P}) \begin{pmatrix} E \\ \vec{P} \end{pmatrix} \\
 &= E^2 - P^2 \\
 &= \left( \sqrt{P^2 + M^2} \right)^2 - P^2 \\
 &= M^2
 \end{aligned} \tag{8.9}$$

This quantity  $M$  is denoted as the invariant mass of the parent particle, and hence the physical mass of the particle irrespective of chosen reference frame.

This invariant mass can be reconstructed from just the knowledge of the energy and momentum parameters of the daughter particles of the decay in the laboratory reference frame. In the case of a two-body decay, this invariant mass reconstruction takes the standard form shown in Eq. (8.10) with the mass of the decay particles species labeled as  $m_1$  and  $m_2$ .

$$\begin{aligned}
 M^2 &= P_\mu P^\mu = (\vec{P}_1 + \vec{P}_2)_\mu (\vec{P}_1 + \vec{P}_2)^\mu \\
 &= (E_1 + E_2)^2 - (\vec{P}_1 + \vec{P}_2)^2 \\
 &= E_1^2 + E_2^2 - P_1^2 - P_2^2 + 2E_1 E_2 - 2\vec{P}_1 \cdot \vec{P}_2 \\
 &= m_1^2 + m_2^2 + 2E_1 E_2 - 2|P_1||P_2| \cos \theta_{12}
 \end{aligned} \tag{8.10}$$

In this formulation  $\theta_{12}$  is the angle between the decay tracks. The analysis can similarly be extended to the case of an N-body final state, where again a set of  $\{m_i\}$  particle species exist with energy/momentum parameters  $\{E_i, \vec{P}_i\}$

$$\begin{aligned}
M^2 &= \left( \sum_{i=1}^N \vec{P}_i \right)_\mu \left( \sum_{i=1}^N \vec{P}_i \right)^\mu \\
&= \left( \sum_{i=1}^N E_i \right)^2 - \left( \sum_{i=1}^N \vec{P}_i \right)^2 \\
&= \sum_{i=1}^N E_i^2 + \sum_{i=1}^N \sum_{j \neq i}^N E_i E_j - \sum_{i=1}^N P_i^2 - \sum_{i=1}^N \sum_{j \neq i}^N \vec{P}_i \cdot \vec{P}_j \\
&= \sum_{i=1}^N m_i^2 + \sum_{i=1}^N \sum_{j \neq i}^N E_i E_j - \sum_{i=1}^N \sum_{j \neq i}^N |P_i| |P_j| \cos \theta_{ij}
\end{aligned} \tag{8.11}$$

We can further simplify the expression by expressing the cosine of the angle between any of the track pairs in terms of their direction cosines.

$$\begin{aligned}
\cos \theta_{ij} &= \sum_{k=1}^D \cos \phi_{x_k} \cos \psi_{x_k} \\
&= \sum_{k=1}^D a_{ik} a_{jk}
\end{aligned} \tag{8.12}$$

In D-dimensions with the usual Euclidean metric the explicit symmetry in the direction cosines further allows the double summations to be reduced to order  $(N^2 - N)/2$ . With this modification Eq. (8.11) becomes:

$$M^2 = \sum_{i=1}^N m_i^2 + 2 \sum_{i=1}^N \sum_{j>i}^N \left( E_i E_j - |P_i| |P_j| \sum_{k=1}^D a_{ik} a_{jk} \right) \tag{8.13}$$

This form of Eq. (8.11) is of use in that it depends only on parameters that are functions of a single particle and are readily obtainable in the laboratory frame of the decay. In the case that partial reconstructions are performed utilizing less than

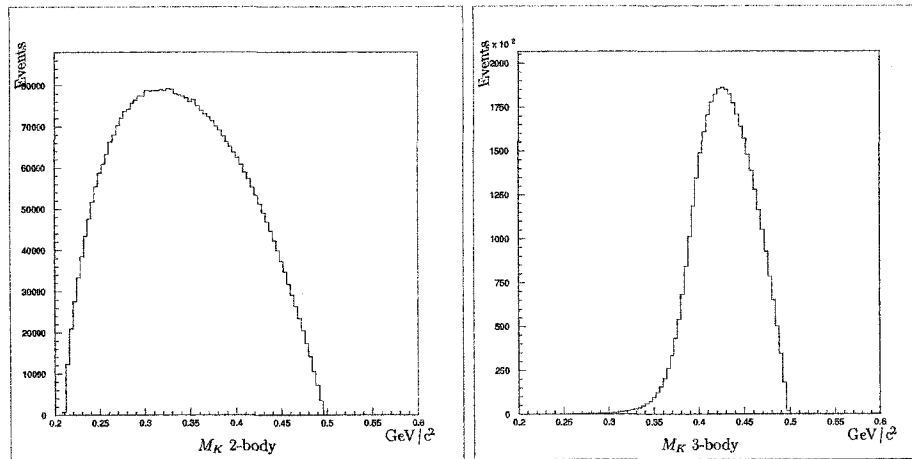


the full number of true decay tracks, higher order reconstructions may be obtained through a simple recursion relation:

$$M_{n+1} = M_n + m_{(n+1)} + 2 \sum_{i=1}^n \left( E_i E_{(n+1)} - |P_i| |P_{(n+1)}| \sum_{k=1}^D a_{ik} a_{(n+1)k} \right) \quad (8.14)$$

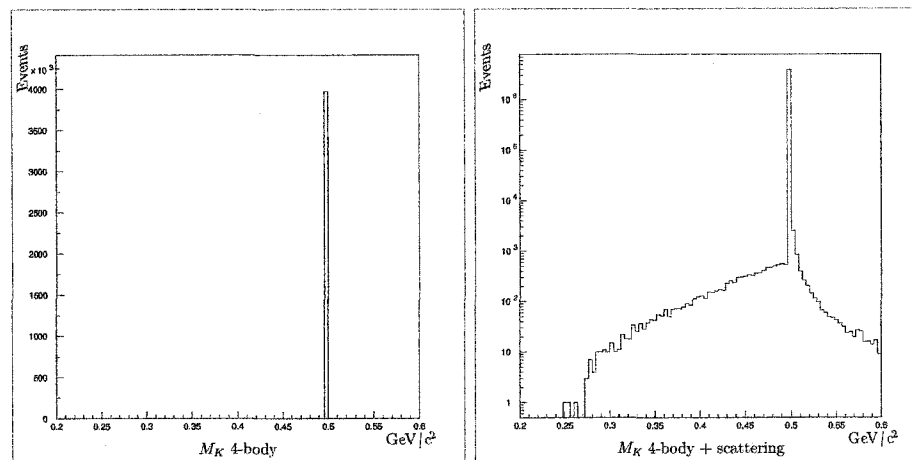
The consequence of the recursion relation is that the  $N$  body reconstruction of  $M^2$  is always greater than or equal to the  $(N-1)$  body reconstruction of the same particle. The  $m$ -body ( $m < N$ ) reconstruction then is always an explicit lower bound on the invariant mass of the parent particle. Calculations sensitive to such a bound can thus utilize a lower order reconstruction without loss of acceptance or when additional tracking information is not available.

In the case of the  $K_L^0 \rightarrow \mu^+ \mu^- e^+ e^-$  analysis, two body invariant mass reconstructions were performed using the  $\mu^+ \mu^-$  pairs in the manner of Eq. (8.10) with higher order reconstructions following the prescriptions of Eq. (8.13) and (8.14). Initial invariant mass reconstruction using the  $e^+ e^-$  pairs was not performed due to the lack of  $e^+ e^-$  track acceptance within the requirements of the E871 spectrometer and trigger. Invariant mass under the  $e^+ e^-$  hypothesis was also omitted from the analysis due to the endpoint of the  $M_{e^- e^+}$  invariant mass at 474.7 MeV/ $c^2$ . The effects of these varying reconstruction methods are shown in Fig. 8.1 using simulated data to obtain the raw reconstruction profiles. Fig. 8.2 shows the reconstruction profiles with the additional restrictions of muon track acceptance and event triggering. The reconstruction profiles exclude the 463MeV lower limit on invariant mass, but demonstrate the high invariant mass bias that the detector geometry and spectrometer settings have upon the sample set.



(a) Two-body invariant mass reconstruction

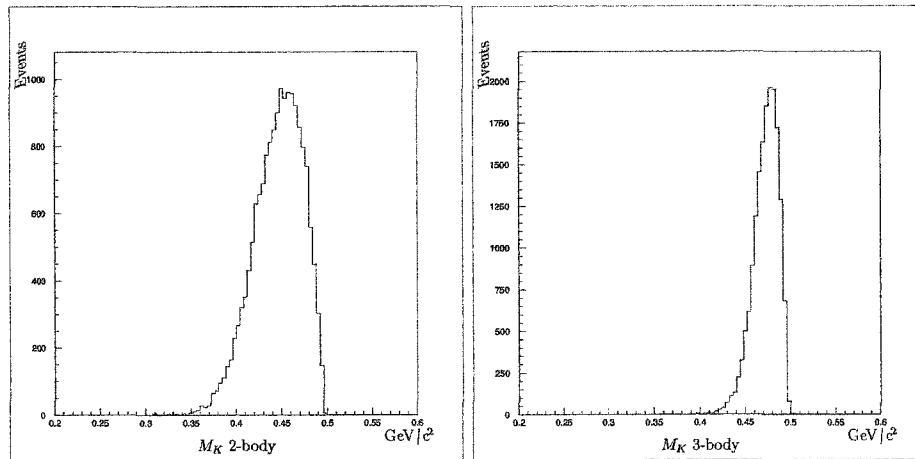
(b) Three-body invariant mass reconstruction



(c) Four-body invariant mass reconstruction

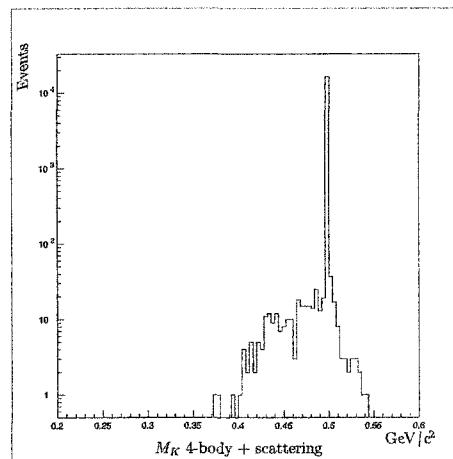
(d) Four-body invariant mass reconstruction with low energy multiple scattering effects

FIG. 8.1: Effects of multi-body invariant mass reconstructions of  $K_L^0 \rightarrow \mu^+ \mu^- e^+ e^-$  events without full geometric acceptance restrictions. Figure 8.1(d) shows the explicit smearing of the invariant mass peak due to multiple scattering of low energy electron tracks



(a) E871 accepted two-body invariant mass reconstruction

(b) E871 accepted three-body invariant mass reconstruction



(c) E871 accepted four-body invariant mass reconstruction with low energy multiple scattering effects

FIG. 8.2: Effects of multi-body invariant mass reconstructions of  $K_L^0 \rightarrow \mu^+ \mu^- e^+ e^-$  events with geometric acceptance restrictions imposed upon the muon tracks. Figure 8.2(c) again shows the explicit smearing of the invariant mass peak due to multiple scattering effects.

### 8.1.2 Vertex Definition

Computation of the invariant mass does not rely upon any knowledge of the spatial location at which the primary decay occurred. As a result of this, computation of the primary decay vertex recovers information independent of the energy and momentum parameters of the reaction. In particular, reconstruction of the spatial vertex allows for correlation of the decay point with the neutral beam profile and for association of spectrometer tracks with a hypothesized decay chain.

Reconstruction of the primary event vertex is accomplished by pairwise consideration of valid spectrometer tracks. In the case of  $K_L^0 \rightarrow \mu^+ \mu^- e^+ e^-$  vertices are reconstructed using  $\mu^+$  and  $\mu^-$  tracks which satisfy the L1 trigger requirements and additional track fitting algorithms referred to as the “FT” and “QT” fitters. Tracks of these types are projected upstream, from the first two sets of straw drift chambers, into the evacuated decay region. For events in which the particles originated from a common decay, the projected tracks should have a common point of intersection which coincides with the neutral beam profile. The intersection point is denoted as the event vertex  $X(t, x, y, z)$ . The geometric distribution of these points is shown in Fig. 8.3 for the X and Y vertex profiles. The event time can be calculated from the hit times in the various fast detectors and knowledge of the particle momentum.

Due primarily to chamber resolution and multiple scattering of low energy particles, the three dimensional intersection of the charged tracks used to reconstruct the vertex position is seldom exact. Valid spatial reconstructions are evaluated by the closest distance that two track trajectories come to each other. The distance of closest approach (doca) figure of merit is defined in the case of two tracks by the length of the line connecting the tracks at perigee as shown in Fig. 8.4. The computation of this figure of merit is discussed in detail in section 8.2 with regard to both the track and stub related situations that were encountered in the analysis

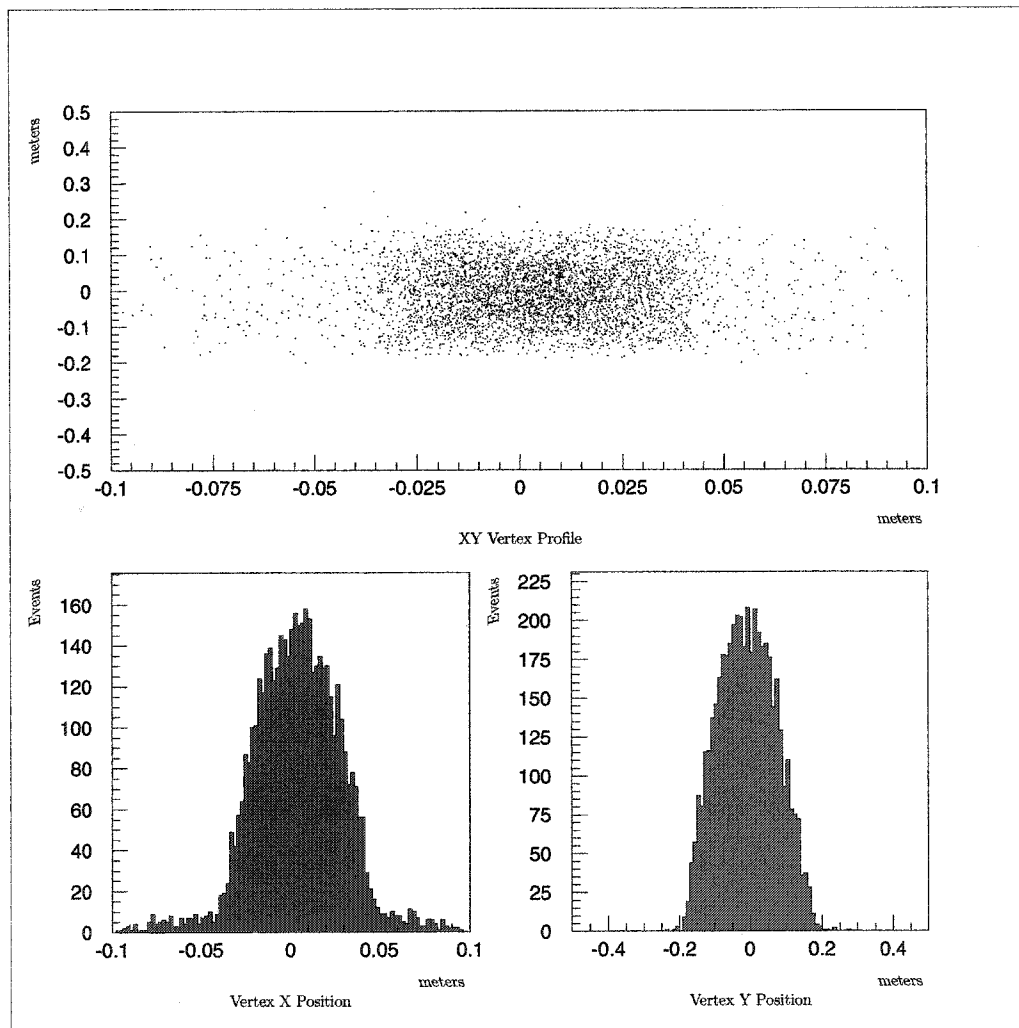


FIG. 8.3: XY Vertex distribution based upon  $\mu^+\mu^-$  track reconstructions under the QT fitting algorithm

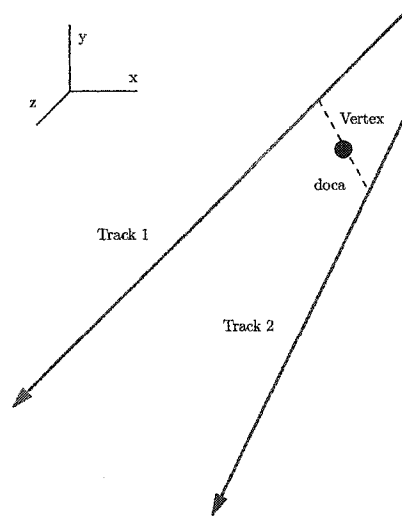


FIG. 8.4: Vertex definition based upon distance of closest approach (doCA) of two tracks in three dimensions

of the  $K_L^0 \rightarrow \mu^+ \mu^- e^+ e^-$  decay.

### 8.1.3 Transverse Momentum and Collinearity

Once the vertex position is established, a second invariant can be constructed from the momentum vectors of the primary decay products. The line between the production target and the computed position of the decay vertex form the boost axis for the transformation between the CM frame of the parent particle and the laboratory frame in which the decay products are measured. While the magnitude of the Lorentz boost is not known, the components transverse to the boost axis are unaffected by the transformation matrix of the form of Eq. (8.2) where the  $x_1$  direction is taken along the axis defined by the line between production target and vertex. In this manner the sum of the momenta for the primary reconstruction tracks,  $p_1 + p_2$  can be computed, and the angle that the momentum sum forms with the boost axis is denoted as the collinearity angle  $\Theta$  as shown in Fig. 8.5. The

transverse momentum for the reconstruction can be trivially computed as

$$p_{\perp} = (p_1 + p_2) \sin \Theta \quad (8.15)$$

Because the tracks used for vertex reconstruction are approximately coplanar, the transverse momentum which lies in the decay plane and collinearity angle computed in this manner are associated with the primary decay plane. Similarly the transverse components for each of the individual particle tracks can be computed through projection onto the boost coordinates and associated also with the decay plane.

Secondary tracks and partial tracking stubs are assigned a collinearity angle based upon their projections into the decay volume. Since partial tracking stubs may not have a valid momentum measurement recorded by passage through the spectrometer magnets, they cannot be assigned a proper transverse momentum measurement through direct measurement. The collinearity angle serves as a surrogate, allowing for determination of events with little to no transverse angular displacement to be associated with the decay planes. Even for the low transverse momentum  $e^+e^-$  pairs expected from  $K_L^0 \rightarrow \mu^+\mu^-e^+e^-$ , the collinearity of the  $\mu^+\mu^-$  reconstruction plane and the collinearity of the electron tracks are found to form an angular correlation that assists in determination of pair associations with computed vertices.

Uncertainties in the collinearity angle arise from the projection of the line from target to computed vertex. The exact position at which the  $K_L^0$  originated in the target is unknown and as such the z position of the target origin receives an uncertainty of  $\pm 63.5mm$ . The uncertainty in the x and y directions results from the cross sectional area of the production target resulting in uncertainties of  $\pm 1.575mm$  and  $\pm 1.27mm$ , respectively. These correspond to maximum angular uncertainties in the collinearity angle of  $157.5 \mu rad$  in x,  $127 \mu rad$  in y as computed for a vertex at the upstream end of the decay tank.

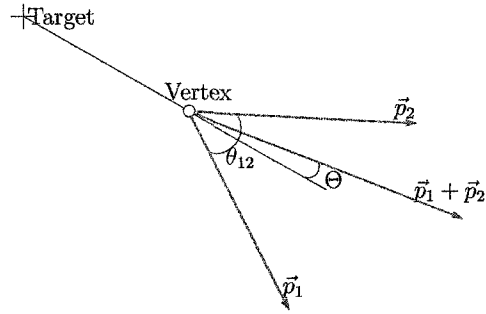


FIG. 8.5: Definition of the collinearity angle  $\Theta$  based upon momentum sum of the primary track pair and the line between the calculated vertex and the production target [44]

While the collinearity angle  $\Theta$  is not invariant, the transverse momentum of the decay is invariant with regard to the full decay process and a conserved quantity. As a result the muon momentum sum  $p_{\mu_1} + p_{\mu_2}$  and collinearity angle  $\Theta_{\mu}$  are balanced by the electron momentum sum  $p_{e_1} + p_{e_2}$  and the electron collinearity angle  $\Theta_e$  as shown in Fig. 8.6. From the diagram the laboratory momentum of the electron pair can be determined from the angular distributions and the measured momentum of the muons. The transverse components of the momentum are conserved such that  $\vec{P}_{\mu\perp} + \vec{P}_{e\perp} = 0$ , yielding the set of relations:

$$P_{\perp} = |\vec{P}_{\mu}| \sin \Theta_{\mu} \quad (8.16)$$

$$P_{\perp} = |\vec{P}_e| \sin \Theta_e \quad (8.17)$$

$$P_e = p_{e_1} + p_{e_2} = |\vec{P}_{\mu}| \frac{\sin \Theta_{\mu}}{\sin \Theta_e} \quad (8.18)$$

This relation indirectly recovers the magnitude of the momentum of the soft electron/positron pair. The asymmetry of momentum within the  $e^+e^-$  pair is determined from the distribution shown in Fig. 8.7. From the figure it is clear that the phase space is dominated by  $e^+e^-$  pairs for which the momentum is shared in an



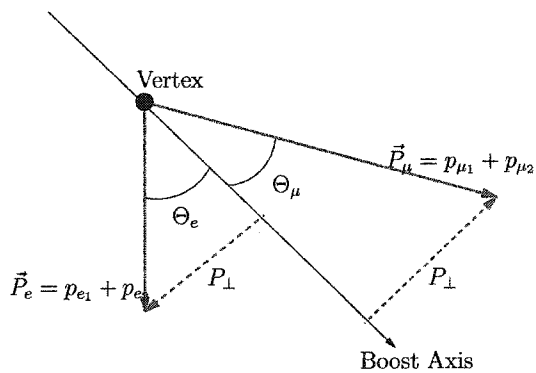


FIG. 8.6: Muon pair transverse momenta to electron pair transverse momenta sum relation through the collinearity angles  $\Theta_\mu$  and  $\Theta_e$

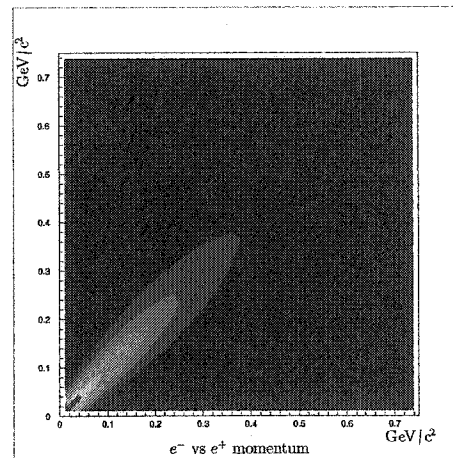


FIG. 8.7:  $e^-$  to  $e^+$  low energy momentum asymmetries for  $K_L^0 \rightarrow \mu^+ \mu^- e^+ e^-$

approximately equal fashion between the particles.

$$p_{e1} \approx p_{e2} \quad (8.19)$$

From this expression and Eq. (8.18) the momentum of the individual electron tracks can be approximately expressed as:

$$p_{e1,2} \approx \frac{1}{2} P_e = \frac{|\vec{P}_\mu| \sin \Theta_\mu}{2 \sin \Theta_e} \quad (8.20)$$

In this manner the momentum of soft  $e^+e^-$  pairs which do not receive a successful momentum measurement in D02 or D03 can be approximately recovered. Higher order invariant mass reconstructions based upon these data are discussed in section 8.4.1.

## 8.2 Distance of Closest Approach (DOCA)

After identification of possible hit points in a tracking chamber, one or more potential tracking paths can be constructed using a series of pattern recognition algorithms. Track and stub construction methods range from exhaustive combinatorial construction utilizing all available points to more sophisticated methods utilizing clustering approaches either alone or in conjunction with weighting functions based on the different probability distributions and wire response schemes. After initial pattern recognition and track construction, a preliminary set  $\{S\}$  of particle tracks through the active regions of the detectors is available to the analysis.

The set  $\{S\}$  is taken to be composed of two subsets, one  $S_{real}$  which represents tracks generated by real (physical) processes of interest, and  $S_{noise}$  generated by random noise or processes not of interest to the analysis. To separate these two subsets from the parent population a figure of merit is devised based on the primary decay vertex. The primary figure of merit used in vertex identification and track filtering is referred to as the “Distance of Closest Approach” (DOCA) between the sets of tracks and with the hypothesized vertex position.

Utilization of the DOCA, as the primary figure of merit in determining track association and vertex quality is justified by considering the initial physical process to occur at a definite spatial and temporal point  $\mathbf{X}^\mu$  as discussed in section 8.1.2. Each of the tracks in the signal set  $S_{real}$  should lie on a trajectory which passes through the vertex point at the same time index. In contrast the tracks attributed to noise or unrelated physical events should not pass through the vertex point. The metric measuring the proximity of the tracks to the vertex point is taken as the quality of the association. Due to experimental uncertainties we expect each signal track to deviate from perfect intersection with the vertex by an error  $\delta x_i$  in each coordinate. The sum of the squares of these residuals forms the standard Euclidean

metric and can be used as a measure of the absolute deviation. At the point where this deviation is minimized it corresponds to the DOCA between the vertex and tracks. Separation of the populations  $S_{real}$  and  $S_{noise}$  is achieved by placing a cut on the DOCA value.

The difficulty with this approach is in quantifying the methods for correctly computing the DOCA between different combinations of particle tracks and vertex points while including additional corrections for event time. The following sections discuss in detail the different methods and corrections used in computing the DOCA values for the primary vertex, primary muon tracks and for the partial tracking stubs left by the  $e^+e^-$  pairs.

### 8.2.1 Track to Track

Valid events used in the analysis were required to have two muon tracks that traversed the spectrometer and had appropriate parallelism in the trigger scintillators. These two muon tracks were used to compute the position of the event vertex by calculating the position at which the tracks when projected into the decay volume were at their closest point. The midpoint of the line segment connecting the two tracks at their closest point was defined as the vertex for the event and the DOCA value for the vertex computed as the sum of the DOCA values that each track had to the vertex.

In contrast to calculating the DOCA between a track and a fixed point, computation of the track to track DOCA points is much more difficult. The trajectory for each track's projection into the decay volume is defined by its hit positions in SDC2 and SDC1 which result in the base point and direction cosine information for each track. Each track can be represented parametrically by the pathlength variable  $S_j$

representing the distance of the current point from the base point.

$$\begin{aligned}(x'_{\mu_1})_i &= (x_{\mu_1})_i - a_i \mathcal{S}_1 \\ (x'_{\mu_2})_i &= (x_{\mu_2})_i - b_i \mathcal{S}_2\end{aligned}\tag{8.21}$$

The DOCA condition is found by simultaneously minimizing the metric between two points on the line with respect to the parameters  $\mathcal{S}$ .

$$\mathcal{S}_1 = \frac{\sum_i a_i \cdot ((x_{\mu_1})_i - (x_{\mu_2})_i)}{1 - (\sum_i a_i b_i)^2} - \frac{\sum_i b_i \cdot ((x_{\mu_1})_i - (x_{\mu_2})_i)}{1 - (\sum_i a_i b_i)^2}\tag{8.22}$$

$$\mathcal{S}_2 = \frac{\sum_i b_i \cdot ((x_{\mu_1})_i - (x_{\mu_2})_i)}{1 - (\sum_i a_i b_i)^2} - \frac{\sum_i a_i \cdot ((x_{\mu_1})_i - (x_{\mu_2})_i)}{1 - (\sum_i a_i b_i)^2}\tag{8.23}$$

The points  $x'_{\mu_1}$  and  $x'_{\mu_2}$  at which the distance of closest approach actually occurs are found by substituting the expressions for the pathlength as found in Eq. (8.22) into Eq. (8.21).

$$(x'_{\mu_1})_i = (x_{\mu_1})_i - a_i \left[ \frac{\sum_i a_i \cdot ((x_{\mu_1})_i - (x_{\mu_2})_i)}{1 - (\sum_i a_i b_i)^2} - \frac{\sum_i b_i \cdot ((x_{\mu_1})_i - (x_{\mu_2})_i)}{1 - (\sum_i a_i b_i)^2} \right]\tag{8.24}$$

$$(x'_{\mu_2})_i = (x_{\mu_2})_i - b_i \left[ \frac{\sum_i b_i \cdot ((x_{\mu_1})_i - (x_{\mu_2})_i)}{1 - (\sum_i a_i b_i)^2} - \frac{\sum_i a_i \cdot ((x_{\mu_1})_i - (x_{\mu_2})_i)}{1 - (\sum_i a_i b_i)^2} \right]\tag{8.25}$$

The DOCA distance is computed

$$\mathcal{D} = \sqrt{\sum_i ((x'_{\mu_1})_i - (x'_{\mu_2})_i)^2}\tag{8.26}$$

## 8.2.2 Vertex Position

The vertex position, when computed from the track to track DOCA method, is taken to be the midpoint of the line connecting the points  $x'_{\mu_1}$  and  $x'_{\mu_2}$  as shown

in Fig. 8.4. In this manner the vertex location can be expressed as:

$$X_i = \frac{(x'_{\mu_1})_i - (x'_{\mu_2})_i}{2} \quad (8.27)$$

The values of  $x_{\mu_i}$  are obtained from the expressions in Eq. (8.24) and (8.25)

### 8.2.3 Track to Point

The most basic geometry for which the DOCA was computed was that of a single track to a fixed spatial point. This geometry corresponded to the method by which the distance between all secondary tracks and partial tracking to the primary vertex were computed. The particle track is denoted as the vector  $\vec{x}$  and defined by a based point  $x_i$  which corresponds to the center of the hit cluster in SDC2 and a set of direction cosines  $\{a_i\}$  which are computed using the hit cluster in SDC1. The vertex position is defined as the point  $V = \{v_x, v_y, v_z\}$ .

With this formulation, the distance between the vertex and any point on the line can be expressed by the standard Euclidean metric.

$$\mathcal{M}(x', V) = \sqrt{\sum_i (x'_i - v_i)^2} \quad (8.28)$$

The point  $x'$  on the line is defined by the set of parametric equations using the path length  $\mathcal{S}$  as the defining parameter:

$$\begin{aligned} x'_i &= (x_i - a_i \mathcal{S}) \\ &\vdots \\ x'_n &= (x_n - a_n \mathcal{S}) \end{aligned} \quad (8.29)$$

In this manner Eq. (8.28) can be rewritten as:

$$\mathcal{M}(x', V) = \sqrt{\sum_i ((x_i - a_i \mathcal{S}) - v_i)^2} \quad (8.30)$$

With the metric definition of Eq. (8.30) it is possible to solve for the exact DOCA. Instead of solving for the DOCA in full form there are a series of approximations that can be made which simplifies the calculations and are used in the analysis code to save processing time during the early stages of filtering the data. It is also used as a check and to remove ambiguities that can arise in the full method. These methods are considered in the next section.

### 8.2.4 Punctured Plane

The simplest approximation to the DOCA is to approximate the distance of closest approach by the distance between the vertex point and the point at which the track “punctures” a given spatial plane. The puncture point can be computed by first computing the distance of the track’s base point from the plane of interest. The plane is denoted by  $\mathcal{P}_{ij}(V_k)$  and is defined to be the surface given by the  $i^{th}$  and  $j^{th}$  coordinate axis passing through the vertex point  $V$ , whose  $k^{th}$  component is  $V_k$ . This then generalizes to any plane by appropriate translation and rotation. For the purposes of the analysis the puncture plane was taken as the plane defined by the x and y coordinate axis at the specified z position of the vertex. Using this formulation the distance between the plane and the track base point is just the z axis distance between the two.

$$d(x, \mathcal{P}_{ij}(V_k)) = |x_k - V_k| \quad (8.31)$$

The coordinates of the point of intersection between the track and the plane are given by:

$$\begin{aligned}x'_i &= x_i + a_i|x_k - V_k|d(x_1, \mathcal{P}_{ij}(p_k)) \\x'_k &= V_k\end{aligned}\tag{8.32}$$

The approximate DOCA is then found by computing the distance between the vertex  $V$  and the point of intersection  $x'$  as defined in Eq. (8.32). Expressed in this manner the DOCA becomes:

$$\begin{aligned}\mathcal{D} &= \sqrt{\sum_i (x'_i - V_i)^2} \\ &= \sqrt{\sum_{i \neq k} (x_i - V_i + a_i|x_k - V_k|)^2}\end{aligned}\tag{8.33}$$

Event time distance is computed between the track's base point and the intersection point with the plane. The particles are relativistic in nature so that  $\beta \approx 1$ . The time difference  $\Delta t$  between the points is then found from:

$$\Delta t = t - t' = \frac{\mathcal{M}(x, x')}{c}\tag{8.34}$$

The punctured plane method exhibits an advantage over the full minimization methods discussed in section 8.2.6 not only due to its speed, but because the approximation is an explicit upper bound on the true value of the DOCA. It can be shown that  $\mathcal{D}_{approx} > \mathcal{D}_{min}$ ; as a result using the value of  $\mathcal{D}_{approx}$  obtained from Eq. (8.33) as maximum value for a cut parameter does not affect the total acceptance of real events.

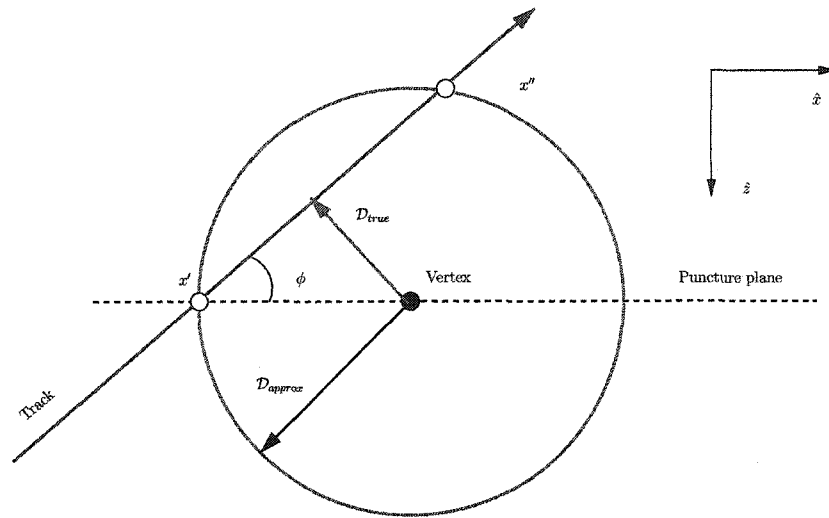


FIG. 8.8: Geometry of the secant correction to the DOCA value obtained from the punctured plane method.

### 8.2.5 Secant Correction

The punctured plane approximation to the DOCA calculated in Eq. (8.33) can be improved upon by considering the angle at which the reconstructed track intersects with the defined plane of interest. Since the approximate DOCA serves as an explicit upper bound on the true DOCA value, the locus of all points whose distance from the vertex is less than or equal to the approximate DOCA value forms a sphere. If the reconstructed track intersects the chosen plane at a non right-angle then the track projections forms a secant across the interior of the sphere as shown in Fig. 8.8. The true position of the DOCA lies along the track at the midpoint of the secant. From this construction the true DOCA,  $\mathcal{D}_{true}$  is given by:

$$\mathcal{D}_{true} = \sqrt{\mathcal{D}_{approx}^2 - \frac{1}{4}\mathcal{M}(x', x'')^2} \quad (8.35)$$



In order to use this expression, the length of the secant,  $\mathcal{M}(x', x'')$  needs to be calculated. The length of the secant can be expressed as

$$\mathcal{M}(x', x'')^2 = 2D_{approx} \cos \phi \quad (8.36)$$

Substitution of this expression leads to the simple expression for the exact DOCA in terms of the angle  $\phi$ :

$$\mathcal{D}_{true} = \mathcal{D}_{approx} \sin \phi \quad (8.37)$$

The track angle  $\phi$  is found by rotation of the coordinate system about the x-axis by an angle  $-\theta_y$  corresponding to the direction cosine  $a_y$  for the track. In this manner the track is rotated into xz-plane and corresponds to Fig. 8.8. The angle  $\phi$  is then given by:

$$\phi = \cos^{-1} a_x \quad (8.38)$$

The true vertex DOCA is then:

$$\begin{aligned} \mathcal{D}_{true} &= \mathcal{D}_{approx} \sin(\cos^{-1} a_x) \\ &= \mathcal{D}_{approx} \sqrt{1 - a_x^2} \end{aligned} \quad (8.39)$$

The value of the secant correction is that it allows for the exact DOCA to be obtained from prior results with knowledge only of the direction cosines of the tracks. In this manner it is possible to refine calculations at successive steps in the analysis.



only one minimization over the parameter  $\mathcal{S}$

$$\begin{aligned}
\frac{\partial}{\partial \mathcal{S}} \mathcal{D} &= \frac{\partial}{\partial \mathcal{S}} \sqrt{\sum_i (x_i - a_i \mathcal{S} - V_i)^2} \\
&= \frac{\partial}{\partial \mathcal{S}} \sqrt{\sum_i (a_i^2 \mathcal{S}^2 + x_i^2 + V_i^2 - 2x_i V_i + 2V_i a_i \mathcal{S} - 2x_i a_i \mathcal{S})} \\
&= 0
\end{aligned} \tag{8.42}$$

Since all coordinates are explicitly real the square root function is monotonically increasing, it suffices to minimize just the argument of the function. This leads to the specialized minimization condition:

$$\begin{aligned}
\frac{\partial}{\partial \mathcal{S}} \mathcal{D}^2 &= \frac{\partial}{\partial \mathcal{S}} \left( \sum_i (a_i^2 \mathcal{S}^2 + x_i^2 + V_i^2 - 2x_i V_i + 2a_i \mathcal{S} (V_i - x_i)) \right) \\
&= \sum_i (2a_i^2 \mathcal{S} + 2a_i (V_i - x_i)) \\
&= 0,
\end{aligned} \tag{8.43}$$

giving:

$$\mathcal{S}_{doca} = \frac{\sum_i a_i (x_i - V_i)}{\sum_i a_i^2} \tag{8.44}$$

The value of the DOCA is:

$$\mathcal{D}_{min} = \sqrt{\sum_i \left( x_i - V_i - \frac{\sum_j a_j a_j (x_j - V_j)}{\sum_j a_j^2} \right)^2} \tag{8.45}$$

The closest approach occurs at the coordinate point  $\bar{x}'$  given by:

$$\begin{aligned} x'_i &= \left( x_i - a_i \frac{\sum_j a_j (x_j - V_j)}{\sum_j a_j^2} \right) \\ &\vdots \\ x'_n &= \left( x_n - a_n \frac{\sum_j a_j (x_j - V_j)}{\sum_j a_j^2} \right) \end{aligned} \quad (8.46)$$

The time correction for the DOCA point found by utilizing the path length of Eq. (8.44):

$$\Delta t = t - t' = \frac{1}{c} \left( \frac{\sum_i a_i (x_i - V_i)}{\sum_i a_i^2} \right) \quad (8.47)$$

For the final analysis of all vertex and stub quality, DOCA values were calculated from Eq. (8.45) and used in conjunction with the time correction of Eq. (8.47).

### 8.3 Partial Tracking Stubs

The E871 track reconstruction algorithms were designed to identify hits in the straw drift chambers and from those hits define candidate particle tracks that traversed the spectrometer and were momentum analyzed in the spectrometer magnets. Particle trajectories which did not fully traverse the forward spectrometer or did not impart sufficient tracking information in the sensitive regions of the magnetic spectrometer were subjected to a separate series of reconstruction routines and analysis cuts designed to recover all possible tracking and event reconstruction information that was available.

Particle trajectories which left valid tracking information only in the forward straw drift chambers, SDC1 and SDC2, were classed as partial tracking *stubs* and used extensively in the analysis of the  $e^+e^-$  pairs arising from the decay  $K_L^0 \rightarrow$

$\mu^+\mu^-e^+e^-$ . The momentum for this class of trajectories is not directly measured, but instead inferred from primary vertex and muon pair information. All other quantities were derived from the hit clusters and associated event characteristics

### 8.3.1 Stub Recognition

Partial tracking stub recognition and identification was performed after both general pattern recognition and tracking fitting. The recognition routines were run only on events that satisfied primary vertex and track quality cuts sufficient to place the candidate event in the  $K_L^0 \rightarrow \mu^+\mu^-$  data summary tapes. In order to maximize overall efficiency while also minimizing event processing time, two algorithmically different approaches to identifying partial tracks were explored. Each method was based on deriving hit clusters in the X and Y planes of the straw drift chambers and then matching valid clusters with other clusters in the adjacent chamber. The methods differed in the search method employed and the resulting combinatorics involved in the resulting candidate set.

#### Cluster to Vertex Search Path

To minimize computation time, the first method of partial track identification employed a directed search algorithm that only considered hit cluster matching along paths defined by external vertex information. In this method hit clusters consisting of at most five wires in the SDC2X and SDC2Y detector viewers were considered. The center of each hit cluster was determined through a simple averaging of wire positions with appropriate drift time ambiguities, and a cut was placed on the total cluster size. For each detector view, X and Y, the central hit position of the cluster was paired with the primary  $\mu^+\mu^-$  event vertex. The resulting track slope was computed along with appropriate direction cosines. The projected intersection of

the computed vertex to SDC2 hit line with the corresponding view of SDC1 was recorded as the projected candidate hit position. The first straw chamber planes were then scanned for valid hit clusters within  $\Delta x = \pm 0.006\text{m}$ ,  $\Delta y = \pm 0.00125\text{m}$  of the projected hit. If a match was found, the resulting X or Y segment was paired with corresponding Y or X segment to form an XY “stub” for which the direction cosines and DOCA to the primary vertex could be computed.

Due to the restricted search path that was allowed when cluster matching, this method was able to quickly identify simple stub events. Initial cuts in stub quality and correlation values were based on the data gathered through this method. These initial cut values were used to set input parameters for the more complex full chamber search routine.

The cluster to vertex search path approach was not used in the final analysis of the data due to its high inefficiency in correctly pairing closely packed hit clusters and events whose trajectories differed from the search path due to low energy multiple scattering.

### **Cluster to Cluster Exhaustive Search**

The second method of partial track identification was developed to provide a more comprehensive and efficient detection method with improved matching criteria that could simultaneously deal correctly with low energy multiple scattering. In this method no information is used regarding the primary vertex so as to prevent inadvertent correlation biasing of the stub sample. Instead the only outside derived data used are the positions in SDC1/SDC2 and PATREC calculated hit cluster centers. These hit positions are used solely as a veto mask to prevent stub matching results that correspond to the already identified primary tracks.

The exhaustive cluster matching algorithm was initiated at the STAGE9 phase of the off-line analysis after primary track re-fitting with the QFT fitting methods

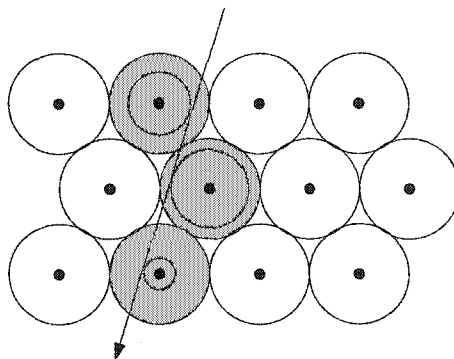


FIG. 8.9: Local track slope is computed from a least squares fit to the PATREC derived hit cluster positions.

and correction of derived wire hits and times. All views of the first two straw drift chambers were first searched for hit clusters satisfying the same criteria as the primary track clusters. Each cluster was then fit to a series of local track slopes based upon the shape of the hit cluster and a weighted least squares fit to the hit line trajectory as show in Fig. 8.9.

Segments were formed by matching cluster positions in SDC2 forward to cluster positions in SDC1 using solid angle limited search paths defined by local track slope with appropriate ambiguities. All approximate cluster to cluster matches were re-fit to provide corrected hit positions in both SDC1 and SDC2 for each track segment. Exhaustive combinatorial matching of all identified track segments was considered to form XY track stubs. The matching ambiguities for an example event with two real electron tracks is shown in Fig. 8.10

All of the valid XY track stubs formed through the matching process were stored and sorted according to a simplified computation of the DOCA value between the candidate track stub and the primary  $\mu^+\mu^-$  vertex. Since for noisy events in excess of 1000 possible ambiguity solutions can be generated from the combinatorial matching procedure, only the first 1024 solutions were considered in this manner for sorting and for further analysis.

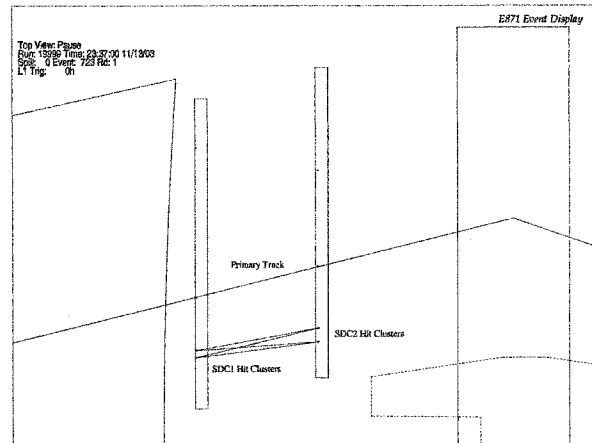


FIG. 8.10: Matching of all possible cluster combinations based upon local track slopes between SDC1 and SDC2.

The sorted list of candidate XY stubs was analyzed to determine the degree to which each stub correlated to the primary vertex. The best 32 candidates determined by the sort ordering based on the simple vertex DOCA were reanalyzed using the more complete full form track to point DOCA calculation. At the same time the point of closest approach was likewise recomputed. The resulting improved list was resorted according to the exact DOCA computation. This list was then further analyzed by the correlation and selection criteria which was established to distinguish between event-associated partial electron tracks and partial tracks from background and detector noise. The computed DOCA values for these signal and noise populations are shown in Fig. 8.11

### 8.3.2 Decay Plane Correlation

The  $K_L^0 \rightarrow \mu^+ \mu^- e^+ e^-$  decay when examined in the laboratory frame of reference, exhibits a distinct kinematic profile which can distinguish it from the other multi body decay streams being examined as backgrounds to the event signal. While



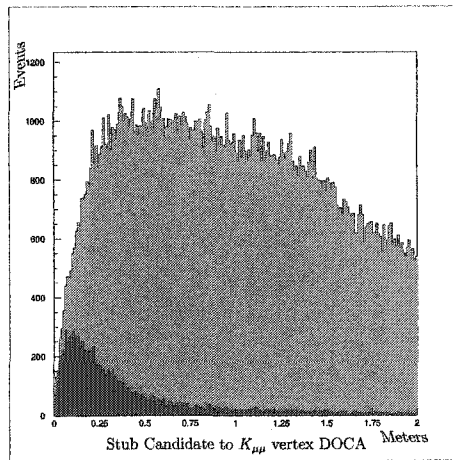


FIG. 8.11: Computed DOCA between SDC1/SDC2 XY partial tracking stub and the primary event vertex. Events in green represent all ambiguity solutions, events in red represent the best stub singlet or best stub pairs.

the final state of the decay results in a four-body formfactor modified phase space, the like-flavor lepton pairs arising from the intermediate state virtual two  $\gamma$ 's retain pairwise correlations. The division of the available invariant mass favoring the  $\mu^+\mu^-$  pair combined with the previously discussed formfactors results in an extremely soft set of  $e^+e^-$  pair combinations. When the decay is Lorentz boosted into the laboratory frame, the resulting lepton pairs are used to define a series of decay planes based on angular distribution of tracks emerging from the event vertex.

Since the two muon tracks encompass the majority of the event's momentum and invariant mass, we always denote this as the primary decay plane for the event. The plane is defined by the standard right handed cross product of the two best muon tracks found through the PATREC and QT algorithms. The plane is oriented by choosing the cross product to be taken from the negatively charged muon (beam right track) to the positively charged muon (beam left track). This orientation of the decay plane results in alignment of the normal to the surface in the positive y direction. This orientation of the primary  $K_{\mu\mu}$  decay plane is shown in Fig. 8.12. The normal to the plane is calculated and normalized to provide a set of direction cosines

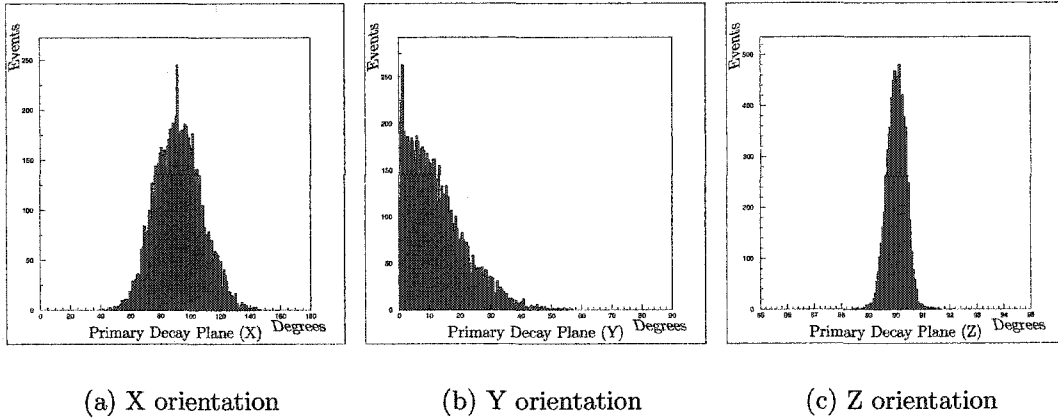


FIG. 8.12: Orientation of the primary  $K_{\mu\mu}$  decay plane in X,Y,Z according to the unit normal  $\hat{n}$  as defined in Eq. (8.48) in relation to the laboratory axis

describing the decay plane. This unit norm transforms as a vector in the usual manner, and is valid measure of the decay plane direction in both the laboratory and decay frames.

$$\hat{n}_{\mu\mu} = \frac{\vec{\mu}^- \times \vec{\mu}^+}{|n|}, \quad (8.48)$$

where the normalization can be computed in component form as:

$$\begin{aligned} |n| &= \sqrt{(\vec{\mu}_1 \times \vec{\mu}_2) \cdot (\vec{\mu}_1 \times \vec{\mu}_2)} \\ &= \sqrt{(\mu_{1i}\mu_{2j})^2 - \mu_{1i}\mu_{2i}\mu_{1j}\mu_{2j}} \end{aligned} \quad (8.49)$$

The remaining tracks from the electron/positron pair were taken as originating from a virtual  $\gamma$  carrying sufficient momentum  $P_\gamma$  to balance the decay kinematics. This intermediate momentum lies initially in the primary decay plane while the real momentum of the electron/positron pair in the center of momentum frame diverge from the plane under the standard Dalitz spectrum. The secondary decay plane was defined by the cross product of the identified tracking stubs taken in pairwise

combinations. The secondary decay plane was oriented by choosing ordering of the track stubs such that their resulting normal is in the positive y direction.

For correct acceptance of the muon tracks into the spectrometer, the available energy of the virtual state cannot exceed 37.5MeV. This missing energy is manifest in the Dalitz pair where at its maximum the pair emerges orthogonal to the defined primary decay plane. Even in this orthogonal arrangement the individual tracks in the center of momentum frame have at most an out of plane momentum of 18.75MeV/c. From the configuration of the spectrometer this momentum is then at its maximum perpendicular to the boost axis of the lab frame. As the boost parameter for transformation from the center of momentum to the laboratory frame is taken as the momentum of the parent kaon the spectrum of the resulting electron/positron pair is dominated by transformation along the z-axis. The resulting combination of high boost and low transverse momentum forces the pair to lie not only in the forward angle of the spectrometer but close to the primary decay plane of the decay.

The high correlation between primary and secondary decay planes was measured by projection of the normal to the secondary decay plane onto the normal of the primary plane.

$$C_{ee} = \hat{n}_{\mu\mu} \cdot \hat{n}_{ee}, \quad (8.50)$$

and represented as the correlation angle  $\xi_{ee}$

$$\xi_{ee} = \cos^{-1}(\hat{n}_{\mu\mu} \cdot \hat{n}_{ee}) \quad (8.51)$$

## Correlation of Singlet Stubs

For events containing only one identified partial track stub, correlation of the candidate electron stub with the primary decay plane was performed in a manner similar to that of an event with two candidate stubs that formed a well defined secondary decay plane.

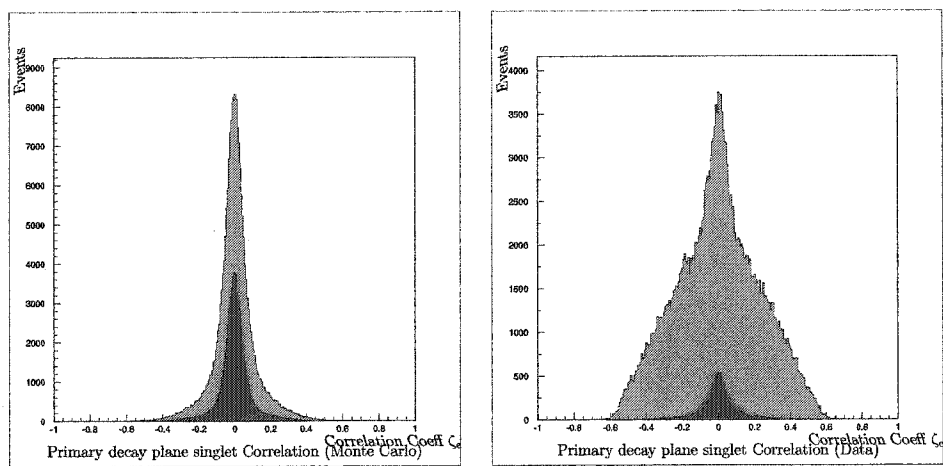
The normal to the primary decay plane was calculated in the manner of Eq. (8.49) to obtain appropriately normalized direction cosines of the  $\mu^+\mu^-$  decay axis. The singlet stub from the electron trajectory was computed as described in section 8.3.1, and direction cosines obtained from the SDC1 and SDC2 cluster centers. The direction cosines were normalized to ensure consistency in event comparisons. The resulting set of normalized tracking cosines  $\hat{a}_e$  were projected onto the computed normal of the primary decay plane to obtain the singlet correlation parameter  $\mathcal{C}_e$ .

$$\mathcal{C}_e = |\hat{n}_{\mu\mu} \cdot \hat{a}_e| \quad (8.52)$$

Similarly, the component of the electron trajectory transverse to the primary decay plane was computed to obtain the angular deviation corresponding to the inclination,  $\zeta_e$ , at which the electron trajectory emerges from the primary decay plane. The angle  $\zeta_e$  was computed as:

$$\zeta_e = \cos^{-1}(\hat{n}_{\mu\mu} \cdot \hat{a}_e) - \frac{\pi}{2} \quad (8.53)$$

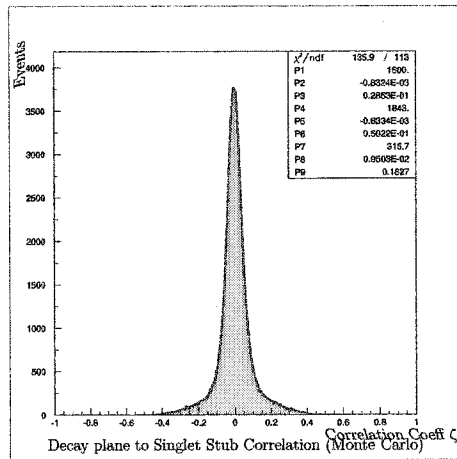
The correlation profiles for singlet stubs are shown in Fig. 8.13. These profiles are fit to determine the width of the correlation as shown in Fig. 8.14



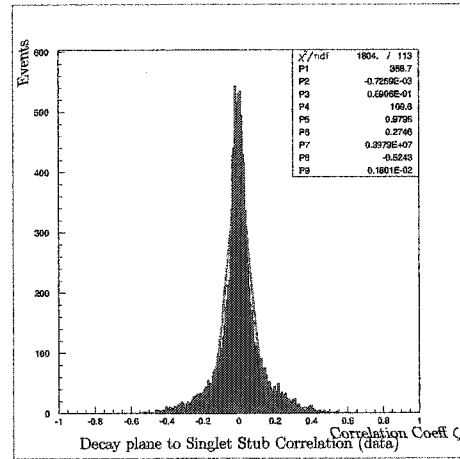
(a) Correlation coefficient  $\zeta_e$  between primary  $\mu\mu$  decay plane and singlet electron stub for all stubs (green) and best stubs (red) for  $\chi PT$  Monte Carlo

(b) Correlation coefficient  $\zeta_e$  between primary  $\mu\mu$  decay plane and singlet electron stub for all stubs (green) and best stubs (red) for data

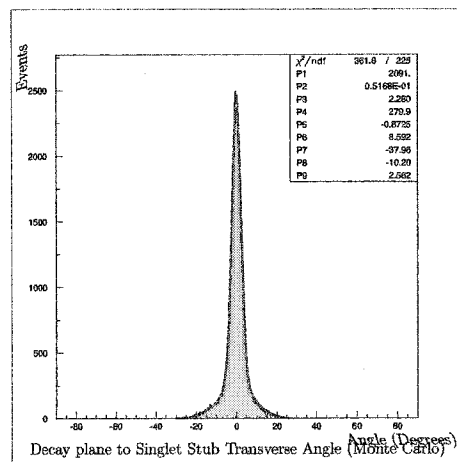
FIG. 8.13: Correlations of singlet candidate electron partial tracking stubs with the identified primary decay plane.



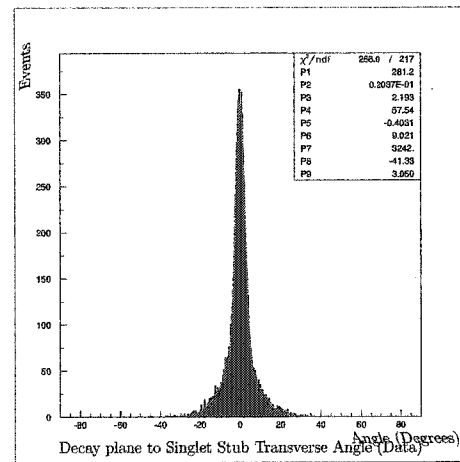
(a) Singlet Correlation coefficient  $\zeta_e$  with fit to Monte Carlo distribution



(b) Singlet Correlation coefficient  $\zeta_e$  with fit to Data distribution



(c) Angle of inclination between primary  $\mu\mu$  decay plane and singlet electron stub from Monte Carlo



(d) Angle of inclination between primary  $\mu\mu$  decay plane and singlet electron stub from data

FIG. 8.14: Fits to the correlations of singlet candidate electron partial tracking stubs with the identified primary decay plane using central Gaussian peaks and independent Gaussian sidebands.

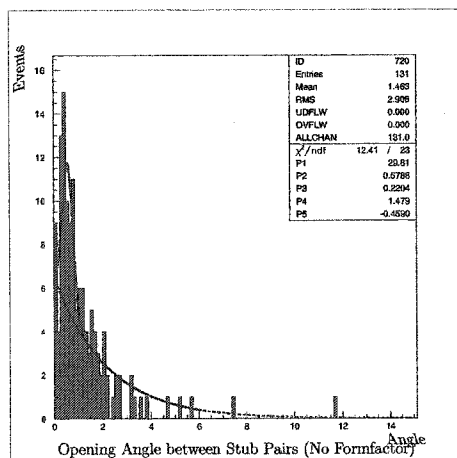
### 8.3.3 Stub Pair Correlation

The formfactor implementations discussed in section 7.5 lead not only to the soft momentum spectrum of the electron/positron pair, but to a tight angular correlation between the two particles when viewed in the laboratory reference frame. The angle was computed both with and without the effects of low energy multiple scattering to determine the appropriate function to use in order to extract the correlation peak. For each model considered in the analysis this angle was computed as shown in Fig. 8.15 and fit first to Gaussian peak plus with exponential tails, and then refit to a proper Lorentzian line shape plus a background offset. The resultant correlation was evident in the angular separation of the partial track stubs identified from the raw data samples as shown in Fig. 8.16.

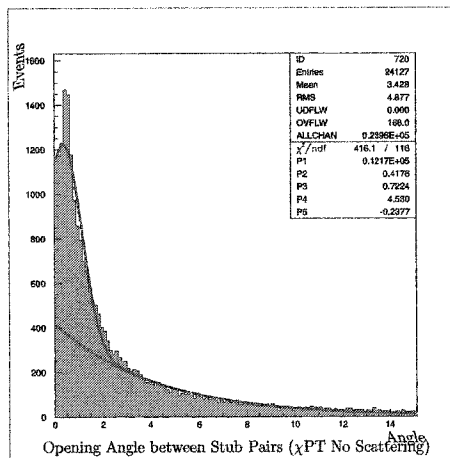
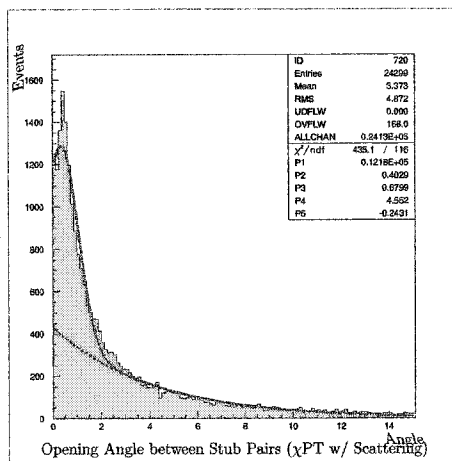
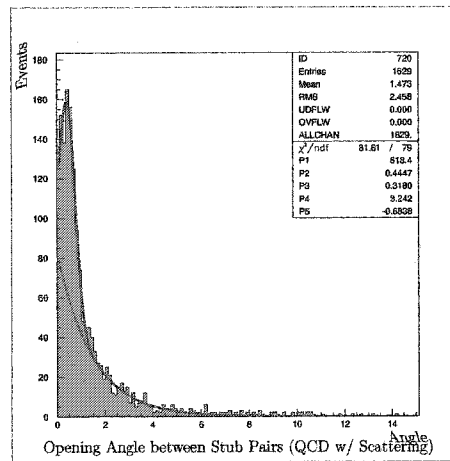
In addition to the tight opening angle correlation, the stub pairs also exhibit a tight joint correlation to the primary decay plane. This correlation is defined by considering the relative angle that the primary decay plane makes with a secondary decay plane defined by the two partial track stubs. The secondary decay plane is found in the same manner as Eq. (8.48) replacing the muon track trajectories by the partial electron tracks. The resulting secondary decay plane normal vector is written as:

$$\begin{aligned} |n_{ee}| &= \sqrt{(\vec{e}_1 \times \vec{e}_2) \cdot (\vec{e}_1 \times \vec{e}_2)} \\ &= \sqrt{(e_{1i}e_{2j})^2 - e_{1i}e_{2i}e_{1j}e_{2j}} \end{aligned} \quad (8.54)$$

Due to the low transverse momentum of each electron stub and the high momentum parent kaon oriented along the z-axis, two possible correlation geometries were allowed for the secondary stub pair. In the first geometry the secondary decay plane is aligned or nearly aligned with the primary decay plane such that the x,y and z projections of the secondary normal onto the primary normal are on the order of



(a) Stub pair opening angle (No formfactor)

(b) Stub pair opening angle ( $\chi^{\text{PT}}$  model without scattering)(c) Stub pair opening angle ( $\chi^{\text{PT}}$  model with scattering)

(d) Stub pair opening angle (QCD model with scattering)

FIG. 8.15: Opening angle of partial track stub both with and without multiple scattering from Monte Carlo models with  $\chi^{\text{PT}}$ , QCD or no formfactor



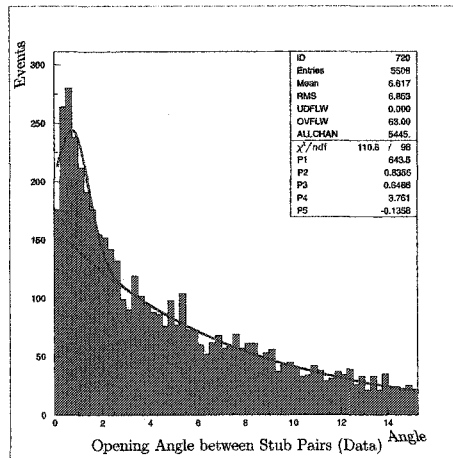


FIG. 8.16: Opening angle of partial track stub pairs from raw data

unity. In the second allowed geometry the  $e^+e^-$  decay plane is perpendicular to the  $\mu^+\mu^-$  while sharing a common z-axis. These geometries are shown in Fig. 8.17.

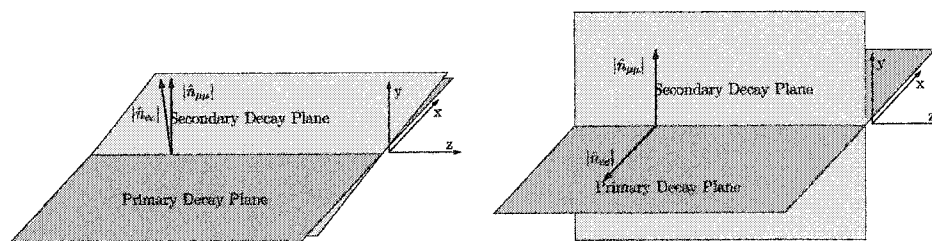
The allowed geometries are recognized through the X,Y and Z angular distributions of the calculated decay planes as shown in Fig. 8.18, 8.19 and 8.20. By using the direction cosines of the secondary decay plane in combination with the primary decay plane for the event the decay plane to decay plane correlation coefficient is computed through projection of the normals onto one another. In analogy to Eq. (8.52) the planar correlation coefficient  $\mathcal{C}_{ee}$  is computed as:

$$\mathcal{C}_{ee} = |\hat{n}_{\mu\mu} \cdot \hat{n}_{ee}| \quad (8.55)$$

The correlation angle is then:

$$\varphi_{ee} = \cos^{-1}(\hat{n}_{\mu\mu} \cdot \hat{n}_{ee}) \quad (8.56)$$

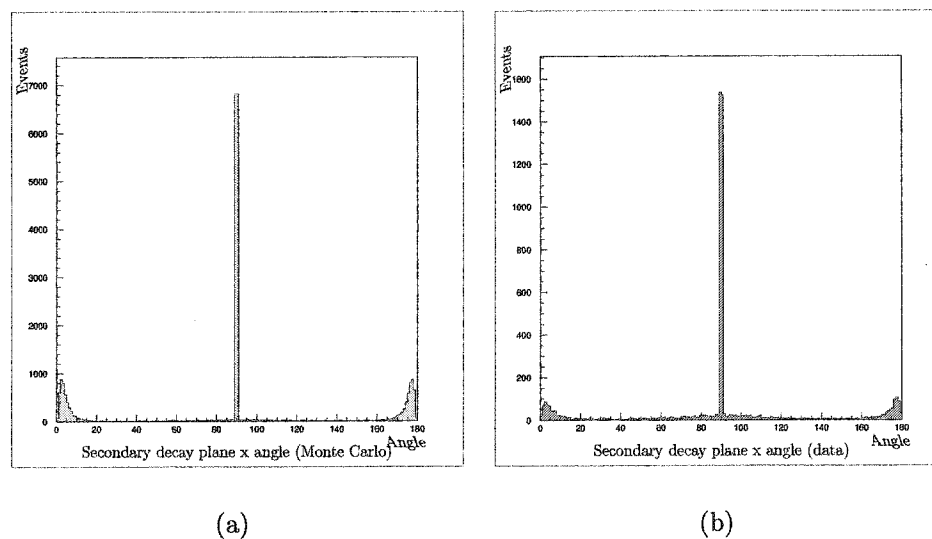
The resulting distributions for both the coefficient and the correlation angle are shown in Fig. 8.21.



(a) Correlation of primary and secondary decay planes in an aligned configuration

(b) Correlation of primary and secondary decay planes in a perpendicular configuration

FIG. 8.17: Possible correlated primary and secondary decay plane geometries for  $K_L^0 \rightarrow \mu^+ \mu^- e^+ e^-$  under high  $z$ -axis momentum boost



(a)

(b)

FIG. 8.18: Secondary decay plane angle in X for Monte Carlo and raw data

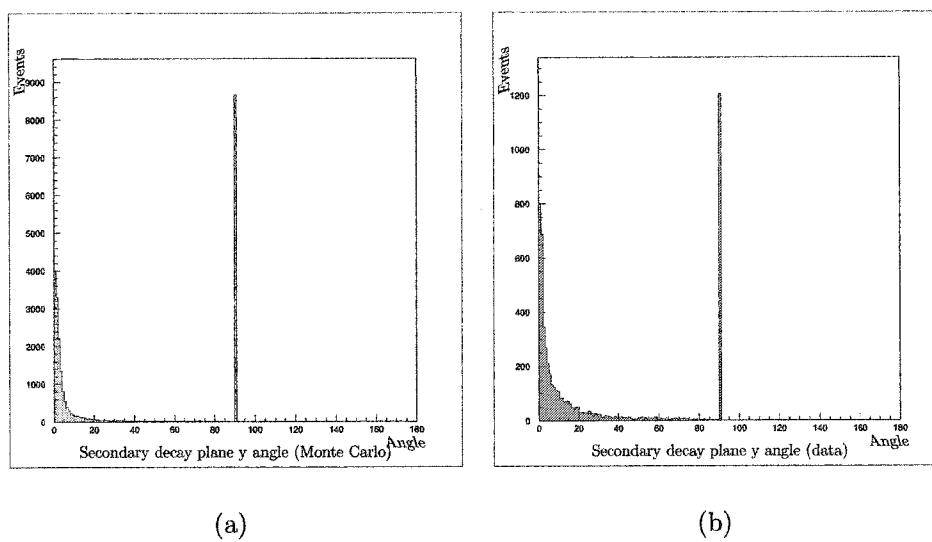


FIG. 8.19: Secondary decay plane angle in Y for Monte Carlo and raw data

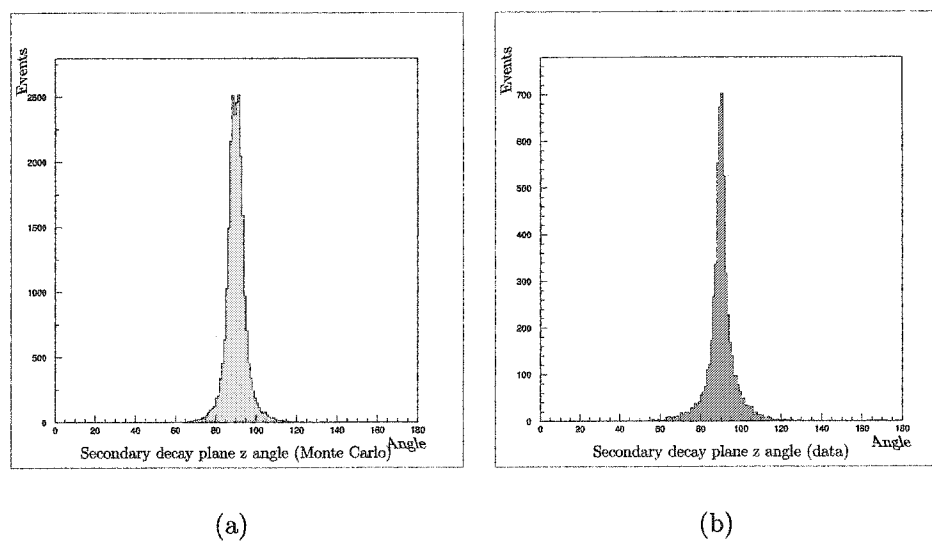


FIG. 8.20: Secondary decay plane angle in Z for Monte Carlo and raw data

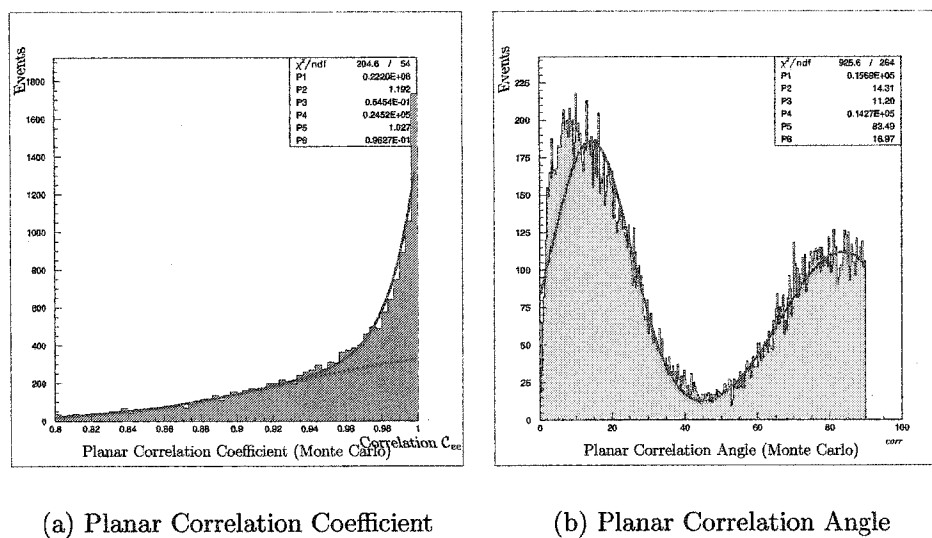


FIG. 8.21: Primary to secondary decay plane correlation coefficient  $C_{ee}$  and angle  $\varphi_{ee}$

## 8.4 Primary vertex reconstruction with partial tracks

The validity of the choice of primary vertex for each event is evaluated by considering the correlation of each stub or stub pair with the defined parameters of the primary decay plane. Events with sufficient correlation are fully reconstructed under a multi-body decay hypothesis allowing for a calculation of the parent kaon's mass under a detected three or four body final state. Final state event size is computed using stub candidates that fulfill the correlation criterion. For events with more than two candidate partial track stubs, only the two best stubs are considered under the pairwise correlation assumptions of section 8.3.3.

For all events, the transverse momentum of each identified particle that fully traversed the spectrometer was directly computed from the track trajectory, spectrometer momentum measurement, and the decay vertex to target direction. Similarly the transverse momentum of the muon pair that form the primary vertex is also computed as shown in Fig. 8.22. For particle trajectories which did not receive

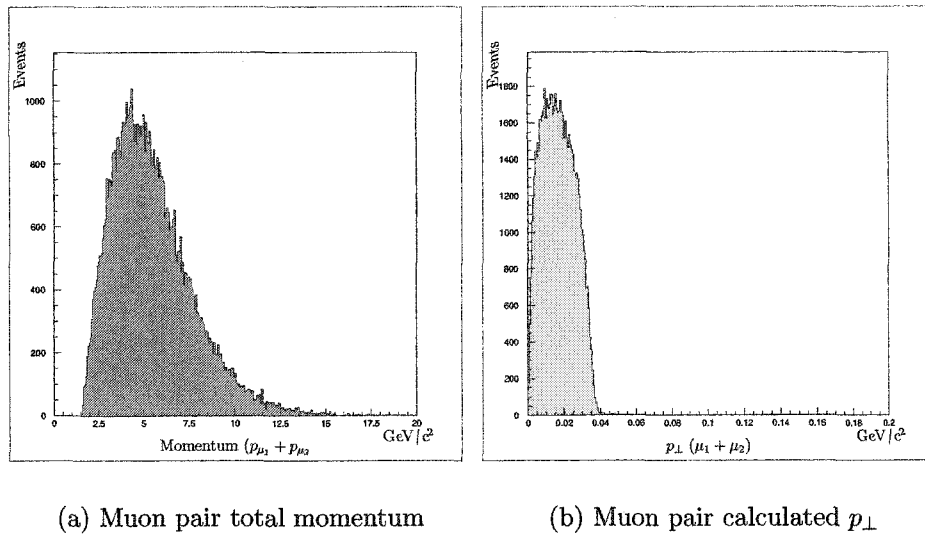
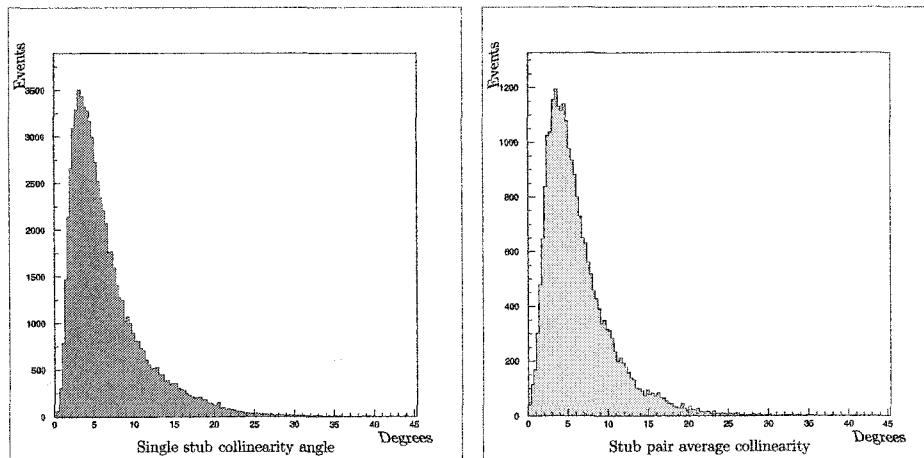


FIG. 8.22: Transverse momentum of primary muon pair as calculated from momentum sum and track collinearity angle.

full momentum analysis in the spectrometer systems, the transverse track momentum was determined from conservation laws imposed at the primary vertex position. Inferred transverse momenta are then used to reconstruct an approximation of the full track momentum for low momentum electrons and positrons.

The approximate reconstruction of low energy electron and positron track momentum was performed using the collinearity angles of each track as defined in section 8.1.3. Events with distinct four body final states consisting of two muon tracks and two electron stubs were reconstructed according to the geometry of Fig. 8.6. The collinearity angle  $\Theta_e$  denoting the angle between the vertex to target line and the momentum sum of the two electron stubs was computed by assuming approximately equal magnitudes for the electron and positron momenta in accordance with the distribution shown in Fig. 8.7. In this manner the angle was determined in terms of the set of direction cosines for the stub trajectories,  $a_i, b_i$  and the direction cosines of the vertex to target line,  $v_i$ . The resulting distribution for  $\Theta_e$  for both



(a) Collinearity angle for singlet stubs

(b) Collinearity angle for stub pairs

FIG. 8.23: Calculated collinearity angle distributions for low energy electron stubs in singlet and pair configurations

single and paired stubs is shown in Fig. 8.23.

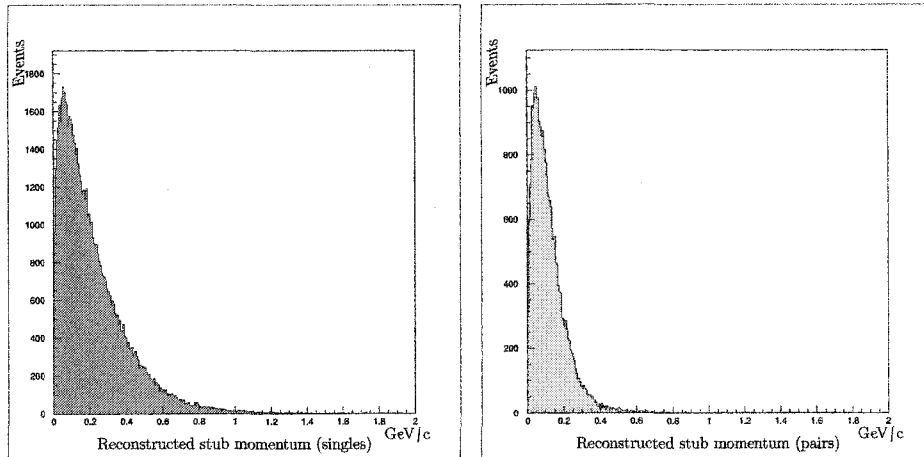
$$\begin{aligned}
 \Theta_e &= \cos^{-1} \left[ \frac{\sum_i |v| |\vec{p}_{12}| v_i (a_i + b_i)}{|v| |\vec{p}_{12}|} \right] \\
 &= \cos^{-1} \left[ \sum_i v_i (a_i + b_i) \right]
 \end{aligned}
 \tag{8.57}$$

The total momentum of the electron pair is found from Eq. (8.18) and split equally between the two particles giving the approximation

$$p_{e_{1,2}} \approx \frac{1}{2} P_e = \frac{|\vec{P}_\mu| \sin \Theta_\mu}{2 \sin \Theta_e} = \frac{|\vec{P}_\mu| \sin \Theta_\mu}{2 \sqrt{1 - (\sum_i v_i (a_i + b_i))^2}}
 \tag{8.58}$$

The resulting momentum spectrum for reconstructed electron/positron pairs is shown in Fig. 8.24(b).

For events with a distinct three body final state consisting of two muon tracks and only one recognized electron stub, the momentum of the singlet stub is deter-



(a) Reconstructed track momentum for singlet stubs

(b) Reconstructed track momentum for paired stubs

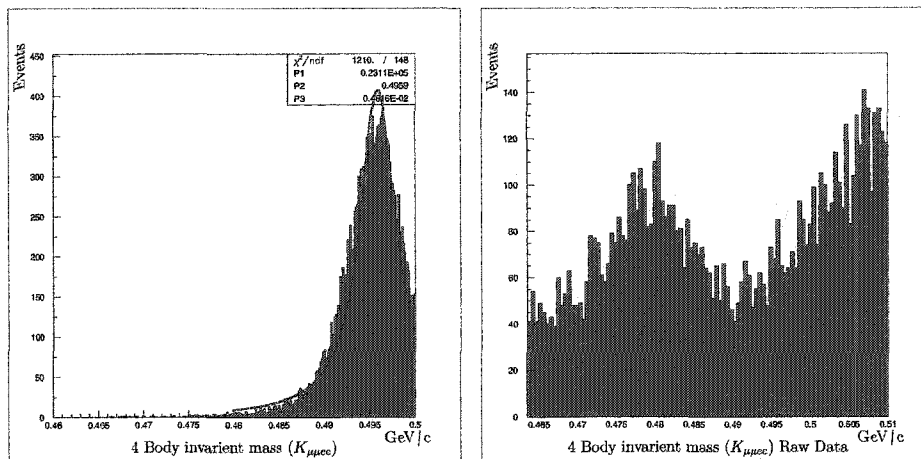
FIG. 8.24: Reconstructed partial track momentum for single and paired stubs using collinearity inferred transverse momenta matching.

mined directly from the measure of its collinearity. As a result, the reconstructed momentum for the electron stub is found to be:

$$p_{e_1} = |\vec{P}_\mu| \frac{\sin \Theta_\mu}{\sin \Theta_{e_1}} \quad (8.59)$$

### 8.4.1 Three and Four body Invariant mass

Events for which the stub momenta could be reconstructed and an inferred measure of the transverse momentum and collinearity angle obtained, were subject to primary vertex reconstruction using the maximum number of reconstructed tracks/stubs. Four body reconstruction was performed in the manner of Eq. (8.13) with the summation taken over stub and track direction cosines. Unmeasured track momenta were assumed through the relation of Eq. (8.58). Track energies were calculated using particle identification for the two muon tracks, and an  $e^-/e^+$  hy-



(a) Four body reconstruction of the  $K_{\mu\mu ee}$  invariant distribution

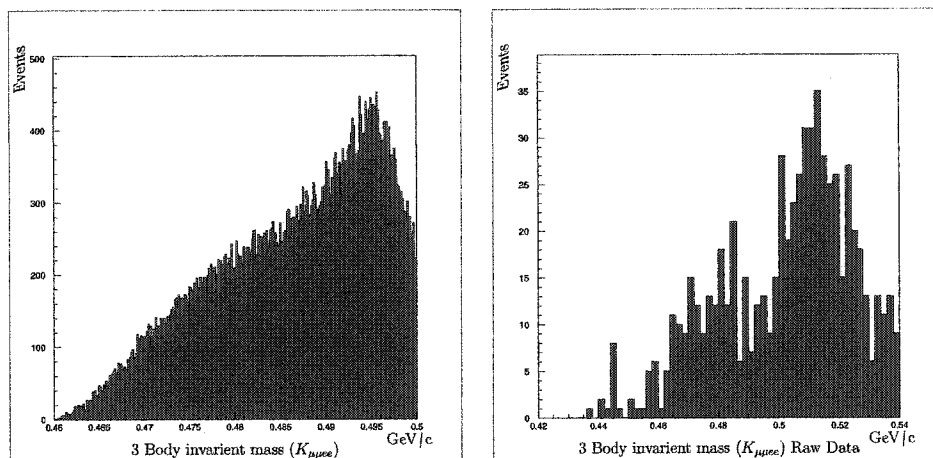
(b) Four body reconstruction of the  $K_{\mu\mu ee}$  invariant distribution from raw data

FIG. 8.25: Reconstruction of the  $K_{\mu\mu ee}$  invariant mass using two muon tracks and two electron tracks with inferred momenta recovered by transverse momentum matching and collinearity angles.

pothesis for the remaining stubs. The resulting distribution for stage 9 accepted events satisfying partial track reconstruction and stub to vertex DOCA requirements is given in Fig. 8.25 for both Monte Carlo and raw uncut  $\mu\mu$  event data. The peak is fit to a Breit-Wigner line shape as shown in Fig. 8.25(a) to determine the central kaon mass and the resolved width of the peak.

Events with only one additional tracking stub are reconstructed using the same method as described by Eq. (8.13) but with the stub momentum determined by Eq. (8.59). The resulting distribution does not sharply peak as in the four body reconstruction, but does move correlated events closer to the kaon mass in a preferential manner to that of uncorrelated background. The distribution of Fig. 8.26 shows the effect of the three body reconstruction on valid stage 9 events passing stub reconstruction but not yet restricted by cuts imposed on angular correlations.





(a) Three body reconstruction of the  $K_{\mu\mu ee}$  invariant distribution

(b) Three body reconstruction of the  $K_{\mu\mu ee}$  invariant distribution from raw data

FIG. 8.26: Reconstruction of the  $K_{\mu\mu ee}$  invariant mass using two muon tracks and one electron track with inferred momenta recovered by transverse momentum matching and collinearity angles.

## 8.4.2 Three and Four Body Event Transverse Momentum

Events that are subject to invariant mass reconstruction under either a three or a four body final state as discussed in section 8.4.1 are also examined to determine the total transverse momentum of the event. The transverse momentum of the event is determined by summing over the measured momenta of the two muon tracks and the inferred momentum of the identified electron stubs. The resulting total event momentum is projected onto the vertex to target line in order to determine the transverse component of the momentum.

In this manner the total final state momentum is a sum over  $i$  final state particles:

$$P_T = \sum_i \sum_j (p_i)_j \hat{x}_j \quad (8.60)$$

The collinearity angle  $\Theta_T$  for the momentum sum is found from the total momentum  $\vec{P}_T$  and the target to vertex vector  $\vec{V}$ :

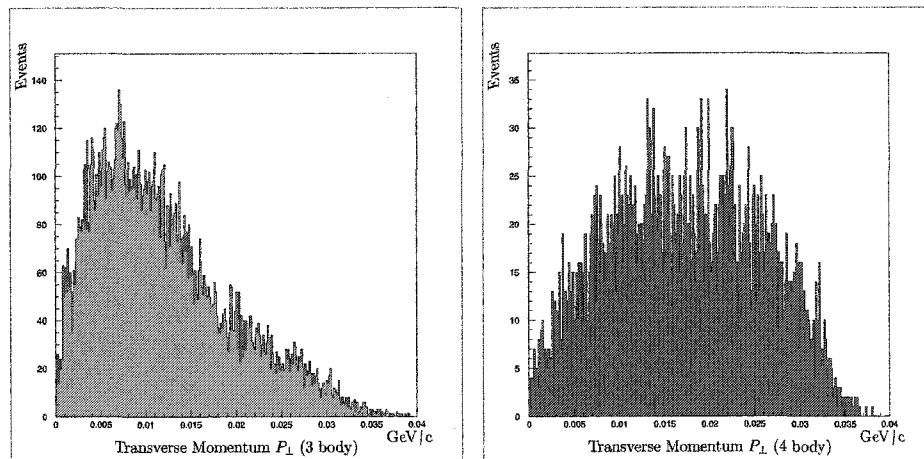
$$\Theta_T = \cos^{-1} \frac{\vec{P}_T \cdot \vec{V}}{|P_T||V|} \quad (8.61)$$

The transverse momentum

$$\begin{aligned} P_{\perp} &= P_T \sin \Theta_T \\ &= P_T \sqrt{1 - \left( \frac{\vec{P}_T \cdot \vec{V}}{|P_T||V|} \right)^2} \end{aligned} \quad (8.62)$$

Due to the manner in which analysis of the three body events infers the missing stub momentum through matching the transverse component of the  $\mu\mu$  momentum sum to the single stub's transverse momentum, the resulting calculation of the total event transverse momentum  $P_{\perp}$  is very close to zero. The cancellation is not exact however due to the manner in which the total event momentum sum is computed and the resulting vector's collinearity with the target to vertex line recomputed.

Similarly the calculation of the four body transverse momentum is also not exactly zero even though it relies on the same matching method to determine the momentum for each of the stubs. Because the average collinearity angle is used to determine the individual stub momenta, while the actual stub angle is used in computing the momentum sum, there is a small deviation from a zero result corresponding to the deviation of the electron/position trajectories from the averaged collinearity angle. In the case where the electron/position pair has a zero opening angle and the actual trajectories approach the average, the transverse momenta reduces to zero by the conservation law, but due to the recalculation of the total momentum sum and the resulting total collinearity angle, this quantity is again not exactly zero.



(a) Three body reconstruction of total transverse momentum  $P_{\perp}$

(b) Four body reconstruction of total transverse momentum  $P_{\perp}$

FIG. 8.27: Total transverse momentum  $P_{\perp}$  as reconstructed for three body and four body  $K_{\mu\mu ee}$  event vertices.

The transverse momentum distributions for three and four body reconstructed events are shown in Fig. 8.27

## 8.5 Tracking and Vertex Corrections

The minimum values for the measured distance of closest approach are dependent primarily on the resolution of the straw tracks. In the absence of any multiple scattering or other physical factors that have the ability to modify the track slopes in the first and second straw drift chambers, the resulting minimum DOCA values and momentum resolutions for both primary tracks and partial tracking stubs would correspond to the details of sections 8.2 and 8.3. In the E871 experimental apparatus it was found that in addition to multiple scattering, track slope deflection of low energy tracks and stubs was present due to the small magnetic fringe field created by the spectrometer magnets. This deflection is calculated as a correction to both

the track slopes and resulting vertex DOCA values.

### 8.5.1 Magnetic fringe field deflection

Charged particles emerging from the downstream window of the decay volume are subject to the magnetic fringe field of the 96D40/D02 analyzing magnet. Deflection of the particle trajectories is influenced by the magnetic field and can result in significant uncertainty in the vertices reconstructed by low transverse momentum tracks. This deflection is of particular concern in the reconstruction of partial tracking stubs and association of such stubs with primary vertices reconstructed from high momentum muon track pairs.

The magnetic field is assumed to be uniform and static from which the relation for the radius of curvature  $a$ , and transverse momentum of the particle can be related by[45]

$$cp_{\perp} = eBa \quad (8.63)$$

Since the particles are of unit magnetic charge the relation can be express as

$$a(cm) = \frac{p_{\perp}(MeV/c)}{3.0 \times 10^{-4}B(gauss)} \quad (8.64)$$

The actual angular deflection experienced by a particle traversing some distance  $\Delta z$  can then be expressed in terms of the incident angle  $\alpha$  as:

$$\begin{aligned} \Delta\alpha &= \frac{1}{2} \sin^{-1} \left( \frac{\Delta z}{a \cos(\alpha)} \right) \\ &= \frac{1}{2} \sin^{-1} \left( \frac{3 \times 10^{-4}B\Delta z}{p_{\perp} \cos(\alpha)} \right) \end{aligned} \quad (8.65)$$

The deflection of the particle in the transverse direction can be expressed as

$$\Delta x = \Delta z \left[ \tan \alpha - \tan \left( \alpha - \frac{1}{2} \sin^{-1} \left( \frac{3 \times 10^{-4} B \Delta z}{p_{\perp} \cos(\alpha)} \right) \right) \right] \quad (8.66)$$

The fringe field upstream of the 96D40/D02 analyzing magnet was not mapped in detail, but was found to average 15 G in the area near the decay tank window and the first set of straw drift chambers. Due to the track and stub reconstruction methods, the uncertainty in track or stub slope between SDC1 and SDC2 is most sensitive to deflections in the first layer of straw tubes in SDC2. The z-axis path length between the front window of the decay volume and the sensitive layer of SDC2 is measured to be 129.1 cm. The maximum incident angle for which a particle can be successfully accepted by the straw drift chambers is  $49.5^{\circ}$ , although the angular distribution of low energy electrons is peaked towards the beam axis, resulting a smaller mean incident angle. The resulting mean value for low energy electron deflection is calculated using an incident 100MeV electron in the 15 G fringe field. In this manner it is determined that the mean transverse deviation at SDC2 is given by:

$$\Delta x(p_{\perp}, B) = \Delta x(100MeV, 15Guass) = 0.375cm \quad (8.67)$$

This average deflection of 3.75mm corresponds to one and a half times the radius of the individual straw tubes. The resulting deflection thus has the effect of smearing the low energy trajectories by an average of one channel. The momentum dependence of this deflection is shown in Fig. 8.28 for the 15 G field. For tracks with steep incident angles the deflection distance  $\Delta x$  is calculated from the series of curves shown in Fig. 8.29(a). Similarly the deflection contours of Fig. 8.29(b) show the effects of magnetic fringe fields in excess of the stated 15 G field.

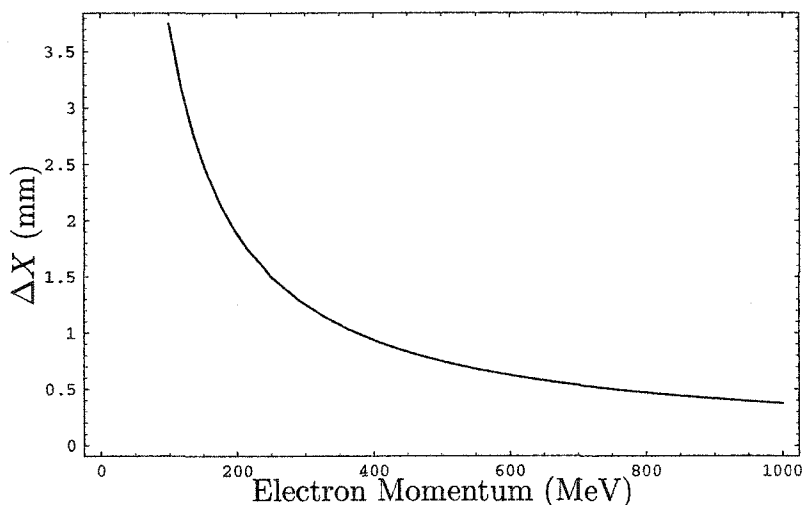


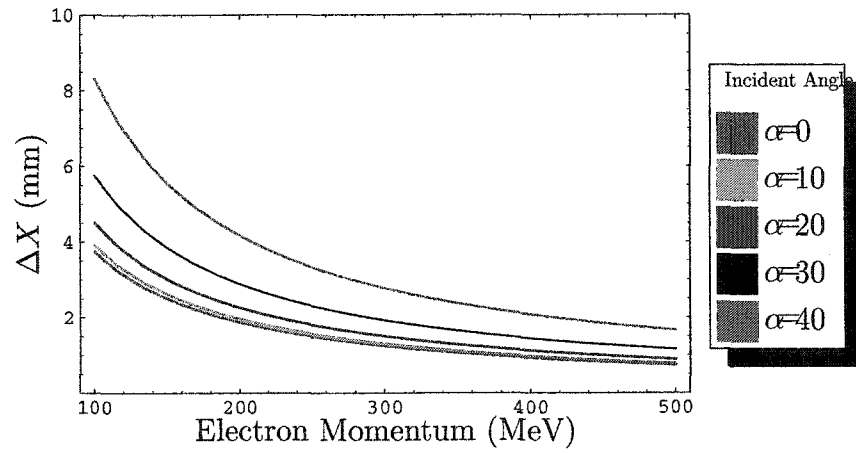
FIG. 8.28: Dependence of low energy electron deflection in the magnetic fringe field with particle momentum.

The effect of the deflection, while small at the SDC2 measuring planes, is magnified during the vertex reconstruction and DOCA calculation by the  $z$ -axis distance that the true vertex position is from the front window of the decay tank. The geometry of this amplification is shown in Fig. 8.30. From the diagram it is clear that the distance  $\Delta x'$  corresponding to the distance by which the deflected track approaches the true reconstructed vertex at the vertex  $z$ -position can be expressed as:

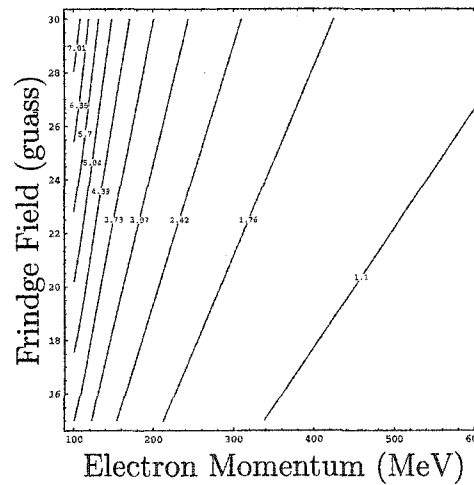
$$\Delta x' = \Delta x \frac{z'}{z} \quad (8.68)$$

For the nominal 3.75mm deflection discussed above the maximum error induced in the track to vertex DOCA can be found by considering a vertex position at the upstream limit of the fiducial volume of the decay tank. At a vertex 10m upstream of the front vacuum window the resulting deflection becomes 2.90cm. This deflection becomes the basis for the analysis cut on reconstruction DOCA to associate low energy electron/positron stub pairs with the primary  $\mu^+\mu^-$  reconstructed vertex.

In addition to being used to compute the limits on the associated DOCA values,



(a) Dependence of low energy electron deflection on incident track angle and particle momenta



(b) Dependence of low energy electron deflection on magnetic fringe field

FIG. 8.29: Dependence of low energy electron deflection in the magnetic fringe field with incident track slope shown by the curves in Fig. 8.29(a) and the dependence on the field strength shown in Fig. 8.29(b)

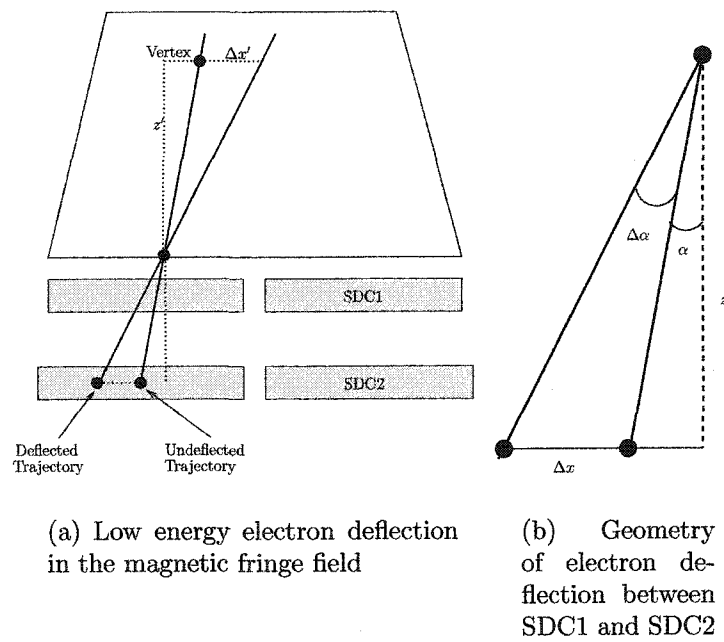


FIG. 8.30: Geometry of low energy electron deflection in the magnetic fringe field forward of 96D40/D02 with reconstruction to the primary vertex and associated increase in DOCA values



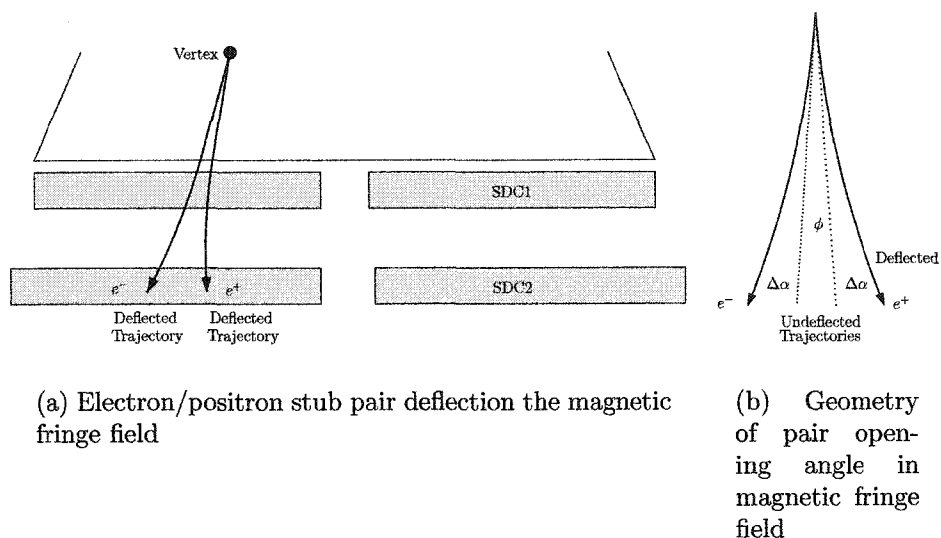


FIG. 8.31: Low energy electron/positron pairs experience in-bend/out-bend deflections in the magnetic fringe field leading to increased opening angle between tracks stubs

the magnetic fringe field serves to increase the opening angle between the low energy electron/positron pairs. Due to the opposite polarity of the particles one of the pair receives an in-bend modification to its trajectory while the other receives an out-bend modification. This situation is shown schematically in Fig. 8.31. Since the low energy electron/positron pairs exhibit near symmetry in their momentum distributions it is possible to calculate the magnitude of the effect. For a pair of 100 MeV particles in the 15 G field it is calculated that the angular deflection in each trajectory will be  $\Delta\alpha = 0.166^\circ$ . Due to the polarity differences between the particles, the in-bend/out-bend nature of the pair splitting results in a total increase in angular separation of  $2\Delta\alpha = 0.332^\circ$ . The track splitting in the fringe field has the effect of increasing low energy stub pair detection in SDC2. The detection of these pairs then allows for the determination of the secondary decay plane and subsequent correlations between primary and secondary planes.

# CHAPTER 9

## Production Analysis and Cuts

The production analysis of the  $\mu^+\mu^-e^+e^-$  data incorporated the building of event ntuples from the E871 Pass 3  $\mu\mu$  data strip. Data ntuples were built forming both a  $K_L^0 \rightarrow \mu^+\mu^-$  data set and a  $K_L^0 \rightarrow \mu^+\mu^-e^+e^-$  data set with no event overlap between the two streams. Each data set was then filtered using a set of tracking and particle identification cuts to determine final event quality.

The ordering, resultant filtering, acceptances and efficiencies were determined for each cut or associated group of cuts and applied to the data sets. These cuts and results are detailed in sections 9.1 to 9.5

### 9.1 $\mu\mu$ Vertex Cuts

The first set of cuts applied to the production data were designed to identify the two primary muon tracks for each event. The cuts were designed to produce a high signal to noise ratio when extracting the  $K_L^0 \rightarrow \mu^+\mu^-$  invariant mass peak from the data stream while maintaining a high efficiency and acceptance to both the  $K_L^0 \rightarrow \mu^+\mu^-$  and  $K_L^0 \rightarrow \mu^+\mu^-e^+e^-$  data streams.

The cuts are divided into vertex, track quality and reconstruction groups. The

track and vertex quality cuts were applied to both data streams in an identical fashion to preserve the similar acceptances and efficiencies in relation to track resolutions and acceptance regions. Cuts on the event reconstruction parameters were set separately for the  $K_L^0 \rightarrow \mu^+\mu^-$  and  $K_L^0 \rightarrow \mu^+\mu^-e^+e^-$  data in accordance with the differing final state profiles and kinematics.

### 9.1.1 Primary Vertex Fiducial Volume Cut

Each event vertex was constrained to occur within the primary decay volume. The event vertex was further constrained to a position within the neutral beam profile as defined by the solid angle subtended along the beam axis as limited by the upstream collimators. A cut was placed upon the value of  $V_x$  and of  $V_y$  as defined by:

$$V_x = \frac{x_{vtx} - x_{target}}{z_{vtx} - z_{target}} \quad (9.1)$$

$$V_y = \frac{y_{vtx} - y_{target}}{z_{vtx} - z_{target}} \quad (9.2)$$

The angular deviation in the X direction was limited such that  $V_x < \pm 2.7 mrad$  and the angular deviation of the vertex in the Y direction was set to  $V_y < \pm 10.0 mrad$ .

The Z-axis position  $V_z$  of the vertex was limited to prevent acceptance of events that interacted either off of the upstream decay window or with the upstream edges of the decay tank itself. This upstream cut reduced the contamination of the signal data with events arising from  $K_S^0$  decays, where the  $K_S^0$  component of the neutral beam arises from the kaon regeneration effect of the beam passing through the upstream window. Additionally this cut removed from the data set a number of  $\Lambda$  decay chains arising from the interaction of the beam halo with the steel walls

Vertex Parameter	Cut (FT)	Cut (QT)
$V_x$	$\pm 2.7$ mrad	$\pm 2.7$ mrad
$V_y$	$\pm 10.0$ mrad	$\pm 10.0$ mrad
$V_z$	$> 9.55$ meters	$> 9.55$ meters
$V_z$	$< 20.6$ meters	$< 20.6$ meters

TABLE 9.1: Vertex position cuts for FT and QT determined vertices.

of the decay tank. The down stream limit of the Z coordinate was set to reduce contamination of the data set from semi-leptonic decays with large angle multiple scatters in the front window of the decay tank.

The limits on the Z coordinate of the decay vertex were set at  $9.55m < V_z < 20.6m$ . These cuts are shown on the vertex distributions in Fig. 9.1 These cuts were performed for event vertices determined by both the FT and QT fitting routines. These values are summarized in Table 9.1. These cuts were applied to both the  $K_L^0 \rightarrow \mu^+\mu^-$  and  $K_L^0 \rightarrow \mu^+\mu^-e^+e^-$  data.

### 9.1.2 Muon Track Momentum Cut

The momentum range of each primary muon track was limited by high and low cut values. These momentum thresholds were implemented to address inefficiencies in the particle identification code arising from low statistics at both ends of the measurable momentum spectrum. The low momentum threshold of 1.05 GeV/c was required to force muon id triggering in the muon hodoscope at detector planes MX0/MY0 which were located at the 1.0 GeV/c momentum gap in the range finder. This cut of 1.05 GeV also increased the efficiency of muon/pion differentiation by reducing the probability that the hadronic shower from a pion converting in the lead glass array would punch through into the range stack, leaving an ambiguous momentum gap stopping point for the 15% momentum match criteria imposed by

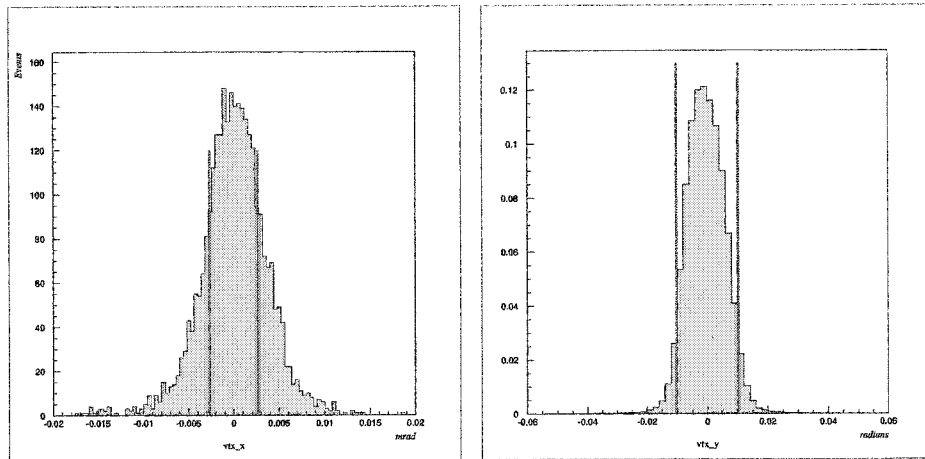
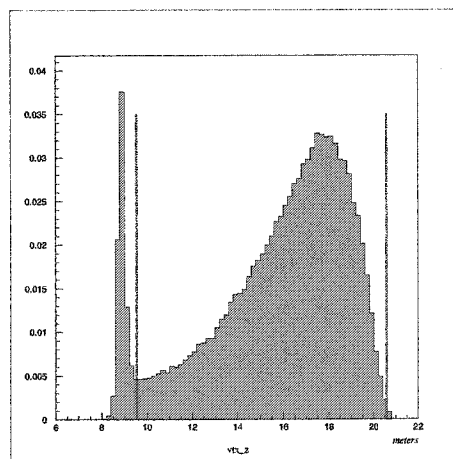
(a)  $V_x$  Vertex Distribution(b)  $V_z$  Vertex Distribution(c)  $V_z$  Vertex Distribution

FIG. 9.1: Vertex Distributions and Fiducial Volume Cuts.

Track Momentum	Cut (FT)	Cut (QT)
$P_{\mu^\pm}$	$> 1.05 \text{ GeV}/c$	$> 1.05 \text{ GeV}/c$
$P_{\mu^\pm}$	$< 6.50 \text{ GeV}/c$	$< 6.50 \text{ GeV}/c$

TABLE 9.2: Vertex position cuts for FT and QT determined vertices.

the range finder.

The upper limit on the muon track momentum was set at  $6.5 \text{ GeV}/c$  in order to maintain a high, measured efficiency for muon identification in the rear detector planes of the muon range finder. This cut also reduced the number of events in which a muon track could trigger a valid hit in the Čerenkov counter, thereby resulting in particle id trigger ambiguities associated with electron/muon identification above the  $6.357 \text{ GeV}/c$  Čerenkov threshold in hydrogen.

The momentum cuts were placed separately for tracks fitted using the FT algorithm and for those fitted with the QT algorithm. These cut values are listed in Table 9.2 and were applied to both the  $K_L^0 \rightarrow \mu^+\mu^-$  and  $K_L^0 \rightarrow \mu^+\mu^-e^+e^-$  data sets.

### 9.1.3 Muon Track $\chi^2$ Cut

Each of the fitting algorithms used a different method to identify and fit primary tracks. Because each fitter had independent methods of determining the tracks trajectories and momentum, both were utilized in determining the overall track quality for a given event. Both the FT and QT fitting routines returned a  $\chi^2$  figure of merit representing the deviation of the detector hit patterns from the determined track trajectory as it was swum through the measured magnetic fields of D01 and D02 (FT) or from the forward/rear segment matched track parameters (QT).

The track  $\chi^2$  returned by the FT fitter was obtained through matrix inversion and the resulting sum over the covariance (error) matrix  $E_{ij}^x$  and the differences be-

Track Momentum	Cut (FT)	Cut (QT)
Track $\chi^2$	25	35

TABLE 9.3: Muon track  $\chi^2$  cuts for FT and QT determined primary muon tracks.

tween the actual hit positions  $x_i$  and the calculated hit positions  $x'_i$  in each chamber.

$$\chi_{FT}^2 = \sum_{ij} (x_i - x'_i) (E_{ij}^x)^{-1} (x_j - x'_j) \quad (9.3)$$

The track  $\chi^2$  returned by the QT fitter was obtained by varying the upstream and down stream momentum and track slope parameters in an iterative matching procedure. A  $\chi^2$  value was obtained for both the x and y views of a track as:

$$\chi_x^2 = \left( \frac{\delta p}{\sigma_{\delta p}} \right)^2 + \left( \frac{\delta \theta_x}{\sigma_{\delta \theta_x}} \right)^2 \quad (9.4)$$

$$\chi_y^2 = \left( \frac{\delta y}{\sigma_{\delta y}} \right)^2 + \left( \frac{\delta \theta_y}{\sigma_{\delta \theta_y}} \right)^2 \quad (9.5)$$

The covariances  $\{\sigma_{\delta p}, \sigma_{\delta \theta_x}, \sigma_{\delta y}, \sigma_{\delta \theta_y}\}$  were set as the RMS deviations found from Monte Carlo. The total track  $\chi_{QT}^2$  is a sum of  $\chi_x^2$  and  $\chi_y^2$  per degree of freedom.

High values of the  $\chi^2$  represent muons which did not conform well to the fitted tracks. This indicates either poor track determination, track ambiguities, accidental hits, track sharing or pion decay in flight. All these factors can contribute to background. The value of  $\chi^2$  is chosen to minimize the contribution of background noise to less than 1% by comparing Monte Carlo to data. For the FT fitter the value of  $\chi^2$  was chosen at 25 while for QT the value was set at 35. These values are summarized in Table 9.3. These cuts were applied to events in both the  $K_L^0 \rightarrow \mu^+ \mu^-$  and  $K_L^0 \rightarrow \mu^+ \mu^- e^+ e^-$  data streams.

Event Vertex	Cut (FT)	Cut (QT)
Vertex $\chi^2$	30	15

TABLE 9.4: Primary event vertex  $\chi^2$  cuts for FT and QT determined primary muon tracks.

#### 9.1.4 $\mu\mu$ Vertex DOCA and $\chi^2$ Cut

The FT and QT fitters return  $\chi^2$  figures of merit for the fit to the vertex parameters similar to that returned for  $\chi^2$  for the track fitting procedure. The FT fitter forms the vertex  $\chi^2$  through matrix inversion over the individual track parameters  $\alpha_i$  consisting of the track x and y positions, x and y direction cosines and one over the track momentum at the vacuum window. The  $\chi^2$  is formed as a sum over the error matrix  $E_{ij}^\alpha$ :

$$\chi_{vtx_{FT}}^2 = \sum_{ij} (\alpha_i - \alpha'_i) (E_{ij}^\alpha)^{-1} (\alpha_j - \alpha'_j) \quad (9.6)$$

The QT fitter forms the vertex  $\chi^2$  from the actual vertex DOCA,  $\mathcal{D}_{vtx}$ , and the standard errors in the left and right direction angles.

$$\chi_{vtx_{QT}}^2 = \frac{\mathcal{D}_{vtx}^2}{(z_{DC1} - z_{vtx})(\sigma_\theta^2 + \sigma_{\theta'}^2)} \quad (9.7)$$

The cut values for the FT and QT vertices were set at values of 30 and 15, respectively corresponding to the 98% efficiency level for each fitter. The cut values are summarized in Table 9.4. These cuts were applied to events in both the  $K_L^0 \rightarrow \mu^+\mu^-$  and  $K_L^0 \rightarrow \mu^+\mu^-e^+e^-$  data streams.



### 9.1.5 $K_{\mu\mu}$ Invariant Mass Cut

The signal region for  $K_L^0 \rightarrow \mu^+\mu^-$  events was determined by measuring the momentum resolution of the FT and QT fitters and then setting a window around the known mass of the kaon,  $497.6 \text{ MeV}/c^2$ . The limits on mass window were set at  $(M_K)^{+3.5\sigma_m}_{-3.25\sigma_m}$ . These limits result in an upper end efficiency loss of 0.087% and lower end efficiency loss of 0.2% resulting in a total signal region efficiency of 99.7%.

The mass resolution of the FT fitter was found to be  $1.26 \text{ MeV}/c^2$  for events in the  $\mu\mu$  data stream. Similarly the QT fitter had a mass resolution of  $1.43 \text{ MeV}/c^2$  for  $\mu\mu$  events. The upper and lower limits on the reconstructed invariant mass  $M_{K_{\mu\mu}}$  set such that:

$$\begin{aligned} 493.5 \text{ MeV}/c^2 < M_{K_{\mu\mu}} < 502.0 \text{ MeV}/c^2 & \quad (\text{FT}) \\ 493.0 \text{ MeV}/c^2 < M_{K_{\mu\mu}} < 502.5 \text{ MeV}/c^2 & \quad (\text{QT}) \end{aligned} \tag{9.8}$$

This mass window was applied only to events in the  $K_L^0 \rightarrow \mu^+\mu^-$  data stream. The summary of the invariant mass window cuts and fitter resolutions is shown in Table 9.5. The distributions in Fig. 9.2 show the resulting mass windows and fits for to the distributions to determine the mass resolution of each fitter.

Determination of the mass window for  $K_L^0 \rightarrow \mu^+\mu^-e^+e^-$  was determined in a similar fashion to that of  $K_L^0 \rightarrow \mu^+\mu^-$  using two body, three body and four body invariant mass reconstructions. The resulting distributions and cuts are discussed in section 9.5.1.

### 9.1.6 $K_{\mu\mu}$ Transverse Momentum Cut

The transverse momentum of each event as determined by the momentum sum of the two muon tracks and their collinearity angle with respect to the target to beam axis was determined. Total transverse momentum for an event was used as a measure

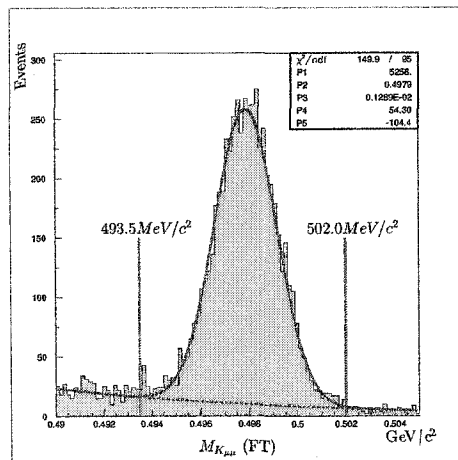
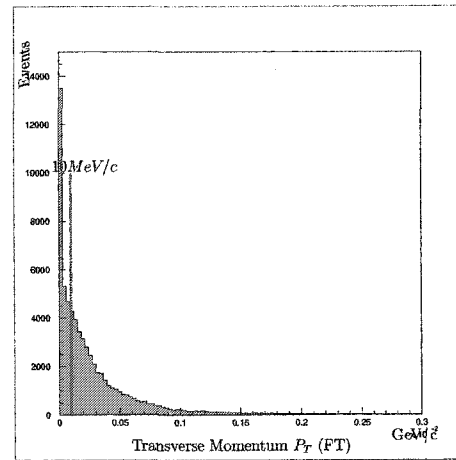
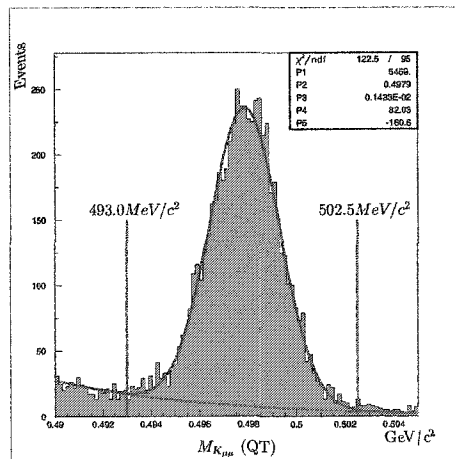
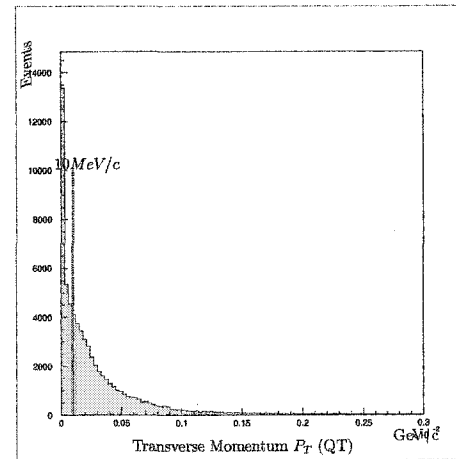
(a) Invariant mass  $K_L^0 \rightarrow \mu^+ \mu^-$  (FT)(b) Transverse Momentum -  $p_t^2$  (FT)(c) Invariant mass  $K_L^0 \rightarrow \mu^+ \mu^-$  (QT)(d) Transverse Momentum -  $p_t^2$  (QT)

FIG. 9.2: Invariant mass window and transverse momentum cuts for the FT and QT fitters with fits determining the mass resolution of each distribution.

Mass Resolution	FT	QT
$\sigma_{M_K}$	1.26 MeV/c <sup>2</sup>	1.43 MeV/c <sup>2</sup>
Invariant Mass ( $K_{\mu\mu}$ )	Cut (FT)	Cut (QT)
$M_{K_{\mu\mu}}$	> 493.5 MeV/c <sup>2</sup>	> 493.0 MeV/c <sup>2</sup>
$M_{K_{\mu\mu}}$	< 502.0 MeV/c <sup>2</sup>	< 502.5 MeV/c <sup>2</sup>

TABLE 9.5: Mass resolutions and  $K_L^0 \rightarrow \mu^+\mu^-$  invariant mass window cuts using the FT and QT fitting algorithms.

Transverse Momentum	Cut (FT)	Cut (QT)
$p_t$	< 0.010 GeV/c	< 0.010 GeV/c

TABLE 9.6: Limits on total event transverse momentum for  $K_L^0 \rightarrow \mu^+\mu^-$ .

of the presence of any unobserved or unaccounted final state particles associated with the event. Measures of  $p_t^2$  near zero represent events with correct momentum conservation and not more than two final state particles in the case of  $K_L^0 \rightarrow \mu^+\mu^-$  and not more than two final state particles in the case of  $K_L^0 \rightarrow \mu^+\mu^-e^+e^-$ . An upper limit of 10 MeV/c was imposed upon the  $p_t$  of each event in the  $K_L^0 \rightarrow \mu^+\mu^-$  data stream for events fit with both the FT and QT routines as shown in Table 9.6.

The cuts on the invariant mass window for  $M_{K_{\mu\mu}}$  and the limit on  $p_t$  were combined to form a two-dimensional signal box in  $p_t^2$  and  $M_K$ . This signal box is shown in Fig. 9.3.

For the  $K_L^0 \rightarrow \mu^+\mu^-e^+e^-$  data stream a similar cut on transverse momentum was performed using two body, three body and four body event reconstruction procedures. These cuts are detailed in section 9.5.2

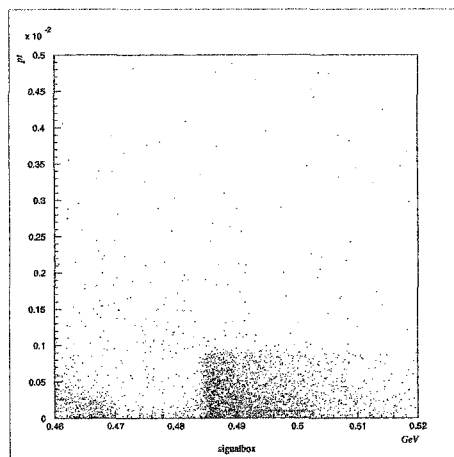


FIG. 9.3:  $K_L^0 \rightarrow \mu^+ \mu^-$  signal box in  $p_t^2$  and invariant mass

## 9.2 Muon Particle Id Cuts

The standard E871 particle identification routines combine the selection criteria in the Čerenkov counter, Lead Glass Array, Muon Hodoscope, Muon Range finder and Trigger scintillators to perform a track associated evaluation of particle type for the given track. For each particle type an identification label of *Good*, *Possible*, or *False* is assigned. For the analysis of the  $K_L^0 \rightarrow \mu^+ \mu^-$  and  $K_L^0 \rightarrow \mu^+ \mu^- e^+ e^-$  data streams the **Electron** and **Muon** identification labels were examined to determine event type.

Any primary track receiving an **Electron** ID rating of *Good* was vetoed to remove contamination of the data stream from  $K_{e3}$  events. This electron veto did not affect  $K_L^0 \rightarrow \mu^+ \mu^- e^+ e^-$  acceptance due to the low invariant mass reconstruction of  $\mu e$  primary track events as shown in Fig. 4.2(b). Primary tracks with an **Electron** ID rating of *Possible* were not vetoed if the track was also flagged with a *Possible* or *Good*, **Muon** ID rating. This preserved acceptance to muon tracks above the Čerenkov threshold in hydrogen, as well as those muons with a lead glass E/P value close to one placing them above the pion/electron contour cut as shown in Fig. 9.4.

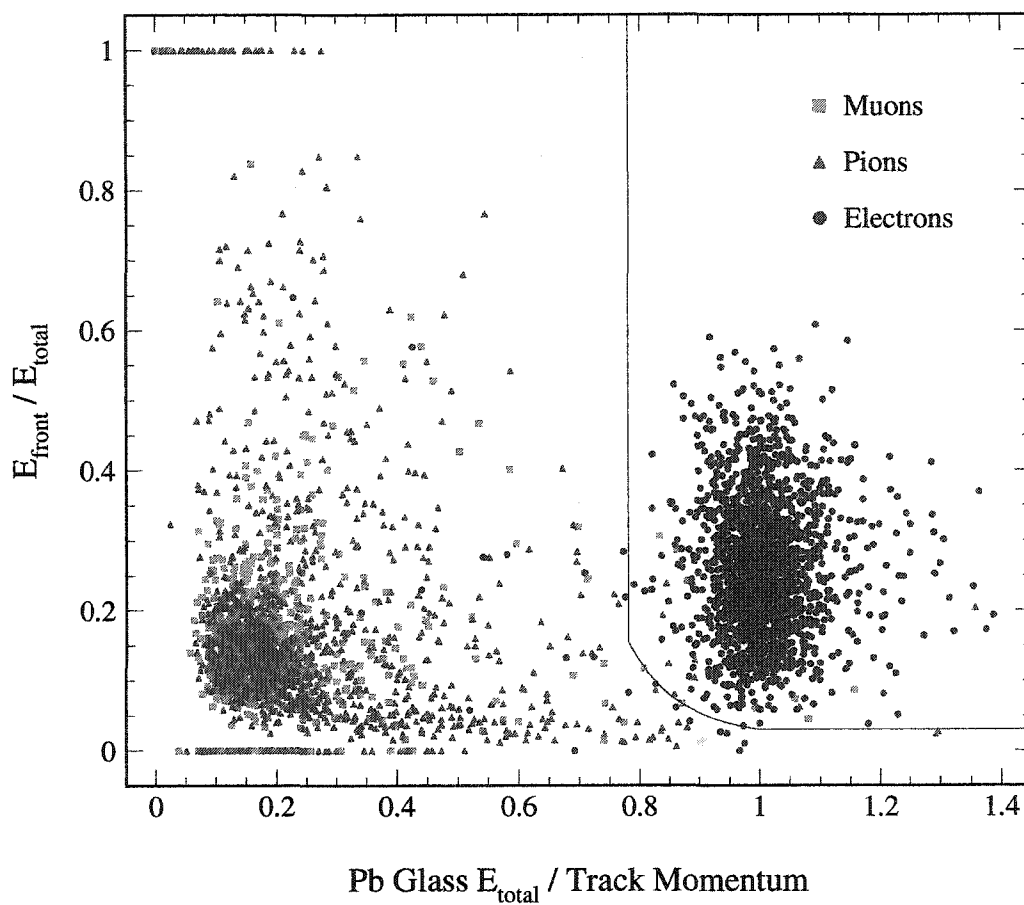


FIG. 9.4: Lead glass array electron/pion separation contour

Tracks with a **Muon** ID rating of *Good* were retained and assumed to be valid muons. Tracks with a **Muon** ID rating of *Possible* were retained and combined with the TSC ID routines before being assumed as a valid muon.

These particle identification labels were applied to both the  $K_L^0 \rightarrow \mu^+\mu^-$  and  $K_L^0 \rightarrow \mu^+\mu^-e^+e^-$  data streams.

## 9.3 Partial Tracking Id Cuts

For events in the  $K_L^0 \rightarrow \mu^+\mu^-e^+e^-$  data stream additional analysis cuts were performed after the general  $\mu\mu$  tracking cuts, to identify the number of partial tracking stubs related to each event. Potential partial tracking stubs identified through the search method described in section 8.3.1 were evaluated first for their relevance to the primary event vertex through a series of basic cuts related to overall event quality and stub DOCA values.

These cuts were intended to reduce background arising from accidentals in the forward straw chambers while preserving a high acceptance to the primary decay.

### 9.3.1 Segment Ambiguity Cut

Events with large numbers of in time hit clusters in SDC1/SDC2 cause reconstruction of large numbers of possible stub segments that need to be considered. Events with more than 1024 segment ambiguities are automatically cut from the analysis based on the failure to reconstruct all possible solutions. These events are considered “noisy” and contribute only to the signal background. For events with less than 1024 segment ambiguities the approximate distance of closest approach is calculated for all solutions and the segments sorted according to the resulting distance score.

The best ten ambiguity solutions are then considered when determining a successful segment to vertex match. The successful vertex match probability for signal events drops off sharply as a function of the number of stub solutions found. The percentage of events with increasing solution ambiguities is shown in Fig. 9.5.

The limit on the total number of stubs solutions found per event was set at 4 to reduce contamination in the data stream from  $K_{e3}$  and  $K_{\mu3}$  pile up as well as noise from accidentals. The event cut at 4 stubs corresponded to a 94.6% acceptance

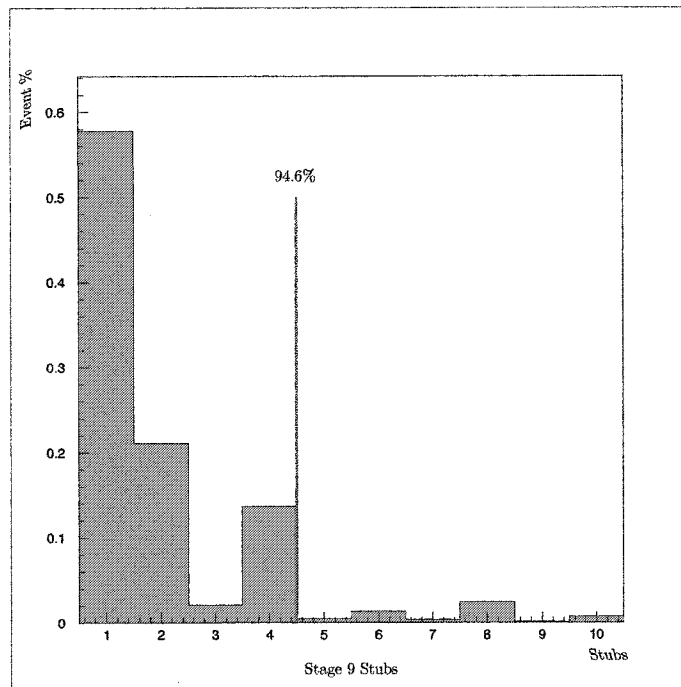


FIG. 9.5: Fraction of accepted  $K_L^0 \rightarrow \mu^+ \mu^- e^+ e^-$  events as a function of partial tracking stub solutions.

efficiency for  $K_L^0 \rightarrow \mu^+ \mu^- e^+ e^-$ .

### 9.3.2 Single Stub Vertex DOCA

Each identified stub was analyzed to determine the distance of closest approach between it and the primary vertex as reconstructed and limited in section 9.1. The DOCA value and resulting DOCA coordinates are cut on in the same manner as for the primary vertex point. Instead of a reduced  $\chi^2$  the actual value of the DOCA in meters is used as the figure of merit for the cut. The distribution is fit to a Lorentzian peak with an exponential background tail. The DOCA distribution is shown in Fig. 9.6 along with the resulting fit.

The distribution is found to peak at a centroid of 2.11cm and have a width  $\Gamma = 1.79$ cm. The cut on the vertex DOCA value is set at  $4\Gamma$  corresponding to a 95.9% efficiency for the signal region.

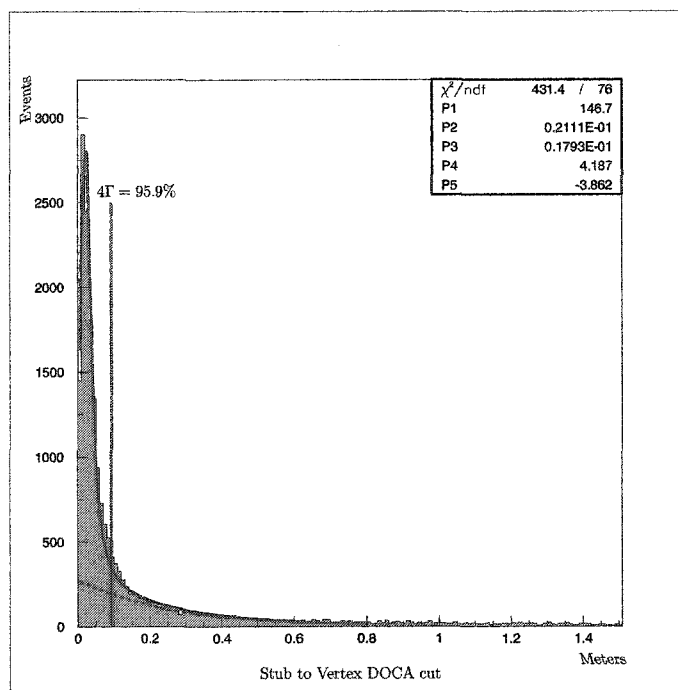


FIG. 9.6: Stub to vertex DOCA cut at  $4\Gamma = 9.27\text{cm}$ .

### 9.3.3 Stub To Stub DOCA

Events that are identified as having more than one stub candidate are analyzed in a pairwise fashion to determine the existence of a secondary vertex. The distance of closest approach as well as secondary vertex position is calculated for each pair of stubs. The DOCA between the stubs is used as the primary figure of merit for the secondary vertex. Events with intersecting stub pairs are ignored in order to properly fit the non-trial solution to the secondary vertex DOCA. The resulting distribution is fit to a Lorentzian peak on top of a flat background.

The width of the distribution is found to be  $\Gamma = 1.805\text{cm}$ , consistent with the width found for the stub to primary vertex in section 9.3.2. The centroid of the distribution is treated as zero owing to the weighting of events with intersecting stubs. An upper limit is placed upon the stub to stub distance of closest approach of  $4\Gamma = 7.22\text{cm}$  corresponding to a 95.9% efficiency for the signal region. This cut



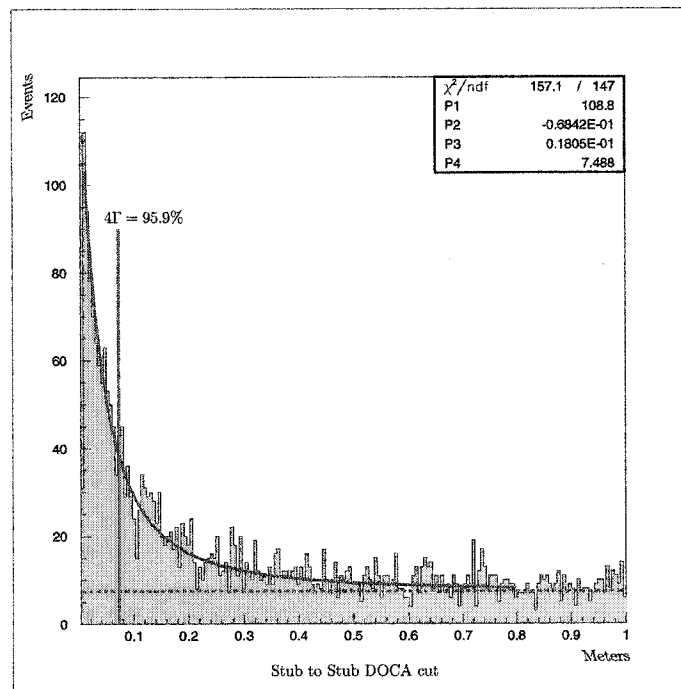


FIG. 9.7: Stub to Stub DOCA cut at  $4\Gamma = 7.22\text{cm}$ .

level is shown in Fig. 9.7.

### 9.3.4 Primary/Secondary Vertex Separation

For events with both a valid primary and secondary vertex the separation between the position of each was computed. The distance between the points was calculated in the usual fashion:

$$D_{vtx} = \sqrt{\sum_i (x_i - x'_i)^2} \quad (9.9)$$

The resulting distribution of the vertex separation is shown in Fig. 9.8. The distribution is fit to a Lorentzian peak on top of an exponential background. Signal peak was found at a centroid value of 1.71cm and had a width  $\Gamma = 2.22\text{cm}$ . The cut on the vertex DOCA value is set at  $4\Gamma = 10.59\text{cm}$  corresponding to a 95.9%

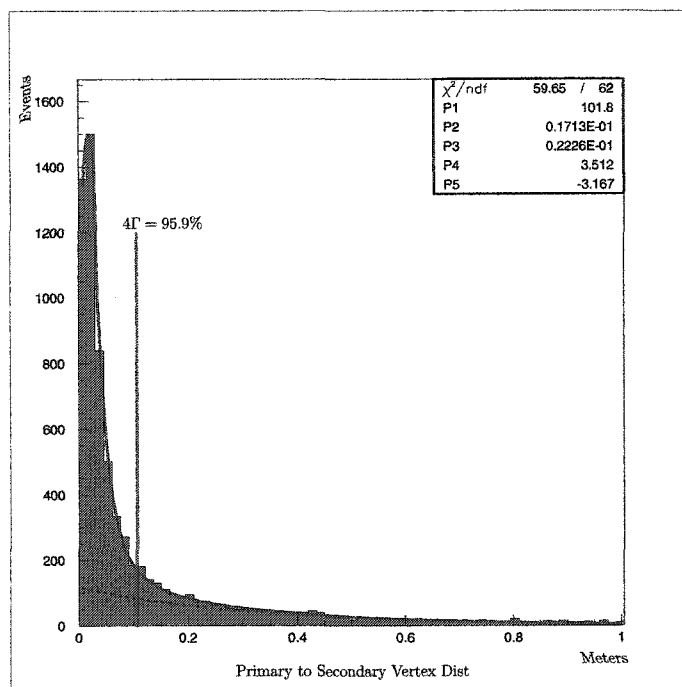


FIG. 9.8: Primary to secondary vertex separation cut at  $4\Gamma = 10.59\text{cm}$ .

efficiency for the signal region.

A summary of the all the vertex and DOCA cuts made during stub identification is shown in Table 9.7.

Value	Cut	Level	Efficiency
Max Segments	< 1024	-	-
Max Stubs	< 4	-	94.6%
Stub to Vertex DOCA	< 9.27 cm	$4\Gamma$	95.9%
Stub to Stub DOCA	< 7.22 cm	$4\Gamma$	95.9%
Primary to Secondary Vertex Dist.	< 10.59 cm	$4\Gamma$	95.9%

TABLE 9.7: Stub identification cuts summary

Secondary Vertex Parameter	Cut (QT)
$V_x$	$\pm 2.7$ mrad
$V_y$	$\pm 10.0$ mrad
$V_z$	$> 9.55$ meters
$V_z$	$< 20.6$ meters

TABLE 9.8: Secondary vertex position fiducial volume cuts based on pair-wise stub reconstruction.

### 9.3.5 Secondary Vertex Fiducial Volume Cut

Limits were placed upon the position of the secondary vertex in the same manner as the primary vertex limits described in section 9.1.1. These fiducial volume cuts were designed to remove correlated stub pairs arising from reactions of the beam halo with the steel decay tank walls or with the upstream and down stream windows. These cuts are shown in Table 9.8

## 9.4 Stub Correlation Cuts

The basic vertex and DOCA cuts described in section 9.3 were designed to separate out  $e^+e^-$  track stubs and stubs pairs from unrelated background noise based upon the spatial proximity of the stubs to the identified primary event decay point. The events from the  $K_L^0 \rightarrow \mu^+\mu^-e^+e^-$  decay mode should in addition exhibit a high degree of angular correlation to the well defined decay planes as well as a tight opening angle between the  $e^+e^-$  pair.

Placing cuts on these angular correlations helps to eliminate contamination of the data stream from background source including large angle multiple scattering and pair production in the front window of the decay tank. The angular correlations also reduce contamination of the data from  $K_{e3}$  and  $K_{\mu3}$  pileup events by forcing the decay plane alignment of paired particles.

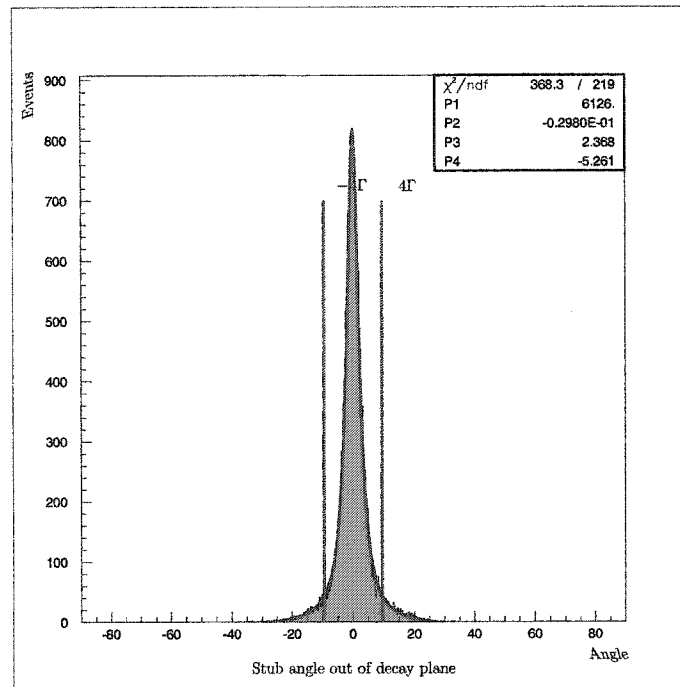


FIG. 9.9: Angle between primary decay plane and single electron stub with cut at  $4\Gamma = 9.472^\circ$

#### 9.4.1 Single Stub To Primary Decay Plane Cut

The angle at which a single stub emerges from the primary decay plane should be small for the extremely low energy electrons/positrons associated with the  $K_L^0 \rightarrow \mu^+\mu^-e^+e^-$  decay as described in section 8.3.2. The angular correlation between a single  $K_L^0 \rightarrow \mu^+\mu^-e^+e^-$  electron and the primary decay plane as shown in Fig. 9.9. The distribution is fit to a Lorentzian peak centered at  $0^\circ$  plus a small constant offset. The width of the distribution was found to be  $\Gamma = 2.368^\circ$ . The correlation cut was set at  $\pm 4\Gamma$  corresponding to a 92.0% efficiency.

#### 9.4.2 Stub To Stub Opening Angle Cut

The opening angle between the electron and positron trajectories should be small owing to the various formfactors, low total momentum of the pair, and the high

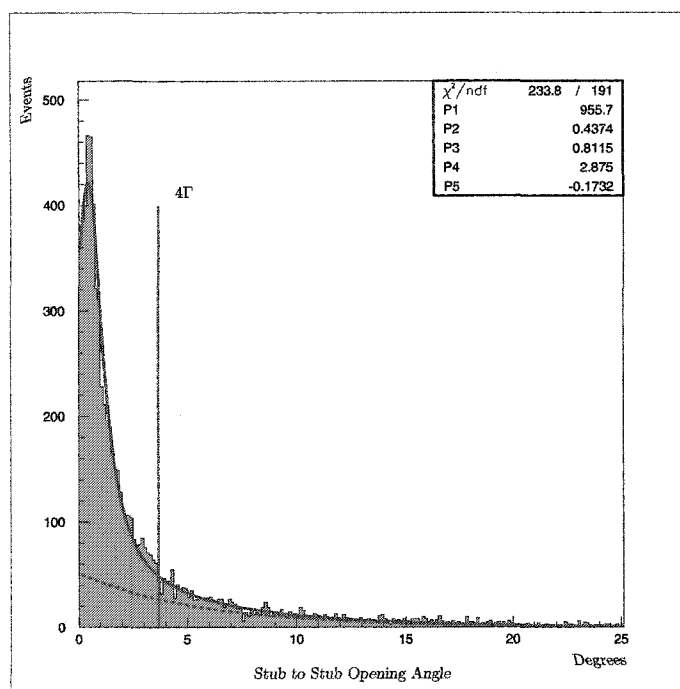


FIG. 9.10: Opening angle between  $e^-/e^+$  trajectories with cut at  $4\Gamma = 3.68^\circ$ .

relativistic boost from the CM frame to the lab reference frame. By placing an upper limit on the allowed angular separation of the stub trajectories, the events arising from  $K_L^0 \rightarrow \mu^+\mu^-e^+e^-$  can be separated from those arising from pair production on the front window of the decay tank, interactions with the residual gas in the decay tank, as well as from events with large multiple scatters forward of SDC2.

The distribution of stub opening angles for  $K_L^0 \rightarrow \mu^+\mu^-e^+e^-$  was fit to a Lorentzian peak and exponential tail. The peak's centroid was found at  $0.4374^\circ$  with a width  $\Gamma = 0.8115^\circ$ . The cut on the opening angle was set  $4\Gamma$  above the centroid at  $3.6834^\circ$  to provide a 95.9% efficiency for the signal peak. The distribution and cut are shown in Fig. 9.10.

### 9.4.3 Secondary To Primary Decay Plane Cut

The angle between the primary and secondary decay planes was computed and checked to look for the high correlation described by the allowed geometries outlined in section 8.3.3 and shown in Fig. 8.17. The computed correlation coefficient between the decay planes was used to construct the exponential distribution shown in Fig. 9.11. The distribution is fit to a double exponential for the high correlation region above a coefficient of 0.6. The primary exponential corresponding to the sharp correlation is found to have a slope  $1/\gamma = 132.6$ . The cut on the coefficient is placed  $5\gamma$  below the zero angle correlation value. The resulting value of the cut was set at 0.962 corresponding to a plane to plane angle  $\zeta = 15.7^\circ$ . This cut preserves 99.3% of the primary peak but is considered a *tight* cut due to its elimination of 55% of the secondary tail. This excluded region is thought not to contribute at substantial levels due to the other angular cuts and the low spectrometer acceptance for the decay geometry of Fig. 8.17(b).

## 9.5 Event Reconstruction Cuts

In section 9.1.5 the cuts on event reconstruction were determined for  $K_L^0 \rightarrow \mu^+\mu^-$  events by placing limits on the invariant mass and transverse momentum of the  $\mu^+\mu^-$  track pair. Cuts on event reconstruction for  $K_L^0 \rightarrow \mu^+\mu^-e^+e^-$  were determined in a similar fashion by reconstructing the invariant mass and transverse momentum using the  $\mu^+\mu^-$  pair's tracks, a three body reconstruction using the  $\mu^+\mu^-$  pair's tracks plus a single electron stub, or using a full four body reconstruction encompassing both muon tracks and both electron stubs. The resulting set of cuts provide increasingly constrained signal regions with better signal to noise resolutions.

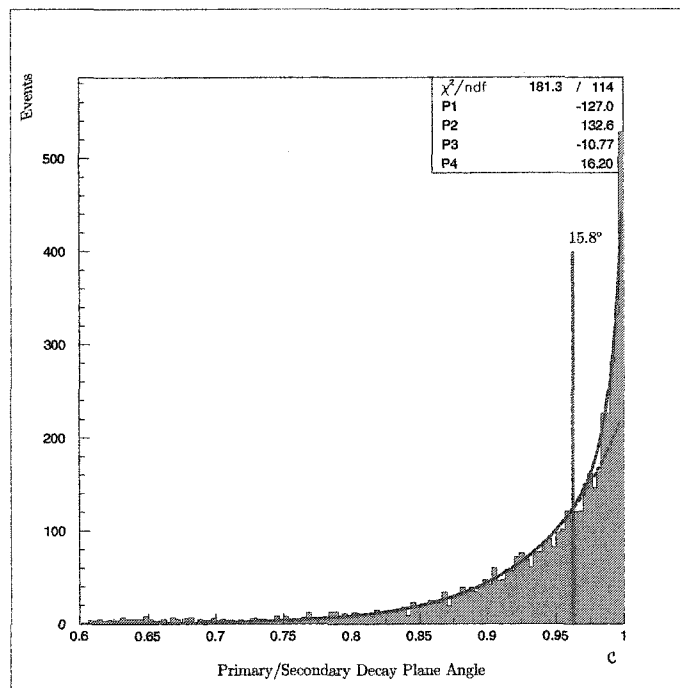


FIG. 9.11: Primary to Secondary Decay Plane Angle Cut

### 9.5.1 Invariant Mass Reconstruction Cuts

Event reconstruction for  $K_L^0 \rightarrow \mu^+ \mu^- e^+ e^-$  is performed in three stages of increasing invariant mass precision designed to separate background events from the data sample. All  $K_L^0 \rightarrow \mu^+ \mu^- e^+ e^-$  event candidates are reconstructed using a 2-body and then a 3-body invariant mass. Events with more than one identified partial tracking stub are further reconstructed using a 4-body invariant mass.

#### Two Body Invariant Mass Reconstruction Cut

Events in the  $K_L^0 \rightarrow \mu^+ \mu^- e^+ e^-$  data stream are first reconstructed using the standard two body reconstruction of  $M_K$  under the  $\mu\mu$  hypothesis. This reconstruction has the same resolution as for the  $K_L^0 \rightarrow \mu^+ \mu^-$  invariant mass reconstruction. Reconstructed masses are required to fall above  $463.5 \text{ MeV}/c^2$  to prevent contamination from double pion misidentification from the decays of the form  $K_L^0 \rightarrow \pi^+ \pi^- + X$ .

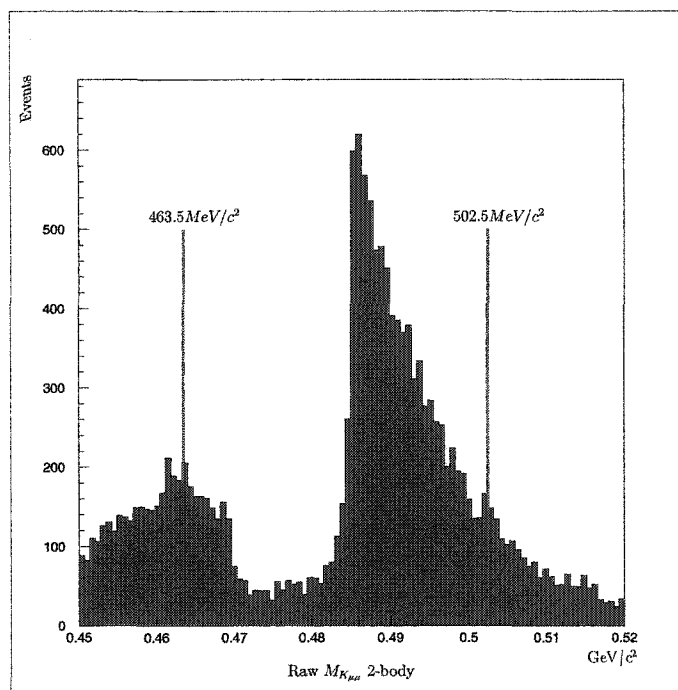


FIG. 9.12: Invariant mass cuts for two body reconstruction of  $K_L^0 \rightarrow \mu^+\mu^-e^+e^-$  under a  $\mu^+\mu^-$  hypothesis for the primary tracks.

The upper limit on the two body invariant mass was set at  $502.5 \text{ MeV}/c^2$  corresponding to the upper edge of the  $K_L^0 \rightarrow \mu^+\mu^-$  signal box. This was done to preserve similar acceptances for the two regions. Events in excess of  $502.5 \text{ MeV}/c^2$  were kept for background subtraction calculations up to  $510.0 \text{ MeV}/c^2$ .

The two-body reconstruction is shown in Fig. 9.12 with the upper and lower limits on invariant mass.

### Three Body Invariant Mass Reconstruction Cut

For events with at least one electron track stub the three body invariant mass was calculated as  $M_{K\mu\mu e}$ . The distribution was skewed towards  $M_K$  with a large low mass tail. Above the kaon mass the distribution should have a sharp drop off with tail extending out to  $520 \text{ MeV}/c^2$ . High and low mass cuts were placed on the 3-body reconstruction in a manner similar to section 9.5.1. To limit contamination



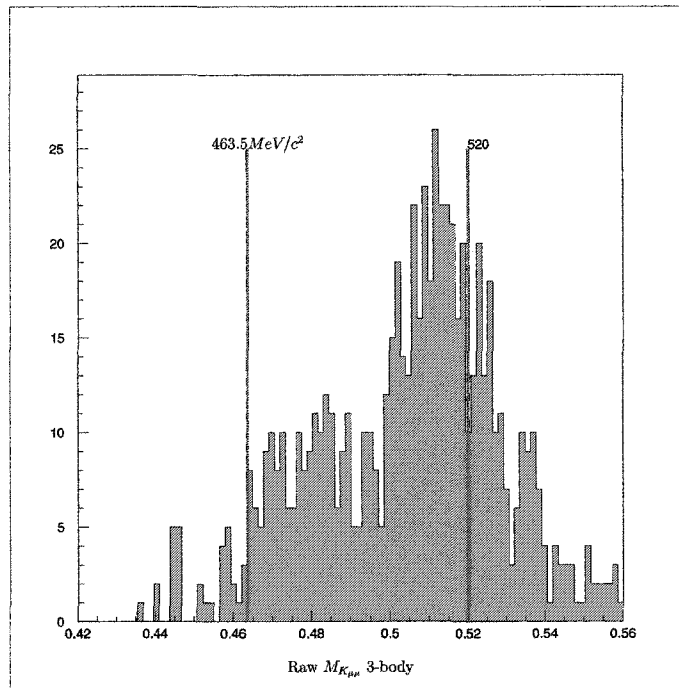


FIG. 9.13: Invariant mass cuts for three body reconstruction of  $K_L^0 \rightarrow \mu^+ \mu^- e^+ e^-$  under a  $\mu^+ \mu^-$  plus electron stub hypothesis.

from particle misidentification a lower limit mass cut was again placed at 463.5 MeV/c<sup>2</sup>. The upper limit on the 3-body invariant mass was set at 520 MeV/c<sup>2</sup> to reduce contamination from  $K_{e3}$  and  $K_{\mu3}$  pileup which have high probabilities of reconstructing under the three body hypothesis to a mass greater than 520 MeV/c<sup>2</sup>. This cut also limits possible contamination from interactions off the decay tank walls and upstream window of the form  $\eta \rightarrow \pi^+ \pi^- \gamma$  by cutting 27 MeV below the  $\eta$  mass.

These cuts are shown in Fig. 9.13 superimposed on the raw, uncut 3-body reconstruction distribution.

#### Four Body Invariant Mass Reconstruction Cut

Events in the  $K_L^0 \rightarrow \mu^+ \mu^- e^+ e^-$  data stream that had two correlated  $e^+ e^-$  stubs were reconstructed using the four body invariant mass prescription as detailed in section 8.4.1. The mass window on the reconstruction was based on the Monte

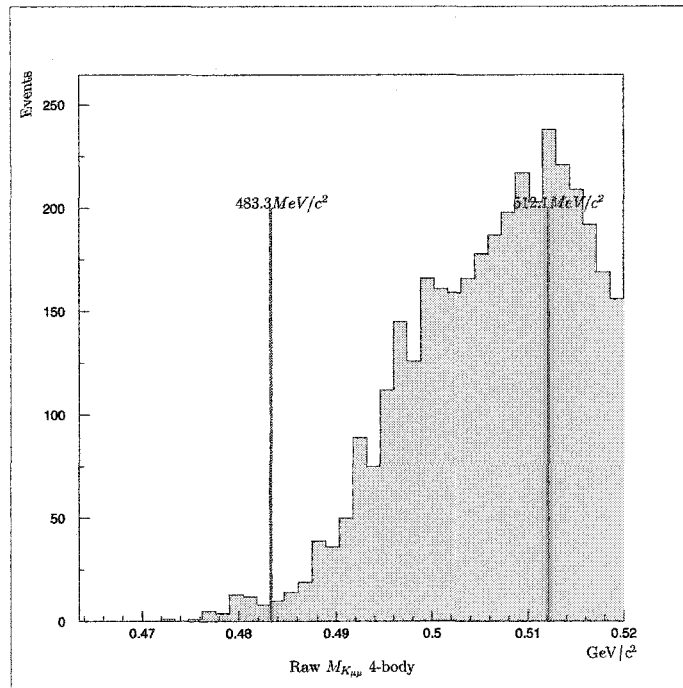


FIG. 9.14: Invariant mass cuts for full four body reconstruction of  $K_L^0 \rightarrow \mu^+ \mu^- e^+ e^-$ . Data shown includes cut on number of track stubs  $\geq 2$  and the two body  $M_{K_{\mu\mu}} > 463.5 \text{ MeV}/c^2$ .

Carlo prediction of a roughly Gaussian peak at the kaon mass of  $497.67 \text{ MeV}/c^2$  with a predicted width given by  $\sigma_m = 4.8 \text{ MeV}/c^2$ . The lower and upper bounds on the window were set at  $3\sigma$  corresponding to  $483.3 \text{ MeV}/c^2$  and  $512.1 \text{ MeV}/c^2$ .

The raw distribution of the resulting invariant mass reconstructed for the  $K_L^0 \rightarrow \mu^+ \mu^- e^+ e^-$  data stream is shown in Fig. 9.14 along with the placement of the  $\mu\mu ee$  mass window. Fig. 9.15 shows the placement of the same mass window but after application of a basic set of “rough” cuts on the events including stub to vertex DOCA and total transverse momentum.

### 9.5.2 Transverse momentum Cuts

The transverse momentum of each  $K_L^0 \rightarrow \mu^+ \mu^- e^+ e^-$  event was calculated in an N-body manner corresponding to the highest available invariant mass reconstruc-

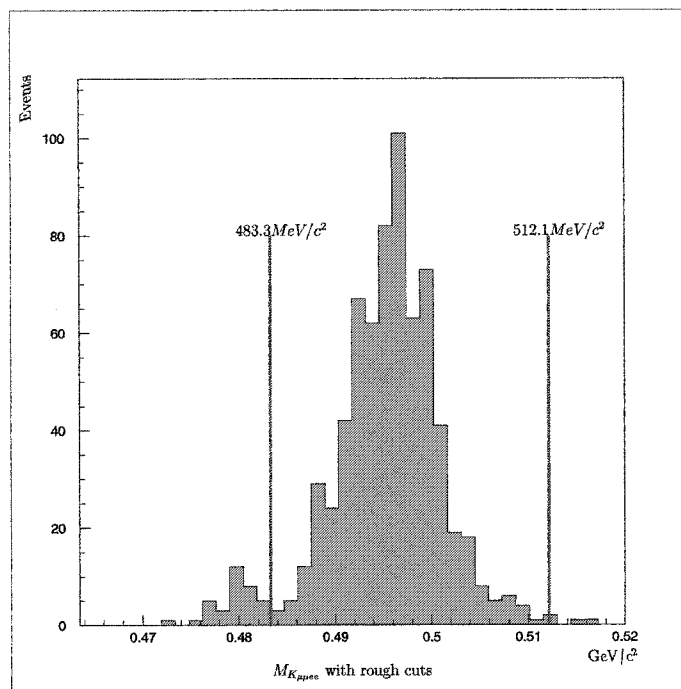


FIG. 9.15:  $K_L^0 \rightarrow \mu^+ \mu^- e^+ e^-$  invariant mass reconstruction using “rough” cuts on stub DOCA and total transverse momentum.

tion. The two body  $p_t$  from each event was used to explicitly veto on the  $K_L^0 \rightarrow \mu^+ \mu^-$  signal box as described in section 9.1.6. The three body transverse momentum was limited to 10 MeV/c for three body final state events. The four body transverse momentum of the events was similarly limited to 10 MeV/c to conform to the manner by which the  $K_L^0 \rightarrow \mu^+ \mu^-$  selection was performed.

## 9.6 Summary of Production Analysis Cuts

A summary of all cuts placed on the  $K_L^0 \rightarrow \mu^+ \mu^- e^+ e^-$  data stream is listed in Table 9.9. From these cuts the distribution for identified  $K_L^0 \rightarrow \mu^+ \mu^- e^+ e^-$  events in the signal box extending in the four body reconstructed invariant mass from 483.3 MeV/c<sup>2</sup> to 512.1 MeV/c<sup>2</sup> and in  $p_t$  below 10 MeV/c was determined. This distribution is discussed fully in Chapter 10.

Cut Parameter	Value	Notes
$V_x$	$\pm 2.7\text{mrad}$	
$V_y$	$\pm 10.0\text{mrad}$	
$V_z$	9.55–20.6meters	
$V'_x$	$\pm 0.0027\text{mrad}$	
$V'_y$	$\pm 0.0100\text{mrad}$	
$V'_z$	9.55–20.6meters	
$P_{\mu^\pm}$	1.05 – 6.5GeV/c	
$\chi_{trk}^2 (FT)$	25	
$\chi_{trk}^2 (QT)$	35	
$\chi_{vtx}^2 (FT)$	30	
$\chi_{vtx}^2 (QT)$	15	
$M_{K_{\mu\mu}} (FT)$	493.5 – 502.0MeV/c <sup>2</sup>	$K_L^0 \rightarrow \mu^+\mu^-$ signal box veto
$M_{K_{\mu\mu}} (QT)$	493.0 – 502.5MeV/c <sup>2</sup>	$K_L^0 \rightarrow \mu^+\mu^-$ signal box veto
$P_t$	10MeV/c	$K_L^0 \rightarrow \mu^+\mu^-$ signal box veto
$\mu - ID (Left/Right)$	<i>Good/Golden</i>	
Total Segments	1024	
Total Stubs	4	
Stub to Vertex DOCA	9.27cm	
Vertex to Vertex Dist.	10.59cm	
Stub to Decay Plane $\sphericalangle$	9.472°	
Stub to Stub Opening $\sphericalangle$	3.68°	
Primary to Secondary Plane $\sphericalangle$	15.8°	
2-Body $M_{K_{\mu\mu}}$ (Low)	463.5MeV/c <sup>2</sup>	Pion Mis-ID background
2-Body $M_{K_{\mu\mu}}$ (High)	502.5MeV/c <sup>2</sup>	
4-Body $M_{K_{\mu\mu ee}}$ (Low)	483.3MeV/c <sup>2</sup>	
4-Body $M_{K_{\mu\mu ee}}$ (High)	512.1MeV/c <sup>2</sup>	
4-Body $P_t$	10MeV/c	

TABLE 9.9: Listing of cuts performed on the  $K_L^0 \rightarrow \mu^+\mu^-e^+e^-$  data stream to obtain the final signal distribution shown in Fig.10.3.

# CHAPTER 10

## Normalization

Normalization of the  $K_L^0 \rightarrow \mu^+\mu^-e^+e^-$  data set was performed by comparing the observed number of events in the  $K_L^0 \rightarrow \mu^+\mu^-e^+e^-$  signal peak to the observed number of events in the  $K_L^0 \rightarrow \mu^+\mu^-$  signal peak. The event ratio was multiplied by the world average for the branching ratio  $B(K_L^0 \rightarrow \mu^+\mu^-)$ [12] and by the ratio of the total acceptances for  $K_L^0 \rightarrow \mu^+\mu^-$  to  $K_L^0 \rightarrow \mu^+\mu^-e^+e^-$  yields the branching fraction for  $K_L^0 \rightarrow \mu^+\mu^-e^+e^-$ . The efficiencies for Level 1 and Level 3 triggers, muon identification, tracking and vertex reconstruction, and stub finding were included as ratios for the two data streams.

$$\begin{aligned} \frac{B(K_L^0 \rightarrow \mu^+\mu^-e^+e^-)}{B(K_L^0 \rightarrow \mu^+\mu^-)} &= \frac{N_{\mu\mu ee}}{N_{\mu\mu}} \cdot \frac{\mathcal{A}_{\mu\mu}}{\mathcal{A}_{\mu\mu ee}} \times \left( \frac{\epsilon_{\mu\mu}^{L1}}{\epsilon_{\mu\mu ee}^{L1}} \right) \times \left( \frac{\epsilon_{\mu\mu}^{L3}}{\epsilon_{\mu\mu ee}^{L3}} \right) \\ &\times \left( \frac{\epsilon_{\mu\mu}^{\mu-ID}}{\epsilon_{\mu\mu ee}^{\mu-ID}} \right) \times \left( \frac{\epsilon_{\mu\mu}^{trk}}{\epsilon_{\mu\mu ee}^{trk}} \right) \times \left( \frac{\epsilon_{\mu\mu}^{vtx}}{\epsilon_{\mu\mu ee}^{vtx}} \right) \times \left( \frac{1}{\epsilon_{\mu\mu ee}^{stubs}} \right) \end{aligned} \quad (10.1)$$

The efficiencies for the trigger, muon identification, primary muon tracking, and primary vertex reconstruction are based upon a similar kinematic event profile and the same set of cut values for the  $K_L^0 \rightarrow \mu^+\mu^-$  and  $K_L^0 \rightarrow \mu^+\mu^-e^+e^-$  data. The ratios of these efficiencies are therefore treated as unity for the purpose of the normalization.

The efficiency for the stub reconstruction was computed from the Monte Carlo using the known distributions and final cut values.

For the purpose of this normalization the stub efficiency was calculated as part of the effective acceptance ratio due to correlations between the geometric acceptance  $\mathcal{A}_{\mu\mu e}$  and  $\epsilon^{stub}$ . The error on  $\epsilon^{stub}$  was however calculated independently by consideration of the individual cut efficiencies. For the purpose of systematic error propagation  $\epsilon^{stub}$  is treated as:

$$\epsilon_{\mu\mu e}^{stub} = 0.766 \pm 0.022 \quad (10.2)$$

## 10.1 $K_L^0 \rightarrow \mu^+ \mu^-$ Data Sample

The analysis of the E871 data using the cuts described in section 9.1 yielded the signal peaks for the FT and QT fitters shown in Fig. 10.1 and Fig. 10.2. The peaks were fit to a Gaussian distribution plus a decaying exponential background tail. The data were integrated between 493.5 MeV/c<sup>2</sup> and 502.0 MeV/c<sup>2</sup> to obtain a total of 6069 events in the signal region for  $K_L^0 \rightarrow \mu^+ \mu^-$  under FT reconstruction. Using QT reconstruction the signal region resulted in 6133 events.

The background in the signal region was subtracted using the fit to the decaying exponential as calculated separately for the FT and the QT distributions. The data were binned at intervals of  $\Delta x = 0.25$  MeV/c<sup>2</sup> resulting in the integrated backgrounds:

$$\int_{0.4935}^{0.5020} (e^{106.0-208.2x}) dx = 412.43 \text{ events (FT)} \quad (10.3)$$

Method	Signal	Background	Total
FT	$5657 \pm 75$	$412.43 \pm 20.29$	6069
QT	$5714 \pm 76$	$419.42 \pm 20.47$	6133
Average	$5685 \pm 75$	$415.5 \pm 20.38$	6101

TABLE 10.1:  $K_L^0 \rightarrow \mu^+\mu^-$  signal and background events as observed in the E871 data set and reconstructed under FT and QT fitting.

$$\int_{0.4935}^{0.5020} (e^{102.5-201.4x}) dx = 419.42 \text{ events (QT)} \quad (10.4)$$

The actual number of  $K_L^0 \rightarrow \mu^+\mu^-$  events is obtained from a subtraction of the background calculation from the total events found within the signal region. Table 10.1 summarizes the signal and background for the  $K_L^0 \rightarrow \mu^+\mu^-$  data sample.

## 10.2 $K_L^0 \rightarrow \mu^+\mu^-e^+e^-$ Data Sample

The analysis of the E871 data using the cuts described in section 9.6 yielded the signal peak shown in Fig.10.3. The central peak was fit to a Gaussian plus a flat background as indicated by the sidebands below 483.3 MeV/c<sup>2</sup> and above 512.1 MeV<sup>2</sup>, in a fashion similar to that used for the  $K_L^0 \rightarrow \mu^+\mu^-$  data. The distribution was integrated over the signal box region to obtain the total number of number of events in the  $K_L^0 \rightarrow \mu^+\mu^-e^+e^-$  signal region.

Background events arising from pion misidentification dominates the distribution as discussed in section 4.4.2 and was manifest in the residual distribution seen below 483.3 MeV/c<sup>2</sup>. This background was projected under the signal region using a 1.03 MeV/c<sup>2</sup> bin size and integrated to determine the level of contamination due to background. The contribution to the signal region arising from background was found to be  $57.56 \pm 7.6$  events. By moving the low side of the 2-body invariant mass

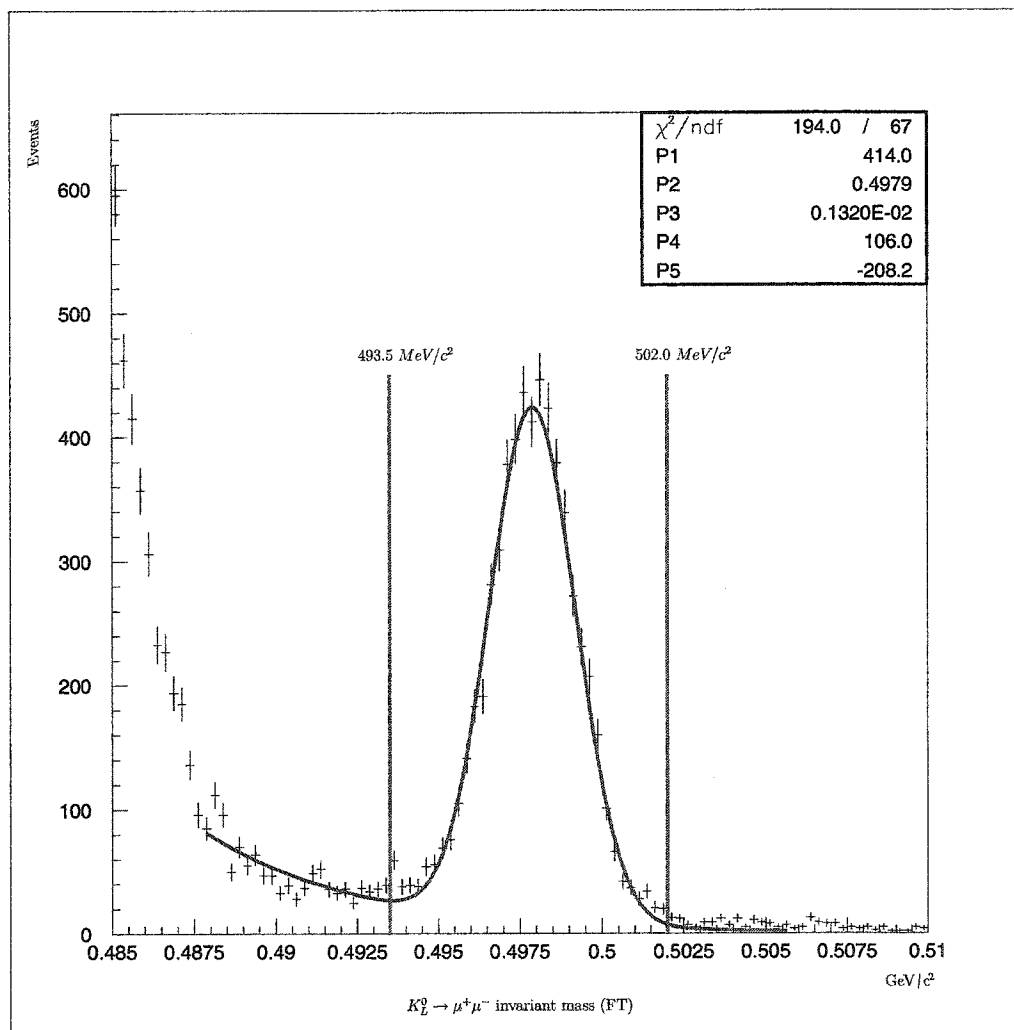


FIG. 10.1:  $K_L^0 \rightarrow \mu^+ \mu^-$  invariant peak showing 6069 events in the signal region consisting of  $5657 \pm 75$  signal events on an exponential background of  $412 \pm 20$  events.



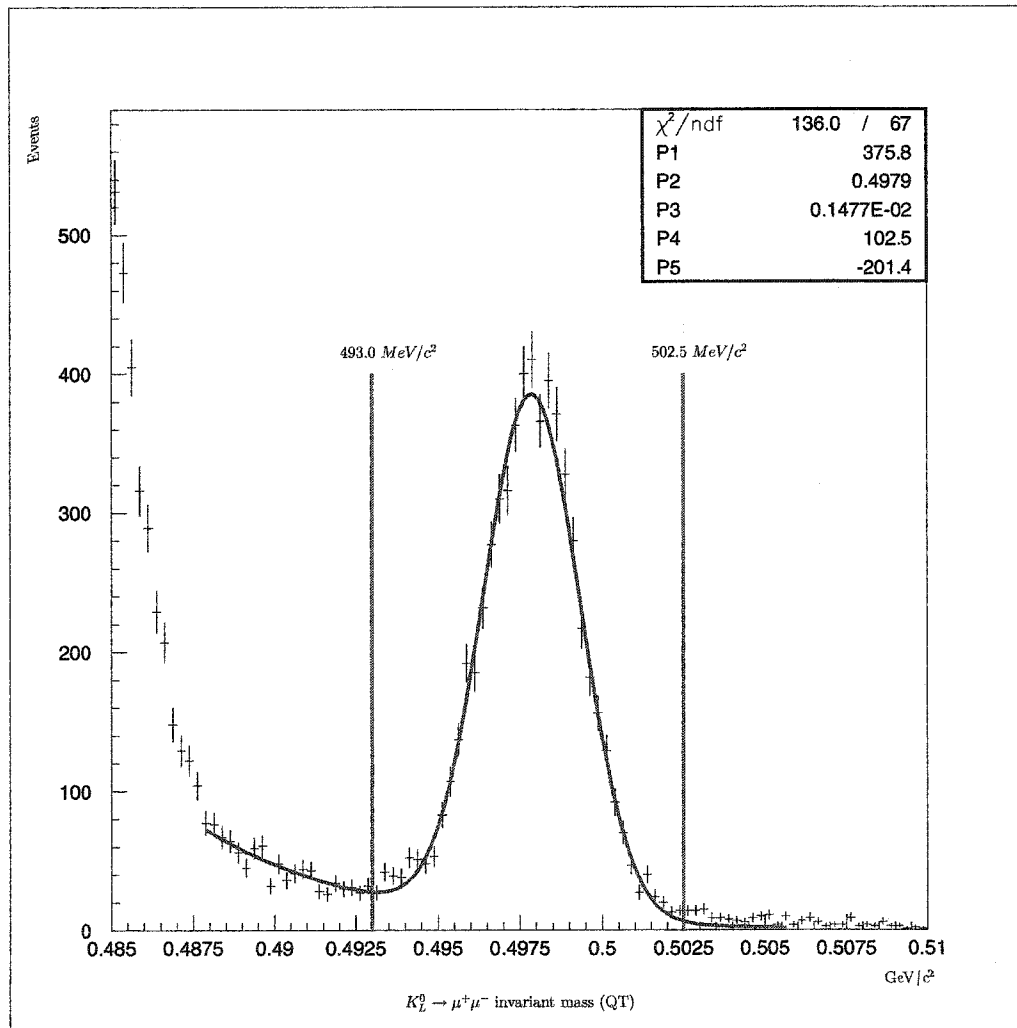


FIG. 10.2:  $K_L^0 \rightarrow \mu^+ \mu^-$  invariant peak showing 6133 events in the signal region consisting of  $5714 \pm 76$  signal events on an exponential background of  $419 \pm 20$  events.

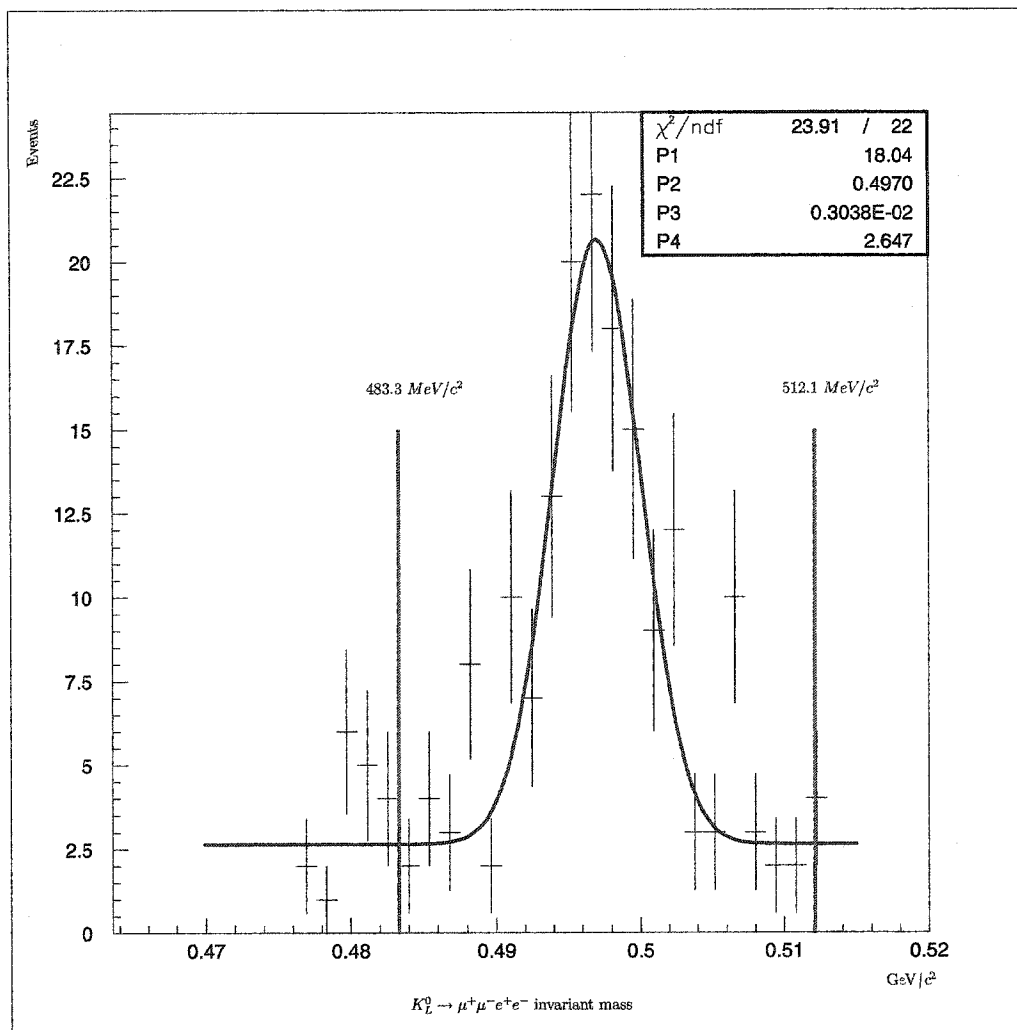


FIG. 10.3:  $K_L^0 \rightarrow \mu^+ \mu^- e^+ e^-$  invariant peak showing 171 events in the signal region composed of 119 signal and 52 background events

reconstruction window from  $463.5 \text{ MeV}/c^2$  to  $470.0 \text{ MeV}/c^2$  the contamination of the signal region was reduced to  $51.75 \pm 7.2$  events.

After proper background subtraction and error analysis as described in section 11.2.1 the  $K_L^0 \rightarrow \mu^+ \mu^- e^+ e^-$  peak was computed to contain  $119.25 \pm 17.31$  events satisfying the strongest signal criteria.

## 10.3 Acceptances

The ratio of acceptances  $\mathcal{A}_{\mu\mu}/\mathcal{A}_{\mu\mu e}$  including the stub finder efficiency  $\epsilon^{stubs}$  was calculated through Monte Carlo simulation of  $9.4 \times 10^6 K_L^0 \rightarrow \mu^+\mu^-$  events and  $1.3 \times 10^7 K_L^0 \rightarrow \mu^+\mu^-e^+e^-$  events. To prevent correlated errors between the geometric acceptance and the stub finder efficiency, factors  $\mathcal{A}_{\mu\mu e}$  and  $\epsilon^{stubs}$  were combined to provide the effective geometric efficiency for  $K_L^0 \rightarrow \mu^+\mu^-e^+e^-$  under the analysis conditions.

$$\mathcal{A}'_{\mu\mu e} = \mathcal{A}_{\mu\mu e} \times \epsilon^{stubs} \quad (10.5)$$

The full set of cuts described in section 9.6 were applied to simulated data sets of  $N_{\mu\mu}^{sim}$  and  $N_{\mu\mu e}^{sim}$  total events. From the simulated data sets the number of events in  $K_L^0 \rightarrow \mu^+\mu^-$  and  $K_L^0 \rightarrow \mu^+\mu^-e^+e^-$  Monte Carlo signal peaks,  $N_{\mu\mu}^{MC}$  and  $N_{\mu\mu e}^{MC}$ , were counted. The ratio of the number of events in each of the resulting signal regions to the total number of simulated events in each data stream was computed to obtain the relative acceptance ratio:

$$\frac{\mathcal{A}_{\mu\mu}}{\mathcal{A}'_{\mu\mu e}} = \frac{N_{\mu\mu}^{MC} N_{\mu\mu e}^{Total}}{N_{\mu\mu e}^{MC} N_{\mu\mu}^{Total}} \quad (10.6)$$

The acceptance ratio  $\mathcal{A}_{\mu\mu}/\mathcal{A}'_{\mu\mu e}$  was calculated separately for each of the applicable form factors discussed in chapter 3. The acceptance ratios as well as individual geometric acceptances  $\mathcal{A}_{\mu\mu}$  and  $\mathcal{A}'_{\mu\mu e}$  are listed in Table 10.2.

## 10.4 Model Dependent Normalization

The normalization of the observed 119  $K_L^0 \rightarrow \mu^+\mu^-e^+e^-$  events to the observed 5685  $K_L^0 \rightarrow \mu^+\mu^-$  events was computed in accordance with Eq. (10.1) using the

Theory	$\mathcal{A}_{\mu\mu}$	$\mathcal{A}_{\mu\mu ee}$	$\mathcal{A}_{\mu\mu}/\mathcal{A}'_{\mu\mu ee}$
$\chi$ PT	$1.900 \times 10^{-2}$	$1.036 \times 10^{-3}$	18.329
QCD	$1.900 \times 10^{-2}$	$1.589 \times 10^{-5}$	1196.090
Uniform ( $F = 1$ )	$1.900 \times 10^{-2}$	$1.224 \times 10^{-6}$	15522.876
VDM	$1.900 \times 10^{-2}$		

TABLE 10.2: Acceptance Ratios for the form factor models considered in the  $K_L^0 \rightarrow \mu^+\mu^-e^+e^-$  analysis.

Theory	$B(K_L^0 \rightarrow \mu^+\mu^-e^+e^-)$	$\sigma$ statistical	$\sigma$ systematic
$\chi$ PT	$2.78 \times 10^{-9}$	$\pm 0.406 \times 10^{-9}$	$\pm 0.091 \times 10^{-9}$
QCD	$1.81 \times 10^{-7}$	$\pm 0.265 \times 10^{-7}$	$\pm 0.059 \times 10^{-7}$
Uniform ( $F = 1$ )	$2.36 \times 10^{-6}$	$\pm 0.344 \times 10^{-6}$	$\pm 0.077 \times 10^{-6}$

TABLE 10.3:  $K_L^0 \rightarrow \mu^+\mu^-e^+e^-$  normalized branching ratio for each of the form factor models considered in the  $K_L^0 \rightarrow \mu^+\mu^-e^+e^-$  analysis.

different acceptance ratios shown in Table 10.2 for each model. The world average for the branching fraction  $B(K_L^0 \rightarrow \mu^+\mu^-) = 7.25 \pm 0.16 \times 10^{-9}$  was used as the baseline for the normalization. The effective branching fractions for  $K_L^0 \rightarrow \mu^+\mu^-e^+e^-$  computed in this manner are listed in Table 10.3 for each of the major theories considered in the analysis.

# CHAPTER 11

## Results and Conclusions

### 11.1 Results

The observation of  $119 \pm 17.3 K_L^0 \rightarrow \mu^+ \mu^- e^+ e^-$  signal events in a Gaussian peak centered at  $497 \text{ MeV}/c^2$  with a measured reconstruction resolution  $\sigma_m = 3.0 \text{ MeV}/c^2$  was found to match the predicted width and characteristics of the Monte Carlo simulations based upon the use of a  $\chi$ P T formfactor exhibiting enhancement of the high  $\mu\mu$  invariant mass region of the decay's phase space. Background contributing to the signal region was removed through subtraction based on fitting of the sidebands of the distribution. The identified background was attributed to a combination of  $K_L^0 \rightarrow \pi^+ \pi^- \gamma$  and  $K_L^0 \rightarrow \pi^+ \pi^- e^+ e^-$  events with double pion misidentification occurring near the endpoint of the reactions resulting in a two body reconstruction of the invariant mass under the false  $\mu\mu$  hypothesis at the upper limit of  $463.5 \text{ MeV}/c^2$ . Due to the finite resolution of the wire detectors, the reconstructions for this type of decay was found to extend slightly above the kinematic endpoint. The background pion misidentification was reduced by placing a  $4\sigma$  extension based on the reconstruction resolution, on the cut window placed on the lower two-body invariant

mass. This procedure extended the lower limit of the region from  $463.5 \text{ MeV}/c^2$  to  $470.0 \text{ MeV}/c^2$ . The other sources of background are consistent with multi-event pile up of the semi-leptonic decays  $K_{e3}$  and  $K_{\mu 3}$  with single pion misidentification. The contribution from pile up was found to provide a linear background as extrapolated from the sidebands to the central distribution. The contribution from all sources of background in the  $K_L^0 \rightarrow \mu^+ \mu^- e^+ e^-$  signal region was calculated at the level of 52 total events in the sample.

The branching fraction for  $K_L^0 \rightarrow \mu^+ \mu^- e^+ e^-$  was calculated using the observed 119 signal events normalized to a simultaneous measurement of 5685 events identified as  $K_L^0 \rightarrow \mu^+ \mu^-$ . Using the accepted world average for  $B(K_L^0 \rightarrow \mu^+ \mu^-) = 7.25 \times 10^{-9}$  the branching fraction  $B(K_L^0 \rightarrow \mu^+ \mu^- e^+ e^-)$  was calculated to be  $2.78 \pm 0.406 \pm 0.091 \times 10^{-9}$  under the conditions of a non-uniform form factor derived from the chiral perturbation theory of Goity and Zhang [23][22][24]. The resulting branching fraction is consistent with the previous world average of  $2.6 \pm 0.4 \times 10^{-9}$  to within less than one standard error.

In addition to the  $\chi$ Pt model of the  $K_L^0 \rightarrow \gamma^* \gamma^*$  vertex, the Quark/QCD model of Ambrosio, Isidori and Portol e [20], and the VDM model of Quigg and Jackson [46] were analyzed in relation to the acceptances of each resulting  $K_L^0 \rightarrow \mu^+ \mu^- e^+ e^-$  distribution in the E871 detector apparatus. None of the other models considered with non-uniform form factors for the  $K_L^0 \rightarrow \gamma^* \gamma^*$  vertex was found to be consistent with the data. In addition, the hypothesis of a uniform distribution was tested and found to be incompatible with the observed experimental signal.

## 11.2 Errors

The errors present in the measurement of  $B(K_L^0 \rightarrow \mu^+ \mu^- e^+ e^-)$  were divided into those arising from the statistical representation of the data, and those arising

from systematic inefficiencies of the analysis and experimental equipment.

### 11.2.1 Statistical Error ( $\sigma_{stat}$ )

The total statistical error in the data sample was computed by adding in quadrature the contributions from the signal and the subtracted background. A systematic error on the background was included to account for fluctuations in the fitting and subtractions of the side bands. This systematic error was obtained in terms of the fractional error  $P$  in the background, computed to be 16.8% from the fitting errors.

$$\sigma_{BG}^{sys} = P * N_{BG} \quad (11.1)$$

The resulting error on the signal was determined as:

$$\sigma_S^2 = (\sigma_{Total})^2 + (\sigma_{BG})^2 + (\sigma_{BG}^{sys})^2 \quad (11.2)$$

In this manner the statistical error on the  $K_L^0 \rightarrow \mu^+ \mu^- e^+ e^-$  data signal was calculated to be  $\sigma_{\mu\mu ee} = \pm 17.31$  events. This corresponded to a 14.5% statistical error on the signal.

In a similar manner the statistical error on the  $K_L^0 \rightarrow \mu^+ \mu^-$  data set was calculated to be  $\sigma_{\mu\mu} = \pm 83.35$  events including a 5% systematic error in the background subtraction. This corresponded to a 1.46% statistical error on the normalization sample.

The calculation of the branching fraction involved the ratio of these quantities

and as such the statistical error in the branching fraction was computed as:

$$\sigma_{B(K_L^0 \rightarrow \mu^+ \mu^- e^+ e^-)^2} = \sqrt{\frac{N_{\mu\mu ee}^2}{N_{\mu\mu}^2} \left( \frac{\sigma_{\mu\mu}^2}{N_{\mu\mu}^2} + \frac{\sigma_{\mu\mu ee}^2}{N_{\mu\mu ee}^2} \right)} \times B(K_L^0 \rightarrow \mu^+ \mu^-) \times \mathcal{A}_{\mu\mu} / \mathcal{A}'_{\mu\mu ee} \quad (11.3)$$

For the chiral model this results in a statistical error on the branching fraction  $\sigma_{stat} = 0.406 \times 10^{-9}$ .

### 11.2.2 Systematic Error ( $\sigma_{sys}$ )

Due to the fact that the branching fraction depends on the ratio of the  $K_L^0 \rightarrow \mu^+ \mu^-$  to  $K_L^0 \rightarrow \mu^+ \mu^- e^+ e^-$  geometric and cut efficiencies, which equaled unity, the systematic errors of the final branching fraction were isolated to the acceptance ratio  $\mathcal{A}_{\mu\mu} / \mathcal{A}'_{\mu\mu ee}$ . This ratio is broken down into the ratio of the pure geometric acceptances and the efficiency of all cuts related to the identification of the  $e^+ e^-$  pair.

$$\mathcal{A}_{\mu\mu} / \mathcal{A}'_{\mu\mu ee} = \mathcal{A}_{\mu\mu} / \mathcal{A}_{\mu\mu ee} \times \frac{1}{\epsilon_{stubs}} \quad (11.4)$$

The systematic error on the geometric acceptances is taken from the  $K_L^0 \rightarrow \mu^+ \mu^-$  analysis[41] in terms of the effects of the  $K_L^0 \rightarrow \mu^+ \mu^-$  cut efficiencies. In this manner it is determined that  $\sigma_{\mathcal{A}} \approx 0.9\%$  for this analysis.

The systematic errors associated with the  $e^+ e^-$ -stub cuts were determined by adding in quadrature the errors associated with each of the cuts listed in Table 9.9. The resulting total fractional systematic error was determined to be on the order of  $\sigma_{stub} = 2.23\%$

The combined systematic error for the branching fraction was found by adding the systematic errors of the Monte Carlo acceptances and the  $e^+ e^-$ -stub efficiencies in quadrature with the error on the  $K_L^0 \rightarrow \mu^+ \mu^-$  branching fraction. The resulting



fractional systematic error was calculated at 3.27%. The systematic error on the branching fraction  $B(K_L^0 \rightarrow \mu^+\mu^-e^+e^-)$ , with a  $\chi$ PT form factor, was found to be:

$$\sigma_{sys} = \pm 0.091 \times 10^{-9} \quad (11.5)$$

### 11.3 Conclusions

The measurement of  $B(K_L^0 \rightarrow \mu^+\mu^-e^+e^-)$  has provided a self consistent measure of the long distance dispersive amplitude  $\mathcal{A}_{LD}$  that is required for extraction of the  $\rho$  parameter in the Wolfenstein formulation of the CKM matrix from the measurement of  $B(K_L^0 \rightarrow \mu^+\mu^-)$  as reported by the E871 collaboration[2]. This side-by-side measurement should reduce the systematic errors involved in the previous extraction procedure which relied upon a QED calculation of the ratio of partial width  $\Gamma(K_L^0 \rightarrow \mu^+\mu^-)_{\gamma\gamma}/\Gamma(K_L^0 \rightarrow \gamma\gamma)$  instead of on a direct measure of the long distance amplitude.

In addition, the measurement of the branching ratio  $B(K_L^0 \rightarrow \mu^+\mu^-e^+e^-)$  from the E871 data set was designed as a sensitive probe into the structure of the  $K_L^0 \rightarrow \gamma^*\gamma^*$  vertex and the formfactors that mediate this reaction. The unique sensitivity of the experimental apparatus to slight differences in the shape of the invariant mass distribution for  $K_L^0 \rightarrow \mu^+\mu^-e^+e^-$  near the kaon mass provided a method in which to determine definitively the validity of competing theories regarding this  $\Delta S = 1$  transition. The result of this measurement has been to provide strong evidence for the existence of a  $\chi$ PT formfactor that provides enhancement to the high mass region of the phasespace while excluding all other theories considered herein based on their inconsistency with the with the observed signal.

Following the results of this measurement, additional investigation into the presence of chiral like formfactors in the kaon system should be conducted. In

particular, the four lepton final state of the decay  $K_L^0 \rightarrow e^+e^-e^+e^-$  should be examined to determine the structure of the resulting phasespace. This research can also be extended to include other flavor changing neutral current processes in energy regimes where the validity of the chiral approach is likely to apply.

## 11.4 Collaborative Effort and Contributions

The work presented here is the result of a collaborative effort started in 1992 and extending over the course of nearly 12 years to today. I began my work with the E871 collaboration in the summer of 1994 during the construction and tuning of the experimental apparatus. At that time I worked primarily with the Muon Ranger Finder system and the hydrogen Čerenkov counter in their maintenance, construction and tuning of the detectors and associated electronics. I continued my work on E871 in the winter of 1994/1995 and assisted in running data shifts during the 1995 run period. In 1997 I took part in the auxiliary experiment, E935, which was run using the E871 apparatus. During this period I extended my involvement with the project to include work on the lead glass array and level 1 trigger electronics.

Since the end of the E871/E935 experimental runs I have worked on the prospect of measuring the decay  $K_L^0 \rightarrow \mu^+\mu^-e^+e^-$ . This work has included extensive work on developing Monte Carlo models that accurately portray the varied characteristics of the decay branch under the effects of the form factors discussed previously. After the process of modeling the decay and determining the possibility for seeing  $K_L^0 \rightarrow \mu^+\mu^-e^+e^-$  at E871 my work focused on the development of analysis tools that could detect the unique signature of the decay. This work led to the development of the current partial track identification algorithms and development of reconstruction methods based on them. In the final phases of my graduate career I have analyzed the data and extracted in an unbiased fashion the results presented

in this dissertation.

The E871 collaboration provided a unique opportunity for individuals to take part in every level of the experimental process, and provided valuable training and insight into the nature of experimental physics.

Andrew J. Norman  
January 3, 2004

# APPENDIX A

## E871 Collaboration

### BNL E871 Collaboration

D. Ambrose, S. Graessle, G. W. Hoffmann, J. McDonough, A. Milder, P.J. Riley,  
J.L. Ritchie, V.I. Vassilakopoulos, C.B. Ware, S. Worm  
*University of Texas, Austin, Texas 78712*

C. Arroyo, K.M. Ecklund, K. Hartman, M. Hebert, G.M. Irwin, M. Pommot-Maia,  
S.G. Wojcicki  
*Stanford University, Stanford, California 94305*

M. Bachman, P. de Cecco, D. Connor, N. Kanematsu, R. Lee, W.R. Molzon  
*University of California, Irvine, California 92697*

M. Eckhause, A.D. Hancock, C.H. Hoff, J.R. Kane, Y. Kuang, R.D. Martin, R.E.  
Welsh, E. Wolin  
*College of William and Mary, Williamsburg, Virginia 23187*

P.D. Rubin  
*University of Richmond, Richmond, Virginia 94305*

### Collaboration Publications

Improved branching ratio measurement of the decay  $K_L^0 \rightarrow \mu^+ \mu^-$ . [2]

First observation of the rare decay mode  $K_L^0 \rightarrow e^+e^-$ . [3]

New limit on muon and electron lepton number violation from  $K_L^0 \rightarrow \mu^\pm e^\mp$  decay. [4]

A compact beam stop for a rare kaon decay experiment. [36]

# APPENDIX B

## Four body phase space transforms

The variables use in the kinematic factors of decay rate as expressed in Eq. (7.18) for  $K_L^0 \rightarrow \mu^+ \mu^- e^+ e^-$  are obtained through a transform of the original particle momenta. For the four body decay the transformation is made according to the relations:

$$\begin{aligned}\vec{p}_{\mu^+} &= \vec{q} + \frac{1}{2}(1 + \lambda)\vec{P} \\ \vec{p}_{e^+} &= \vec{q}' + \frac{1}{2}(1 + \mu)\vec{P} \\ \vec{p}_{\mu^-} &= -\vec{q} + \frac{1}{2}(1 - \lambda)\vec{P} \\ \vec{p}_{e^-} &= -\vec{q}' + \frac{1}{2}(1 - \mu)\vec{P} \\ \vec{q} \cdot \vec{P} &= 0 \\ \vec{q}' \cdot \vec{P}' &= 0\end{aligned}\tag{B.1}$$

From these relations the differential volume elements are obtained as:

$$\begin{aligned} d^3 p_{\mu^+} d^3 p_{\mu^-} &= \frac{1}{2} |\vec{q}| |\vec{P}| |d\vec{q}| d\lambda d\phi d^3 P \\ d^3 p_{e^+} d^3 p_{e^-} &= \frac{1}{2} |\vec{q}'| |\vec{P}'| |d\vec{q}'| d\lambda d\phi d^3 P \end{aligned} \quad (\text{B.2})$$

The phase space volume element  $d\Phi$  is calculated as:

$$d\Phi = \frac{m_\mu^2 m_e^2}{2M_K (2\pi)^8} \frac{d^3 p_{\mu^+} d^3 p_{\mu^-} d^3 p_{e^+} d^3 p_{e^-}}{p_{\mu^+}^0 p_{\mu^-}^0 p_{e^+}^0 p_{e^-}^0} \delta^{(4)}(p_{\mu^+} + p_{\mu^-} + p_{e^+} + p_{e^-} - P_K) \quad (\text{B.3})$$

$P_K$  is introduced as the parent kaon's momentum in order to preserve momentum conservation. Making the substitutions  $\vec{K} = \vec{p}_{\mu^+} + \vec{p}_{\mu^-} = \vec{P}$  and  $\vec{K}' = \vec{p}_{e^+} + \vec{p}_{e^-} = \vec{P}' = -\vec{P}$  Eq. (B.3) may be integrated as:

$$\begin{aligned} I_1 &= \int \frac{d^3 p_{\mu^+} d^3 p_{\mu^-}}{p_{\mu^+}^0 p_{\mu^-}^0} \delta^{(4)}(p_{e^+} + p_{e^-} - K) \\ &= \frac{\pi |\vec{K}|}{K^0} \int d\lambda \end{aligned} \quad (\text{B.4})$$

$$\begin{aligned} I_2 &= \int \frac{d^3 p_{e^+} d^3 p_{e^-}}{p_{e^+}^0 p_{e^-}^0} \delta^{(4)}(p_{\mu^+} + p_{\mu^-} - K') \\ &= \frac{\pi |\vec{K}'|}{K'^0} \int d\mu \end{aligned} \quad (\text{B.5})$$

In Eq. (B.4) and (B.5) the variables  $K^0$  and  $K'^0$  are found through the relations  $K^0 = p_{\mu^+}^0 + p_{\mu^-}^0 = P^0$  and  $K'^0 = p_{e^+}^0 + p_{e^-}^0 = P'^0$ . The full integral then becomes:

$$I = \int d\Phi |\mathcal{M}|^2 = \frac{m_\mu^2 m_e^2 \pi}{8M_K^2 (2\pi)^8} \int dx_1^2 dx_2^2 d\lambda d\mu d\phi d\phi' \frac{|\vec{P}|^3}{P^0 P'^0} |\mathcal{M}|^2 \quad (\text{B.6})$$

The limits of integration for  $\lambda$  and  $\mu$  are determined from the relations:

$$|\vec{q}|^2 = \frac{1}{4}x_1 \left( 1 - \frac{|\vec{P}|^2}{(P^0)^2} \lambda^2 \right) - m_\mu^2 \quad (\text{B.7})$$

$$|\vec{q}'|^2 = \frac{1}{4}x_2 \left( 1 - \frac{|\vec{P}'|^2}{(P'^0)^2} \mu^2 \right) - m_e^2 \quad (\text{B.8})$$

In this manner the integration variables are identified in such a way that  $q$  and  $q'$  correspond to  $y_1$  and  $y_2$  in Eq. (7.18), while  $P$  and  $P'$  correspond to the variables  $x_1$  and  $x_2$ .



## BIBLIOGRAPHY

- [1] GU *et al.*, Phys. Rev. Lett. **76**, 4312 (1996).
- [2] Ambrose *et al.*, Phys. Rev. Lett. **87**, 1398 (2000).
- [3] D. Ambrose *et al.*, Phys. Rev. Lett. **81**, 4309 (1998).
- [4] D. Ambrose *et al.*, Phys. Rev. Lett. **81**, 5734 (1998).
- [5] N. Cabibbo, Phys. Rev. Lett. **10**, 531 (1963).
- [6] M. Kobayashi and T. Maskawa, Prog. Theor. Phys. **49**, 652 (1973).
- [7] L. Wolfenstein, Phys. Rev. Lett. **51**, 1945 (1983).
- [8] L. Sehgal, Phys. Rev. Lett. **183**, 1511 (1969).
- [9] L. Sehgal, Phys. Rev. D **4**, 1582 (1971).
- [10] G. Rochester and C. Butler, Nature (London) **160**, 855 (1947).
- [11] J. Christenson, J. Cronin, V. Fitch, and R. Turlay, Phys. Rev. Lett. **13**, 138 (1964).
- [12] C. Caso *et al.*, European Physical Journal **C**, 010001 (1998).
- [13] N. Collaboration, European Physical Journal **C**, 231 (2001).
- [14] M. Fabbrichesi, Phys. Rev. D **62**, 097902 (2000).
- [15] C. Jarlskog, Phys. Rev. Lett. **55**, 1039 (1985).
- [16] C. Geng and J. Ng, Phys. Rev. D **D41**, 2351 (1990).
- [17] L. Bergström, E. Masso, P. Singer, and D. Wyler, Phys. Lett. **B134**, 373 (1984).

- [18] P. Ko, Phys. Rev. D **45**, 174 (1992).
- [19] J. O. Eeg, K. Krešimir, and I. Picek, preprint (unpublished).
- [20] G. Ambrosio, G. Isidori, and J. Portolé, Phys. Lett. **B**, 385 (1998).
- [21] L. Bergström, E. Masso, and P. Singer, Phys. Lett. **131 B**, 229 (1983).
- [22] J. Goity and L. Zhang, Phys. Lett. **B 398**, 387 (1997).
- [23] J. Goity, Z. Phys. **C**, 341 (1987).
- [24] L. Zhang and J. Goity, Phys. Rev. D **57**, 7031 (1998).
- [25] T. Miyazaki and E. Takasugi, Phys. Rev. D **8**, 2051 (1973).
- [26] C. Yang, Phys. Rev. **77**, 242 (1950).
- [27] Z. E. Uy, Phys. Rev. D **43**, 1572 (1991).
- [28] Z. E. Uy, Phys. Rev. D **43**, 802 (1991).
- [29] A. Alavi-Harati *et al.*, Phys. Rev. Lett. **87**, 111802 (2001).
- [30] J. Belz, hep-ex/9903025 (unpublished).
- [31] Y. Lin and G. Valencia, Phys. Rev. D **37**, 143 (1988).
- [32] A. Alvai-Harati *et al.*, Phys. Rev. Lett. **84**, 408 (2000), kTeV Collaboration.
- [33] A. Heinson *et al.*, Phys. Rev. D **51**, 985 (1995).
- [34] P. Skubic *et al.*, Phys. Rev. D **18**, 3115 (1978).
- [35] M. T. Witkowski, Ph.D. thesis, College of William and Mary in Virginia, 1993.
- [36] J. Belz *et al.*, Nucl. Instrum. Methods **A**, 239 (1999).
- [37] M. Diwan, M. Mar, and M. Pommot-Maia, Technical Report No. KL-445, Brookhaven National Laboratory AGS, (unpublished), e871 internal memorandum.

- [38] M. Sivertz, Technical Report No. KL-115, Brookhaven National Laboratory AGS, (unpublished), e871 internal memorandum.
- [39] D. H. Perkins, *Introduction to High Energy Physics*, 4th ed. (Cambridge University Press, Cambridge, UK, 2000).
- [40] R. C. Fernow, *Introduction to experimental particle physics* (Cambridge University Press, Cambridge, UK, 1986), p. 46.
- [41] D. A. Ambrose, Ph.D. thesis, The University of Texas at Austin, 1998.
- [42] P. Ko, *Phys. Rev. D* **44**, 139 (1991).
- [43] H. Goldstein, *Classical Mechanics* (Addison-Wesley, Reading, MA, 1981).
- [44] A. J. Norman, Honors thesis, College of William and Mary in Virginia, 1995.
- [45] J. Jackson, *Classical Electrodynamics* (John Wiley & Sons, New York, 1975).
- [46] C. Quigg and J. Jackson, Technical Report No. UCRL-18487, University of California, Lawrence Radiation Laboratory (unpublished).

## VITA

### Andrew John Norman

Andrew John Norman was born the fifth day of May 1973 in Towson, Maryland. Graduated from the Thomas Jefferson High School for Science and Technology, Annandale, Virginia in June of 1991. Received a Bachelor of Science in physics and mathematics with high departmental honors, from the College of William and Mary in Virginia, May of 1995. Received a Master of Science degree in physics from the College of William and Mary in Virginia, May of 1998. This dissertation was defended on January 16, 2004 at the College of William and Mary in Virginia.